University Pablo de Olavide
Department of Physical, Chemical and
Natural Systems

METAL-HALIDE PEROVSKITES FOR PHOTOCONVERSION: FABRICATION AT AMBIENT CONDITIONS AND PHOTOELECTROCHEMICAL CHARACTERIZATION

Author:
Lidia Contreras Bernal

Supervisors:

Prof. Dr. Juan A. Anta
Dr. Jesús Idígoras

Seville, March 2019

Universidad Pablo de Olavide
Departamento de Sitemas Físicos, Químicos y Naturales

Juan Antonio Anta, profesor titular vinculado al Departamento de Sistemas Físicos, Químicos y Naturales de la Universidad Pablo de Olavide.

Certifica:

Que la presente memoria titulada **“Metal-Halide Perovskite for Photoconversion: Fabrication at Ambient Conditions and Photoelectrochemical Characterization”** presentada por *Lidia Contreras Bernal* para la obtención del título de Doctor, ha sido realizada bajo mi dirección en el Departamento de Sistemas Físicos, Químicos y Naturales de la Universidad Pablo de Olavide, dentro del programa de doctorado “*Medio Ambiente y Sociedad*” y que cumple los requisitos para poder optar a la Mención Internacional.

Juan A. Anta

Sevilla, Marzo 2019

Papa, esto es lo que he estado haciendo
mientras he estado fuera de casa

Abstract

As a result of the increasing worldwide energy demand and the environmental impacts resulting from the use of fossil fuels, the search for alternative energy resources is gaining more and more importance. In this context, among the different renewable energies, the field of photovoltaics has undergone rapid progress in the last few years due to the development of solar cells based on hybrid organic-inorganic halide perovskite materials. The natural abundance of the precursors employed to synthesise these materials and their excellent optoelectronic properties make them potential competitors of well-established thin-film photovoltaic technologies such as those based on silicon. However, perovskite solar cells have several fundamental issues such as the lack of long-term stability under environmental conditions (moisture, oxygen, heat and light), the requirement of expensive materials as contacts and technical limitations to their industrial scaling that restrict their widespread commercialisation.

The main aim of this thesis is to provide fundamental knowledge and understanding of the physicochemical processes that determine the stability and photovoltaic performance of perovskite solar devices. In particular, small perturbation optoelectronic techniques have been used to look at electronic-ionic processes that cause hysteresis phenomena. They have also been used to identify the main routes of charge recombination for different perovskite devices and under different moisture conditions. Regarding this, simple models for the interpretation of the different signals obtained from small perturbation techniques are also provided in this thesis. Another important contribution of this work refers to the preparation of perovskites under ambient conditions. Here we have found that the traditional use of relative humidity as control parameter to fabricate cells should be replaced by the absolute water amount in the atmosphere in the form of partial water vapour pressure. This last point opens a new window to facilitate the industrial implementation of perovskite solar cells because no glove box would limit the area of the devices.

Contributions to the Scientific Community

The most relevant publications resulting from this thesis are:

1 *Specific cation interactions as the cause of slow dynamics and hysteresis in dye and perovskite solar cells: a small-perturbation study.*
L. Contreras-Bernal, J. Idígoras, A. Todinova, M. Salado, S. Kazim, S. Ahmad and J. A. Anta. *Phys. Chem. Chem. Phys.*, **2016,** 18, 31033–31042.

2 *Origin and Whereabouts of Recombination in Perovskite Solar Cells.*
L. Contreras-Bernal, M. Salado, A. Todinova, L. Calio, S. Ahmad, J. Idígoras and J. A. Anta. *J. Phys. Chem. C*, **2017**, 121, 9705–9713.

3 *Impact of moisture on efficiency-determining electronic processes in perovskite solar cells.*
M. Salado†, L. Contreras-Bernal †, L. Caliò, A. Todinova, C. López-Santos, S. Ahmad, A. Borras, J. Idígoras and J. A. Anta, Impact of moisture on efficiency-determining electronic processes in perovskite solar cells, *J. Mater. Chem. A*, **2017,** 5, 10917–10927.

4 *The Role of Surface Recombination on the Performance of Perovskite Solar Cells: Effect of Morphology and Crystalline Phase of TiO_2 Contact.*
J. Idígoras†, L. Contreras-Bernal †, J. M. Cave, N. E. Courtier, Á. Barranco, A. Borras, J. R. Sánchez-Valencia, J. A. Anta and A. B. Walker. *Adv. Mater. Interfaces*, **2018,** 0, 1801076.

5 *Homeopathic Perovskite Solar Cells: Effect of Humidity during Fabrication on the Performance and Stability of the Device.*
L. Contreras-Bernal, C. Aranda, M. Valles-Pelarda, T. T. Ngo, S. Ramos-Terrón, J. J. Gallardo, J. Navas, A. Guerrero, I. Mora-Seró, J. Idígoras and J. A. Anta,. *J. Phys. Chem. C*, **2018**, 122, 5341–5348.

6 *Water Vapour Pressure as Determining Control Parameter to Fabricate High Efficiency Perovskite Solar Cells at Ambient Conditions.*
L. Contreras-Bernal, J. J. Gallardo, J. Navas, J. Idígoras and J. A. Anta.
Manuscript submitted to Energy & Environmental Science and ArXiv.**2019**.

7 *Impedance Analysis of Perovskite Solar Cells: a Case Study.*
L. Contreras-Bernal†, S. Ramos-Terrón†, A. Riquelme, P. Boix, J. Idígoras, I. Mora-Seró and J. A. Anta.
Manuscript in preparation.

Other publications closely related to this thesis are listed below:

1 *Towards a Universal Approach for the Analysis of Impedance Spectra of Perovskite Solar Cells: Equivalent Circuits and Empirical Analysis.*
A. Todinova, L. Contreras-Bernal, M. Salado, S. Ahmad, N. Morillo, J. Idígoras and J. A. Anta. *ChemElectroChem*, **2017**, 4, 2891–2901.

2 *Enhancing Moisture and Water Resistance in Perovskite Solar Cells by Encapsulation with Ultrathin Plasma Polymers.*
J. Idígoras, F. J. Aparicio, L. Contreras-Bernal, S. Ramos-Terrón, M. Alcaire, J. R. Sánchez-Valencia, A. Borras, Á. Barranco and J. A. Anta. *ACS Appl. Mater. Interfaces*, **2018**, 10, 11587–11594.

3 *Understanding the Influence of Interface Morphology on the Performance of Perovskite Solar Cells.*
M. Salado, L. Calió, L. Contreras-Bernal, J. Idígoras, J. A. Anta, S. Ahmad and S. Kazim. *Materials*, **2018**, 11, 1073.

[†] The authors have equally contributed for the paper

Contents

Chapter 1

Introduction

In this Chapter, the global and specific context in which this thesis has been developed is described. In particular, a brief introduction of how energy landscape and emerging photovoltaic technologies have changed in the last years is presented. A detailed description of organic-inorganic halide perovskites including physicochemical information and their potential properties to govern the photovoltaic field is shown. Finally, the motivation and objectives of this thesis are exposed.

1.1 General context

Starting from the idea that the climate change is already a current reality due to the greenhouse gases produced as consequence of human actions,[1,2] part of the scientific and industrial community have focused its efforts on the development of technology able to exploit alternative energy resources. From industrial revolution (1760), the carbon dioxide (CO_2) levels in the atmosphere have dramatically increased due to the use of fossil fuels (coal and oil) as energy resource. In particular, CO_2 levels surpass 400 ppm in current times.[3] This trend is associated with a higher global energy demand which is predicted to even increase 30% in 2040.[4]

In this context, renewable energies have arisen as alternative to fossil fuels. In fact, it was forecasted that renewable sources will provide 30% of power demand in 2023 up from 24% recorded in 2017.[5] Considering the different types of renewables, solar energy is the most promising alternative to fossil fuels due to the constant energy flux from the Sun and its incidence all over the planet Earth. In this scenario, the scientific community has paid special attention to the development of photovoltaic (PV) technologies in order to take advantage this inexhaustible source of energy.[4,6]

1.1.1 Development of PV technology

The first generation of solar cells was rapidly developed in 1950s and it was based on either single crystalline or polycrystalline silicon wafers as well as gallium arsenide wafers (Scheme 1.1).[6,7] Currently, they are the most widely commercialised solar cells due to its high power conversion efficiency (PCE) (current world records are 24.4 % and 19.9 % for single and polycrystalline crystalline silicon modules, respectively).[8] The problem with this technology is that efficient devices do not only require a huge amount of material (thickness of 100-500 µm), but also a high purity level. These two factors result in high manufacturing costs.

As consequence, a second generation of PV technology arose in 1970s (Scheme 1.1) based on thin-films solar cells. These PV devices reduce the cost due to the smaller amount of material employed to fabricate them with a thickness in the nm-µm range. Commercial thin-film devices of this second generation include amorphous silicon (a-Si)[9], cadmium telluride (CdTe)[10] and copper indium gallium selenide (CIGS)[11]. Among them, the solar modules based on CdTe and CIGS show competitive PCE of 18.6 % and 19.2 %, respectively.[12] The drawback of these devices is that they require high temperature treatment as well as raw materials with a low availability.

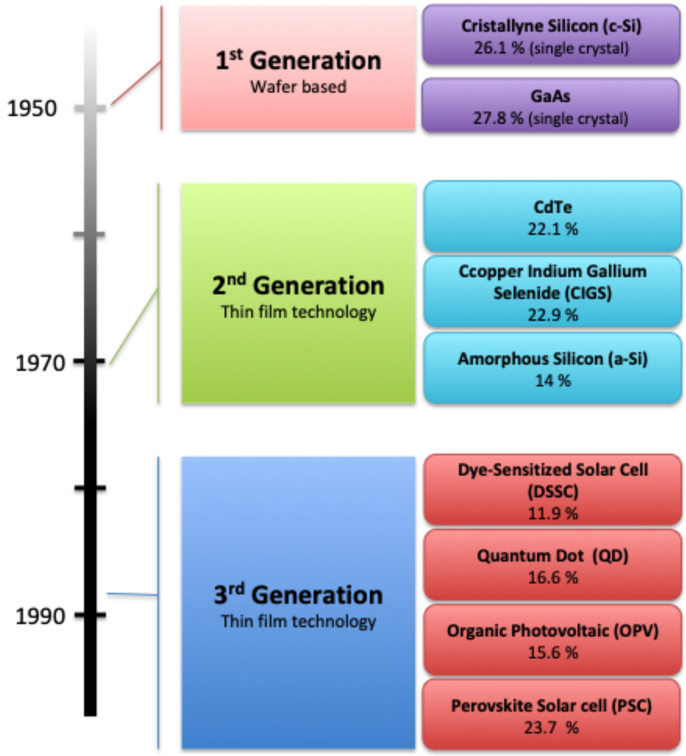

Scheme 1.1 Scheme of evolution of photovoltaic technology. Here we shown the record efficiency for every solar cell type certified by National Renewable Energy Laboratory (NREL) (5 February 2019).[8]

The recent development of nanotechnology led to third generation PV generation of PV devices in 1980s (Scheme 1.1).[7] In particular, this technology is based on non-toxic, cheap and abundant materials. The third generation PV technology involves dye-sensitized solar cells (DSSCs),[13] organic photovoltaic (OPV),[14] quantum dot (QD)[15] and perovskite solar cells (PSCs)[16], being the latest the main research topic of this thesis.

1.1.2 Perovskite solar devices

A perovskite material was for the first time used in the PV field in 2009 for Miyasaka *et. al* as a visible light sensitizer for TiO_2 electrodes in DSSCs, obtaining a PCE of 3.8%.[17] However, the fabricated devices were very unstable due to the employment of liquid solvent electrolyte similar to DSSCs, and to the incompatibility between the solvent electrolyte and the perovskite material. Thus, new solid-state hole conductor materials compatible with perovskites were investigated in order to guarantee long-tern device stability. In this way, a PCE of 15% was achieved in 2013 for perovskite solar cells in a planar device configuration.[18] More interestingly, it was demonstrated that the perovskite material itself in contact with an insulating mesoporous (Al_2O_3) scaffold was also capable of producing efficiencies exceeding 12%.[19] This finding was crucial because it demonstrated that this material was not only a good light harvester, but also, an efficient intrinsic semiconductor able to separate photogenerated charges.[20,21] Since then, these excellent optoelectronic properties fuelled intense research aimed at improving the photovoltaic performance of these PV devices by using different deposition methods, synthesis techniques and new perovskite compositions and selective contacts.[22–26] Indeed, the published papers rate related to PV field has growth in the same way that those related with perovskite solar cells (Fig. 1.1). Up today, the current certificated PCE published for a perovskite solar cell is 23.7% (February 2019), meaning that this concept is already a potential competitor of well-established thin film photovoltaic technologies such as those based on silicon.[20,21,27]

Nevertheless, some issues must be solved before commercialization. For instance, it has been demonstrated a thermal and electrical instability under operation as well as a short lifetime at environmental conditions. In addition, new manufacturing methods are required to be industrially scalable.[28,29]

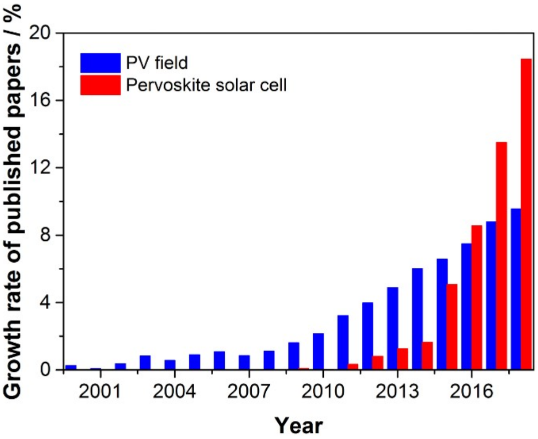

Figure 1.1. Growth rate of published articles in the photovoltaic (PV) field (blue bar) and those attributed to perovskite solar cells (PSCs) (red bar). Data have been obtained from the ScienceDirect web for the time period between 1 January 2000 and 31 December 2018.

In spite of these limitations, it has been recently demonstrated that perovskite materials can be used as a ground technology not just for PV applications but also for light emission (LED, lasing) and photocatalysis. The latter is based on the direct conversion of solar energy into chemical products of high-added value. This is the case of the water splitting process to generate H_2 and O_2 or the photoreduction of CO_2 to obtain carbon-based fuels.[30,31]

1.1.2.1 Photovoltaic perovskites

The perovskite term covers a wide range of materials with a characteristic crystal structure, similar to the mineral perovskite $CaTiO_3$. The generic formula of perovskite material is ABX_3 where A and B are cations of different size (A being larger than B) and X is an anion. The charge balance, expressed by the equation $q^A + q^B + 3q^X = 0$, can be achieved in a variety of ways. For an oxidised perovskite material (ABO_3), the formal oxidation state of the cations must be equal to six to compensate the negative charge from oxygen anions ($q^A + q^B = - 3q^O = 6$), so different combinations of A and B cations valences are possible.[32] For these perovskites, A is usually a rare or alkaline earth metal and B is a first row transition metal, for example $GaFeO_3$ and $KTaO_3$. These materials have been used as electronic, structural, magnetic and refractory materials in numerous applications due to its ferro-, piezo-, and pyroelectrical properties and optoelectronic characteristics.[33]

However, for PV applications, X is a halide anion (F^-, Cl^-, Br^-, I^-), so there is only a possible combination of the cations valences to achieve a compensated charge balance ($q^A + q^B = - 3q^X = 3$): A must be an organic or inorganic monovalent cation such as methylammonium (MA: $CH_3NH_3^+$), formamidinium (FA: $CH_2(NH_2)_2^+$), Cesium (Cs^+) or Rubidium, (Rb^+), whereas B is a divalent inorganic cation like lead (Pb^{2+}) or tin (Sn^{2+}).

1.1.2.2 Crystal structure

In the case of halide perovskite, B and X ions form BX_6^{4-} octahedral cages, where the A cation is placed in the cavity between eight of these octahedra to balance the charge of the entire three-dimensional network (Fig. 1.2).

In the *3D* perovskite structure, infinite sheets of inorganic layer (BX_6^{4-} octahedral) are formed ($n = \infty$). Within BX_6^{4-} anionic frameworks, a mixture of ionic and covalent interactions are established as bonds, while the nature of the interaction between A cation and the BX_6^{4-} frameworks is mainly an electrostatic interaction.[34]

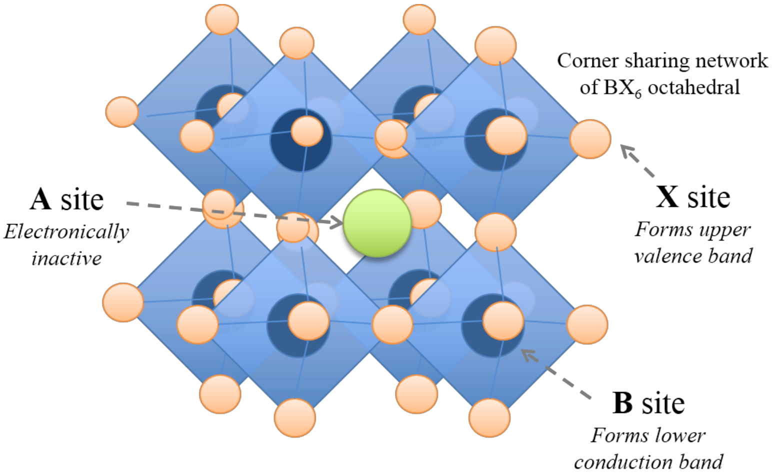

Figure 1.2. Schematic of the perovskite crystal structure with respect A, B and X lattice sites.

Although the orthorhombic crystal structure is the most stable,[35] the fact is that different crystal structures are possible for metal halide perovskites depending on two geometrical parameters: the *tolerance factor* (t) and the *octahedral factor* (μ). The first one, t parameter, was defined in 1927 by Goldschmidt for ABX_3 type perovskite as criteria to determine the crystal structure. It can be written as

$$t = \frac{(r_A + r_x)}{\left(2^{\frac{1}{2}}[r_B + r_x]\right)} \qquad (1.1)$$

where r_A, r_B and r_x are the ionic radius of A cation, B metal cation and X anions, respectively. For a stable perovskite structure, the t parameter must have values in the range of 0.81-1.11. Nevertheless, depending on the ionic radius, different crystal structures can exist. In particular, for t values in the range of 0.89-1.00, the cubic structure is more probable, while for a lower t value a less-symmetric tetragonal or orthorhombic structure is more probable.[36] However, materials such as $KNiCl_3$, $RbMnBr_3$ or $CsMnI_3$ with a t value within the most favorable range (0.976, 0.933 and 0.952, respectively) show an unstable perovskite structure. Therefore, the t parameter is not enough by itself to predict the formation of a stable perovskite structure. For this reason, the octahedral factor is also used, in combination with the t parameter for ABX_3 type perovskite. The μ parameter is given by

$$\mu = \frac{r_B}{r_X} \qquad (2.2)$$

The μ parameter determines the stability of the coordination octahedral structure BX_6^{4-} and takes values in the range 0.44-0.90 for a stable perovskite crystalline structure. By using both the t and μ parameters almost all perovskite structures can be predicted.[37]

The introduction of large organic cations in the perovskite structure leads to lower-dimensional systems: *2D* perovskite (n=1) and quasi-*2D* perovskite (or a *2D* + *3D* perovskite) (n >1), with a t value higher than 1.[38] For these perovskites, the BX_6^{4-} octahedral are separated by the large organic cations which do not fit into the structure. In these types of perovskites the hydrogen bonds are essential to stabilize the structure. *2D* and quasi-*2D* perovskites show a lower thermal stability and PCE than *3D* perovskites. However, due to its enhanced resistance towards humidity, they are receiving a lot of attention nowadays as alternative to *3D* perovskite.

As said above, the introduction of the ions with different sizes in the crystal structure leads to perovskite materials with different crystal phases due to a change of t and μ values. However, another factor that highly determine the transitions between the different phases is temperature. For instance, although $MAPbI_3$ (the most widely used perovskite) satisfies perfectly the tolerance and octahedral factor (t= 0.83 and μ= 0.54), it shows three different phases depending on the temperature: orthorhombic, tetragonal and cubic crystalline phase. In particular, the phase transitions for that perovskite material occur at 165 K and 327 K. This behaviour is due to disorder of the organic cation in the crystal as well as to the response of the PbI_6^{4-} octahedra in MA orientations under different temperatures.[39]

1.1.2.3 Optoelectronic properties

Organic-inorganic halide perovskites are semiconductors in which the conduction band (*CB*) is originated from combining antibonding *p* orbitals (π*) of *B* cations and antiboding *s* orbitals (s*) of *X* anions, whereas the valence band (*VB*) is determined by hybridation between s* of *B* cations and π* of *X* anions.[34] Thus, substitution of *B* and *X* sites involves the alteration of the *VB* and *CB*, while the *A* site only can have an indirect influence on the band gap, via a change in the crystal structure (Fig. 1.2). For instance, it has been reported that the replacement of MA-cation with FA-cation leads to red-shift in the emission peak, owing to the band gap change from 1.57 eV to 1.48 eV, respectively (Fig. 1.3).[40,41] In general, perovskite material shows a *tuneable band gap* from 1.5 to 3.6 eV,[42] which means that perovskites can show an optical absorption along solar spectrum. Regarding this, a *direct band gap* has been attributed to this material due to rapid increase of the absorption coefficient with the band gap as well as the increase of radiative recombination by decreasing the temperature.[43,44]

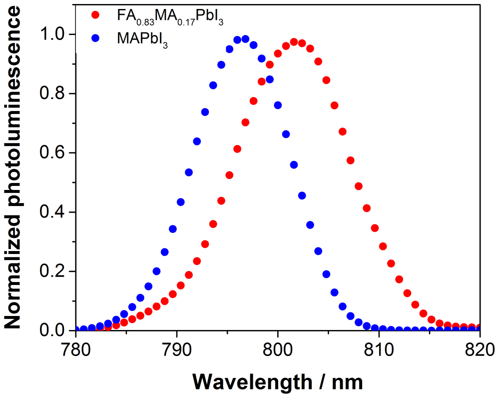

Figure 1.3. Steady-state photoluminescence spectra for $MAPbI_3$ and $FA_{0.83}MA_{0.17}PbI_3$ perovskite films prepared at ambient conditions of 1.7 kPa (see *Chapter* 10).

On the other hand, one of the main properties of perovskites is its *high defect tolerance,* which arises from the antibonding nature of *VB* and low defect density within the band gap.[43] This property is associated with the high photoluminescence (PL) yields[45] and a low non-radiative recombination rate.[46] These properties make that perovskite devices show open-circuit photovoltages very close to the thermodynamic limit (see *Chapter* 2 Eqs. 2.23 and 2.24). For instance, open-circuit photovoltage higher than 1.2 V are obtained for materials with a band gap 1.6 eV.[43]

Another interesting property of these materials is its *high charge mobility* of the order of tens $cm^2/V\cdot s$, which is related to a relatively strong ionicity of the metal-halide bond and the weak carrier-phonon interaction.[46,47] As a consequence of this high charge mobility and low non-radiative recombination, perovskite materials are characterized by charge *diffusion lengths* close to micrometres under solar illumination density.[20,48]

1.1.2.4 Architecture of perovskite solar cells

In perovskite solar cells, light absorption is produced in a perovskite layer that is sandwiched between an electron selective material (ESM) and a hole selective material (HSM). The complementary selectivities allow for separation and collection of the photogenerated charge carriers. These contacts are also called electron transport material (ETM) and hole transport material (HTM), respectively. To electrically close these devices, one of selective materials is usually deposited on a front electrode (glass coated of fluorine-doped tin oxide (FTO) or Tin Oxide (ITO)), while over the other selective layer is evaporated a metallic contact (Au, Ag, or Ni) or carbon film as a counter electrode.

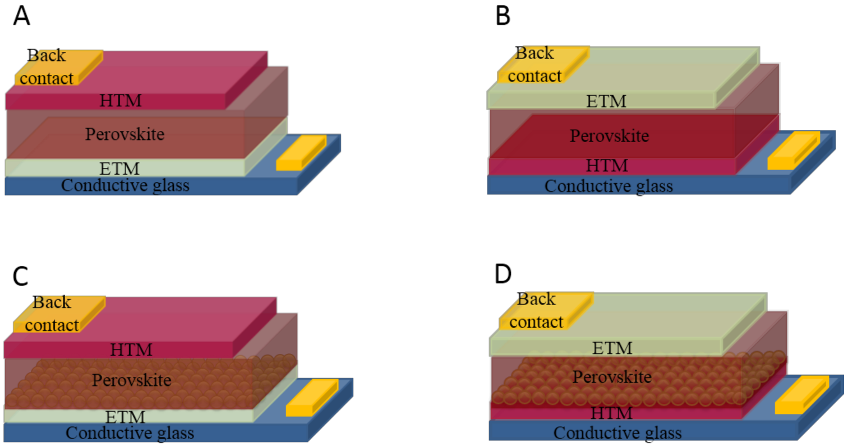

Figure 1.4. Schematic of regular (A and C) and inverted (B and D) architecture of perovskite solar cells. A) and B) represent a planar configuration while C) and D) include a mesoporous layer.

Depending on the position of ETM with respect to the front electrode, two different architectures are distinguished: regular (*n-i-p*) and inverted (*p-i-n*) architecture in which the ETM or HTM is in contact with the glass substrate, respectively.[23,49] On the other hand, depending on the presence or absence of mesoporous materials as scaffold to the perovskite deposition, two other different architectures have been studied: planar and mesoporous (Fig. 1.4).[50,51]

The most common PSC design is based on a regular mesoporous (*n-i-p*) architecture that involves a mesoporous TiO_2 scaffold in which the perovskite is infiltrated, enhancing the contact area between active layer and ETM. The mesoporous layer is usually deposited on top of a compact TiO_2 layer to avoid the direct contact between deposited perovskite material and FTO (Fig. 1.4C). The highest efficiencies have been reported for PSCs with regular mesoporous architecture.[23,52] However, the high temperatures required during the TiO_2 deposition method make impossible the fabrication of flexible solar cells, where substrates based on conductive plastic would be employed.

Although the most common material employed as ESM is TiO_2, different metal oxides such as ZnO, Al_2O_3, ZrO_2, SiO_2 or even hetero-structures nanoparticles as Al_2O_3/ZnO have been investigated.[19,24,53–55] In fact, not only different materials have been employed, but also different nanostructures. Nevertheless, up to date, the state-of-the-art photovoltaic performance in PSCs has been found for devices based on TiO_2 as ESM, in which a small molecule called 2,2',7,7'-tetrakis-(N,N-di-4-methoxyphenyl-amino)-9,9'spirobi-fluorene (spiro-OMeTAD) has been used as HSM (Fig. 1.5). [23,56] However, this molecule needs to be doped with lithium and cobalt salts to increase the mobility of the spiro-

OMeTAD and with 4-tert-butylpiridine (TBP) to improve the hole density. The addition of these substances reduce the stability of the device under ambient conditions, due to, among other factors, their tendency to absorb water.[57]

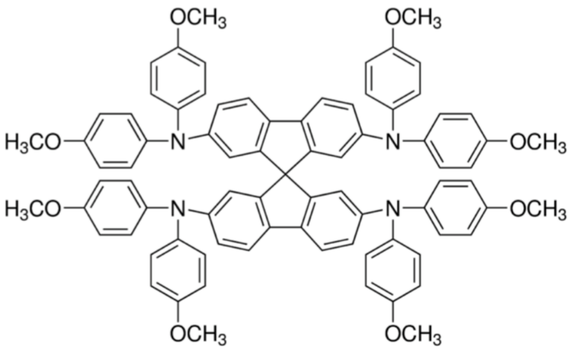

Figure 1.5. Chemical structure of spiro-OMeTAD.

In addition, the spiro-OMeTAD needs a high-purity sublimation-grade and expensive multi-step synthesis to obtain high performance devices which leads to higher fabrication cost per devices. For these reasons, alternative HTMs based on small molecules[58], polymeric[59], carbon based[60] and inorganic materials[61], and the use of new dopants[62] have been investigated.

1.2 Motivation and objectives

In connection with the above, understanding the physicochemical and electronic processes that determine the photovoltaic performance and stability of PSCs is the key factor for the optimization and commercialization of these solar devices. In this context, two general objectives are set in this thesis:

1. To provide a deep and fundamental knowledge of the different electronic mechanisms that determine the photovoltaic behaviour of perovskite solar cells.

2. The study of PSCs prepared under ambient conditions to optimize its fabrication towards their application in industry.

In relation to the first objective, small perturbation optoelectronic techniques have been used to understand the charge recombination mechanisms that determine the photovoltage performance in PSCs of different architectures and under different moisture conditions. These techniques were also applied to explain the hysteresis phenomenon, which is known to be linked to the instability issues in perovskite devices. Simultaneously, we bring here models for the interpretation of information extracted from small perturbation techniques. Finally, we will provide a new parameter control to develop high efficiency PSCs deposited under ambient conditions in order to avoid the use of a glove box, which limits the area of devices.

A brief theoretical description of PSCs as well as of the materials and methods used for this thesis are collected in *Chapters* 2 and 3, respectively. The main results are presented and discussed in the subsequent seven chapters. In particular, in *Chapter* 4, the hysteresis behaviour in PSCs is studied by comparing these devices with “traditional” dye sensitized solar cells, DSSCs, which are used as a model to understand the processes occurring in the ionic lattice of the perovskite materials. In *Chapter* 5, we analyse small perturbation measurements and, propose a model that describes adequately charge recombination in PSCs at open circuit. In *Chapter* 6, the effect of morphology and crystalline phase of electron selective contact in the performance of perovskite devices is analysed. In *Chapter* 7, the impact of moisture on the photovoltaic response of different PSC configurations is investigated. In *Chapter* 8, we show what information can be extracted of small perturbation techniques and how it is used it to explain different electronic phenomena in PSCs. In *Chapter* 9, we studied the stability of PSCs prepared under different humidity conditions to relate it with the relative humidity of ambient. In *Chapter* 10, we demonstrate that it is the water vapour pressure the determining control parameter to fabricate high efficiency PSCs at ambient conditions.

1.3 References

1 N. Oreskes, The Scientific Consensus on Climate Change, *Science*, 2004, **306**, 1686–1686.

2 P. C. Jain, Greenhouse effect and climate change: scientific basis and overview, *Renew. Energy*, 1993, **3**, 403–420.

3 Climate Change, https://climate.nasa.gov/, (accessed January 27, 2019).

4 Emissions, https://www.iea.org/geco/emissions/, (accessed January 9, 2019).

5 Renewables 2018, https://www.iea.org/renewables2018/, (accessed January 28, 2019).

6 V. V. Tyagi, N. A. A. Rahim, N. A. Rahim and J. A. /L. Selvaraj, Progress in solar PV technology: Research and achievement, *Renew. Sustain. Energy Rev.*, 2013, **20**, 443–461.

7 T. M. Razykov, C. S. Ferekides, D. Morel, E. Stefanakos, H. S. Ullal and H. M. Upadhyaya, Solar photovoltaic electricity: Current status and future prospects, *Sol. Energy*, 2011, **85**, 1580–1608.

8 Photovoltaic Research | NREL, https://www.nrel.gov/pv/, (accessed February 5, 2019).

9 R. Galloni, Amorphous silicon solar cells, *Renew. Energy*, 1996, **8**, 400–404.

10 T. Repän, S. Pikker, L. Dolgov, A. Loot, J. Hiie, M. Krunks and I. Sildos, Increased Efficiency inside the CdTe Solar Cell Absorber Caused by Plasmonic Metal Nanoparticles, *Energy Procedia*, 2014, **44**, 229–233.

11 C. Radue, E. E. van Dyk and E. Q. Macabebe, Analysis of performance and device parameters of CIGS PV modules deployed outdoors, *Thin Solid Films*, 2009, **517**, 2383–2385.

12 Photovoltaic Research | NREL, https://www.nrel.gov/pv/, (accessed January 29, 2019).

13 B. O’Regan and M. Grätzel, A low-cost, high-efficiency solar cell based on dye-sensitized colloidal TiO2 films, *Nature*, 1991, **353**, 737–740.

14 A. M. Bagher, Introduction to Organic Solar Cells, *Sustain. Energy*, 2014, **2**, 85–90.

15 J. H. Song and S. Jeong, Colloidal quantum dot based solar cells: from materials to devices, *Nano Converg.*, 2017, **4**, 21.

16 M. A. Green, A. Ho-Baillie and H. J. Snaith, The emergence of perovskite solar cells, *Nat. Photonics*, 2014, **8**, 506.

17 A. Kojima, K. Teshima, Y. Shirai and T. Miyasaka, Organometal Halide Perovskites as Visible-Light Sensitizers for Photovoltaic Cells, *J. Am. Chem. Soc.*, 2009, **131**, 6050–6051.

18 M. Liu, M. B. Johnston and H. J. Snaith, Efficient planar heterojunction perovskite solar cells by vapour deposition, *Nature*, 2013, **501**, 395–398.

19 J. M. Ball, M. M. Lee, A. Hey and H. J. Snaith, Low-temperature processed meso-superstructured to thin-film perovskite solar cells, *Energy Environ. Sci.*, 2013, **6**, 1739.

20 G. Xing, N. Mathews, S. Sun, S. S. Lim, Y. M. Lam, M. Gratzel, S. Mhaisalkar and T. C. Sum, Long-Range Balanced Electron- and Hole-Transport Lengths in Organic-Inorganic CH3NH3PbI3, *Science*, 2013, **342**, 344–347.

21 S. D. Stranks, G. E. Eperon, G. Grancini, C. Menelaou, M. J. P. Alcocer, T. Leijtens, L. M. Herz, A. Petrozza and H. J. Snaith, Electron-Hole Diffusion Lengths Exceeding 1 Micrometer in an Organometal Trihalide Perovskite Absorber, *Science*, 2013, **342**, 341–344.

22 E. H. Anaraki, A. Kermanpur, L. Steier, K. Domanski, T. Matsui, W. Tress, M. Saliba, A. Abate, M. Grätzel, A. Hagfeldt and J.-P. Correa-Baena, Highly efficient and stable planar perovskite solar cells by solution-processed tin oxide, *Energy Environ. Sci.*, 2016, **9**, 3128–3134.

23 M. Saliba, T. Matsui, J.-Y. Seo, K. Domanski, J.-P. Correa-Baena, M. K. Nazeeruddin, S. M. Zakeeruddin, W. Tress, A. Abate, A. Hagfeldt and M. Grätzel, Cesium-containing triple cation perovskite solar cells: improved stability, reproducibility and high efficiency, *Energy Environ. Sci.*, 2016, **9**, 1989–1997.

24 M. Saliba, T. Matsui, K. Domanski, J.-Y. Seo, A. Ummadisingu, S. M. Zakeeruddin, J.-P. Correa-Baena, W. R. Tress, A. Abate, A. Hagfeldt and M. Gratzel, Incorporation of rubidium cations into perovskite solar cells improves photovoltaic performance, *Science*, 2016, **354**, 206–209.

25 J. Ávila, C. Momblona, P. P. Boix, M. Sessolo and H. J. Bolink, Vapor-Deposited Perovskites: The Route to High-Performance Solar Cell Production?, *Joule*, 2017, **1**, 431–442.

26 S. Carli, J. P. C. Baena, G. Marianetti, N. Marchetti, M. Lessi, A. Abate, S. Caramori, M. Grätzel, F. Bellina, C. A. Bignozzi and A. Hagfeldt, A New 1,3,4-Oxadiazole-Based Hole-Transport Material for Efficient CH $_3$\$ NH $_3$\$ PbBr $_3$\$ Perovskite Solar Cells, *ChemSusChem*, 2016, **9**, 657–661.

27 W. Tress, N. Marinova, O. Inganäs, M. K. Nazeeruddin, S. M. Zakeeruddin and M. Graetzel, Predicting the Open-Circuit Voltage of CH $_3$ NH

$_{3}$ PbI $_{3}$ Perovskite Solar Cells Using Electroluminescence and Photovoltaic Quantum Efficiency Spectra: the Role of Radiative and Non-Radiative Recombination, *Adv. Energy Mater.*, 2015, **5**, 1400812.

28 L. Qiu, L. K. Ono and Y. Qi, Advances and challenges to the commercialization of organic–inorganic halide perovskite solar cell technology, *Mater. Today Energy*, 2018, **7**, 169–189.

29 A. Abate, J.-P. Correa-Baena, M. Saliba, M. S. Su'ait and F. Bella, Perovskite Solar Cells: From the Laboratory to the Assembly Line, *Chem. - Eur. J.*, 2018, **24**, 3083–3100.

30 M. Schreier, L. Curvat, F. Giordano, L. Steier, A. Abate, S. M. Zakeeruddin, J. Luo, M. T. Mayer and M. Grätzel, Efficient photosynthesis of carbon monoxide from CO2 using perovskite photovoltaics, *Nat. Commun.*, 2015, **6**, 7326.

31 M. Moniruddin, B. Ilyassov, X. Zhao, E. Smith, T. Serikov, N. Ibrayev, R. Asmatulu and N. Nuraje, Recent progress on perovskite materials in photovoltaic and water splitting applications, *Mater. Today Energy*, 2018, **7**, 246–259.

32 J. M. Frost and A. Walsh, in *Organic-Inorganic Halide Perovskite Photovoltaics*, eds. N.-G. Park, M. Grätzel and T. Miyasaka, Springer International Publishing, Cham, 2016, pp. 1–17.

33 E. Grabowska, Selected perovskite oxides: Characterization, preparation and photocatalytic properties—A review, *Appl. Catal. B Environ.*, 2016, **186**, 97–126.

34 A. Walsh, Principles of Chemical Bonding and Band Gap Engineering in Hybrid Organic–Inorganic Halide Perovskites, *J. Phys. Chem. C*, 2015, **119**, 5755–5760.

35 F. Shojaei and W.-J. Yin, Stability Trend of Tilted Perovskites, *J. Phys. Chem. C*, 2018, **122**, 15214–15219.

36 Z. Wang, Z. Shi, T. Li, Y. Chen and W. Huang, Stability of Perovskite Solar Cells: A Prospective on the Substitution of the A Cation and X Anion, *Angew. Chem. Int. Ed.*, 2017, **56**, 1190–1212.

37 C. Li, X. Lu, W. Ding, L. Feng, Y. Gao and Z. Guo, Formability of (= F, Cl, Br, I) halide perovskites, *Acta Crystallogr. B*, 2008, **64**, 702–707.

38 The merit of perovskite's dimensionality; can this replace the 3D halide perovskite? - Energy & Environmental Science (RSC Publishing), https://pubs.rsc.org/en/content/articlelanding/2018/ee/c7ee03397d#!divAbstract, (accessed October 11, 2018).

39 M. T. Weller, O. J. Weber, P. F. Henry, A. M. Di Pumpo and T. C. Hansen, Complete structure and cation orientation in the perovskite photovoltaic methylammonium lead iodide between 100 and 352 K, *Chem. Commun.*, 2015, **51**, 4180–4183.

40 N. Pellet, P. Gao, G. Gregori, T.-Y. Yang, M. K. Nazeeruddin, J. Maier and M. Grätzel, Mixed-Organic-Cation Perovskite Photovoltaics for Enhanced Solar-Light Harvesting, *Angew. Chem. Int. Ed.*, 2014, **53**, 3151–3157.

41 G. E. Eperon, S. D. Stranks, C. Menelaou, M. B. Johnston, L. M. Herz and H. J. Snaith, Formamidinium lead trihalide: a broadly tunable perovskite for efficient planar heterojunction solar cells, *Energy Environ. Sci.*, 2014, **7**, 982.

42 M. Saliba, J.-P. Correa-Baena, M. Grätzel, A. Hagfeldt and A. Abate, Perovskite Solar Cells: From the Atomic Level to Film Quality and Device Performance, *Angew. Chem. Int. Ed.*, **57**, 2554–2569.

43 W. Tress, Perovskite Solar Cells on the Way to Their Radiative Efficiency Limit - Insights Into a Success Story of High Open-Circuit Voltage and Low Recombination, *Adv. Energy Mater.*, 2017, **7**, 1602358.

44 V. Sarritzu, N. Sestu, D. Marongiu, X. Chang, Q. Wang, S. Masi, S. Colella, A. Rizzo, A. Gocalinska, E. Pelucchi, M. L. Mercuri, F. Quochi, M. Saba, A. Mura and G. Bongiovanni, Direct or Indirect Bandgap in Hybrid Lead Halide Perovskites?, *Adv. Opt. Mater.*, 2018, **6**, 1701254.

45 F. Deschler, M. Price, S. Pathak, L. E. Klintberg, D.-D. Jarausch, R. Higler, S. Hüttner, T. Leijtens, S. D. Stranks, H. J. Snaith, M. Atatüre, R. T. Phillips and R. H. Friend, High Photoluminescence Efficiency and Optically Pumped Lasing in Solution-Processed Mixed Halide Perovskite Semiconductors, *J. Phys. Chem. Lett.*, 2014, **5**, 1421–1426.

46 C. S. Ponseca, T. J. Savenije, M. Abdellah, K. Zheng, A. Yartsev, T. Pascher, T. Harlang, P. Chabera, T. Pullerits, A. Stepanov, J.-P. Wolf and V. Sundström, Organometal Halide Perovskite Solar Cell Materials Rationalized: Ultrafast Charge Generation, High and Microsecond-Long Balanced Mobilities, and Slow Recombination, *J. Am. Chem. Soc.*, 2014, **136**, 5189–5192.

47 L. M. Herz, Charge-Carrier Mobilities in Metal Halide Perovskites: Fundamental Mechanisms and Limits, *ACS Energy Lett.*, 2017, **2**, 1539–1548.

48 M. B. Johnston and L. M. Herz, Hybrid Perovskites for Photovoltaics: Charge-Carrier Recombination, Diffusion, and Radiative Efficiencies, *Acc. Chem. Res.*, 2016, **49**, 146–154.

49 S. Ye, W. Sun, Y. Li, W. Yan, H. Peng, Z. Bian, Z. Liu and C. Huang, CuSCN-Based Inverted Planar Perovskite Solar Cell with an Average PCE of 15.6%, *Nano Lett.*, 2015, **15**, 3723–3728.

50 K. Yao, F. Li, Q. He, X. Wang, Y. Jiang, H. Huang and A. K.-Y. Jen, A

copper-doped nickel oxide bilayer for enhancing efficiency and stability of hysteresis-free inverted mesoporous perovskite solar cells, *Nano Energy*, 2017, **40**, 155–162.

51 B. Hailegnaw, G. Adam, H. Heilbrunner, D. H. Apaydin, C. Ulbricht, N. S. Sariciftci and M. C. Scharber, Inverted (p–i–n) perovskite solar cells using a low temperature processed TiO interlayer, *RSC Adv.*, 2018, **8**, 24836–24846.

52 A. D. Jodlowski, C. Roldán-Carmona, G. Grancini, M. Salado, M. Ralaiarisoa, S. Ahmad, N. Koch, L. Camacho, G. de Miguel and M. K. Nazeeruddin, Large guanidinium cation mixed with methylammonium in lead iodide perovskites for 19% efficient solar cells, *Nat. Energy*, 2017, **2**, 972–979.

53 X. Xu, Z. Liu, Z. Zuo, M. Zhang, Z. Zhao, Y. Shen, H. Zhou, Q. Chen, Y. Yang and M. Wang, Hole Selective NiO Contact for Efficient Perovskite Solar Cells with Carbon Electrode, *Nano Lett.*, 2015, **15**, 2402–2408.

54 A. K. Chandiran, M. Abdi-Jalebi, A. Yella, M. I. Dar, C. Yi, S. A. Shivashankar, M. K. Nazeeruddin and M. Grätzel, Quantum-Confined ZnO Nanoshell Photoanodes for Mesoscopic Solar Cells, *Nano Lett.*, 2014, **14**, 1190–1195.

55 S. H. Hwang, J. Roh, J. Lee, J. Ryu, J. Yun and J. Jang, Size-controlled SiO nanoparticles as scaffold layers in thin-film perovskite solar cells, *J Mater Chem A*, 2014, **2**, 16429–16433.

56 K. T. Cho, S. Paek, G. Grancini, C. Roldán-Carmona, P. Gao, Y. Lee and M. K. Nazeeruddin, Highly efficient perovskite solar cells with a compositionally engineered perovskite/hole transporting material interface, *Energy Environ. Sci.*, 2017, **10**, 621–627.

57 Z. Hawash, L. K. Ono and Y. Qi, Recent Advances in Spiro-MeOTAD Hole Transport Material and Its Applications in Organic–Inorganic Halide Perovskite Solar Cells, *Adv. Mater. Interfaces*, 2017, **5**, 1700623.

58 L. Caliò, S. Kazim, M. Salado, I. Zimmermann, M. K. Nazeeruddin and S. Ahmad, Design of cyclopentadithiophene-based small organic molecules as hole selective layers for perovskite solar cells, *Sustain. Energy Fuels*, , DOI:10.1039/C8SE00119G.

59 S. Park, J. H. Heo, J. H. Yun, T. S. Jung, K. Kwak, M. J. Ko, C. H. Cheon, J. Y. Kim, S. H. Im and H. J. Son, Effect of multi-armed triphenylamine-based hole transporting materials for high performance perovskite solar cells, *Chem. Sci.*, 2016, **7**, 5517–5522.

60 Q.-D. Yang‡, J. Li, Y. Cheng, H.-W. Li, Z. Guan, B. Yu and S.-W. Tsang, Graphene oxide as an efficient hole-transporting material for high-performance perovskite solar cells with enhanced stability, *J. Mater. Chem. A*,

2017, **5**, 9852–9858.

61 J. Chen and N.-G. Park, Inorganic Hole Transporting Materials for Stable and High Efficiency Perovskite Solar Cells, *J. Phys. Chem. C*, 2018, **122**, 14039–14063.

62 L. Caliò, M. Salado, S. Kazim and S. Ahmad, A Generic Route of Hydrophobic Doping in Hole Transporting Material to Increase Longevity of Perovskite Solar Cells, *Joule*, , DOI:10.1016/j.joule.2018.06.012.

Chapter 2

Theoretical Background

Physical and chemical fundamentals to understand the working principles of perovskite solar cells are presented.

2.1 Solar spectrum

The hydrogen fusion to helium inside of Sun releases photons that travel through space reaching the Earth´s atmosphere with a solar power of 1366 W/cm^2, a figure known as *Solar constant*. Before reaching the surface of the Earth, due to the atmospheric conditions, the solar energy spectrum changes in intensity and distribution, as it is shown in Figure 2.1. In fact, once solar radiation passes through the atmosphere, its power density is reduced to around 800-900 W/cm^2. From Figure 2.1, it is also observed that the Earth´s atmosphere is almost transparent in the visible region. However, the irradiation that finally achieves the surface will also depend on other variables such as the season, the time of day or even the actual latitude of a location. For these reasons, to develop and design new solar cell as well as compare the response and behaviour of devices it is necessary to define a standard solar spectrum.

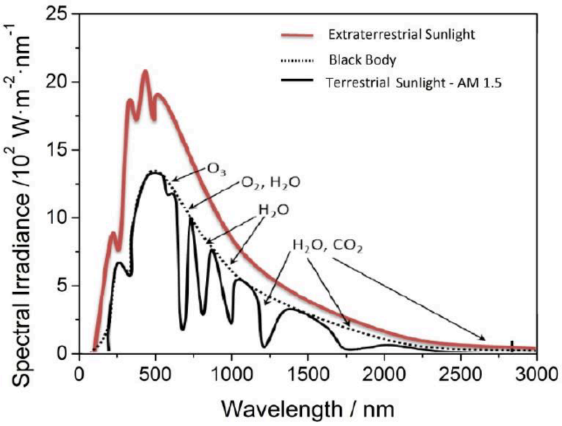

Figure 2.1. Black body irradiance at 5670K (dotted line) compared with the extraterrestrial and terrestrial (AM 1.5) solar spectrum.

Atmospheric absorption attenuates the solar radiation that ultimately reaches the surface. This depends on the position of the sun and it is taken into account by the so-called *Air Mas* (AM) parameter. This is defined as AM= 1/cos(Θ), where Θ is the angle of elevation of the Sun.[1] The American Society for Testing and Materials (ASTM) defined a standard spectral distribution of the light at AM1.5 and Θ = 48.2° (ASTM G173).[2,3] In PV applications, for convenience, the AM1.5 spectrum is normalized so that the integrated irradiance of this spectrum per unit area and unit time is 1000 W/cm^2. This figure is known as 1 *sun* illumination. Most results in this thesis for current-voltage characteristics are measured at 1 sun using an AM1.5G filter, corresponding to *global* irradiation (direct + diffuse).

2.2 Photovoltaic solar cells

Photovoltaic solar cells are devices that generate electrical energy using the Sun as energy resource. They are generally based on a semiconductor material that absorbs the photons energy by exciting the valence electrons (bound in the solid) up to higher energy levels where they have freedom of movement. Hence, an electron vacant state is created in the place from which an electron was excited. This empty place is known as a *hole* and it shows equal but opposite electrical charge to that of an electron. Because of the *potential difference* between electrons and holes, an electric field or any other adequate mechanism is required to separate both charge carriers.

2.2.1 Electronic states in semiconductor

Solid materials may behave like conductor, insulators or semiconductors depending on its energy *band gap* (E_g) and the excitation energy. Unlike molecular systems characterized by discrete molecular orbital energy levels, in solids energy levels form broad energy bands where the charge can be delocalized. The highest energy that contains electrons is called *valence band* (*VB*) while the lowest unoccupied energy band is the *conduction band* (*CB*). The highest energy of the *VB* and the lowest energy of the *CB* define the E_g ($E_g = E_{CB} - E_{VB}$).

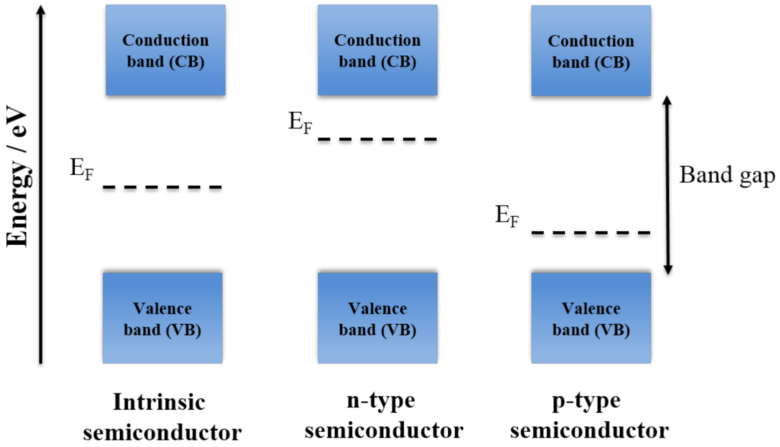

Figure 2.2. Electronic band structure of different types of semiconductors. E_F represents the Fermi level.

The band gap determines the thermal and/or electrical conductivity properties. For instance, if the *VB* is partly full or it is overlapped in energy with the *CB* (E_g ~0), the valence electrons can act as *carrier units* of heat or charge. This is the case of *conductor* materials. In the opposite case, *insulator* materials are characterized by $E_g > 3$ eV,[1] which makes impossible the excitation of valence electrons to the *CB* by thermal excitation or light absorption in the UV/Vis spectral range. *Semiconducto*r materials show E_g values in the range of 0.5 – 3 eV, an energy difference that can be overcome by UV/vis absorption, as that provided by the Sun. In particular, for semiconductor materials, at the absolute zero (0 K), valence electrons need an energy equivalent (or higher) to the energy band gap to catch the nearest available unoccupied level of *CB* (Fig. 2.2). [4]

The occupation probability of electronic states by electrons at a given temperature is governed by the Fermi-Dirac distribution function

$$f(E) = \frac{1}{1 + exp\left(\frac{E_c - E_F}{k_B T}\right)} \tag{2.1}$$

where k_B is the Boltzmann constant, E_C is the lower energy edge of the conduction band, T is the absolute temperature and E_F is the Fermi level. This latter parameter is actually the chemical potential (μ) of electrons in a solid material. At 0 K, the Fermi level coincides with the threshold energy below which all states are occupied by valence electrons.

In a situation where E_C-E_F >> k_BT, the Fermi-Dirac distribution can be approximated by the Boltzmann distribution to describe the occupation of the conduction band. Thus, the total electron density in the *CB* from E_C to infinite is determined by the following integral

$$n_c = \int_{E_c}^{\infty} N_c(E) f(E) dE \approx N_c exp\left(-\frac{E_c - E_F}{k_B T}\right) \tag{2.2}$$

where N_c is the density of states in the *CB*.

A similar calculation for holes in the valence band can be used. Thus, the concentration of holes in the *VB* is given by

$$n_v = N_v exp\left(+\frac{E_v - E_F}{k_B T}\right) \tag{2.3}$$

where E_v is the upper energy edge of the *VB* and N_v is the density of states of holes in the band.

From Eqs. 2.2 and 2.3, we can infer that the conductivity of a semiconductor, which is proportional to the concentration of carriers, varies exponentially with the position of Fermi level in the band gap. For an ideal defect-free semiconductor (*intrinsic semiconductors*), in which there are no localized states levels in the band gap, the number of electrons in the *CB* equals the number of holes in the *VB* ($n_C = n_V$). In this case, the concentration of charge carriers is obtained from

$$n_i^2 = n_c n_v = N_c N_v exp\left(\frac{E_v - E_C}{k_B T}\right) = N_c N_v exp\left(-\frac{E_g}{k_B T}\right) \qquad (2.4)$$

For intrinsic states, the Fermi level (at 0 K) is symmetric with respect to the middle of energy gap which is reflected in the relatively small conductivity of these materials (Fig. 2.2).

On the other hand, in the case of semiconductors containing defects (*extrinsic semiconductors*), impurities levels can be introduced within the band gap. These impurities modify the electronic properties of the semiconductor. Defects usually stem from introducing donor or acceptor species of electrons in the semiconductor. These are known as *dopants* or *doping* materials. If the doping is carried out by introduction of donor atoms, majority charge carriers will be electrons. In consequence, the Fermi level is raised, giving rise to a *n*-type semiconductor. However, if the doping is with acceptor atoms, the majority charge carriers will be holes. In this case, the Fermi level is lowered and the semiconductor is known as *p*-type (Fig. 2.2). Because the carrier density is increased both in *n*- and *p*-type semiconductors (majority electrons or holes, respectively), the conductivity is always enhanced in extrinsic semiconductors with respect to their intrinsic forms.

2.2.2 Theoretical description of perovskite solar cells

As it has been explained above, the first step of PV conversion is the photon absorption by the semiconductor and the excitation of electrons from valence band (ground state) to conduction band (excited stated). To complete the photovoltaic conversion process, the charge carriers (electrons and holes) must be efficiently separated and collected by external contacts. If the charge separation is not effective, excited electrons relax to lower energy states (*recombination*) which is deleterious for the solar cell performance (Fig. 2.3). For this reason, some intrinsic asymmetry needs to be introduced in the solar devices to drive the charge away.

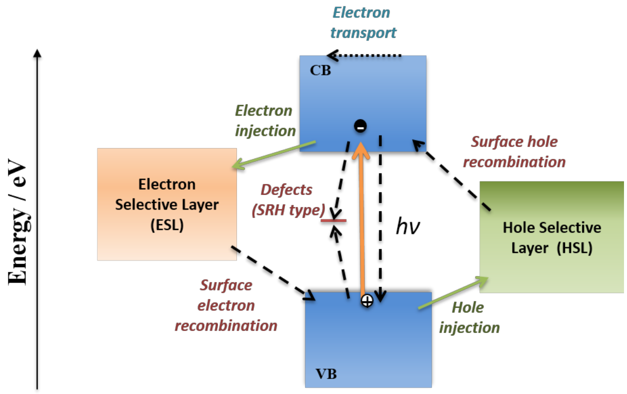

Figure 2.3. Simplified scheme of electronic band structure of a perovskite solar cell. Solid and dashed arrows represent processes that is happening in favour or against the *photocurrent*, respectively.

2.2.2.1 Photovoltage and photocurrent

Perovskite solar cells are based on an asymmetric sandwich configuration. The simplest model to describe it is based on the traditional *p*-*i*-*n* junction [5–7](Fig. 2.4). The sun light-active material (*i*), in our case a perovskite layer, is sandwiched between selective contacts with different Fermi level positions, such as *n*-type and *p*-type semiconductors. Under illumination, the difference in Fermi level (chemical potential) between the contacts provides an electrochemical gradient that separates the photogenerated charge carriers. Electrons in excited states and holes in the ground state are collected by *n*-type and *p*-type semiconductors, respectively. Both *n*- and *p*-type semiconductor contacts are known as *electron selective layer* (ESL) and *hole selective layer* (HSL), respectively.

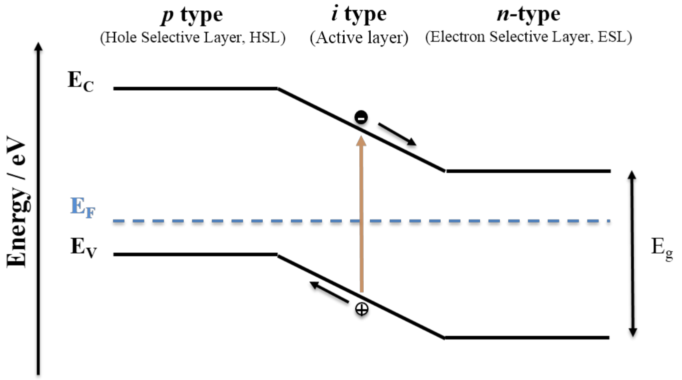

Figure 2.4. Band profile of a *p*-*i*-*n* junction. E_C and E_V are the lower and upper energy of the conduction band and valence band, respectively. E_F represents the Fermi level while E_g is the band gap energy.

Although the *p-i-n* picture is one of the most used to describe the band structure of a perovskite solar cell, there are many indications in the literature that metal-halide perovskites can be or can *act* as if they were *p*- or *n*-type semiconductors. Even they can change their character depending on the nature of the material they are in contact with, or for different preparation conditions. The electronic character of the perovskite depends on the most abundant type of chemical defect that is present in the crystalline structure. There is a growing consensus that these defects are actually iodine vacancies, which would mean that the perovskite is *p*-type. In any case the topic is complex and it is still under vigorous debate. [8–12]

Regardless what is the true nature of the perovskite active layer, the *photovoltage* (V) arises from the Fermi level difference between ESL and HSL as

$$qV = E_F{}^p - E_F{}^n \tag{2.5}$$

where q is the electron charge, $E_F{}^p$ and $E_F{}^n$ are the Fermi levels of the *p*-type and *n*-type semiconductor, respectively.[13]

If the electron and hole selective contact are good enough (ohmic), the Fermi levels at the contacts will coincide with Fermi level splitting *within* the active layer. Accordingly, the electron (n) and hole (p) densities in the perovskite are given, using equations 2.2 and 2.3, by

$$n = N_c exp\left(-\frac{E_c - E_F{}^n}{k_B T}\right) \tag{2.6}$$

$$p = N_v exp\left(+\frac{E_v - E_F{}^p}{k_B T}\right) \tag{2.7}$$

From Eqs. 2.5, 2.6 and 2.7, we arrive to the important relationship

$$np = N_C N_V exp\left(-\frac{E_g - (E_F^P - E_F^n)}{k_B T}\right) = N_C N_V exp\left(-\frac{E_g - qV}{k_B T}\right) \tag{2.8}$$

Let us assume that n and p correspond to photogenerated carriers inside the active layer. Solving for the voltage in Eq. 2.8 we have for the *open-circuit voltage* (V_{OC}).

$$qV_{OC} = E_g - k_B T ln\frac{N_C N_V}{np} \tag{2.9}$$

Hence, at 0 K (no entropy generation), the band gap determines the maximum attainable photovoltage.

Under dark conditions and for applied external voltage larger than V_{OC} (threshold photovoltage), the potential difference between the selective contacts generates a current due to charge injection into the cell (Fig. 2.5). This current is called *dark current* and acts in the opposite direction to the photocurrent depending on the applied external voltage. Most solar cells behave like a diode in the dark, admitting a much larger current under forward bias than under reverse bias (rectifying behaviour). For an ideal diode the dark current density J_{dark}(V) is expressed as[1,14]

$$J_{dark}(V) = J_o\left(e^{\frac{qV}{k_BT}} - 1\right) \tag{2.10}$$

where J_0 is a constant that defines the saturation current in the dark.

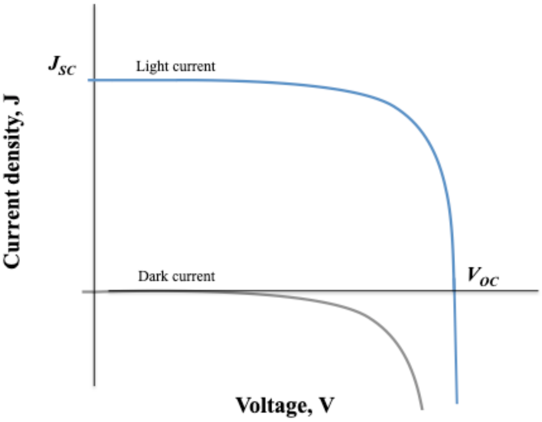

Figure 2.5. Current-voltage characteristic of ideal diode under light and dark. J_{sc} and V_{OC} are the short-circuit photocurrent and the open-circuit voltage, respectively.

Under illumination and under an applied external potential, the photogenerated charge carriers are collected by n-type and p-type semiconductors due to the potential difference at both interfaces. According to thermodynamics, this effect acts as *driving force* for the charge-transfer across interfaces which depends of the external applied potential and Fermi level of perovskite under illumination. As a consequence, a photocurrent *J(V)* due to efficient charge separation and collection is obtained (Fig. 2.5).[15] The maximum generated photocurrent is obtained when J_{dark} is 0 (the current resistance is zero and the recombination processes are minimized). This is called *short-circuit photocurrent* (J_{SC}) which is equal to the net current density of the solar device (Eq. 2.11).

$$J(V) = J_{SC} - J_{dark} \tag{2.11}$$

The J_{SC} can be calculated by the overlap between the spectral *External Quantum Efficiency* (EQE), defined as the number of electrons collected to the external circuit with respect to the number of incident photons, and the spectral photon flux of the incident illumination for a given wavelength $I_0(\lambda)$[16]

$$J_{SC} = \int_{\lambda_{min}}^{\lambda_{max}} I_0(\lambda) \cdot EQE(\lambda) \cdot d\lambda \qquad (2.12)$$

The EQE depends on the efficiency of three different processes that determine the photon-to-electron conversion in solar cells,

$$EQE(\lambda) = \eta_{lh}(\lambda) \cdot \eta_g(\lambda) \cdot \eta_{col}(\lambda) \qquad (2.13)$$

Here, η_{lh} is the sunlight-harvesting efficiency (the *absorptance*), η_g is the generation efficiency of charge separation under sunlight irradiation and η_{col} is the charge collection efficiency through selective contacts to the external circuit (Fig. 2.6).

In the particular case of PSCs, η_{lh} indicates how efficiently the perovskite layer absorbs the incident photons. The η_g corresponds to the probability that free carriers are generated from the *excitons* formed following photon absorption plus the probability of charge carriers being injected into the contacts (electrons and holes into *n*-type and *p*-type semiconductors, respectively). Finally, η_{col} is an indicator of the probability that photogenerated charges reach the external circuit before they are lost by recombination.

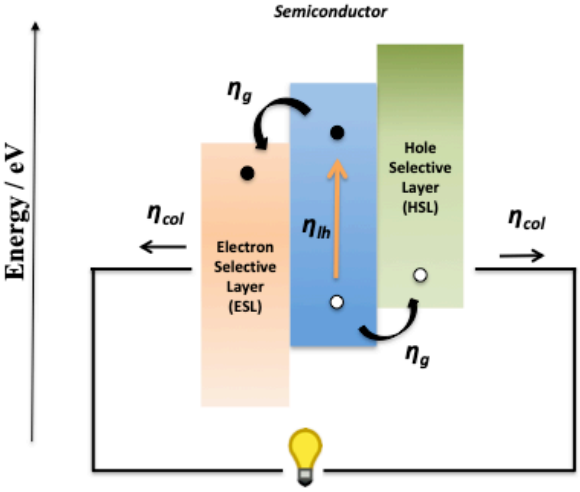

Figure 2.6. Simplified scheme of the three different processes that determine the photon-to-electron conversion in a solar cells with a sandwich configuration. η_{lh} is the absorption efficiency of active material, η_g is the charge separation efficiency by the contacts and η_{col} is the charge collection efficiency from contacts to external circuit.

For an ideal diode, considering Eqs 2.10 and 2.11, the photocurrent is written as

$$J = J_{SC} - J_0\left(e^{\frac{qV}{k_BT}} - 1\right) \tag{2.14}$$

However, the behaviour of a solar cell is generally expressed by a non-ideal diode form[1]

$$J = J_{SC} - J_0\left(e^{\frac{qV}{mk_BT}} - 1\right) \tag{2.15}$$

where m is an ideality factor that measures how closely the device behaves like an ideal diode ($1 \leq m \leq 2$). For an ideal diode, m=1.

Figure 2.5 shows that solar cells generate electrical power ($P = I{\cdot}V$) when the voltage is between 0 and V_{OC} only. At open circuit conditions, the dark current and short circuit photocurrent are cancelled out, so the V_{OC} can be written as

$$V_{OC} = \frac{mk_BT}{q} ln\left(\frac{J_{SC}}{J_0} + 1\right) \tag{2.16}$$

This equation shows that a higher threshold photovoltage (V_{OC}) can be achieved with increased light intensity.

Equation 2.16 also shows that a semilogarithmic plot of *Voc* versus the short-circuit photocurrent should give a straight line, from whose slope the ideality factor can be extracted. For an ideal diode the slope would be 26 mV at 298 K ($=k_BT/q$, the *thermal voltage*). This is one of the methods used in this thesis to extract the ideality factor. As shown in the following, the ideality factor provides information about the nature and type of recombination that is going on in a solar cell.

2.2.2.2 Electron recombination

In PV cells, the photogenerated charge carrier transfer rate and transport rate compete with the charge recombination processes. This concept can be defined as the loss of electron-hole pairs through the decay of an electron to a lower energy state.[1] Different recombination mechanisms coexist in PSCs (Fig. 2.7):

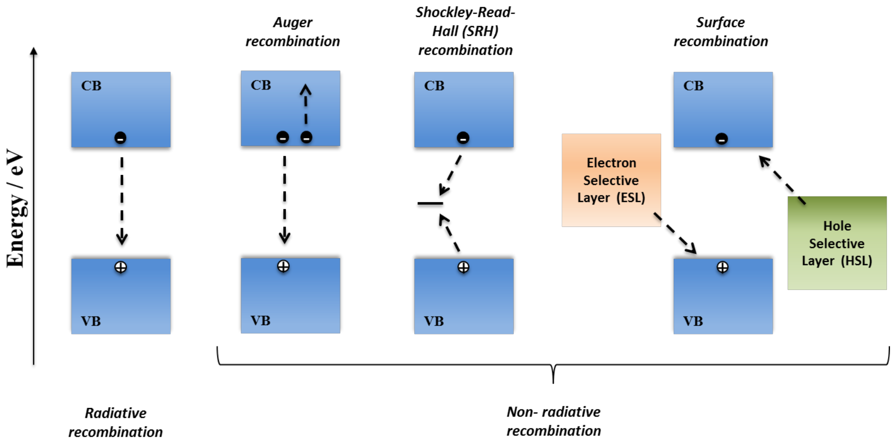

Figure 2.7. Schematic of different recombination mechanisms.

Radiative recombination

It is a direct band-to-band recombination in which an electron drops from the conduction band to react with a hole in the *VB*. A photon with an energy similar to band gap is released, which can be reabsorbed, and thus recycled.[17] This is one of the reasons why, counter-intuitively, a material which is highly luminescent (strong radiative recombination), is also a good material to make efficient solar cells.

Auger recombination

It is a recombination process where three carriers are involved. The energy of a recombining electron-hole pair is transferred to a third carrier, hole or electron, in the valence band or conduction band, respectively. Nevertheless, the recombination rate of this process is 10 - 100 times lower than the radiative rate. Thus, for a direct band gap and under non-concentrated sunlight, Auger recombination will not be considered as a significant contribution.

Shockley-Read-Hall recombination (SRH recombination)

It is an indirect recombination process mediated by defects that introduce recombination centers in the crystal lattice. The defects are usually caused by impurities as well as by grain boundaries, dislocation, ionic vacancies… These defects are energetically localized within the band gap (*deep traps*) and they can capture the charge mobile carriers (electrons or holes). The captured charge by the trap releases energy through phonon emission (*non-radiative recombination*). This recombination is also known as trap-assisted recombination and it is the limiting mechanism of many solar cells.

Surface recombination

It is also a *non-radiative recombination* mechanism that takes place *across* or in the *vicinity* of the contact/active layer interface. Many times this type of recombination is associated to electron o hole selective contacts characterized by a low charge extraction efficiency and/or a low charge conductivity, that favour accumulation of charges at interfaces.

Regardless the actual type of recombination, the recombination rate (U_{rec}) can always be described with expressions borrowed from classical chemical kinetics like

$$U_{rec} = -\frac{dn}{dt} = k_{rec}n^{\gamma} \tag{2.17}$$

where t is time, k_{rec} is a recombination constant and γ is the reaction order. For radiative recombination, the U_{rec} is proportional to the densities of electrons and holes, hence $\gamma = 2$. In Auger recombination $\gamma = 3$ because three carriers are involved. Meanwhile, for SRH recombination, the charge carriers interact with a fixed concentration of recombination centers, being $\gamma = 1$.[18]

For intrinsic semiconductor in which $n_C = n_V$, we find from Eq. 2.8,

$$n = (N_C N_V)^{\frac{1}{2}} exp\left(-\frac{E_g - qV}{2k_B T}\right) \tag{2.18}$$

At high-injection conditions the photogenerated carrier densities well exceed intrinsic and majority carrier values.[19] In this situation electroneutrality require that the charge carriers concentrations are equal (n=p) and we end up with the same situation as that of Eq. 2.18.

Combining Eqs. 2.17 and 2.18, and applying the open-circuit condition in Eq. 2.16, it is easy to find that the reaction order can be related to the the ideality factor values (m) as [20]

$$m = \frac{2}{\gamma} \tag{2.19}$$

Thus, ideality factor values of 1, 2 and 2/3 will be expected for radiative recombination, SRH recombination and Auger recombination, respectively.[21]

Combining Eqs. 2.17 and 2.18, photogenerated carriers (J_{rec}) can be related to the photopotential acting in the cell as

$$J_{rec} = qdU_{red} = J_{00}\left(e^{-\gamma\frac{E_g-qV}{2k_BT}}\right) \tag{2.20}$$

where d is the thickness of the active layer and J_{00} depends on the rate constant ($J_{00} = qd(N_CN_V)^{1/2}\,k_BT\,p_0$). The recombination resistance is the reciprocal of the voltage derivative of this expression. Hence,[22]

$$R_{rec} = \left(\frac{\partial J_{rec}}{\partial V}\right)^{-1} = R_{00}\left(e^{-\gamma\frac{E_g-qV}{2k_BT}}\right) \tag{2.21}$$

or

$$R_{rec} = \left(\frac{\partial J_{rec}}{\partial V}\right)^{-1} = R_{00}\left(e^{-\frac{\beta qV}{k_BT}}\right) \tag{2.22}$$

with $R_{00} = (2k_BT\ J_{00}\ /q\gamma)exp(\gamma E_g/2k_BT)$. The β parameter is the transfer or recombination parameter. This is related to the ideality factor, as $m = 1/\beta$.

For an ideal solar cell where recombination is purely radiative, the generation of electron-hole pairs should exactly compensate the net emitted photon flux ($\phi_{(em,0)}$) at open circuit conditions. This leads to the expression[17]

$$V_{OC} = V_{OC,rad} = \frac{k_BT}{q}ln\left(\frac{J_{SC}}{\phi_{em,0}}+1\right) \tag{2.23}$$

In real solar cells, the number of free charge carriers is mainly reduced by non-radiative recombination mechanisms, which leads to a decrease the maximum threshold photovoltage[17]

$$V_{OC} = V_{OC,rad} - \Delta V_{OC,non-rad} = \frac{k_BT}{q}ln\left(EQE_{EL}\frac{J_{SC}}{\phi_{em,0}}+1\right) \tag{2.24}$$

Here, EQE_{EL} is the quantum yield of electroluminescence (charge recombining radiatively per total number of injected charge). Because higher V_{OC} is achieved from increasing EQE_{EL}, we conclude that any photovoltaic material should be highly luminescent if we want to achieve good photovoltaic performance.

2.3 Chemistry of metal halide perovskites

It follows from the exposed above that the photovoltaic performance of perovskite solar cells is directly related with the film quality of perovskite materials, because this determines the appearance of defect states, both in the bulk or at interfaces, that can promote several routes of non-radiative recombination.[23–25] In particular, the morphological, structural and optoelectronic properties of perovskite films strongly depend on the synthesis method as well as ambient conditions in which these films are fabricated.[26,27]

2.3.1. Synthesis of metal halide perovskites

Two effective methods to prepare high PCE solar cells have been described in the literature: that based on two-step spin-coating and the so-called antisolvent method (adduct approach) (Fig.2.8). Using as example the $MAPbI_3$ perovskite, the *two-step method* consists of the deposition of PbI_2 by spin-coating followed by the deposition of MAI solution either by spin-coating or by immersing the PbI_2-coated substrate in a MAI solution.[28,29] This method allows the perovskite to be successfully infiltrated in mesoporous scaffolds. However, it can also lead to incomplete conversion of PbI_2 to perovskite. Another problem is that there is a certain possibility that the mesoporous layer is exposed to the hole selective material, which would enhance non-radiative recombination mechanisms.[25]

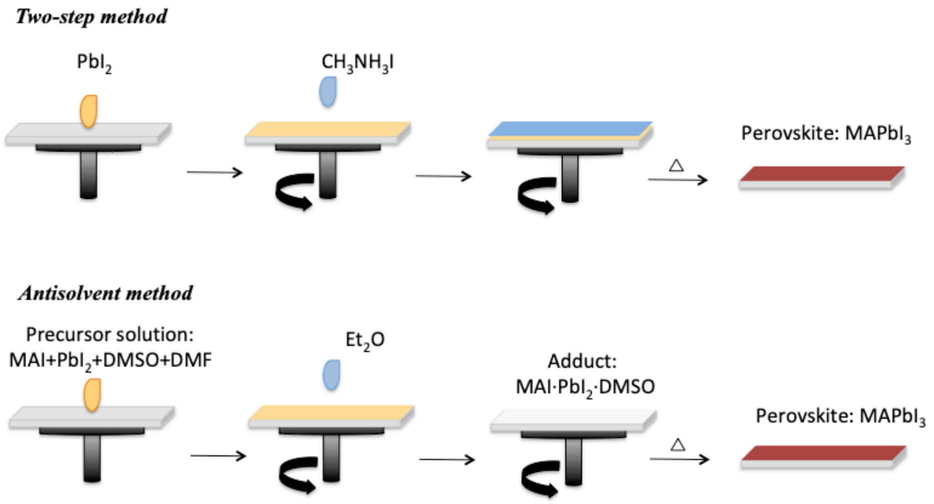

Figure 2.8. Scheme to the preparation of perovskite solutions by two-step method and antisolvent method.

For these reasons, an *antisolvent method* has been proposed as a more effective route to prepare high quality $MAPbI_3$ perovskite films.[30] For that, a perovskite precursor solution is deposited by spin-coating on the substrate, which is washed with an anti-solvent while spinning to get rid of solvent and to form the white intermediate phase, the adduct. A uniform perovskite film is obtained after mild annealing.

2.3.1.1 Adduct approach

The success of the last method is based on the control of *coordination chemistry* of lead and the *anti-solvent engineering*. In particular, in the case of $MAPbI_3$, the perovskite is synthesised by reaction of PbI_2 with MAI using a polar solvent such as dimethylsulphoxide (DMSO), N,N-dumethylformamide (DMF) or *γ*-butyrolactone (GBL).[30,31] It is known that these Lewis bases interact with the Lewis acid PbI_2 by donating a lone electron pair from the oxygen to the lead. Indeed, these solvents compete with the iodide ions from MAI to fill the octahedral coordination sphere of lead atoms.[30,32,33] Thus, in the perovskite precursor solution a variety of coordination complexes can be found:[32]

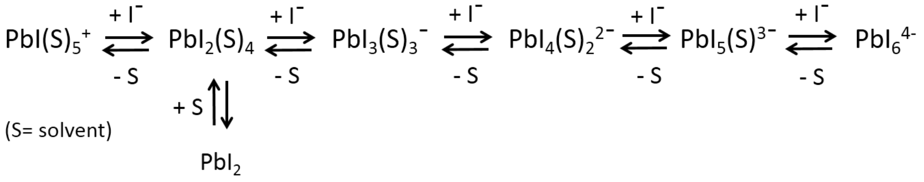

Different proportions of the complexes are detected in each solvent, since these have different affinity to coordinate with the lead (DMSO>DMF>GBL).[32] Among the different complexes, the PbI_6^{4-} species are those that provide the right environment for perovskite crystallization, owing to the fact that they already show an octahedral structure (see Fig. 1.2 in *Chapter* 1). Thus, a suitable solvent medium (pure or mixed solvents) will be the one that dissolve the precursors and permit the generation of PbI_6^{4-}.[32,33]

In connection with this, high quality film for $MAPbI_3$ was reported for perovskite precursor solution based on mixed solvent, DMSO and DMF.[30] In this case, to obtain a suitable morphology of perovskite films (homogeneous and fully covered substrate), it was necessary to wash the precursor solution with nonpolar diethyl ether (antisolvent) while spinning to remove the DMF and leave the DMSO for adduct formation (Fig. 2.8). The adduct $MAI{\cdot}PbI_2{\cdot}DMSO$ looked like a white film. This was then converted to perovskite by annealing. In conclusion, the formation of adduct by the antisolvent washing seems to be the critical step for crystal growth and to achieve a good quality in the final film. Using the antisolvent method, perovskite devices based on $MAPbI_3$ or mixed cations (Cs, FA and MA) have achieved PCEs of 21.2% and 22% in the last years, respectively.[25]

On the other hand, H_2O molecule is also a Lewis base that can coordinate with the lead complex in the same way that the solvents mentioned above. Indeed, the H_2O shows a higher affinity to coordinate with lead than the DMSO.[32] Taking this into account, high efficiency $MAPbI_3$ devices have been fabricated under moisture conditions by the antisolvent method.[34,35] For these devices, the content of DMSO was adjusted in the perovskite precursor solution as a function of ambient moisture. In this way, the adduct MAI·PbI_2·S (S= DMSO and/or H_2O) is obtained with the most suitable stoichiometry in order to get homogeneous perovskite film. This latter procedure is the one that we mostly used and studied in this thesis.

2.3.2 Chemical stability of metal halide perovskites

Due to the chemical composition of the perovskite material (see *Chapter* 1), this material tends to suffer from degradation upon exposure to humidity, heat, oxygen or light. In particular, the humidity and heat are commonly observed in a wide range of hybrid perovskites.

In the case of $MAPbI_3$, it has been proposed that the decomposition under humidity conditions could be due mainly to the hygroscopic nature of the methylammonium component. Since the H_2O is a Lewis base, this molecule could take a proton from the ammonium moiety in the perovskite framework and cause the whole degradation of the perovskite. This can be described as follows:[36]

$$CH_3NH_3PbI_3\ (s) \overset{H_2O}{\rightleftarrows} PbI_2\ (s) + CH_3NH_3I\ (aq.)$$

$$CH_3NH_3I\ (aq.) \rightleftarrows CH_3NH_2\ (aq.) + HI\ (aq)$$

$$4HI\ (aq.) + O_2 \rightleftarrows 2I_2\ (s) + 2H_2O\ (l)$$

It should be noted that this mechanism has been proposed to explain the degradation of perovskite once the film has been formed and, therefore, it does not affect the formation of the adduct intermediate explained above. On the other hand, at temperatures higher than 150ºC, $MAPbI_3$ is degraded into its components as:[36]

$$CH_3NH_3PbI_3\ (s) \overset{\Delta}{\rightleftarrows} PbI_2\ (s) + CH_3NH_3I\ (aq.) + HI\ (aq)$$

An important fact regarding stability is the composition of the perovskite itself. It was already explained in previous *Chapter* that the introduction of ions with different sizes in the perovskite crystal leads to different values of the tolerance factor and octahedral factor. This gives rise to perovskites with different optoelectronic properties and stability. For example, for $MAPbI_3$, the partial substitution of MA cation by other cations such as FA, Cs, guanidinium (Gua) or rubidium (Rb) has brought improvement in stability mainly under humidity and illumination.[36–39] On the other hand, the presence of Br^- in mixed anions perovskite enhances the stability of material in humidity and under illumination but decrease the device performance.[36]

2.4 References

1 J. Nelson, *The Physics of Solar Cells*, Imperial College Press, 2003.

2 Reference Air Mass 1.5 Spectra | Grid Modernization | NREL, https://www.nrel.gov/grid/solar-resource/spectra-am1.5.html, (accessed January 14, 2019).

3 ASTM G173 - 03(2012) Standard Tables for Reference Solar Spectral Irradiances: Direct Normal and Hemispherical on 37° Tilted Surface, https://www.astm.org/Standards/G173.htm, (accessed January 14, 2019).

4 A. C. Fischer-Cripps, *The Materials Physics Companion*, CRC Press, New York, 1 edition., 2007.

5 S. van Reenen, M. Kemerink and H. J. Snaith, Modeling Anomalous Hysteresis in Perovskite Solar Cells, *J. Phys. Chem. Lett.*, 2015, **6**, 3808–3814.

6 K. Miyano, N. Tripathi, M. Yanagida and Y. Shirai, Lead Halide Perovskite Photovoltaic as a Model *p* – *i* – *n* Diode, *Acc. Chem. Res.*, 2016, **49**, 303–310.

7 N.-G. Park, Perovskite solar cells: an emerging photovoltaic technology, *Mater. Today*, 2015, **18**, 65–72.

8 A. Pockett, G. E. Eperon, T. Peltola, H. J. Snaith, A. Walker, L. M. Peter and P. J. Cameron, Characterization of Planar Lead Halide Perovskite Solar Cells by Impedance Spectroscopy, Open-Circuit Photovoltage Decay, and Intensity-Modulated Photovoltage/Photocurrent Spectroscopy, *J. Phys. Chem. C*, 2015, **119**, 3456–3465.

9 E. Edri, S. Kirmayer, S. Mukhopadhyay, K. Gartsman, G. Hodes and D. Cahen, Elucidating the charge carrier separation and working mechanism of CH3NH3PbI3−xCl x perovskite solar cells, *Nat. Commun.*, , DOI:10.1038/ncomms4461.

10 L. A. Frolova, N. N. Dremova and P. A. Troshin, The chemical origin of the p-type and n-type doping effects in the hybrid methylammonium–lead iodide (MAPbI 3) perovskite solar cells, *Chem. Commun.*, 2015, **51**, 14917–14920.

11 L. Contreras-Bernal, M. Salado, A. Todinova, L. Calio, S. Ahmad, J. Idígoras and J. A. Anta, Origin and Whereabouts of Recombination in Perovskite Solar Cells, *J. Phys. Chem. C*, 2017, **121**, 9705–9713.

12 C. Eames, J. M. Frost, P. R. F. Barnes, B. C. O’Regan, A. Walsh and M. S. Islam, Ionic transport in hybrid lead iodide perovskite solar cells, *Nat. Commun.*, , DOI:10.1038/ncomms8497.

13 C. Xiong, R.-H. Yao and K.-W. Geng, Photovoltage analysis of a

heterojunction solar cell, *Chin. Phys. B*, 2011, **20**, 057302.

14 P. Würfel and U. Würfel, *Physics of Solar Cells: From Basic Principles to Advanced Concepts*, John Wiley & Sons, 2009.

15 A. M. D, N. A. J and A. Xin, *Nanostructured And Photoelectrochemical Systems For Solar Photon Conversion*, World Scientific, 2008.

16 J. Halme, P. Vahermaa, K. Miettunen and P. Lund, Device physics of dye solar cells, *Adv. Mater.*, 2010, **22**, E210–E234.

17 W. Tress, Perovskite Solar Cells on the Way to Their Radiative Efficiency Limit - Insights Into a Success Story of High Open-Circuit Voltage and Low Recombination, *Adv. Energy Mater.*, 2017, **7**, 1602358.

18 C.-T. Sah, R. N. Noyce and W. Shockley, Carrier generation and recombination in pn junctions and pn junction characteristics, *Proc. IRE*, 1957, **45**, 1228–1243.

19 L. Calió, S. Kazim, M. Grätzel and S. Ahmad, Hole-Transport Materials for Perovskite Solar Cells, *Angew. Chem. Int. Ed.*, 2016, **55**, 14522–14545.

20 P. Calado, D. Burkitt, J. Yao, J. Troughton, T. M. Watson, M. J. Carnie, A. M. Telford, B. C. O'Regan, J. Nelson and P. R. F. Barnes, Identifying dominant recombination mechanisms in perovskite solar cells by measuring the transient ideality factor, *ArXiv180409049 Cond-Mat Physicsphysics*.

21 V. Sarritzu, N. Sestu, D. Marongiu, X. Chang, S. Masi, A. Rizzo, S. Colella, F. Quochi, M. Saba, A. Mura and G. Bongiovanni, Optical determination of Shockley-Read-Hall and interface recombination currents in hybrid perovskites, *Sci. Rep.*, , DOI:10.1038/srep44629.

22 J.-P. Correa-Baena, S.-H. Turren-Cruz, W. Tress, A. Hagfeldt, C. Aranda, L. Shooshtari, J. Bisquert and A. Guerrero, Changes from Bulk to Surface Recombination Mechanisms between Pristine and Cycled Perovskite Solar Cells, *ACS Energy Lett.*, 2017, **2**, 681–688.

23 B. Slimi, M. Mollar, I. B. Assaker, I. Kriaa, R. Chtourou and B. Marí, Perovskite FA1-xMAxPbI3 for Solar Cells: Films Formation and Properties, *Energy Procedia*, 2016, **102**, 87–95.

24 N.-G. Park, M. Grätzel and T. Miyasaka, Eds., *Organic-Inorganic Halide Perovskite Photovoltaics: From Fundamentals to Device Architectures*, Springer International Publishing, 2016.

25 H.-S. Kim, A. Hagfeldt and N.-G. Park, Morphological and compositional progress in halide perovskite solar cells, *Chem. Commun.*, 2019, **55**, 1192–1200.

26 G. E. Eperon, S. N. Habisreutinger, T. Leijtens, B. J. Bruijnaers, J. J. van Franeker, D. W. deQuilettes, S. Pathak, R. J. Sutton, G. Grancini, D. S. Ginger, R. A. J. Janssen, A. Petrozza and H. J. Snaith, The Importance of Moisture in Hybrid Lead Halide Perovskite Thin Film Fabrication, *ACS Nano*, 2015, **9**, 9380–9393.

27 M. Wang, Y. Feng, J. Bian, H. Liu and Y. Shi, A comparative study of one-step and two-step approaches for MAPbI3 perovskite layer and its influence on the performance of mesoscopic perovskite solar cell, *Chem. Phys. Lett.*, 2018, **692**, 44–49.

28 J. Burschka, N. Pellet, S.-J. Moon, R. Humphry-Baker, P. Gao, M. K. Nazeeruddin and M. Grätzel, Sequential deposition as a route to high-performance perovskite-sensitized solar cells, *Nature*, 2013, **499**, 316–319.

29 J.-H. Im, I.-H. Jang, N. Pellet, M. Grätzel and N.-G. Park, Growth of CH3NH3PbI3 cuboids with controlled size for high-efficiency perovskite solar cells, *Nat. Nanotechnol.*, 2014, **9**, 927–932.

30 N. Ahn, D.-Y. Son, I.-H. Jang, S. M. Kang, M. Choi and N.-G. Park, Highly Reproducible Perovskite Solar Cells with Average Efficiency of 18.3% and Best Efficiency of 19.7% Fabricated via Lewis Base Adduct of Lead(II) Iodide, *J. Am. Chem. Soc.*, 2015, **137**, 8696–8699.

31 M. I. Saidaminov, A. L. Abdelhady, B. Murali, E. Alarousu, V. M. Burlakov, W. Peng, I. Dursun, L. Wang, Y. He, G. Maculan, A. Goriely, T. Wu, O. F. Mohammed and O. M. Bakr, High-quality bulk hybrid perovskite single crystals within minutes by inverse temperature crystallization, *Nat. Commun.*, , DOI:10.1038/ncomms8586.

32 S. Rahimnejad, A. Kovalenko, S. M. Forés, C. Aranda and A. Guerrero, Coordination Chemistry Dictates the Structural Defects in Lead Halide Perovskites, *ChemPhysChem*, 2016, **17**, 2795–2798.

33 K. Yan, M. Long, T. Zhang, Z. Wei, H. Chen, S. Yang and J. Xu, Hybrid Halide Perovskite Solar Cell Precursors: Colloidal Chemistry and Coordination Engineering behind Device Processing for High Efficiency, *J. Am. Chem. Soc.*, 2015, **137**, 4460–4468.

34 C. Aranda, C. Cristobal, L. Shooshtari, C. Li, S. Huettner and A. Guerrero, Formation criteria of high efficiency perovskite solar cells under ambient conditions, *Sustain. Energy Fuels*, 2017, **1**, 540–547.

35 L. Contreras-Bernal, C. Aranda, M. Valles-Pelarda, T. T. Ngo, S. Ramos-Terrón, J. J. Gallardo, J. Navas, A. Guerrero, I. Mora-Seró, J. Idígoras and J. A. Anta, Homeopathic Perovskite Solar Cells: Effect of Humidity during Fabrication on the Performance and Stability of the Device, *J. Phys. Chem. C*, 2018, **122**, 5341–5348.

36 Z. Wang, Z. Shi, T. Li, Y. Chen and W. Huang, Stability of Perovskite Solar Cells: A Prospective on the Substitution of the A Cation and X Anion, *Angew. Chem. Int. Ed.*, 2017, **56**, 1190–1212.

37 M. Saliba, T. Matsui, K. Domanski, J.-Y. Seo, A. Ummadisingu, S. M. Zakeeruddin, J.-P. Correa-Baena, W. R. Tress, A. Abate, A. Hagfeldt and M. Gratzel, Incorporation of rubidium cations into perovskite solar cells improves photovoltaic performance, *Science*, 2016, **354**, 206–209.

38 M. Deepa, M. Salado, L. Calio, S. Kazim, S. M. Shivaprasad and S. Ahmad, Cesium power: low Cs levels impart stability to perovskite solar cells, *Phys. Chem. Chem. Phys.*, 2017, **19**, 4069–4077.

39 A. D. Jodlowski, C. Roldán-Carmona, G. Grancini, M. Salado, M. Ralaiarisoa, S. Ahmad, N. Koch, L. Camacho, G. de Miguel and M. K. Nazeeruddin, Large guanidinium cation mixed with methylammonium in lead iodide perovskites for 19% efficient solar cells, *Nat. Energy*, 2017, **2**, 972–979.

Chapter 3

Material and Methods

In this Chapter, materials and methods used for the synthesis, preparation and characterization of perovskite layers are described. A fundamental description of the small perturbation optoelectronic techniques is also brought. Finally, the fabrication of perovskite devices under dry and wet conditions is shown.

3.1 Characterization techniques

3.1.1 Structural characterization

The morphological and compositional characteristics of the perovskite films were analysed using microscopy and spectroscopy techniques.

3.1.1.1 Scanning electron microscopy (SEM) and electron dispersive spectroscopy (EDS)

SEM is a type of microscopy that is capable of obtaining information of the sample in the range of Angstroms. When an electron beam streaks the surface sample, a wide range of electron-sample interactions produce different signals.[1] In this thesis, the secondary electrons are analysed by an *In Lens*-type detector which provides information about the morphological characteristics and the thicknesses of the different layers that composed the PSC (Fig. 3.1). The signal from the backscattered electros (BSE) has also been detected to obtain information about the composition of the different layers.

For a deeper compositional analysis, EDS detection can be used. An EDS detector collects X-rays emitted by the electron-atom interactions at the electron cores. From the X-rays signal, the chemical elemental composition of the sample can be determined.

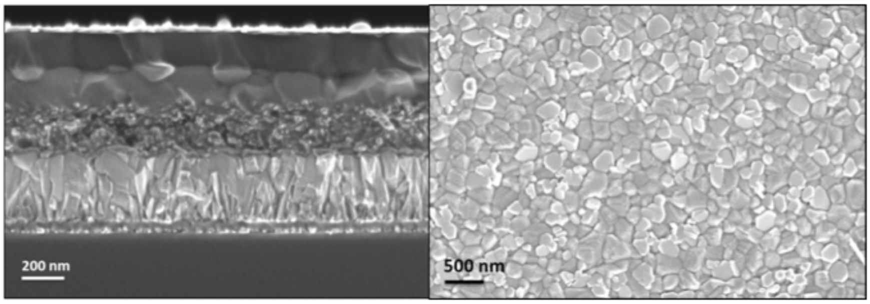

Figure 3.1. Scanning electron microscopy (SEM) images of samples prepared in this thesis: (left) cross-section of a FTO/c-TiO_2/m-TiO_2/$MAPbI_3$/Spiro/Au device and (right) plane-view of a $MAPbI_3$ perovskite film fabricated under ambient condition.

SEM and EDS images have been obtained with a *Zeiss GeminiSEM-300* microscope working at 2 kV and using a *Nordlys Max3* detector (Oxford Instruments) for SEM images and a Silicon Drift Detector (Oxford Instruments) for EDS mapping.

3.1.1.2 X-Ray Diffraction (XRD)

XRD is the most widely used technique for the identification of crystalline phase of materials. When a beam of X-rays incidents on the sample, the crystalline structures from that sample diffract the beam into many specific directions. By measuring the angle and intensities of the diffracted beams, the crystalline structure can be determined.

In this thesis, XRD has been used to confirm perovskite formation in standard and novel protocols. It has also been very useful to analyse the impact of high humid environmental conditions on the composition of the perovskite films (see *Chapter* 7) as well as to determine the crystalline phase of the $MAPbI_3$ perovskite films and the $PbI_2/MAPbI_3$ ratio (see *Chapter* 10). As an example, in Figure 3.2, a X-ray powder diffractogram for $MAPbI_3$ perovskite prepared in ambient conditions is shown. Peaks corresponding to a tetragonal $MAPbI_3$ perovskite and small proportion PbI_2 can be clearly identified.

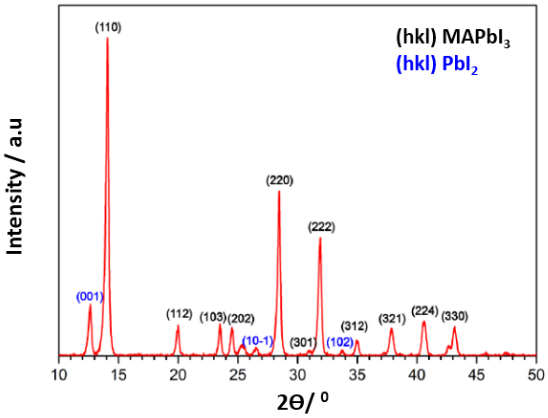

Figure 3.2. Diffraction peaks found for a thin $MAPbI_3$ perovskite film. This perovskite was prepared under 10 mbar of partial water pressure and using a ratio DMSO: Pb_2^+ equal to zero in the preparation procedure (see *Chapter* 10).

3.1.1.3 X-ray Photoelectron Spectroscopy (XPS)

XPS was used to analyse the chemical composition and the oxidation state of atomic constituents of perovskite films. In this thesis, XPS has been used to detect the presence of water in the crystalline structure of a perovskite. The XPS spectra were recorded using a Kratos Axis UltraDLD spectrometer, with monochromatized Al Kα radiation (1486.6 eV), 20 eV pass energy, and an accuracy of 0.1 eV. Electrostatic charging effects can be stabilized with the help of a specific device developed by Kratos. To avoid excessive moisture absorption during handling, samples are kept in dry sealed boxes after preparation and opened just before the XPS analysis.

3.1.2 Optical spectroscopy

An analysis of the spectral dependence of the light absorbed and emitted by perovskite films have been performed for the PSC using ultraviolet-visible (UV-Vis) and photoluminescence spectroscopy, respectively.

3.1.2.1 UV-Visible spectroscopy

UV-Vis absorption spectroscopy measures the attenuation of a light beam after it passes through a sample or after reflection from a film surface. According to the Beer-Lambert Law, the concentration of an absorbing compound (c) is linearly related to the absorbance A as

$$A = -\,log\,T = log\frac{I_o}{I} = \varepsilon l c \tag{3.1}$$

where T is the transmittance, I_o is the incident intensity, I is the transmitted intensity, ε is the molar absorption coefficient and l is the length over which attenuation occurs.[2] The UV-Vis measurement is useful to detect and quantify compounds in the sample that absorb ultraviolet and visible electromagnetic radiation. From this measurement, the reflection of the incident light by the sample can be determined using the formula $A+T+R=1$, where A, T and R are the relative intensities of absorbed, transmitted and reflected radiation, respectively.

From UV-Vis spectra it is possible to determine the optical band gap of an active material using a *Tauc plot*.[3] For a direct allowed transition, the optical band gap from the perovskite can be calculated by the equation

$$(h\gamma\varepsilon)^{\frac{1}{2}} = A\left(h\gamma - E_g\right) \tag{3.2}$$

where h and γ are the Plank constant and frequency, respectively, while A is a proportionality constant. In this work, the UV−visible absorption spectra have been recorded by using a *Cary 100* UV−vis spectrophotometer (*Agilent*) in the range of 200-800 nm.

3.1.2.2 Photoluminescence spectroscopy

To analyse charge separation at the perovskite/contact interface, photoluminescence (PL) measurements have been performed.

In PL measurements, one records the light emitted from a substance when it is illuminated by an optical excitation at a certain wavelength. As electrons fall from excited states to the ground state during the relaxation process light is emitted producing a signal. The PL signal intensity depends on the radiative recombination processes inside the active layer and it is consequently a direct function of the population of the excited state. If there are processes that compete with the radiative recombination the PL signal get reduced ("quenched"). This is precisely the case when a perovskite layer is placed in contact with an electron or hole selective contact.

The intensity of the PL signal is then a direct measure of the capability of the ESL and HSL to extract the photogenerated electrons and holes from the perovskite layer, respectively. [4,5] Figure 3.3 shows an example of the PL spectrum for mixed cation perovskite. PL measurements have been performed using a *Hitachi F-7000* Fluorescence spectrophotometer.

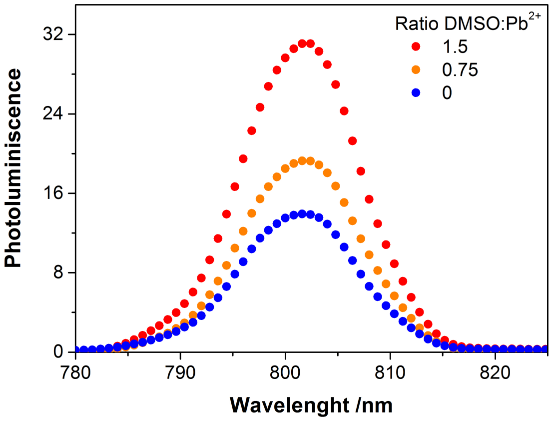

Figure 3.3. Photoluminescence spectra of $FA_{0.83}MA_{0.17}PbI_3$ films deposited on TiO_2 substrates from precursor solution with different DMSO:Pb^{2+} ratios.

3.1.3 Intensity current-voltage (IV) curve

The IV curve is the most important characteristic of a solar cell. To obtain an IV curve, the photocurrent density is recorded while a linear variable external potential is applied to the device under illumination (Fig. 3.4)

As it was explained in *Chapter* 2, the photovoltaic behaviour of a solar cell can be described by the diode equation (Eq. 2.14) for which the maximum generated photocurrent (*short circuit photocurrent density*) is obtained when the applied voltage (V_{app}) is zero. Under forward potential, the photocurrent stays constant until it balanced to zero by the dark current. In this point, the potential difference between the terminals has its maximum value (V_{app} corresponds to Fermi Level splitting under illumination), the *open circuit voltage*. [6]

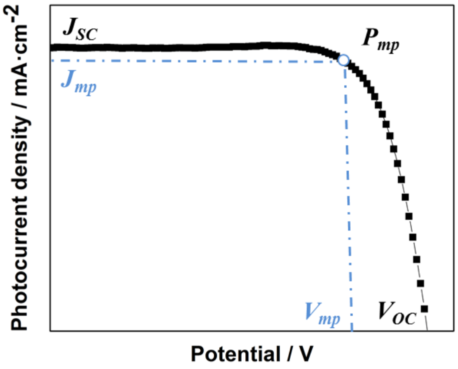

Figure 3.4. An example of the IV curve of a solar cell obtained under illumination. In the graph the main photovoltaic parameters are indicated: J_{sc} short circuit photocurrent density, V_{oc} open circuit voltage, P_{mp} maximum power point, J_{mp} photocurrent density at P_{mp}, V_{mp} voltage at P_{mp}.

From the IV curve under illumination different parameters can be extracted (Fig. 3.4). One of them is the *maximum power point* (P_{mp}). This parameter corresponds to the point where the product of photocurrent density and voltage reaches its maximum ($P_{mp} = J \cdot V$). The current and voltage associated to that point are expressed as J_{mp} and V_{mp}, respectively.

Considering the J_{mp}, V_{mp}, J_{SC} and $V_{OC,}$ it is possible to estimate the "squareness" of the IV curve, which defines the *fill factor* (*FF*) as

$$FF = \frac{J_{mp} \cdot V_{mp}}{J_{SC} V_{OC}} \tag{3.3}$$

Another parameter, the *power conversation efficiency* (*PCE*) of the device is given by

$$PCE = \frac{J_{SC} \cdot V_{OC} \cdot FF}{P_{sun}} \tag{3.4}$$

where P_{sun} is the incident light power density. From Eq. 3.4, for given J_{SC} and V_{OC} values, a lower PCE is expected for lower fill factors. The FF is also affected by *series resistance* (R_s) (resistance of the cell material to the current flow) and *shunt resistance* (R_{sh}) (resistance due to the leakage of currents through the device, around the edge of the device and between contacts of different polarity).[7] The R_s and R_{sh} can be estimated from the IV curve by the inverse slope near the V_{OC} and J_{SC}, respectively. An example of how the IV curve shape is affected by the R_s and R_{sh} is shown in Figure 3.5.

In this work, two different light sources have been used to register the IV curve of solar cells:

1. A solar simulator (*ABET-Sun2000*) with an AM 1.5G filter is used to study the response of solar cells to the illumination and to obtain the photovoltaic paramerers describe above. The light intensity is calibrated at 100 mW ·cm $^{-2}$ using a reference monocrystalline silicon solar cell with temperature output (*ORIEL, 91150*). Typically, we have used a metal mask to define an active area of 0.16 cm^2. As standard measurement, IV curves were obtained using a scan rate of 100 mV/s and a sweep delay of 20 s.

2. An alternative illumination system based on different light emitting diode (LED, LUXEON) has also been used. The light intensity is recorded using a reference solar cell with temperature output (Oriel, 91150). The current-voltage characteristics is obtained by applying an external bias to the cell and then the photocurrent response is measured using an Autolab/PGSTAT302N potentiostat.

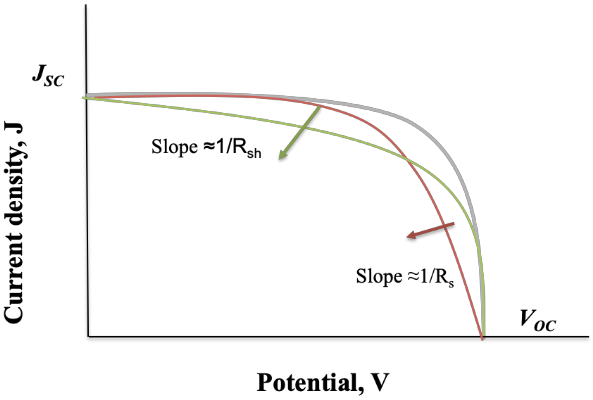

Figure 3.5. An example of the influence of a series resistance, R$_s$ (red line) and shunt resistance, R$_{sh}$ (green line) on the IV curve.

3.1.4 External Quantum Efficiency (EQE)

The EQE, also known as IPCE (Incident-Photon-to-Current-Efficiency), is defined as the number of electrons delivered to the external circuit with respect to the number of incident photons, for a given wavelength

$$EQE\ (\lambda) = \frac{h \cdot c \cdot J_{SC}(\lambda)}{e \cdot \lambda \cdot P_{light}(\lambda)} \cdot 100 \tag{3.5}$$

where c is the light velocity, λ is the wavelength, e is the elementary charge, J_{SC} is the short-circuit photocurrent at a given wavelength and P_{light} is the power density of the incident light. In practical terms the following formula is commonly used:

$$EQE\ (\lambda) = 1240 \cdot \frac{J_{SC}(\lambda)}{\lambda \cdot P_{light}(\lambda)} \cdot 100 \qquad (3.6)$$

here, J_{SC} and P_{light} are expressed in mA·cm^{-2} and W·m^{-2}, respectively.

As it was mentioned in *Chapter* 2, the EQE depends upon three different processes that determine the photon-to-electron conversion in a solar cell[7] (see Eq. 2.13 and Fig. 2.6) :

1. The absorption coefficient of the active material, e.g. the dye and the perovskite in DSSC and PSC, respectively.
2. The efficiency of charge separation which is governed by the interfacial charge transfer processes.
3. The efficiency of charge collection at the contact, which is related to charge recombination.

Thus, electronic and optical properties from the devices can be extracted by this measurement. Figure 3.6 shows an example of EQE spectrum for $MAPbI_3$ perovskite devices.

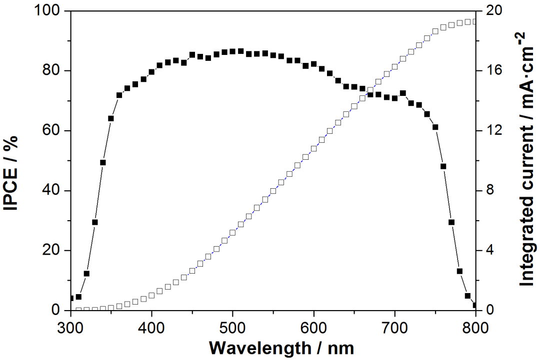

Figure 3.6. EQE measured for a $MAPbI_3$ perovskite solar cells with mesoporous TiO_2 and spiro-OMeTAD as electron and hole transport materials, respectively. Empty symbols indicate the calculated integrated short circuit current of the corresponding EQE curve, using the AM1.5G solar spectrum (see Eq. 2.12 in *Chapter* 2).

From EQE spectra, *internal quantum efficiency* (IQE) can be also extracted. The IQE is defined like the fraction of absorbed photons that are being converted to electron-hole pairs in the device. The IQE is calculated by

$$IQE = EQE \cdot T \qquad (3.7)$$

IQE measurement normalizes the EQE by the actual light harvesting efficiency, and thus provides useful information about the internal electrical properties, that is, processes 2. and 3. as described above: efficiency of charge separation and efficiency of charge collection.[8]

3.1.5 Small-perturbation electrochemical techniques

Electrochemical small-perturbation techniques are powerful tools to characterize solar cells such as DSSC and PSC. These techniques make it possible to extract information about dynamical electrical processes occurring in solar cells. In this type of experiments, a sinusoidal modulation in light intensity or voltage is superimposed on a dc component and the phase and magnitude of the response relative to that input is measured. The modulation amplitude is small enough to ensure a linear response of the system. The measurement comprises a wide range of frequencies (mHz to MHz), corresponding to timescales relevant for processes occurring in the photoconversion process of the solar cell or any other photoelectrochemical system. In this thesis, the small-perturbation electrochemical techniques utilized comprise Impedance Spectroscopy (IS) and Intensity-Modulated Photocurrent Spectroscopy (IMPS). The Nova 1.7 software NOVA has been used to generate and analyse IS and IMPS data.

3.1.5.1 Impedance spectroscopy (IS)

IS allows to distinguish between resistive and capacitive processes occurring in the device at different time scales, including electron transport, recombination and processes related to ionic motion. [9,10–12]

In IS, the potential applied to the solar cell is perturbed by small amplitude sinusoidal modulation and the resulting sinusoidal current response is measured at different modulation frequencies (Fig 3.7).[13]

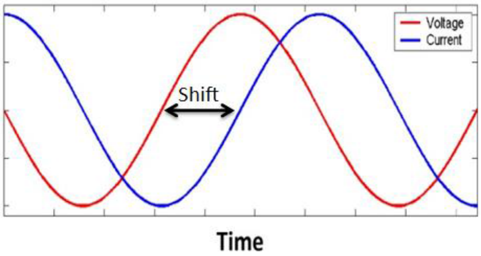

Figure 3.7. Sinusoidal current response in a linear system. The graph shows that shift that may exist between input (voltage) and output (current).

The impedance measurement describes the electrical resistance (R) in an alternating current (AC) circuit. In other words, impedance measures the ability of a circuit to resist the flow of electrical current. For a direct current (DC) circuit, the ratio between potential (V) and current (I) is given by the well-known Ohm's Law

$$V=I\cdot R \tag{3.8}$$

where V, I and R are expressed in volt, ampere and ohms, respectively. However, for an alternating signal, this expression is adapted to

$$V=I\cdot Z \tag{3.9}$$

where Z is the impedance of the circuit, which also has units of resistance (ohms). In the most common IS theoretical description, it is convenient to describe the current and potential like a vector rotating with a constant angular frequency $\omega = 2\pi f$, where f is the frequency in s^{-1} or Hz and ω is in radians s^{-1}. Hence, the excitation signal can be written as:

$$V(\omega)=V_0 \sin \omega t \tag{3.10}$$

here, $V(\omega)$ is the AC potential applied to the system and V_0 is the amplitude signal. On the other hand, the sinusoidal current response will show an amplitude and phase shift, and the same frequency, with respect to the applied potential. Thus, the AC electrical current response signal ($I(\omega)$) can be represented as

$$I(\omega)=I_0 \sin (\omega t + \varphi) \tag{3.11}$$

where I_0 the amplitude and φ the phase shift (Fig. 3.7). The phase represents the time lag of the current with respect to the voltage. From Eqs. 3.9, 3.10 and 3.11 we can express the impedance analogously to Ohm's Law such as

$$Z(\omega) = \frac{V(\omega)}{I(\omega)} = \frac{V_0 \sin \omega t}{I_0 \sin (\omega t + \varphi)} \tag{3.12}$$

The use of complex numbers simplifies mathematical operations. Using Euler´s equation

$$e^{j\theta} = \cos \theta + j \sin\theta \tag{3.13}$$

It is possible to write the potential applied and the current response in complex form

$$V(\omega) = V_0 \cdot e^{j\omega t} \tag{3.14}$$

$$I(\omega) = I_0 \cdot e^{j(\omega t+\varphi)} \tag{3.15}$$

The usefulness of complex numbers is demonstrated when the complex forms of voltage and current (Eqs. 3.14 and 3.15) are introduced in Eq. 3.12. The exponential exp($j\omega t$) cancels out, so that

$$Z = \frac{V_0}{I_0} e^{-j\varphi} = Z_0 e^{-j\varphi} \tag{3.16}$$

Using again Eq. 3.13, it is possible to represent the impedance of electrochemical processes as

$$Z_0 e^{-j\varphi} = Z_0 cos\,(\varphi) - Z_0\, j\, sin(\varphi) \tag{3.17}$$

which shows that the impedance has a real Z' and an imaginary part Z'', both containing the phase shift o phase angle φ as primary piece of information. As this phase shift is in principle different for each frequency ω probed in the experiment, we can write the impedance response of a sample

$$Z(\omega) = Z'(\omega) + j\, Z''(\omega) \tag{3.18}$$

On the basis of Eqs. 3.16 and 3.18, there are two fundamental ways to represent impedance results:

1. *Nyquist plot*: imaginary (Z'') versus real (Z') impedance plot.

2. *Bode plot*: magnitude (|*Z*|) versus frequency plot and phase (φ) versus frequency plot.

While the Nyquist plot does not contain all the information about frequency explicitly, the Bode plots contain all the necessary information.[14] Indeed, frequency-dependent apparent capacitance can be obtained from Bode plot (Fig. 3.9C), which shows information about different polarization processes.[15–18] An example of Nyquist and Bode plot corresponding to a very simple equivalent circuit commonly used in many systems (including solar cells) is displayed in Figure 3.8.

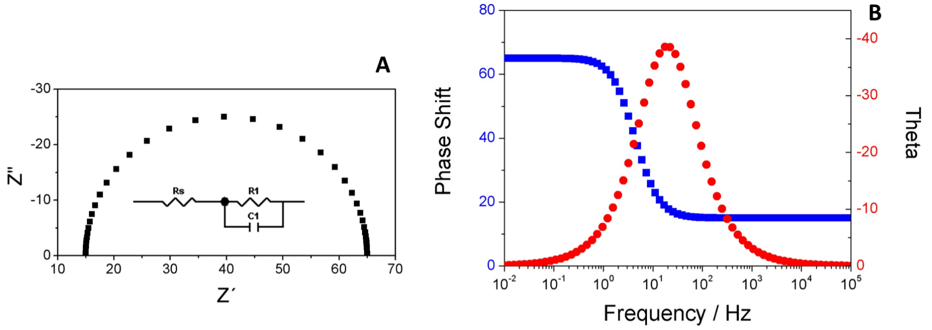

Figure 3.8. (A) Nyquist plot and (B) Bode plot obtained for the equivalent circuit shown (inset of A).

As shown in Figure 3.8 and discussed above, the response of many electrochemical systems is a signal in the first quadrant, corresponding to negative values of the imaginary part of the impedance (a lag in time due to the system capacitance). Nevertheless, impedance spectra many times include values in the second quadrant, corresponding to a "negative capacitance".

To understand impedance spectra, IS data are usually fitted to equivalent circuits. From the fitting, parameters such a resistance, capacitance and less commonly, inductances, as well as their product (time constants) can be extracted for each feature observed in the impedance spectra and related to the operation model of the device. It must be noted that there is not a unique equivalent circuit that fits reasonably well given Nyquist/Bode plots, as several different equivalent circuits can approximate the same experimental data.[10] For this reason it is very important that the equivalent circuit chosen, not only serves its fitting purpose well, but it must have a physical meaning too. For instance, to fit the Nyquist plot shown in Figure 3.8.A, a simple equivalent circuit can be used (inset of Fig. 3.8A). This model consists of the combination of a *resistance in series* (R_s) with a RC element. The RC element includes a capacitor (C) in parallel to a resistance (R). The C, measured in farads, and R, measured in ohms, in parallel define the time constant, $\tau = R{\cdot}C$, measured in seconds. This time constant defines the relaxation time of the system.

Using Kirchoff's circuit laws,[19] it is easy to demonstrate that the impedance of the circuit of Figure 3.18 is

$$Z(\omega) = R_s + \left(\frac{1}{R} + j\omega C\right)^{-1} \tag{3.19}$$

which corresponds to a semicircle in the first quadrant, whose origin on the real-part axis is given by R_S.

For real systems such as DSSC and PSC, a depressed semicircle in the complex impedance plane can be observed in the Nyquist plot. Currently, this behaviour has not been completely explained, but it is usually associated with surface porosity and roughness at an electrode as well as chemical reactions that involve several steps.[20] In any case, a *Constant Phase Element* (*CPE*) replaces the capacitance C in the equivalent circuit. The impedance of a *CPE* can be expressed as,

$$Z_{CPE} = \frac{B}{j\omega^{n}} \tag{3.20}$$

where B and n are frequency-independent parameters of the *CPE* ($0 \leq n \leq 1$). For $n = 0$, and $n = 1$, *CPE* becomes a resistor and a capacitor, respectively. It is generally accepted that if $n \geq 0.8$, *CPE* can still be seen as a capacitor whose capacitance is given by[21]

$$C = \frac{(R_{ct} \cdot B)^{1/n}}{R_{ct}} \tag{3.21}$$

In PSC, two well-distinguishable time constants are usually observed, resulting in two semicircle or arcs in the first quadrant of the complex plane or two peaks in the Bode plots (Figs. 3.9A and 3.9B). The meaning of these signals has been widely discussed in the literature.[11,22,23] In particular, the high frequency (*HF*) region (up to 10^4-10^5 Hz) has been mainly associated to electronic transport and recombination processes either in selective layers or in the bulk of the perovskite absorber,[9,11,12] whereas the low frequency (*LF*) region (< 10^2-10^3 Hz) is attributed to the diffusion of ions and charge accumulation at interfaces.[22,24] On the other hand, different polarization processes result in different plateaus for apparent capacitance-dependent frequency plot (Fig. 3.9C).[15–18] The *HF* component is determined by the dielectric polarization of the perovskite in the bulk, whereas the *LF* plateau has been associated with the ETM/perovskite interface charge accumulation.[25]

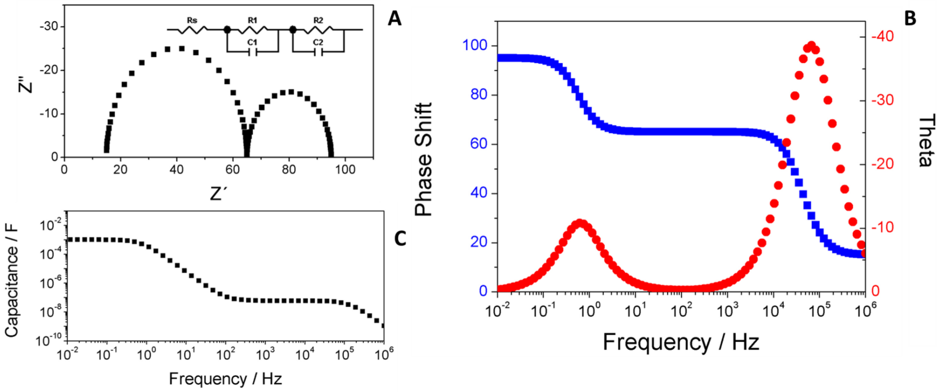

Figure 3.9. (A) Nyquist plot, (B) Bode plot and (C) apparent capacitance-dependent frequency plot obtained from equivalent circuit inserted in A.

For these types of impedance spectra, it has been reported a wide variety of equivalent circuits capable to fit experimental data equally.[10] From them, the most frequently used is the *Voight* circuit which contains different RC elements connected in series.[11,26] This equivalent circuit is inserted on Figure 3.9A and it has been chosen to fit impedance data of the PSCs from this thesis. *R1* and *R2* are the resistance of the electrochemical processes happening at HF and LF, respectively, while *CPE1* and *CPE2* are used to model the capacitive elements for those signals (depressed semicircles are usually obtained).

For this work, *ZView* software (*Scribner Associates Inc.*) has been used to fit impedance spectra to the equivalent circuit and to obtain parameters such as R_S, recombination resistance and capacitance.

As mentioned above, from these capacitive and resistance data, the *time constant* of each process can be calculated as

$$\tau_i = R_i \cdot C_i \tag{3.22}$$

But also, τ can be obtained from the corresponding frequency peak as

$$\tau_i = \frac{1}{2\pi f_i} \tag{3.23}$$

In this thesis, IS measurements have been mainly carried out at the open-circuit potential under varying DC illumination intensities to achieve different positions of the Fermi level in the semiconductor. However, in some cases measurements away from short-circuit conditions and varying DC potential have also been performed. The impedance response has been measured using a potentiostat PGSTAT302N/FRA2 Autolab and the NOVA 1.7 software is used to analyse the data.

3.1.5.2 Intensity-modulated photocurrent spectroscopy (IMPS)

In IMPS measurements, solar devices are perturbed by a small amplitude modulation of the photon flux incident (optical perturbation) on the cell superimposed on a steady-state illumination level. Then, the magnitude and the phase of the frequency-dependent photocurrent response at short circuit are recorded. In analogy to Eq. 3.12, the IMPS transfer function (*Y*) is defined as

$$Y(\omega) = \frac{J(\omega)}{I(\omega)} = \frac{j_0 \, sin\,(\omega t + \varphi\,)}{I_0 \, sin\ \omega t} \tag{3.24}$$

and

$$Y(\omega) = \ Y_0 \, cos\, \varphi + Y_0 \, j\ sin\varphi \tag{3.25}$$

where *I(ω)* is the incident light flux signal. Note that *Y* is nothing else but a frequency-dependent EQE. The zero frequency limit of the transfer function ($\omega \rightarrow 0$) should then reproduce the stationary value defined by Eq. 3.6.

In IMPS is also possible to determine the time constant (τ_{IMPS}) for the photocurrent response which could be a signature of transport, recombination and other kind of processes occurring in the device.[11] For PSC, three peaks are usually observed in different frequency range for the Bode plot, Figure 3.10. According to the literature,[11,27] the two peaks at *HF*, (around 10^4 and 10^3 Hz) are associated with electron transport in mesoporous TiO_2 network and the electrical coupling between series resistance and geometric capacitance. While, *LF* peak (about 1 Hz) has been attributed to the ionic reorganization movements.

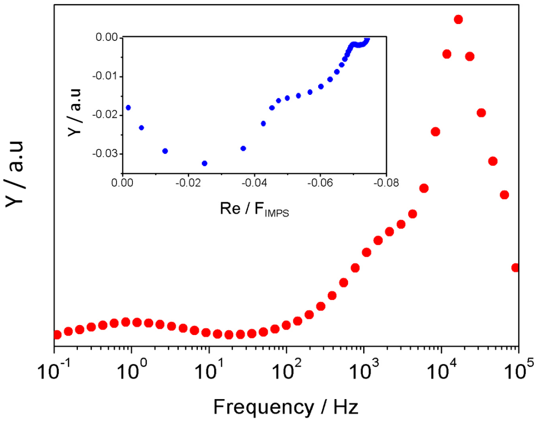

Figure 3.10. Frequency plot of the imaginary part of the IMPS transfer function in $MA_{0.6}FA_{0.4}PbI_3$ perovskite solar cells at 258K.

In this thesis, IMPS has been measured by using a potentiostat PGSTAT302N/FRA2 module coupled to a LED via an AUTOLAB LED driver. The light perturbation corresponds to 10% of the DC background illumination intensity in all cases.

3.2 Fabrication of perovskite solar cells

Fabrication of perovskite solar cells, which are apt for fundamental characterization and testing, is a very critical and delicate procedure. In this section we focus on the preparation of the perovskite layer as well as on the fabrication and deposition of the electron and hole selective contacts, that have been used to fabricate the devices studied in this thesis.

In the appendix, some important details to prepare reproducible and high efficiency PSCs are listed. Also the materials and chemicals used for fabricating these devices are collected in the Table A-3.1 in appendix A.

3.2.1 Substrate cleaning

FTO TEC15 (Pilkington, resistance 15Ω/square, 82-84.5% visible transmittance), patterned by laser etching, is used as substrate. Firstly, the glasses are brushed using Hellmanex solution in water (2:98 vol %) and rinsed with deionized water. The glasses are washed using an ultrasonic bath and the following the solvent sequence: 1. Hellmanex solution; 2. Deionized water; 3. Ethanol; 4. Isopropanol. For every solvent, the substrates are sonicated for 15min. The isopropanol has to be dried with compressed air.

Immediately after that, the substrates are annealing at 500 ºC for 5 min to remove the organic matter (30 min are required to reach the 500 ºC). For this step, a high-temperature furnace is used. Finally, FTO glasses are left to cool down to room temperature.

3.2.2 Electron selective contact

3.2.2.1 TiO_2 compact locking layer (c-TiO_2)

TiO_2 blocking layer is deposited onto hot FTO by spray pyrolysis (Fig. 3.11). The sprayed solution is obtained by addition of 1 mL of titanium diisopropoxide bis(acetylacetonate) solution (75% in 2-propanol, Sigma-Aldrich) in 14 mL of absolute ethanol. The titanium solution is sprayed using oxygen as the carrier gas. Once the compact TiO_2 solution is totally sprayed, the substrates are kept at 450 °C for 30 min for the formation of the anatase phase with a thickness of 40 nm. Finally, the substrates are left to cool down to room temperature.

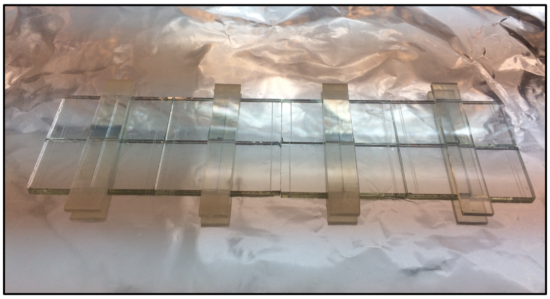

Figure 3.11. 16 substrate placed onto a hot plate where some pieces of glass are covering a side of FTO. The side protected works like the anode in the solar.

3.2.2.2 TiO_2 mesoporous layer (m-TiO_2)

TiO_2 mesoporous solution is obtained by diluting a commercial TiO_2 paste (Dyesol, 18NRT) in absolute ethanol with a 1:5 weight rate followed by strong stirring. The solution has to be prepared 24h before use. Once the solution is completely dispersed, 100 µL are taken and deposited on FTO/*c*-TiO_2 by spin-coating at 2000 rpm for 10 s. Then, the samples are quickly dried at 100 °C for 10 min using a hot plate. Finally, TiO_2 mesoporous layer (*m*-TiO_2) is sintered inside a high-temperature furnace using the temperature programme shown in Table 3.1. The substrates are left to cool down to room temperature. The thickness of the resulting *m*-TiO_2 layer is around 200 nm.

Table 3.1 Temperature sequence to sinterize mesoporous TiO_2 films.

	Step 1	***Step 2***
Initial temp. (ºC)	120	370
Ramp (min)	30	25
Final temp. (ºC)	370	500
Hold (min)	10	30

3.2.2.3 TiO_2 nanocolumns layer (Nc-TiO_2)

TiO_2 nanocolumns deposition (anatase phase and amorphous) is carried out in a microwave electron cyclotron resonance (MWECR) plasma enhanced chemical vapour deposition (PECVD) reactor working in downstream configuration. The utilized plasma source is of the SLAN type operated with a power of 400 W with O_2 as plasma gas at a pressure of $5 \cdot 10^{-3}$ Torr. Titanium tetraisopropoxide, $Ti(OC_3H_7)_4$ (TTIP), is used as precursor bubbled to the plasma chamber by means of an O_2 flow. The deposition at room temperature produced the formation of 1D amorphous TiO_2 nanocolumns (Nc-amorphous), meanwhile heating of the substrates during deposition up to 300 ºC provided the crystallization to the anatase phase (Nc-anatase).

The amorphous TiO_2 nanocolumnar samples are deposited onto a 40 nm compact TiO_2 thin film fabricated by electron-beam evaporation using TiO_2 pellets as target material. Deposition is carried out under a pressure of $5 \cdot 10^{-4}$ mbar by flowing O_2 into the chamber to obtain a full oxidation to TiO_2. These TiO_2 layers deposited at room temperature are amorphous and the crystallization to the anatase phase is accomplished by annealing the samples in air at a temperature of 450 ºC for 1 h. This compact anatase films is deposited to provide a crystalline layer that facilitates the electron transport at the interface with the FTO.

This procedure has been carried in the labs of ICMSE (Drs. Ana Borrás and Angel Barranco)

3.2.3 Perovskite film deposition

Two different laboratory recipes have been employed in this thesis to prepare perovskite films: under environmental conditions (humid conditions) or inside a glove box (dry conditions).

3.2.3.1 Perovskite deposition at environmental conditions

Organic-inorganic halide perovskite

Two type of organic-inorganic halide perovskite have been deposited at humidity conditions: $MAPbI_3$ and $FA_{0.83}MA_{0.17}PbI_3$. The preparation and deposition perovskite precursor solutions are organized in three steps (Scheme 3.1): 1) preparation of a perovskite solution 1.5 M; 2) dilution of the perovskite solution 1.5 M to obtain a perovskite precursor solution 1.35 M taking into account the content of H_2O in the environment; 3) deposition of the perovskite precursor solution by spin coating.

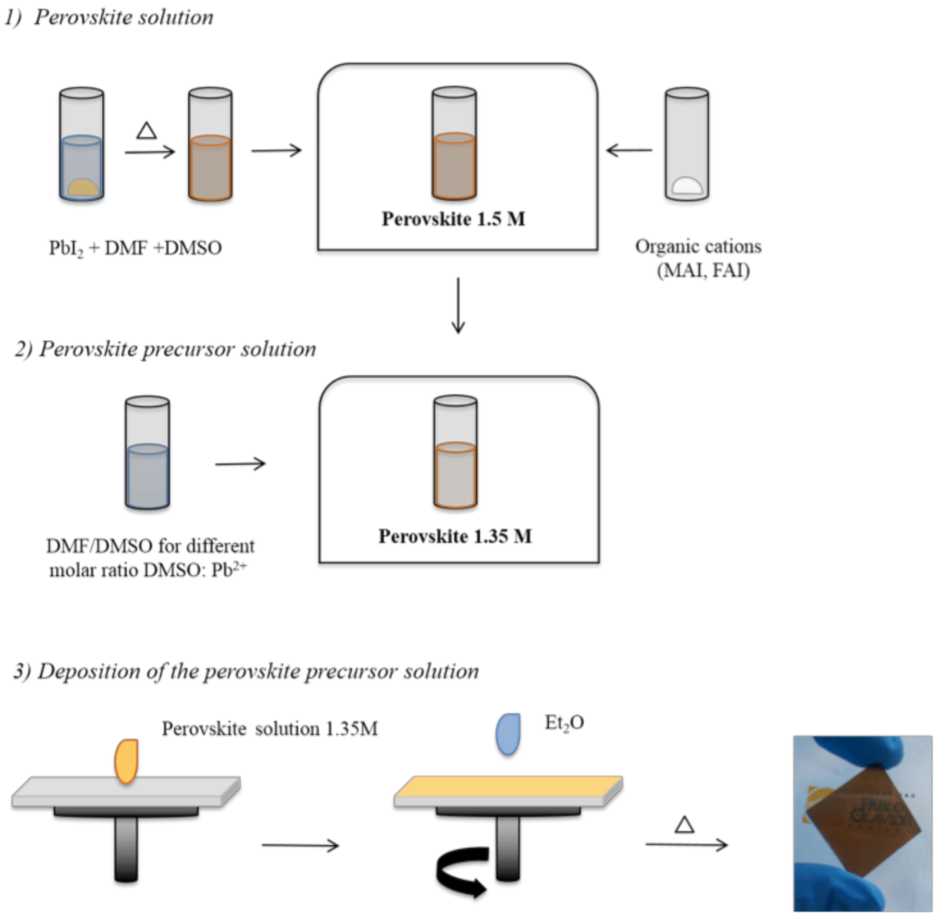

Scheme 3.1. Scheme to the preparation of perovskite solutions (step 1 and 2) and deposition of perovskite under ambient conditions (step 3).

1) Perovskite solution 1.5 M

Inside a glove box, the precursors of the $MAPbI_3$ perovskite are set aside to obtain a molar ratio 1:1:1 in methylammonium iodide (MAI), lead (II) iodide (PbI_2) and (dimethyl sulfoxide) DMSO. $FA_{0.83}MA_{0.17}PbI_3$ is prepared with a molar ratio 0.83:0.17:1:1 in formamidinium iodide (FAI), MAI, PbI_2 and DMSO. The solvent used is N,N-dimethylformamide (DMF) in a volume ratio of 1:0.095 DMF/DMSO. It is important that, firstly, the PbI_2 is dissolved in the DMSO/DMF mixture. For this, the solution has to be warmed at 100 ºC without stirring. Once the lead solution is completely homogeneous, it is left to cool and then mixed with the organic cations outside the glove box. In this way, 1.5 M perovskite solutions are obtained.

2) *Perovskite precursor solution 1.35 M*

Outside the glove box, the ratio DMSO:Pb^{2+} in the perovskite solution above needs to be adapted to the amount of water vapour present in the atmosphere. Both, H_2O and DMSO compete to coordinate with the lead atom for generation of the PbI_2·MAI·additive complex (see *Chapter* 2).[28] In general, the higher H_2O amount in the ambient (in the laboratory), the smaller DMSO amount should be used in the perovskite precursor solution. The perovskite precursor solution 1.35 M is obtained by diluting the 1.5 M perovskite solution with a solvent mixture (DMSO/DMF) with a volume ratio of 1:0.46.

Table 3.2. Volume ratio DMSO/DMF (%) for different molar ratio DMSO: Pb^{2+} in the $MAPbI_3$ perovskite precursor solution.

Ratio DMSO:Pb^{2+}	DMSO (V %)	DMF (V %)
0	0	100
0.5	7.7	92.3
0.75	17.5	82.5
1.0	23.0	77.0
1.25	26.4	73.6
1.5	30.6	69.4

This DMSO/DMF mixture is prepared taking into account the H_2O amount in the environment as well as the molar ratio of DMSO:Pb^{2+} in the resulting perovskite precursor solution (Table 3.2). In *Chapter* 10 we will discuss in detail how the amount of water in the air has to be correctly considered for a given temperature and relative humidity ratio to obtain high efficiency PSC devices.

3) *Deposition of the perovskite precursor solution*

Once the perovskite precursor solution is adjusted to ambient conditions, it is deposited on the FTO/*c*-TiO_2/*x*-TiO_2 substrate (*x*= mesoporous, amorphous and anatase nanocolumns) and then spin-coated in a one-step setup at 4000 rpm for 50 s. During the spinning, DMF is selectively washed with a non-polar solvent as diethyl ether just before the white solid begins to form in the substrate (Fig. 3.12 left). Afterward the substrate is annealed at 100 °C for 3 min to obtain a crystalline $MAPbI_3$ films (Fig. 3.12 right) of thickness about of 400 nm with tetragonal phase. For the $FA_{0.83}MA_{0.17}PbI_3$ films, the substrate is annealed at 150 ºC for 15 min.

Figure 3.12. (Left) White solid formed on the substrate when the antisolvent is not added during the spin-coating step. (Right) $MAPbI_3$ perovskite film fabricated at ambient conditions.

Fully Inorganic perovskite

$CsPbBr_3$ based devices are prepared in this thesis by a two-step sequential deposition technique. Firstly, dissolution of $PbBr_2$ in DMF (1M) is prepared by heating at 75 ºC for 20 min and filtered (pore size 0.45μm). This solution is spin-coated (2500 rpm for 30 s) on FTO/*c*-TiO_2/m-TiO_2 substrate. During the deposition process, the dissolution is kept at 75 ºC. Afterward, the substrates are dried on a hot plate at 70 ºC for 30 min and then dipped for 10 min in a solution of 17 mg/mL CsBr in methanol at 60 ºC. Subsequently, the substrate is annealed at 250ºC for 10 min.

3.2.2.2 Perovskite deposition inside a glove box

Depending on the desired composition of perovskite, different perovskite precursor solutions are prepared inside an argon glove box under controlled moisture and oxygen conditions (H_2O level: <1 ppm and O_2 level: <10 ppm):

$MAPbI_3$

The pure methylammonium perovskite precursor solution is prepared by mixing 1.2 M MAI and PbI_2 with a 1:1 molar ratio in DMSO. First, the lead salt needs to be dissolved in DMSO by annealing a 70 ºC overnight, then it is left to cool down to glove box temperature. Finally, the MAI is added to the PbI_2 solution and stirred for a few seconds (10-20 s). Thinner and thicker perovskite films have been obtained changing the Pb^{2+} precursor concentration (0.8 M and 1.4 M).

$MA_{0.6}FA_{0.4}PbI_3$

The double cation (with only iodide as anion) perovskite precursor solution is composed of 1.2 M MAI, FAI and PbI_2 (0.6:0.4:1.5 molar) in DMSO (15%

excess PbI_2). As for pure methylammonium perovskite, first the lead salt has to be dissolved in DMSO to add the organic cations.

$FA_{0.85}MA_{0.15}PbI_{0.85}Br_{0.15}$

The double cation perovskite (with iodide and bromide as anions) is prepared by dissolving FAI, MABr, PbI_2 (1.2 M) and $PbBr_2$ (0.85:0.15:1.5:0.15 molar, (15% excess PbI_2)) in a mixture of solvents DMSO/DMF (1:4 V/V %). It is important that, first, the lead salts are dissolved in the DMSO/DMF mixture. For this, the solution has to be warmed at 80 ºC without stirring overnight. The solution is left to cool down to room temperature and added to the MAI and FAI. Thinner and thicker perovskite films have been obtained changing the precursor concentration (Pb^{2+} = 0.8 M and 1.4 M).

$Cs_{0.05}FA_{0.81}MA_{0.14}PbI_{0.85}Br_{0.15}$

The triple cation perovskite is prepared by dissolving FAI (1.01M), MABr (0.20 M), PbI_2 (1.21 M) and $PbBr_2$ (0.20 M) in a mixture of solvents DMSO/DMF (1:4 V/V %). It is important that, firstly, the lead salts are dissolved in the DMSO/DMF mixture. For this, the solution has to be warmed at 80 ºC without stirring overnight. The solution is left to cool down to room temperature and added to the MAI and FAI. After that, CsI (5 wt %) is added (from a stock solution 1.5 M in DMSO) to the precursor solution.

The perovskite precursor solution desired is dropped on the substrate and then spin-coated in a two-step setup at 1000 and 6000 rpm for 10 and 20s, respectively. During the second step, 110µL of chlorobenzene is dropped on the spinning substrate 15 seconds before the end of the spinning program. The samples are then annealed to 100 ºC for 1h in the argon filled glove box. Different thicknesses are obtained depending on the perovskite composition, 3.4.

Table 3.4. Thickness obtained for different perovskite composition and precursors concentration when they are deposited by spin coating in two steps: 1) 1000 rpm, 10 s; 2) 6000 rpm, 20 s.

Perovskite	**Concentration Pb2+ [M]**	**Thickness [nm]**
$MAPbI_3$	0.8	300
	1.2	500
$MA_{0.6}FA_{0.4}PbI_3$	1.2	300
$FA_{0.85}MA_{0.15}PbI_{0.85}Br_{0.15}$	0.8	300
	1.2	500
$Cs_{0.05}FA_{0.81}MA_{0.14}PbI_{0.85}Br_{0.15}$	1.4	950

3.2.4 Hole selective contacts

3.2.4.1 Spiro-OMeTAD

A 59 mM solution of 2,2´,7,7´-Tetrakis(N,N-di-pmethoxyphenylamine)-9,9´spirobifluor-ene (spiro-OMeTAD) in clorobencene is used as hole transport material. This solution is prepared dissolving the 72 mg of spiro-OMeTAD in 1mL of chlorobencene. After this, 17.5 µL of lithium bis- (trifl uoromethylsulphonyl)imide (LiTFSI) stock solution (520 mg of LiTFSI in 1 mL of acetonitrile), and 28.8 µL of 4-tert-butylpyridine (TBP) are added like additives.

A 50 µL of the spiro-OMeTAD solution is deposited on perovskite. Immediately after this, the HTM is spin-coated at 4000 rpm for 30 s. In this way, a purple spiro-OMeTAD film with a thickness around 600 nm is obtained (Fig. 3.13A). For perovskite film fabricated inside a glove box, spiro-OMeTAD solution is doped with 21.9 µL of a cobalt (III) salt (FK209 (tris(2-(1Hpyrazol-1-yl)-4-tert-butylpyridine)-cobalt(III)tris(bis(trifluoromethyl-sulfonyl)imide)) stock solution (400 mg in 1 mL of acetonitrile)) as well.

3.2.4.2 P3HT

For the preparation of this HTM, 15 mg/mL of poly(3-hexylthiophene-2,5-diyl) (P3HT) in chlorobencene is dissolved and doped with 6.8 mL of LiTFSI stock solution (28.3 mg/mL of LiTFSI in acetonitrile). To deposit the P3HT on the top of the perovskite film, 50 µL of the HTM is placed on the substrate and spin-coated at 4000 rpm for 20 seconds.

3.2.5 Metallic back contact

3.2.5.1 Gold evaporation

Before the gold deposition, selective contacts (m-TiO_2 and HTM) and perovskite layer are removed from part of the substrate to facilitate the deposition of gold contact directly on FTO (Fig. 3.13B). Then, the samples are covered with a mask to define the electrodes (1.5 x 0.3 cm^2) and transferred into a gold evaporator (Fig. 3.13D). Finally, a 60 nm layer of gold is deposited by thermal evaporation under a vacuum level between $1\cdot10^{-6}$ and $1\cdot10^{-5}$ torr.

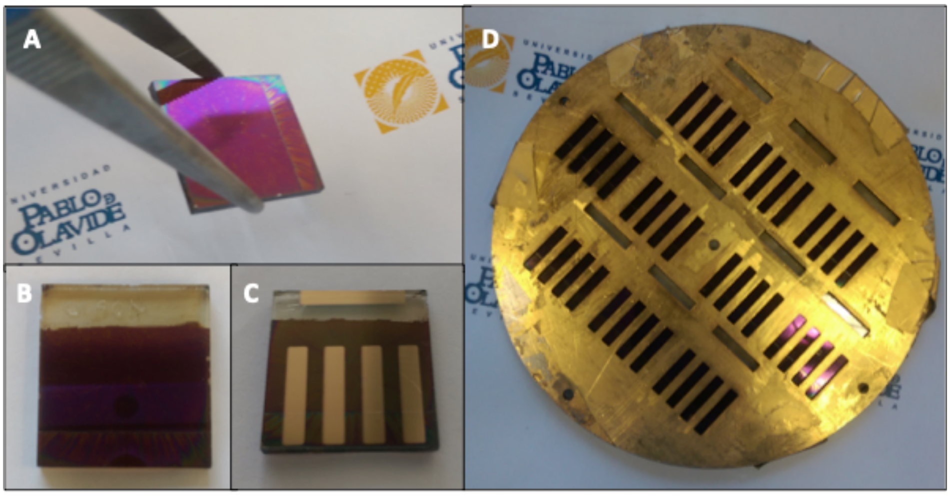

Figure 3.13. Images of (A) spiro-OMeTAD film on $MAPbI_3$, (B) substrate with scratched anode, (C) perovskite complete device and (D) mask for gold deposition.

3.3 References

1 Principles and Practice of Variable Pressure / Environmental Scanning Electron Microscopy (VP-ESEM), https://www.wiley.com/en-bd/Principles+and+Practice+of+Variable+Pressure+Environmental+Scanning+Electron+Microscopy+%28VP+ESEM%29-p-9780470065402, (accessed November 15, 2018).

2 D. A. Skoog, S. R. Crouch and F. J. Holler, *Principles of instrumental analysis.*, Thomson Brooks/Cole, Belmont, CA, 2007.

3 Optical Properties and Electronic Structure of Amorphous Germanium - Tauc - 1966 - physica status solidi (b) - Wiley Online Library, https://onlinelibrary.wiley.com/doi/pdf/10.1002/pssb.19660150224, (accessed November 14, 2018).

4 M. Salado, J. Idigoras, L. Calio, S. Kazim, M. K. Nazeeruddin, J. A. Anta and S. Ahmad, Interface Play between Perovskite and Hole Selective Layer on the Performance and Stability of Perovskite Solar Cells, *ACS Appl. Mater. Interfaces*, 2016, **8**, 34414–34421.

5 J. Idígoras, L. Contreras-Bernal, J. M. Cave, N. E. Courtier, Á. Barranco, A. Borras, J. R. Sánchez-Valencia, J. A. Anta and A. B. Walker, The Role of Surface Recombination on the Performance of Perovskite Solar Cells: Effect of Morphology and Crystalline Phase of TiO2 Contact, *Adv. Mater. Interfaces*, 2018, **5**, 1801076.

6 T. Nyokong and V. Ahsen, Eds., *Photosensitizers in Medicine, Environment, and Security*, Springer Netherlands, 2012.

7 The Physics of Solar Cells, https://www.worldscientific.com/worldscibooks/10.1142/p276, (accessed November 13, 2018).

8 G. F. Burkhard, E. T. Hoke and M. D. McGehee, Accounting for Interference, Scattering, and Electrode Absorption to Make Accurate Internal Quantum Efficiency Measurements in Organic and Other Thin Solar Cells, *Adv. Mater.*, 2010, **22**, 3293–3297.

9 I. Zarazua, G. Han, P. P. Boix, S. Mhaisalkar, F. Fabregat-Santiago, I. Mora-Seró, J. Bisquert and G. Garcia-Belmonte, Surface Recombination and Collection Efficiency in Perovskite Solar Cells from Impedance Analysis, *J. Phys. Chem. Lett.*, 2016, **7**, 5105–5113.

10 A. Todinova, L. Contreras-Bernal, M. Salado, S. Ahmad, N. Morillo, J. Idígoras and J. A. Anta, Towards a Universal Approach for the Analysis of Impedance Spectra of Perovskite Solar Cells: Equivalent Circuits and Empirical Analysis, *ChemElectroChem*, 2017, **4**, 2891–2901.

11 E. Guillén, F. J. Ramos, J. A. Anta and S. Ahmad, Elucidating Transport-Recombination Mechanisms in Perovskite Solar Cells by Small-Perturbation Techniques, *J. Phys. Chem. C*, 2014, **118**, 22913–22922.

12 F. Fabregat-Santiago, G. Garcia-Belmonte, I. Mora-Seró and J. Bisquert, Characterization of nanostructured hybrid and organic solar cells by impedance spectroscopy, *Phys. Chem. Chem. Phys.*, 2011, **13**, 9083.

13 A. Hagfeldt, G. Boschloo, L. Sun, L. Kloo and H. Pettersson, Dye-Sensitized Solar Cells, *Chem. Rev.*, 2010, **110**, 6595–6663.

14 A. Lasia, *Electrochemical Impedance Spectroscopy and its Applications*, Springer-Verlag, New York, 2014.

15 H.-S. Kim, I.-H. Jang, N. Ahn, M. Choi, A. Guerrero, J. Bisquert and N.-G. Park, Control of $I - V$ Hysteresis in CH $_3$ NH $_3$ PbI $_3$ Perovskite Solar Cell, *J. Phys. Chem. Lett.*, 2015, **6**, 4633–4639.

16 H.-S. Kim and N.-G. Park, Parameters Affecting $I - V$ Hysteresis of CH $_3$ NH $_3$ PbI $_3$ Perovskite Solar Cells: Effects of Perovskite Crystal Size and Mesoporous TiO $_2$ Layer, *J. Phys. Chem. Lett.*, 2014, **5**, 2927–2934.

17 M. Bag, L. A. Renna, R. Y. Adhikari, S. Karak, F. Liu, P. M. Lahti, T. P. Russell, M. T. Tuominen and D. Venkataraman, Kinetics of Ion Transport in Perovskite Active Layers and Its Implications for Active Layer Stability, *J. Am. Chem. Soc.*, 2015, **137**, 13130–13137.

18 A. Guerrero, G. Garcia-Belmonte, I. Mora-Sero, J. Bisquert, Y. S. Kang, T. J. Jacobsson, J.-P. Correa-Baena and A. Hagfeldt, Properties of Contact and Bulk Impedances in Hybrid Lead Halide Perovskite Solar Cells Including Inductive Loop Elements, *J. Phys. Chem. C*, 2016, **120**, 8023–8032.

19 E. Barsoukov and J. R. Macdonald, *Impedance Spectroscopy: Theory, Experiment, and Applications*, John Wiley & Sons Inc, Hoboken, N.J, Edición: 2nd Edition., 2005.

20 W. H. Mulder and J. H. Sluyters, An explanation of depressed semi-circular arcs in impedance plots for irreversible electrode reactions, *Electrochimica Acta*, 1988, **33**, 303–310.

21 L. Kavan, M. Zukalova, O. Vik and D. Havlicek, Sol-Gel Titanium Dioxide Blocking Layers for Dye-Sensitized Solar Cells: Electrochemical Characterization, *ChemPhysChem*, 2014, **15**, 1056–1061.

22 M. Bag, L. A. Renna, R. Y. Adhikari, S. Karak, F. Liu, P. M. Lahti, T. P. Russell, M. T. Tuominen and D. Venkataraman, Kinetics of Ion Transport in Perovskite Active Layers and Its Implications for Active Layer Stability, *J. Am. Chem. Soc.*, 2015, **137**, 13130–13137.

23 A. R. Pascoe, N. W. Duffy, A. D. Scully, F. Huang and Y.-B. Cheng,

Insights into Planar $CH_3NH_3PbI_3$ Perovskite Solar Cells Using Impedance Spectroscopy, *J. Phys. Chem. C*, 2015, **119**, 4444–4453.

24 A. Guerrero, G. Garcia-Belmonte, I. Mora-Sero, J. Bisquert, Y. S. Kang, T. J. Jacobsson, J.-P. Correa-Baena and A. Hagfeldt, Properties of Contact and Bulk Impedances in Hybrid Lead Halide Perovskite Solar Cells Including Inductive Loop Elements, *J. Phys. Chem. C*, 2016, **120**, 8023–8032.

25 I. Zarazua, J. Bisquert and G. Garcia-Belmonte, Light-Induced Space-Charge Accumulation Zone as Photovoltaic Mechanism in Perovskite Solar Cells, *J. Phys. Chem. Lett.*, 2016, **7**, 525–528.

26 A. Todinova, J. Idígoras, M. Salado, S. Kazim and J. A. Anta, Universal Features of Electron Dynamics in Solar Cells with TiO_2 Contact: From Dye Solar Cells to Perovskite Solar Cells, *J. Phys. Chem. Lett.*, 2015, **6**, 3923–3930.

27 J.-P. Correa-Baena, M. Anaya, G. Lozano, W. Tress, K. Domanski, M. Saliba, T. Matsui, T. J. Jacobsson, M. E. Calvo, A. Abate, M. Grätzel, H. Míguez and A. Hagfeldt, Unbroken Perovskite: Interplay of Morphology, Electro-optical Properties, and Ionic Movement, *Adv. Mater.*, 2016, **28**, 5031–5037.

28 C. Aranda, C. Cristobal, L. Shooshtari, C. Li, S. Huettner and A. Guerrero, Formation criteria of high efficiency perovskite solar cells under ambient conditions, *Sustain. Energy Fuels*, 2017, **1**, 540–547.

Chapter 4

Specific Cation Interactions as the Cause of Slow Dynamics and Hysteresis in Dye and Perovskite Solar Cells

Hysteresis is one of the most remarkable features of perovskite solar cells; however, it is also present in other kinds of devices such as dye-sensitized solar cells. Hysteresis is due to underlying slow dynamic processes that interfere with the process of charge separation that depends critically on the selective contacts used. In this Chapter we focus on the low-frequency (0.1–10 Hz) dynamics using small-perturbation optoelectronic techniques and found that both perovskite solar cells and ''viscous electrolyte containing'' dye-sensitized solar cells can be described on the same fundamental grounds. A connection between the polar nature of the cations and the low-frequency component of these solar cells is found. There is evidence that in both cases ion transport and specific chemical interactions with the TiO_2 *surface give rise to the slow dynamics and the hysteresis.*

This chapter is based on Publication 1 of this Thesis: Contreras-Bernal *et al*. Phys. Chem. Chem. Phys., 2016, 18, 31033–31042.

4.1 Introduction

Despite perovskite solar cells have undergone a rapid development in the last few years, mainly in terms of efficiency,[1] the origin and behaviour of many physical processes are not yet completely understood.

One of these processes is the hysteresis found in the current–voltage characteristics. As a result of this hysteretic behaviour, the real photovoltaic performance is difficult to be determined using the conventional IV curve method. The shape of the curve dramatically depends on the scan rate, voltage sweep direction and pre-polarization time (poling).[2–7] Thus, the output current while sweeping the voltage could lead to an overestimation or underestimation of the real efficiency. The hysteresis not only depends on the conditions under which the IV curves are recorded, but also on other factors related to the device configuration such as the charge selective contacts (structural properties and the nature of *n*- and *p*-type contact crystal formation and deposition techniques).[8–11] Additionally, rapid degradation and low stability have also been found for PSCs characterized by a pronounced hysteresis.[4,12] Ferroelectric behaviour,[13–16] ionic migration,[3,4,17,18] interfacial charge accumulation due to trapping–detrapping processes[7,8,19] and structural changes[20,21] of the perovskite material have been proposed in the literature as possible explanations for this phenomenon. However, recent papers point to the slow dynamic processes as the origin of hysteresis. In particular, dielectric relaxation and interfacial charge accumulation processes connected to ion migration, observed in the seconds–milliseconds time scale, have been pointed out as the decisive cause of the hysteresis.[2,4,10,12,21–25]

In this connection, it is interesting to stress that the hysteresis is also a feature of other kinds of solar cells, at is the case of dye-sensitized solar cell.[26,27] Yang *et al.* proposed an equivalent circuit model to simulate the IV curves of DSSCs and study the influence of delay times on the hysteresis.[26] Yang related the large time constant of DSSCs to the large capacitance and the slow Nernstian ionic diffusion in the electrolyte. Sarker *et al.* developed a theoretical model whose numerical solution allowed estimating the hysteresis in IV curves of DSSCs.[27] The chemical capacitance of a TiO_2 photoanode and the double layer capacitance at the substrate/electrolyte and counterelectrode/electrolyte interfaces were suggested as the determining factors of hysteresis in DSSCs. Nevertheless, this model does not consider the ion diffusion in the electrolyte.

In spite of the many papers that have hinted at the effect of ionic motion on the hysteresis, many points still remain obscure, such as the nature of the moving species and the specific effects produced by different contacts. In this respect it is important to stress that many reports are based on theoretical studies done in the bulk with no consideration of the effect of specific interactions between the mobile species causing the hysteresis and the chemical nature of the surface of the selective contact.

In this *Chapter* a deeper insight into these hysteresis-determining factors in DSSCs and PSCs by using impedance and intensity-modulated photocurrent spectroscopies is provided. DSSCs containing a highly viscous room temperature ionic-liquid (RTIL) and large organic cations with low mobility serve as a good model for the processes occurring in the ionic lattice of the perovskite, because the functioning of a DSSC relies on efficient ionic motion in the liquid electrolyte. Hence, we study the influence of viscosity of the electrolyte solvent and the nature of the perovskite organic cations (MA- and FA- cations) on the hysteretic behaviour of both kinds of solar devices, with the intention of finding out the common features and the relevant differences. To perform this study, the viscosity of the electrolyte in DSSCs was controlled not only by mixing the RTIL with acetonitrile at various mixing ratios, but also by varying the device temperature up to 318 K, since, as it was indicated in *Chapter* 1, a higher temperature the tetragonal to cubic transition appeared for $MAPbI_3$ perovskite. In this *Chapter*, we focus on the low-frequency component of both DSSCs and PSCs in order to determine the slow dynamic processes causing the hysteresis. Similar features in relation to the hysteresis have been found.

4.2 Fabrication and characterization of devices

Fabrication of dye-sensitized solar cell

The working electrodes were made using 12 μm thick films consisting of a layer of 8 μm of 20 nm TiO_2 nanoparticles (18NR-T, Dyesol) and a layer of 4 μm of 400 nm TiO_2 particles (18NR-AO, Dyesol) with an active area of 0.16 cm^2. Prior to the deposition of the TiO_2 paste, the conducting glass substrates (Pilkington–TEC15) were firstly cleaned in ultrasonic baths of detergents, deionized water, isopropanol and ethanol successively, and heated to 500ºC for 30 min. Secondly, conducting glass substrates were immersed in a solution of $TiCl_4$ (40 mM) for 30 minutes at 70ºC and heated to 500ºC. The TiO_2 nanoparticle paste was deposited onto a conducting glass substrate using the screen printing technique. The TiO_2 electrodes were gradually heated under airflow at 325 ºC for 5 min, 375 ºC for 5 min, 450 ºC for 15 min and 500 ºC for 15 min. The heated TiO_2 electrodes were immersed again in a solution of $TiCl_4$ (40 mM) at 70 ºC for 30 min and heated again at 500 ºC for 30 min. The dye solution was composed of 0.3 mM N719 and 0.3 mM chenodeoxycholic acid in ethanol. The counter-electrode was made by spreading a Platisol solution

(Solaronix) onto a conducting glass substrate (Pilkington–TEC8), followed by heating at 390 ºC for 15 minutes. Finally, the working- and counter-electrodes were sandwiched together using a thin thermoplastic frame (Surlyn, Solaronix). The cells were filled with electrolytes of varying composition aimed to tune the viscosity (see Table A-4.1 in appendix B) through a hole previously made in the back of a platinized counter electrode. Then, the hole was sealed with a thermoplastic polymer and a cover slide glass. For more details see appendix B.

Fabrication of perovskite solar cells

Perovskite devices with mesoporous regular architecture were fabricated following the methodology described in *Chapter* 3. First, FTO TEC15 were cleaned following the solvent sequence: Hellmanex solution; Deionized water; Ethanol; Isopropanol. Then the TiO_2 compact layer was deposited by spray pyrolysis. After that, a mesoporous layer of TiO_2 was deposited on top of a TiO_2 compact layer. Then pure methyl ammonium ($MAPbI_3$) and mixed cation perovskite ($MA_{0.6}FA_{0.4}PbI_3$) were deposited as active layer inside a glove box. For that, perovskite precursor solutions of 1.2 M were used. Homogeneous and free-pin holes perovskite layers were obtained (Fig.A-4.1). The thickness obtained for the different perovskite compositions are shown in Table 3.4 in *Chapter* 3. Later perovskite deposition, spiro-OMeTAD was spin coated. Finally, 80 nm of gold was deposited by thermal evaporation. (See *Chapter* 3 for details)

Characterization of devices

The devices were characterized using two different light sources: (1) a solar simulator (ABET-Sun2000) with AM 1.5G filter and (2) a green light emitting diode (LED, LUXEON) (see *Chapter* 3 for details). The current-voltage characteristic was measured with different scan rates: 200, 100, 50 and 10 mV/s in the temperature range of 278-338 K. To avoid any degradation process related with the temperature, the measurements were carried out under N_2-atmosphere. For the time-dependent photocurrent measurements, the devices were kept in dark at short-circuit condition and then the sample was illuminated to measure J_{SC} with time. The illumination for IS measurements was provided by a green LED over a wide range of DC light intensities. To avoid voltage drop due to series resistance, IS measurements were performed at the open circuit potential. A 20 mV perturbation in the 10^6-10^{-2} Hz range was utilized to obtain the spectra. IMPS measurements were performed at short-circuit in the 10^5 to 10^{-2}Hz range with a light perturbation corresponding to 10% of the DC background illumination intensity. The both IS and IMPS were carried out at different temperatures. Z-view equivalent circuit modeling software (Scribner) was used to fit the IS spectra, including the distributed element DX11 (transmission line model) for the DSSC measurements (see *Chapter* 3 for details).

4.3 Results and discussion

The power conversion efficiencies for the different DSSCs and PSCs measured under standard conditions (1 sun - AM 1.5 illumination) were in the range of 0.7-7% and 11-13%, respectively. To test the reproducibility of the samples, three devices were characterized for each configuration, and no significant deviations were found between them (see appendix B, Table A-4.2 and Fig. A-4.2). Note that the large range of efficiencies obtained for DSSCs was a consequence of the different electrolyte solvents employed in each DSSC configuration (Table A-4.1).

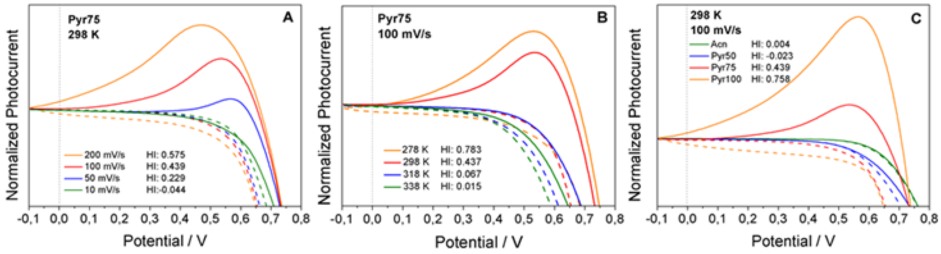

Figure 4.1. Normalized (reference voltage: -0.1V) current-voltage curves of DSSCs measured in the reverse scan (line) and forward scan (dash line) under light intensity of 10 mW·cm^{-2} using a green LED. The influence of hysteresis-determining factors is specifically shown: (A) scan rate, (B) temperature and (C) electrolyte solvent.

Figure 4.1 and Figure 4.2 show current-voltage characteristics of DSSCs and PSCs of varying composition measured by cyclic voltammetry. The measurement was started with a reverse scan (to short-circuit condition) after waiting 10 s at 1 V and 1.2 V for DSSCs and PSCs respectively, and was then continued with a forward scan (to open-circuit condition). The measurements were performed with different scan rates (200, 100, 50 and 10 mV/s) and in the temperature range of 278 – 338 K. In all cases, the photocurrent was normalized with respect to its value at -0.1V.

In order to quantify the hysteresis effect, the dimensionless hysteresis index (*HI*) has been defined in the following way

$$HI = \frac{(J_{mp})_{reverse} - (J_{mp})_{forward}}{(J_{mp})_{reverse}} \tag{4.1}$$

where, J_{mp} is the photocurrent at the maximum power point. As shown in Figure 4.1, the following trends are observed. As higher RTIL/Acn ratio, lower temperature and faster scan rate was applied to the device, the hysteresis becomes more pronounced (higher *HI*) giving rise to significant differences in the IV curves. In detail, this hysteretic behaviour involves remarkable differences in the IV curve measured in reverse and forward scans not only affecting the open-circuit photovoltage or the fill factor but also the short-circuit photocurrent as shown Figure A-4.3A in appendix B.

As it was explained in *Chapter* 2, the IV curves are based on the photocurrent measurement during the stepwise change of the applied bias voltage. Thus, long delay times at each applied potential, which correspond to slow scan rates, are necessary to reach the steady-state photocurrent. As it was also previously reported by X. Yang *et al.*,[26] there is hysteresis at open-circuit condition when short delay times are employed for the IV curves characterization of DSSCs. In line with our results, higher V_{OC} values were found in the reverse scan than in the forward scan. The hysteretic behaviour has been attributed to the slow Nernstian diffusion of ions in the electrolyte.[26] Therefore, it is expected that for smaller ionic diffusion coefficients, longer delay times (slower scan rates) are required to measure the steady-state photocurrent. Consequently, for a particular ionic diffusion coefficient, the faster the scan rate, the more pronounced hysteresis is found (Fig. 4.1A). In the same way, the higher the solvent electrolyte viscosity and the smaller the ionic diffusion coefficient, as it is expected for higher RTIL/Acn ratios and/or lower temperatures, more pronounced hysteresis at the same scan rate is also found (Fig. 4.1B and 4.1C). This behaviour is in line with the time-dependent photocurrent density measurements as shown in Figure A-4.4. Before reaching the steady-state photocurrent, a stronger exponential decay, attributed to the accumulated capacitive current, was found for the situations of stronger hysteresis (smaller ionic diffusion coefficients). Different capacitive elements were previously associated to the hysteresis found in the different regions of the IV curve.[27]

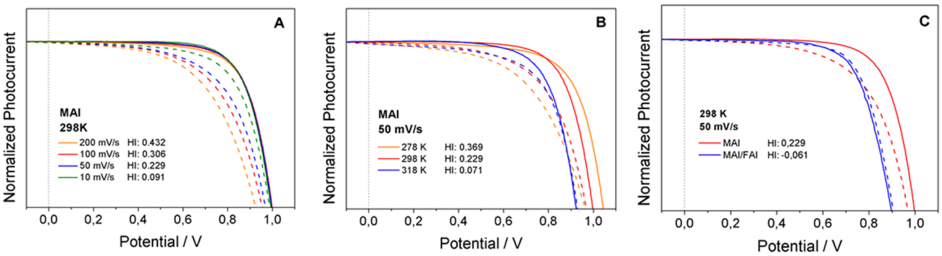

Figure 4.2. Normalized (reference voltage: -0.1V) current-voltage curves of PSCs measured in the reverse scan (line) and forward scan (dash line) under light intensity of 10 mW·cm^{-2} using a green LED. The influence of different determining factor-dependence on hysteresis is shown: (A) scan rate, (B) temperature and (C) perovskite composition.

In analogy to DSSCs, the hysteretic behaviour appears at open-circuit condition, short-circuit condition (see Fig. A-4.3B) and at the maximum power point. Although no bumps are found for the scan rates and poling conditions explored, bumps have also been observed in PSCs before.[4] For this reason, we found more convenient to define the hysteresis index according to[11]

$$HI = \frac{(J_{0.8 \cdot Voc})_{reverse} - (J_{0.8 \cdot Voc})_{forward}}{(J_{0.8 \cdot Voc})_{reverse}} \tag{4.2}$$

where, $J_{0.8 \cdot Voc}$ is the photocurrent at 80% of V_{OC}. (Note that this different definition of *HI* does not affect the discussion of the results). In relation to the scan rate effect, the hysteresis between reverse and forward scans is more pronounced when faster scan rates were employed, whereas it tends to disappear at slow scan rates (Fig. 4.2A). Note that no significant difference appeared in the reverse scans, being the forward scans the most affected. As in DSSCs, higher efficiencies were expected in the reverse scan due to the higher V_{OC}, J_{SC} and *FF*. This hysteretic behaviour could be related to the inevitable poling a high positive voltage (1 V for DSSCs and 1.2 V for PSCs) carried out in the reverse scans as was proposed by Zou *et al.*[6] This different response is expected as charge separation/collection depends on the voltage sweep direction.[4,11,28]

On the other hand, the same temperature dependence was also found in PSCs. As shown in Figure 4.2B, the hysteresis is almost negligible at the highest temperature, 318K, (below the orthorhombic-to-cubic transition of $MAPbI_3$) and becomes more pronounced with decreasing temperature, which suggests that the hysteresis is a temperature-dependent process. Additionally, the temperature dependence does not only affect the hysteretic behaviour, but also the V_{OC}. For the both DSSC and PSC configurations, as it is expected from the general diode model,[29,30] the lower the temperature the higher the V_{OC} values. As shown in Figure A-4.5, the temperature-dependent V_{OC} can also be rationalized as a consequence of the behaviour of the electron recombination resistances with respect to temperature. At higher temperature electron acceptors (tri-iodides in DSSCs and holes in PSCs[30]) move faster and, consequently, the number of recombination events is likely to increase. Additionally, slower transport promotes the charge accumulation at the contact which is one of the origins of the hysteresis according to recent literature.[3,4,17,18] In particular, this charge accumulation at the interface between the perovskite and the electron selective layer is intimately related with the ionic migration within the 3D framework created by vertex-shared PbI_6^{4-} octahedral (see Fig. 1.2 in *Chapter* 1). In relation to these ionic migration processes, as shown in Figure 4.2C, the cationic composition of the active layer appears to be critical.

PSCs based on mixture of the MA and FA cations show insignificant hysteresis effect with respect to PSCs based on pure MA. [12,31,32]

Bearing in mind that the hysteresis seems to be related to slow charge diffusion and interfacial charge accumulation, impedance spectroscopy and intensity-modulated photocurrent spectroscopy measurements were performed to investigate the influence of the different electronic and ionic processes. In Figure 4.3, the complex impedance and apparent capacitance-dependent frequency plots for DSSC and PSC configurations are shown.

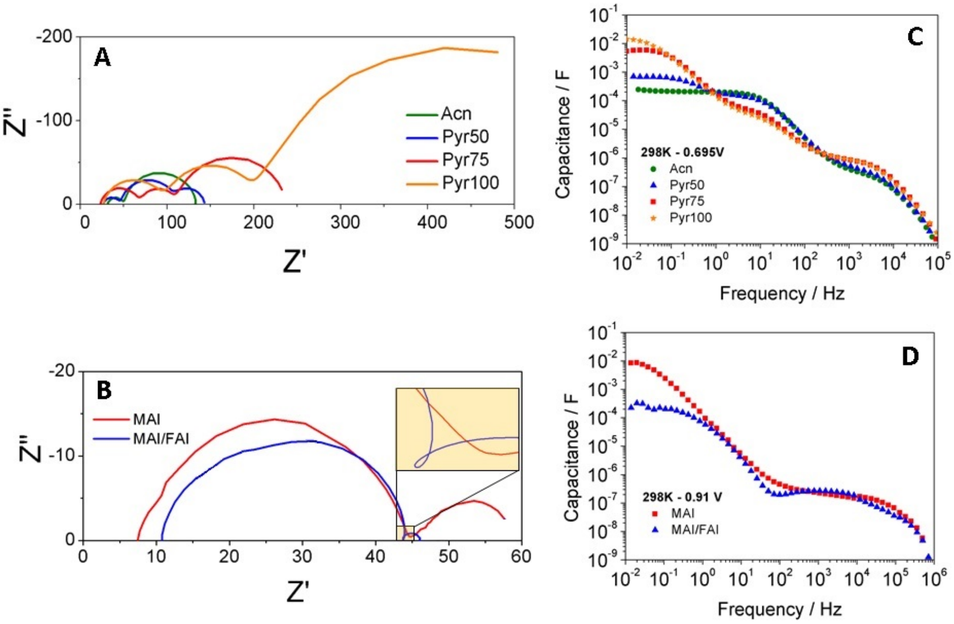

Figure 4.3. Complex-impedance plots for different (A) DSSCs and (B) PSCs obtained under illumination at the open-circuit photovoltage of each cell at 1 sun. The inset is a blow-up of the intermediate frequency region to show the occurrence of a loop in the MAI/FAI system. Frequency-dependent apparent capacitance for (C) DSSCs and (D) PSCs at 0.695V and 0.910V, respectively.

As shown Figure 4.3A, the spectra are characterized by the three semicircles typically observed in DSSCs. As it is well-known,[33–35] the high-frequency (*HF*) semicircle, the closest one to the origin, is related to charge transfer at the platinum counter-electrode, the one at mid frequencies (*MF*) arises from electronic processes at the oxide/electrolyte interface and the semicircle appearing at low frequencies (*LF*) reflects the diffusion of redox species in the electrolyte. It is important to mention that, this semicircle only appears in the cells with the most viscous electrolytes (higher RTIL/Acn ratio), as a consequence of significant mass-transport limitation. However, PSCs show only two well-differentiated semicircles (Fig. 4.3B) whose meanings were already described in *Chapter* 3. In addition a loop at intermediate frequencies appears for the mixed perovskite. The origin of this feature will be discussed below.

In order to study the general evolution of capacitive processes, Figure 4.3C and 4.3D show the frequency-dependent apparent capacitance for DSSCs and PSCs at 0.695 V and 0.910 V (values close to open-circuit conditions), respectively. Different plateaus are observed in succession, which are related with different polarization processes.[8,11,12,36] In particular, the *MF* and *HF* plateaus for DSSCs and PSCs, which show capacitance values in the range of 10^{-4} - 10^{-5} F/cm^{-2} and 10^{-6} - 10^{-7} F/cm^{-2}, were associated with the chemical capacitance of TiO_2 and the dielectric polarization of the perovskite material in the bulk, respectively. However, *LF* plateaus, with an apparent capacitance values in the range of 10^{-2} - 10^{-4} F/cm^{-2}, were previously attributed to the interfacial charge accumulation upon application of an external electrical field. Zarazua *et al.*, found that interfacial charge accumulation could modify the space charge layer of electron selective layer affecting the charge separation and/or collection efficiency.[37] Therefore, it is expected that the higher the *LF* capacitance values are, the more pronounced is the hysteresis, as can be easily confirmed by comparing with the data in Figures 4.1C, 4.2C, 4.3C and 4.3D. Similar results were found in previous papers where the hysteresis was studied in relation to the selective contacts and the perovskite crystal size.[33–35] It is important to stress that exactly the same rule holds for DSSC, a feature that has not been reported before.

In order to make efficient PSCs, it is very important to understand the molecular origin of the different hysteretic behaviour observed. In this context, the analogies observed between DSSCs and PSCs can be very illuminating. As mentioned, hysteresis has been attributed to ionic migration. However some authors have assumed that it is the migration of the organic cations the cause of the slow transport process causing the hysteresis,[12] whereas others claim that is halide ions and/or ion vacancies the mobile species.[24] Nevertheless, the results might also be related to the formation of TiO_2/perovskite interfacial dipoles, which could induce an energetic barrier modifying electron extraction.[6] Therefore, our results could be explained in terms of polarity. The differentiated dipole moments previously reported for MA and FA cations (2.28 and 0.21D, respectively)[38] can explain the lower *LF* apparent capacitance values found for MAI/FAI samples with respect to MAI samples and the smaller *LF* semicircle in complex-impedance plot (Fig. 4.3B), because MA^+ cations are more likely to interact with the TiO_2 surface than FA^+ ones.

Exactly the same effect can be inferred from the DSSC data bearing in mind the nature of RTIL (high polarity) with respect to Acn (low polarity).[39] The highest *LF* capacitance values found for Pyr100 could be related with the highest charge (cations) accumulation at the TiO_2/electrolyte interface as a consequence of the generated interfacial dipoles. This assumption is confirmed by the trends observed in the chemical capacitance (extracted from the *MF* feature) as a function of electrolyte composition (see Fig. A-4.6). This effect is analogous to the typical result obtained in a DSSC when substances like Li^+ or TBP are added to the electrolyte.[40] These results point to the strong impact of TiO_2/electrolyte and TiO_2/perovskite interface on the *LF* capacitive response, which is in practice, and together with ion migration, the ultimate cause of hysteresis.

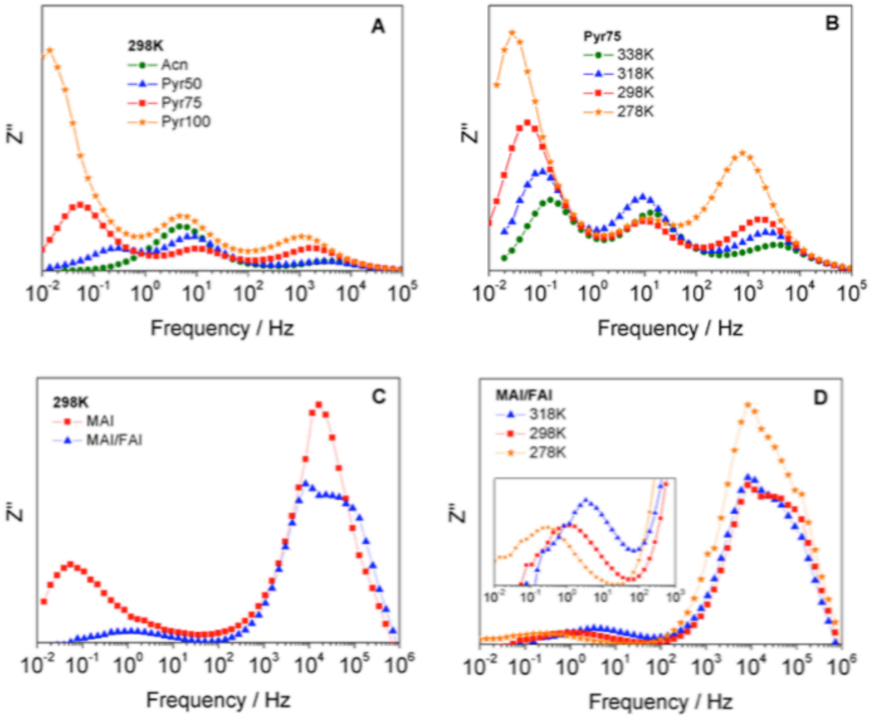

Figure 4.4. IS Frequency plots of the imaginary part for DSSCs and PSCs at different temperatures and compositions.

To cast more light on these phenomena, and to evaluate the effect of ionic diffusion on the hysteresis together with the interfacial charge accumulation upon the application of an external electrical field, we focused our attention on the *LF* component. Bearing in mind the wide variety of equivalent circuits proposed to the IS fitting for PSCs, the time constant (τ) of the *LF* component has been directly extracted from IS frequency plots, where the imaginary part of impedance (Z'') is plotted versus frequency. The time constants were extracted from Eq. 3.23 (*Chapter* 3). Figure 4.4 shows the IS frequency plots obtained for the DSSCs and PSCs at room temperature and the influence of different temperatures on the *LF* component for Pyr75 and MAI/FAI devices.

As shown in Figure 4.4, for both DSSCs and PSCs the *LF* components appear in the range of 0.01-1 Hz and consequently, their characteristic time constants are in the time scale of seconds-milliseconds. Taking into account that they cannot be associated with recombination processes, which show up in the range of 10^{-2} - 10^{-3} s and 10^{-4} - 10^{-5} s for DSSCs and PCSs (see *Chapter* 3), respectively,[36,41] these slow dynamic processes can be ascribed to ionic-Warburg diffusion either in the bulk or in the vicinity of the contact surface. The ionic diffusion coefficient (D_n) from IS frequency plots was extracted as[42]

$$D_n = \frac{L_D^2}{\tau_{LF}} \tag{4.3}$$

where τ_{LF} is the characteristic time constant of the *LF* component and L_D is the distance between working and counter-electrode in DSSCs and the thickness of the active perovskite layer in PSCs. Values of 25 μm (spacer thickness) and 300 nm (thickness of the perovskite film) were assumed for this in DSSCs and PSCs, respectively. For DSSCs, the characteristic peak of this ion-induced *LF* component shifts to smaller frequencies when the RTIL/Acn ratio increases or the temperature decreases (Figs. 4.4A and 4.4B). This behaviour points to smaller ionic diffusion coefficients as a consequence of higher electrolyte viscosity as shown Figure A-4.7A. Analogous results were obtained for PSCs. For MAI/FAI samples the *LF* component appears at higher frequencies than for MAI samples, which suggests faster ionic transport within the perovskite layer. Furthermore, as shown in Figure A-4.7B, the same ionic diffusion temperature trend was found for both PSCs. It is also important to emphasize that there is no voltage dependence of the diffusion coefficient, in contrast to the electronic one, as reported before by our group.[41]

It is important to identify the mobile species that give rise to the low-frequency feature in the spectrum. In this respect, there is conflicting information in the literature. For instance, Bag *et al.* claimed that the motion of iodide anions is too fast to be captured by the low frequency region of the impedance spectrum, and that the ammonium cations are the mobile species.[12] In contrast, based on theoretical calculations, Meloni and coworkers[9] claim that it is the iodides what migrate under the application of an external field. In our results we observe however that the "slow" process is much "faster" in the case of MAI/FAI samples with respect to MAI, hence producing lower hysteresis. As the organic component is the only difference between the two types of samples, this strongly suggests that the ionic diffusion coefficients extracted from the *LF* component can be attributed to the cation movement, and not to the halides.

Furthermore, the ionic diffusion coefficients extracted from the impedance are in the same range as those reported in the literature.[12]

The fact that transport is faster for the MAI/FAI samples is confirmed by IMPS. Figure 4.5 shows the IMPS frequency plots for the PSCs studied at the two compositions and at different temperatures.

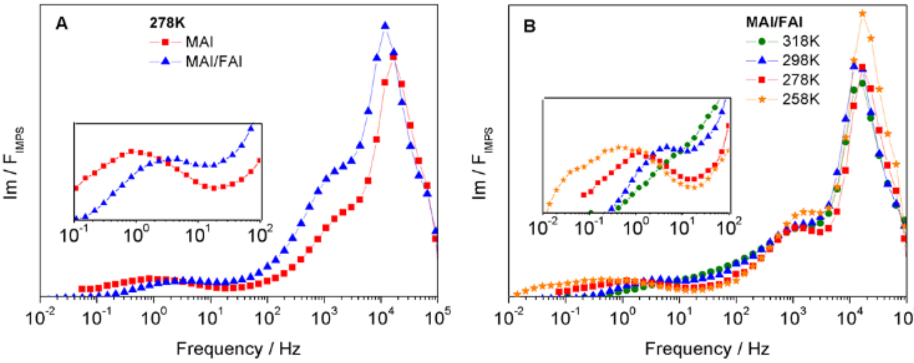

Figure 4.5. IMPS frequency plots of the imaginary part for both PSCs at different temperatures.

IMPS has been extensively used to provide information about the electron transport processes in DSSCs.[43] For these systems, the IMPS Nyquist plot is characterized by only one semicircle, whose characteristic time constant is related to the electron transport through the nanocrystalline mesoporous semiconductor. However, as shown in Figure A-4.8, three semicircles were found for PSCs. As also shown in Figure 4.5, the IMPS frequency plot shows three well-differentiated peaks at different frequency range, which point to three different charge transport processes characterized by different time constants. According to previous works,[23,36] the two *HF* components, which appear in the range of 10^4 Hz and 10^3 Hz and are voltage-dependent, were attributed to electron transport processes in HTM or perovskite layer and mesoporous TiO_2 network, respectively. Nevertheless, the *LF* component, whose characteristic time constant appears in the seconds time scale (≈1Hz), has been recently associated with the ionic movement. Focusing on this latter component, a lower ionic diffusion coefficient is expected for MAI samples, whose peak appears at lower frequencies as shown Figure 4.5A. This behaviour is in line with the ionic diffusion coefficient extracted from IS for both PSC configurations (Fig. 4.4C).

In spite of the qualitative consistency shown by both small-perturbation techniques, larger characteristic time constants of *LF* component extracted from IS with respect to the ones extracted from IMPS were found as shown Figure A-4.9. To account for this difference, we have to bear in mind that a different kind of perturbation is applied in IS and IMPS measurements, which is electrical and optical, respectively. Additionally, IS and IMPS are carried out at open-circuit and short-circuit condition, respectively. Nevertheless, the similar temperature dependence was found for this ion-induced *LF* component extracted from IMPS. As shown in Figure 4.5B, this characteristic peak shifts to higher frequencies when the temperature increases suggesting a faster charge diffusion coefficient.

These results are in a good agreement with the hysteresis indexes found for the different device configurations. In particular, hysteretic behaviour has an inverse proportionality to the charge diffusion coefficients. They also reveal, as shown below, an Arrhenius-like dependence on the temperature.

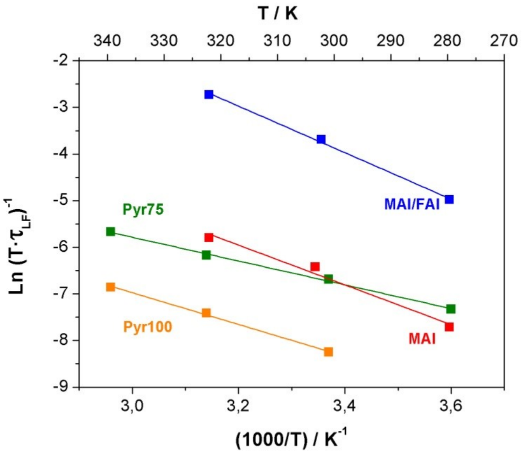

Figure 4.6. Arrhenius-like plot ln(T/τ_{LF})$^{-1}$ versus 1000/T for Pyr75, Pyr100, MAI and MAI/FAI samples. τ_{LF} was extracted from the IS low-frequency component.

In order to investigate the temperature dependence of ionic diffusion coefficient, Arrhenius plots were elaborated from the low frequency data extracted from IS (Fig. 4.6). As linear plots are obtained in the semilogarithmic representation, it is demonstrated that the slow dynamics is thermally activated in all studied cases. This is consistent with both the ionic transport nature of the low frequency features and with the interaction of these ions with the TiO_2 surface, as hinted above. The activation energy (E_a) was extracted from Arrhenius law, which relates in this case the low frequency component (τ_{LF}) and temperature according to

$$\frac{1}{\tau_{Lf}} = A \cdot e^{-\frac{E_a}{k_B \cdot T}} + C \tag{4.4}$$

where *A* is the Arrhenius prefactor and *C* is a constant. As shown in Figure 4.6, the activation energies of the ionic diffusion processes for the most viscous electrolytes employed in DSSC and for the both PSC configurations were extracted plotting ln(T/τ_{LF})$^{-1}$ versus 1000/*T*.

By measuring the impedance spectra at different temperatures, activation energies of 21.2 and 30.1 kJ/mol were found for Pyr75 and Pyr100, respectively, whereas for PSCs, activation energies of 35.4 kJ/mol for MAI and 41.5 kJ/mol for MAI/FAI were obtained. These results indicate that the viscosity of the electrolyte solvent and the nature of the perovskite cation determine the temperature dependence of charge diffusion as well as surface accumulation and, consequently, the hysteretic behaviour. In relation to the two perovskite compositions, higher activation energies for $MA_xFA_{1-x}PbI_3$ (61 kJ/mol) with respect to $MAPbI_3$ (56 kJ/mol) in the same low temperature range as it has been used here (< 320K) were reported by M. Bag and coworkers.[12] However, a better agreement with the activation energy values previously reported by Meloni (32.9 kJ/mol)[9] and Yuang (34.7 kJ/mol)[44] has been found for $MAPbI_3$. The wide range of activation energies reported in the literature are a consequence of the different perovskite configurations and characterization technique employed,[9] which could also explain the different activation energies extracted from IMPS (see Fig. A-4.10).

Although the IS and IMPS results are in general consistent, it must be pointed out that neither the absolute values of the diffusion coefficients nor the activation energies do coincide between both techniques. As mentioned, this should be considered as a consequence of the different impact that either an electrical perturbation, as it is the case of IS, or an optical one, as in IMPS, can produce on the perovskite. In fact, structural changes have been reported under illumination[19] and the conductivity has been found to increase under illumination.[37] In spite of these differences, it is a general result that in both cases the chemical composition of the active layer of the device and, in addition, the nature of the electron selective contact significantly determines ion transport and surface accumulation, and hence the occurrence of hysteresis. Therefore, the two phenomena have to take place simultaneously to give rise to the hysteresis. This conclusion appears to be in line with recent theoretical models.[45]

To provide further evidence about the effect of the surface and the nature of the mobile species that gives rise to the low-frequency feature in the IS and IMPS spectra and the hysteresis, the variation of the low-frequency limit of the capacitance (Figs. 4.3C and 4.3D) with respect to photovoltage has been also analysed. Results are shown in Figure 4.7.

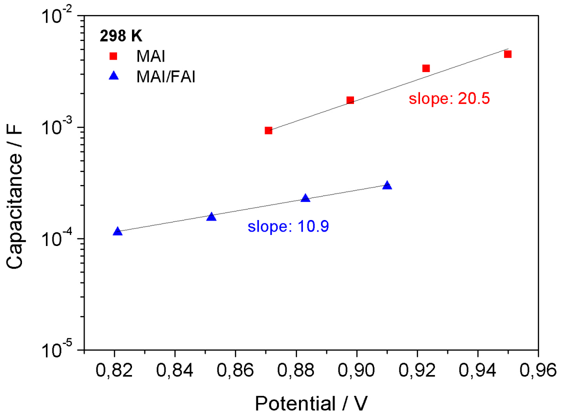

Figure 4.7. Low-frequency capacitance (Fig. 4.3D) with respect to open-circuit potential. Results for the two perovskite compositions studied are shown. The labels indicate the slope in V^{-1} extracted from both data sets.

According to Zarazua *et al.*[37] accumulation of electrons at the TiO_2 interface is evidenced by a $(2k_BT)^{-1}$ slope in the C_s-V semilogarithmic plot (19.2 V-1 at 298 K). We indeed observe a straight line with a slope close to this value for the cells made of pure MAI. In contrast, the mixed perovskite gives a much lower value. This result strongly suggests that an accumulation regime is taking place in the case of MAI as a consequence of the effective interaction of MA^+ cations with the TiO_2 surface, which compensate the surface accumulation of the majority carrier. This interaction almost does not occur when FA^+ is present, on account of its lower dipole moment. A similar behaviour was found for DSSCs (Fig. A-4.11), for which the cell with pyrrolidinium in the electrolyte also show a slope close to the theoretical value of $(2k_BT)^{-1}$. Hence, it is the nature of the cation and its interaction with the surface what determines the low-frequency feature and the hysteresis. This seems to be in contradiction with the theoretical studies that point to halide anions as the reason of ionic motion and hysteresis. However, it has to be born in mind that these studies are carried out in the bulk of the perovskite, while the processes that matter take place at the selective contact/perovskite interface. This is why perovskite devices made with different contacts, but with the same perovskite, show a very distinct hysteretic phenomenology, even with no apparent hysteresis found for certain contacts such as organic layers.[8] The accumulation regime creates a surface dipole at the TiO_2/perovskite interface that involves electrons and cations and affects the extraction of charge and hence the hysteresis. An analogous phenomenon has been described in polymer solar cells.[45] Further evidence that there is charge accumulation in the case of MAI samples is the absence of the inductive loop in the impedance spectrum (inset in Fig. 3B). According to Guerrero *et al.*[46] a good extraction of charges at the contacts appears to be related with the appearance of such an inductive component in the mid-frequency region of the spectrum. In the present study such a feature only appears for MAI/FAI samples suggesting a better charge separation and/or charge extraction.

4.4 Conclusion

In this *Chapter,* the hysteretic phenomena occurring in the *IV* curves of dye-sensitized solar cells as well as in perovskite solar cells have been studied by a small-perturbation optoelectronic analysis, including both impedance spectroscopy and intensity modulated photocurrent spectroscopy. By studying the devices of various compositions and at different temperatures, we have found that the hysteresis in both kinds of solar cells can be rationalized on the same grounds, with a slow transport process, thermally activated and appearing in the low-frequency region of the spectra, being the cause of the hysteresis. A correlation between the polar nature of the electroactive species and the magnitude of the low-frequency limit of the capacitance is observed as well. This correlation, together with the previously reported results for different selective layers in perovskite solar cells, suggests that it is not only a slow transport in the bulk what causes the hysteresis, but also the specific interaction of electroactive species with the electron selective material, TiO_2 in this case.

4.5 References

1 *Photovoltaic Research \textbar NREL*, .

2 A. Dualeh, T. Moehl, N. Tétreault, J. Teuscher, P. Gao, M. K. Nazeeruddin and M. Grätzel, Impedance Spectroscopic Analysis of Lead Iodide Perovskite-Sensitized Solid-State Solar Cells, *ACS Nano*, 2014, **8**, 362–373.

3 E. L. Unger, E. T. Hoke, C. D. Bailie, W. H. Nguyen, A. R. Bowring, T. Heumüller, M. G. Christoforo and M. D. McGehee, Hysteresis and transient behavior in current–voltage measurements of hybrid-perovskite absorber solar cells, *Energy Env. Sci*, 2014, **7**, 3690–3698.

4 W. Tress, N. Marinova, T. Moehl, S. M. Zakeeruddin, M. K. Nazeeruddin and M. Grätzel, Understanding the rate-dependent J–V hysteresis, slow time component, and aging in CH NH PbI perovskite solar cells: the role of a compensated electric field, *Energy Environ. Sci.*, 2015, **8**, 995–1004.

5 B. C. O'Regan, P. R. F. Barnes, X. Li, C. Law, E. Palomares and J. M. Marin-Beloqui, Optoelectronic Studies of Methylammonium Lead Iodide Perovskite Solar Cells with Mesoporous TiO_2: Separation of Electronic and Chemical Charge Storage, Understanding Two Recombination Lifetimes, and the Evolution of Band Offsets during *J* – *V* Hysteresis, *J. Am. Chem. Soc.*, 2015, **137**, 5087–5099.

6 Y. Zou and R. J. Holmes, Temperature-Dependent Bias Poling and Hysteresis in Planar Organo-Metal Halide Perovskite Photovoltaic Cells, *Adv. Energy Mater.*, 2016, **6**, 1501994.

7 H. J. Snaith, A. Abate, J. M. Ball, G. E. Eperon, T. Leijtens, N. K. Noel, S. D. Stranks, J. T.-W. Wang, K. Wojciechowski and W. Zhang, Anomalous Hysteresis in Perovskite Solar Cells, *J. Phys. Chem. Lett.*, 2014, **5**, 1511–1515.

8 H.-S. Kim, I.-H. Jang, N. Ahn, M. Choi, A. Guerrero, J. Bisquert and N.-G. Park, Control of *I* – *V* Hysteresis in $CH_3NH_3PbI_3$ Perovskite Solar Cell, *J. Phys. Chem. Lett.*, 2015, **6**, 4633–4639.

9 S. Meloni, T. Moehl, W. Tress, M. Franckevičius, M. Saliba, Y. H. Lee, P. Gao, M. K. Nazeeruddin, S. M. Zakeeruddin, U. Rothlisberger and M. Graetzel, Ionic polarization-induced current–voltage hysteresis in CH3NH3PbX3 perovskite solar cells, *Nat. Commun.*, , DOI:10.1038/ncomms10334.

10 R. S. Sanchez, V. Gonzalez-Pedro, J.-W. Lee, N.-G. Park, Y. S. Kang, I. Mora-Sero and J. Bisquert, Slow Dynamic Processes in Lead Halide Perovskite Solar Cells. Characteristic Times and Hysteresis, *J. Phys. Chem. Lett.*, 2014, **5**, 2357–2363.

11 H.-S. Kim and N.-G. Park, Parameters Affecting *I* – *V* Hysteresis of CH

$_3$ NH $_3$ PbI $_3$ Perovskite Solar Cells: Effects of Perovskite Crystal Size and Mesoporous TiO $_2$ Layer, *J. Phys. Chem. Lett.*, 2014, **5**, 2927–2934.

12 M. Bag, L. A. Renna, R. Y. Adhikari, S. Karak, F. Liu, P. M. Lahti, T. P. Russell, M. T. Tuominen and D. Venkataraman, Kinetics of Ion Transport in Perovskite Active Layers and Its Implications for Active Layer Stability, *J. Am. Chem. Soc.*, 2015, **137**, 13130–13137.

13 E. J. Juarez-Perez, R. S. Sanchez, L. Badia, G. Garcia-Belmonte, Y. S. Kang, I. Mora-Sero and J. Bisquert, Photoinduced Giant Dielectric Constant in Lead Halide Perovskite Solar Cells, *J. Phys. Chem. Lett.*, 2014, **5**, 2390–2394.

14 J. M. Frost, K. T. Butler and A. Walsh, Molecular ferroelectric contributions to anomalous hysteresis in hybrid perovskite solar cells, *APL Mater.*, 2014, **2**, 081506.

15 Y. Yuan, Z. Xiao, B. Yang and J. Huang, Arising applications of ferroelectric materials in photovoltaic devices, *J Mater Chem A*, 2014, **2**, 6027–6041.

16 J. Wei, Y. Zhao, H. Li, G. Li, J. Pan, D. Xu, Q. Zhao and D. Yu, Hysteresis Analysis Based on the Ferroelectric Effect in Hybrid Perovskite Solar Cells, *J. Phys. Chem. Lett.*, 2014, **5**, 3937–3945.

17 C. Eames, J. M. Frost, P. R. F. Barnes, B. C. O'Regan, A. Walsh and M. S. Islam, Ionic transport in hybrid lead iodide perovskite solar cells, *Nat. Commun.*, , DOI:10.1038/ncomms8497.

18 Z. Xiao, Y. Yuan, Y. Shao, Q. Wang, Q. Dong, C. Bi, P. Sharma, A. Gruverman and J. Huang, Giant switchable photovoltaic effect in organometal trihalide perovskite devices, *Nat. Mater.*, 2015, **14**, 193–198.

19 A. K. Jena, H.-W. Chen, A. Kogo, Y. Sanehira, M. Ikegami and T. Miyasaka, The Interface between FTO and the TiO $_2$ Compact Layer Can Be One of the Origins to Hysteresis in Planar Heterojunction Perovskite Solar Cells, *ACS Appl. Mater. Interfaces*, 2015, **7**, 9817–9823.

20 R. Gottesman, L. Gouda, B. S. Kalanoor, E. Haltzi, S. Tirosh, E. Rosh-Hodesh, Y. Tischler, A. Zaban, C. Quarti, E. Mosconi and F. De Angelis, Photoinduced Reversible Structural Transformations in Free-Standing CH $_3$ NH $_3$ PbI $_3$ Perovskite Films, *J. Phys. Chem. Lett.*, 2015, **6**, 2332–2338.

21 R. Gottesman, E. Haltzi, L. Gouda, S. Tirosh, Y. Bouhadana, A. Zaban, E. Mosconi and F. De Angelis, Extremely Slow Photoconductivity Response of CH $_3$ NH $_3$ PbI $_3$ Perovskites Suggesting Structural Changes under Working Conditions, *J. Phys. Chem. Lett.*, 2014, **5**, 2662–2669.

22 E. Mosconi, C. Quarti, T. Ivanovska, G. Ruani and F. De Angelis, Structural and electronic properties of organo-halide lead perovskites: a combined IR-spectroscopy and ab initio molecular dynamics investigation, *Phys*

Chem Chem Phys, 2014, **16**, 16137–16144.

23 J.-P. Correa-Baena, M. Anaya, G. Lozano, W. Tress, K. Domanski, M. Saliba, T. Matsui, T. J. Jacobsson, M. E. Calvo, A. Abate, M. Grätzel, H. Míguez and A. Hagfeldt, Unbroken Perovskite: Interplay of Morphology, Electro-optical Properties, and Ionic Movement, *Adv. Mater.*, 2016, **28**, 5031–5037.

24 J. M. Azpiroz, E. Mosconi, J. Bisquert and F. De Angelis, Defect migration in methylammonium lead iodide and its role in perovskite solar cell operation, *Energy Environ. Sci.*, 2015, **8**, 2118–2127.

25 T. Watson, Observable Hysteresis at Low Temperature in "Hysteresis Free" Organic–Inorganic Lead Halide Perovskite Solar Cells, *J. Phys. Chem. Lett.*, 2015, **6**, 3190–3194.

26 X. Yang, M. Yanagida and L. Han, Reliable evaluation of dye-sensitized solar cells, *Energy Env. Sci*, 2013, **6**, 54–66.

27 S. Sarker, H. W. Seo, Y.-K. Jin, K.-S. Lee, M. Lee and D. M. Kim, On the Hysteresis of Current Density-Voltage Curves of Dye-sensitized Solar Cells, *Electrochimica Acta*, 2015, **182**, 493–499.

28 L. K. Ono, S. R. Raga, S. Wang, Y. Kato and Y. Qi, Temperature-dependent hysteresis effects in perovskite-based solar cells, *J. Mater. Chem. A*, 2015, **3**, 9074–9080.

29 J. Nelson, *The Physics of Solar Cells*, Imperial College Press, 2003.

30 W. L. Leong, Z.-E. Ooi, D. Sabba, C. Yi, S. M. Zakeeruddin, M. Graetzel, J. M. Gordon, E. A. Katz and N. Mathews, Identifying Fundamental Limitations in Halide Perovskite Solar Cells, *Adv. Mater.*, 2016, **28**, 2439–2445.

31 G. E. Eperon, S. D. Stranks, C. Menelaou, M. B. Johnston, L. M. Herz and H. J. Snaith, Formamidinium lead trihalide: a broadly tunable perovskite for efficient planar heterojunction solar cells, *Energy Environ. Sci.*, 2014, **7**, 982.

32 N. J. Jeon, J. H. Noh, W. S. Yang, Y. C. Kim, S. Ryu, J. Seo and S. I. Seok, Compositional engineering of perovskite materials for high-performance solar cells, *Nature*, 2015, **517**, 476–480.

33 F. Fabregat-Santiago, J. Bisquert, E. Palomares, S. A. Haque and J. R. Durrant, Impedance spectroscopy study of dye-sensitized solar cells with undoped spiro-OMeTAD as hole conductor, *J. Appl. Phys.*, 2006, **100**, 034510.

34 J. Bisquert, Theory of the Impedance of Electron Diffusion and Recombination in a Thin Layer, *J. Phys. Chem. B*, 2002, **106**, 325–333.

35 E. Guillén, J. Idígoras, T. Berger, J. A. Anta, C. Fernández-Lorenzo, R. Alcántara, J. Navas and J. Martín-Calleja, ZnO-based dye solar cell with pure

ionic-liquid electrolyte and organic sensitizer: the relevance of the dye–oxide interaction in an ionic-liquid medium, *Phys Chem Chem Phys*, 2011, **13**, 207–213.

36 E. Guillén, F. J. Ramos, J. A. Anta and S. Ahmad, Elucidating Transport-Recombination Mechanisms in Perovskite Solar Cells by Small-Perturbation Techniques, *J. Phys. Chem. C*, 2014, **118**, 22913–22922.

37 I. Zarazua, J. Bisquert and G. Garcia-Belmonte, Light-Induced Space-Charge Accumulation Zone as Photovoltaic Mechanism in Perovskite Solar Cells, *J. Phys. Chem. Lett.*, 2016, **7**, 525–528.

38 J. M. Frost, K. T. Butler, F. Brivio, C. H. Hendon, M. van Schilfgaarde and A. Walsh, Atomistic Origins of High-Performance in Hybrid Halide Perovskite Solar Cells, *Nano Lett.*, 2014, **14**, 2584–2590.

39 J. Idigoras, R. Tena-Zaera and J. A. Anta, Control of the recombination rate by changing the polarity of the electrolyte in dye-sensitized solar cells, *Phys Chem Chem Phys*, 2014, **16**, 21513–21523.

40 J. Idígoras, G. Burdziński, J. Karolczak, J. Kubicki, G. Oskam, J. A. Anta and M. Ziółek, The Impact of the Electrical Nature of the Metal Oxide on the Performance in Dye-Sensitized Solar Cells: New Look at Old Paradigms, *J. Phys. Chem. C*, 2015, **119**, 3931–3944.

41 A. Todinova, J. Idígoras, M. Salado, S. Kazim and J. A. Anta, Universal Features of Electron Dynamics in Solar Cells with TiO $_2$ Contact: From Dye Solar Cells to Perovskite Solar Cells, *J. Phys. Chem. Lett.*, 2015, **6**, 3923–3930.

42 F. Fabregat-Santiago, G. Garcia-Belmonte, I. Mora-Seró and J. Bisquert, Characterization of nanostructured hybrid and organic solar cells by impedance spectroscopy, *Phys. Chem. Chem. Phys.*, 2011, **13**, 9083.

43 J. Bisquert, Chemical Diffusion Coefficient of Electrons in Nanostructured Semiconductor Electrodes and Dye-Sensitized Solar Cells, *J. Phys. Chem. B*, 2004, **108**, 2323–2332.

44 Y. Yuan, J. Chae, Y. Shao, Q. Wang, Z. Xiao, A. Centrone and J. Huang, Photovoltaic Switching Mechanism in Lateral Structure Hybrid Perovskite Solar Cells, *Adv. Energy Mater.*, 2015, **5**, 1500615.

45 S. van Reenen, M. Kemerink and H. J. Snaith, Modeling Anomalous Hysteresis in Perovskite Solar Cells, *J. Phys. Chem. Lett.*, 2015, **6**, 3808–3814.

46 A. Guerrero, G. Garcia-Belmonte, I. Mora-Sero, J. Bisquert, Y. S. Kang, T. J. Jacobsson, J.-P. Correa-Baena and A. Hagfeldt, Properties of Contact and Bulk Impedances in Hybrid Lead Halide Perovskite Solar Cells Including Inductive Loop Elements, *J. Phys. Chem. C*, 2016, **120**, 8023–8032.

Chapter 5

Origin and Whereabouts of Recombination in Perovskite Solar cells

The choice of selective contacts is critical to achieve high voltages according to experimental evidence. In this Chapter, the impedance and the open-circuit photopotential are measured for two excitation wavelengths (blue and red light), two illumination directions (back and front) and at different temperatures. The open-circuit recombination characteristics of two different perovskite compositions, and with two different hole selective layers have been studied. Our results indicate that, for the studied devices, the recombination process that determines V_{OC} *is governed by the bulk of the perovskite layer via a trap-limited mechanism, but surface-mediated recombination cannot be ruled out for degraded devices or with "inadequate" contacts. Furthermore we propose a model that provides a general interpretation of the nature of recombination in perovskite solar cells.*

This chapter is based on Publication 2 of this Thesis: Contreras-Bernal *et al*. J. Phys. Chem. C, 2017, 121, 9705–9713.

5.1 Introduction

As it was explained in *Chapter* 1, one of the most exciting properties of PSCs is the capability of reaching photovoltages very close to the thermodynamic limit, indicative of very low non-radiative recombination losses (see Eqs. 2.23 and 2.24 in *Chapter* 2).[1–3]Although this property seems to be related with the nature of the perovskite material itself,[4–7] the fact is that the choice of electron and hole selective contact impacts significantly the apparent recombination rate and the open-circuit voltage that can be reached in working devices.[8–11] This latter observation points to an important contribution of recombination events taking place at the perovskite interfaces, with some materials allowing for a faster recombination and hence producing a deleterious effect on the photovoltage. Recently Zarazúa and co-workers have proposed a surface recombination model that actually involves surface photogenerated carriers in the recombination kinetics of perovskite solar cells.[12]

In this *Chapter* we aim to address the concern, where in working devices the main recombination pathway is occurring. In other words, is photovoltage determined by the bulk of the absorbing perovskite layer, by interfacial recombination or by a combination of both? To unravel this, we have combined a collection of experiments where the optical generation spatial profile produced by the optical excitation is varied. On the other hand, we work with working devices at open circuit and at illumination intensities close to 1-sun. This is an important point because many previous studies on recombination kinetics has been based on time-resolved emission and absorption experiments, done (1) under excitation intensities not necessarily coincident with those relevant at 1-sun photovoltaic working conditions and (2) with isolated perovskite layers deposited on different substrates.[1,13,14] It must be noted that the recombination kinetics, and thus the mechanism, varies significantly with charge density.[15] Furthermore, the morphology and stability of the perovskite layer can be very different depending on the substrate in which it was deposited and the preparation conditions, which are likely to affect the recombination mechanism as well.[16,17]

In this *Chapter,* experiments were made with PSCs based on two different perovskite compositions: $MAPbI_3$ (MAI) and $FA_{0.85}MA_{0.15}PbI_{0.85}Br_{0.15}$ (MIX), and two different HTM: Spiro-OMeTAD (Spiro) and P3HT. For simplicity we will use the following notation to refer to the device configurations: MAI/P3HT, MAI/Spiro and MIX/Spiro.

5.2 Fabrication and characterization of devices

Fabrication of perovskite solar cells

Perovskite devices with mesoporous regular architecture were fabricated following the methodology described in *Chapter* 3. First, FTO TEC15 were cleaned following the solvent sequence: Hellmanex solution; Deionized water; Ethanol; Isopropanol. Then the TiO_2 compact layer was deposited by spray pyrolysis. After that, a mesoporous layer of TiO_2 was deposited on top of a TiO_2 compact layer. Then pure methyl ammonium ($MAPbI_3$) and mixed ions perovskite ($FA_{0.85}MA_{0.15}PbI_{0.85}Br_{0.15}$) were deposited as active layer inside a glove box using different concentrations in precursor solutions (0.8M, 1.2M and 1.4M). The thickness obtained for the different perovskite compositions and precursors concentration are shown in Table 3.4 (*Chapter* 3). After perovskite deposition, a spiro-OMeTAD or P3HT solution was spin coated. Finally, 80 nm of gold was deposited by thermal evaporation. (See *Chapter* 3 for details). SEM cross-sectional images of different perovskite are shown in Figure A-5.1 (see appendix C).

Characterization of devices

IV curves were documented with a solar simulator (*ABET-Sun2000*) with an AM 1.5G filter. Photovoltaic parameters including J_{SC}, V_{OC}, FF, and PCE were extracted from the IV curves of the solar cells. The scan rate and the active area used for measuring the devices were optimized as such to calculate the real value for efficiencies without having hysteresis effect. (Active area: 0.16 cm^2, scan rate: 100 mV/s, pre sweep delay: 20s). Absorbance measurements were carried out of the different perovskite thickness onto FTO. The illumination for the Impedance Spectroscopy (IS) measurements was provided by a red and blue LEDs (λ_{blue} = 465 nm and λ_{red} = 635 nm) over a wide range of DC light intensities, starting from the one that gives the same *Voc* under AM 1.5 G, 100 mW/cm^2 illumination. This allows for probing the devices at different positions of the Fermi level in the semiconductor. As in the previous *Chapter* 4, IS measurements were performed at the open circuit potential, the Fermi level (related to the open-circuit voltage) being fixed by the DC illumination intensity. A 20 mV perturbation in the 10^6-10^{-2} Hz range was utilized to obtain the spectra. A hermetic chamber filled with nitrogen was used to avoid degradation during the impedance experiments. Z-view equivalent circuit modeling software (Scribner) was used to fit the IS spectra (see *Chapter* 3 for details).

5.3 Results and discussion

Figure 5.1 shows the current-voltage characteristic obtained under standard conditions (1 sun - AM 1.5 illumination) for the different devices employed. The photovoltaic performance of the devices was very much dependent on the perovskite composition and the material used as HTM (Fig. 5.1 and Table A-5.1 in appendix C).

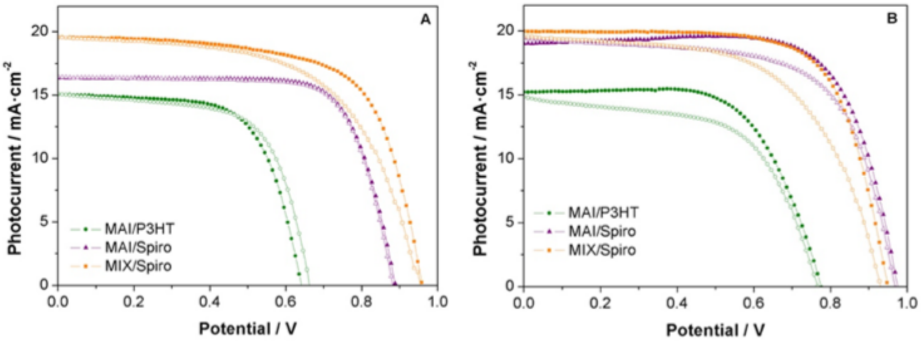

Figure 5.1. IV curves for backward (solid symbols) and forward (open symbols) scans (scan rate = 100 mV/s) for solar cell devices where the perovskite were made starting from (A) 0.8M and (B) 1.2M precursor solutions.

The best efficiency of 13.5 % was obtained for the intermediate precursor concentration of 0.8 M, with mixed-ion perovskite as active layer and Spiro as HTM. On the other hand, replacement of Spiro by P3HT brings about a substantial reduction in the J_{SC} and V_{OC} when MAI is used as active layer. These results are in line with the current empirical knowledge about compositional engineering of the perovskite material[18] and choice of HTM.[9,11,19]

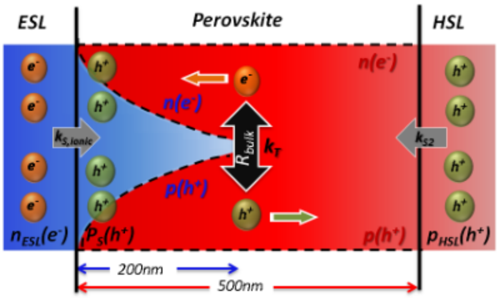

Scheme 5.1. Light induced (wavelength dependent) electron-hole generation and bulk and surface mediated recombination processes.

Impedance spectroscopy at open-circuit and under illumination was used as a small-perturbation optoelectronic technique to probe the magnitude and behaviour of the recombination rate. By using different illumination wavelengths it is possible to control the spatial penetration of the optical excitation inside the perovskite layer and hence the generation profile of carriers in it. A similar strategy, but for steady-state measurements, has been employed before.[20] Figure A-5.2 shows that the absorbance in the blue light part of the spectrum is much more intense than in the red light part. Therefore, from Beer-Lambert law, an optical length of ~150-200 nm can be estimated for pure perovskite (MAI) at 450 nm, which means that at least 90% of the light is absorbed in the first 200 nm. In contrast, red light penetrates deeper in the film. The contrast between blue and red light excitations is much more disparate for the mixed-ion perovskite (MIX). Bearing this optical properties in mind, wavelengths of λ_{blue} = 465 nm and λ_{red} = 635 nm were used to generate the DC voltage in the impedance experiments. This means that the availability of photogenerated carriers at the perovskite/HSL interface would be much smaller when blue light is used and that allows us to detect possible spatial inhomogeneities in the recombination kinetics or a more important contribution of the mesoporous TiO_2/perovskite layer (Scheme 5.1).

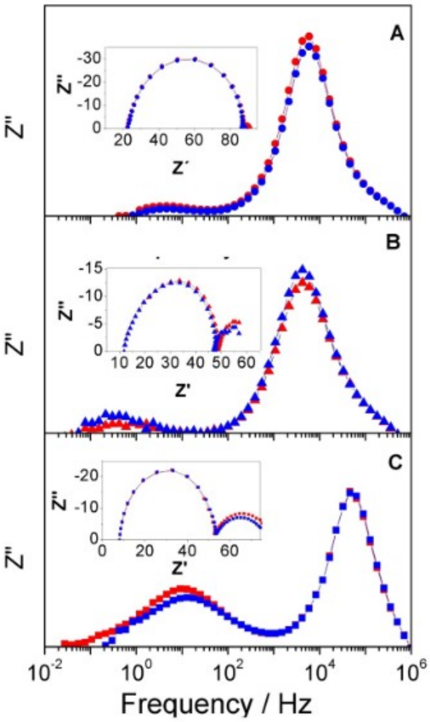

Figure 5.2. Impedance spectra at open-circuit under the excitation wavelengths of (blue) λ_{blue} = 465 nm and (red) λ_{red} = 635 nm the configurations described in Table A-5.1 and for a precursor concentration of 1.2 M: (A) MAI/P3HT, (B) MAI/Spiro and (C) MIX/Spiro. Both the imaginary part of the impedance and the Nyquist plots (insets) are shown.

In Figure 5.2 typical Nyquist and frequency plots of the imaginary part of the impedance are shown. The experiments were performed for fresh cells at open-circuit and the data shown correspond to an illumination intensity that generates a potential very close to the one measured under 1-sun AM1.5 illumination and open-circuit conditions (Table A-5.1). As extensively reported before[10,12,21–23] two kinetic signals, embodied as arcs in the Nyquist plot and as peaks in the frequency and Bode plots, can be observed in the spectra. According to the results of *Chapter* 4, the *LF* signal is associated to slow processes (ion motion and surface accumulation) causing hysteresis.[24] While the *HF* signal has been attributed to recombination processes.[21,23]

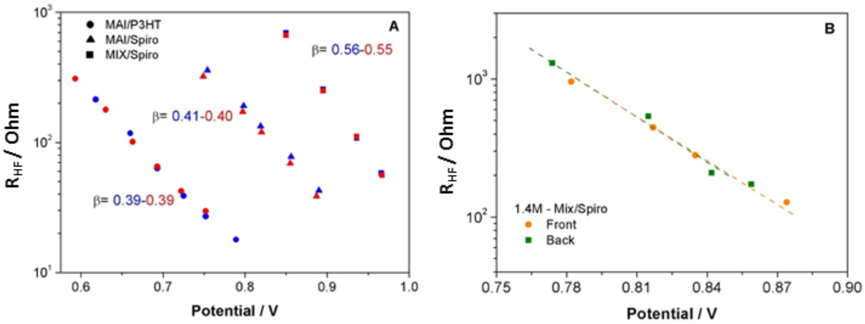

Figure 5.3. (A) High frequency resistance versus open-circuit potential as extracted from fittings of the impedance spectra using the two excitation wavelengths of (blue) λ_{blue} = 465 nm and (red) λ_{blue} = 635 nm for the configurations described in Table A-5.1 and for a precursor concentration of 1.2 M. (B) Same as (A) but comparing results obtained for "front" (TiO_2 side) and "back" (gold side) blue light illumination. The data shown correspond to the thickest MIX/Spiro device (see Figure A-5.4 in appendix C).

Inspection of the results indicate that the *HF* signal is not affected by the wavelength of the optical excitation and hence by the optical depth of the electron-hole generation profile. By fitting the high-frequency impedance response to a *Voight* circuit (inset of Fig. 3.9A in *Chapter* 3),[25] values of the *HF* resistance (R_{HF}) can be obtained as a function of the open-circuit potential. Results are presented (Fig. 5.3A) for the three device configurations. The *HF* resistance is found to be basically independent of the electron-hole generation profile used in the small-perturbation measurement for all the device configurations. Furthermore, by varying the thickness of the optically active layer by a factor of almost two, the observed similarity remains unaltered between the blue and the red light (Fig. A-5.3). Besides, there is no significant dependence of the R_{HF} on thickness. It should not be forgotten that using red light does not imply that carriers are generated at the HSL interface *only*, but that the profile is simply more homogeneous. As we perform our comparison at the same value of the photogenerated open-circuit potential, the effect of a different absorption of light in absolute terms is hence compensated and we are capable of detecting possible inhomogeneities in the recombination loss. The same argument applies for the experiments using different illumination directions as described below.

The electron-hole generation profile can also be modified by changing the illumination direction. Bearing this in mind, we have also performed the impedance experiment where the cell was illuminated from the cathode side and using the blue light as excitation source. Although the gold layer removes a substantial part of the incident light, reducing the open-circuit potential at the same light intensity, it is possible to plot the recombination resistance at the same values of the potential for both back and front illumination. The results are presented in Figure 5.3B, showing that the *HF* (recombination) resistance, and thus the recombination rate of electron-hole annihilation, appears to be not-dependent on whether the electron-hole pairs are generated close to any of the two selective contacts. This experiment also demonstrates that depletion regions possibly appearing in the vicinity of the interfaces[26] would not be critical in terms of recombination.

Recently reports have appeared which suggest that the low-frequency signal in the impedance spectrum is also connected to recombination losses. Pockett *et al.*[27] attributed the voltage correlation of the *LF* and *HF* resistances to a coupling of the slow ionic motion (causing the low-frequency signal[24]) and non-radiative recombination. Zarazúa *et al.*[12] assumed that the *LF* resistance is coupled to the surface accumulation capacitance and the *HF* resistance, both due to surface recombination. Although these two reports refer to perovskite solar cells with planar configuration, we have also analysed the *LF* signal in view of these assumptions. Remarkably, the *LF* part of the impedance spectrum shows indeed small differences between the red and blue light data (Fig. 5.2). The extracted *LF* resistances (Fig. A-5.5) exhibit approximately the same potential dependence as their *HF* counterparts, but with small differences between the red and blue light excitations, especially for MAI/P3HT devices. In contrast to the *HF* component, in this case there is a clear dependence on the thickness of the perovskite layer. Bode plots of the impedance modulus (Fig. A-5.6) confirm this finding.

To further analyse the effect of the electron-hole generation profile, the open-circuit potential was measured as a function of light intensity (Fig. 5.4). A surface sink of electron-hole pairs would appear in the form of a significant difference between the open-circuit potentials obtained with blue and red light as observed in Ref.[20] In line with the *HF* resistances, there is no significant difference between the two types of excitation for all the configurations and thicknesses studied.

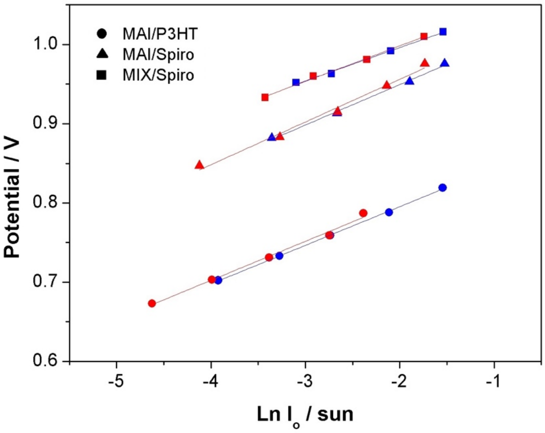

Figure 5.4. Open-circuit photovoltage versus light intensity for devices with 1.2M precursor concentration and for excitation wavelengths of λ_{blue} = 465 nm and λ_{red} = 635 nm.

To check whether the invariance between red and blue light excitations of the *HF* signal is not an experimental artifact, we have repeated the experiment with degraded devices (Fig. A-5.7). Interestingly, degradation of the cells causes a very different response for the two excitation wavelengths. Thus, red light appears to accelerate the recombination, which suggests that the region close to the HSL becomes more active to remove free charges than the TiO_2 interface or that the diffusion length of the carriers becomes significant shorter upon ageing. This effect is more critical if the cell was illuminated during the degradation experiment. For this particular case, light-induced degradation produces a substantial reduction of the J_{SC}, an almost uniform potential and a change of the slope of the *HF* resistance which indicates that a different recombination mechanism takes over.

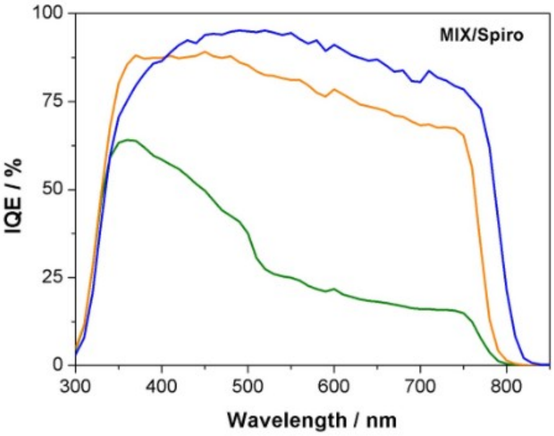

Figure 5.5. Internal quantum efficiencies for fresh (blue) 1.2 M MIX/Spiro devices and degraded MIX/Spiro devices shown in Figure A-5.7. Orange: dark degradation, Green: degradation under illumination.

To further investigate this point, the IQE of the fresh and degraded devices was extracted from IPCE measurements and the absorption data (Fig. 5.5). We found the IQE of the fresh devices was relatively flat, which suggests that the carriers diffusion length, at least at short-circuit conditions, is much longer than the perovskite film thickness, allowing for quantitative collection at the contacts. In contrast, the IQE of the degraded devices drops substantially, especially at long wavelengths (red part of the spectrum). This behaviour indicates that in degraded devices either surface recombination at the perovskite/HSL interface becomes more important or that the carrier diffusion length is substantially shorter.

If we assume that recombination kinetics is mainly associated to the *HF* signal of the impedance spectrum, the preliminary conclusion from Figure 5.2 – 5.4 and A-5.3 is that for the fresh cells either recombination takes place in the bulk of the perovskite layer or that the carrier diffusion length at open-circuit conditions is long enough as surface recombination cannot be discriminated by varying the charge generation profile within the active layer. The first interpretation would be in line with the findings of Leong *et al*[6]. who state that interfacial recombination "plays a minor role". Following their methodology, we have measured the V_{OC} as a function of temperature (Fig. 5.6 and Fig. A-5.8).

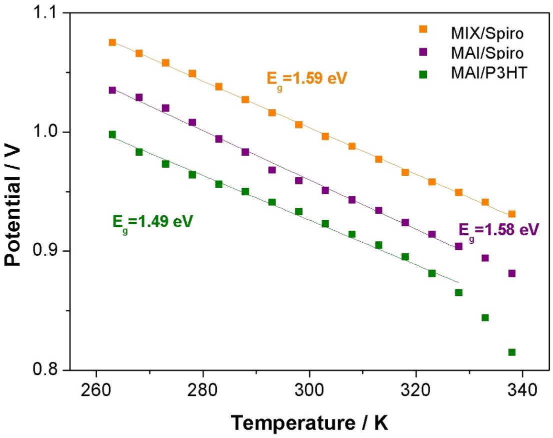

Figure 5.6. Open-circuit potential as a function of temperature for the configurations described in Table 5.1 for white light and a light intensity of 14.15 W/m^2.

Open-circuit photopotential data plotted as a function of temperature fits into a straight line for both fresh and aged devices except at higher temperature, due to the phase transition on MAPbI$_3$ from cubic to tetragonal phase (see *Chapter* 1).[28]According to the methodology described in Ref.[6] extrapolation of the data to *T = 0* should give the activation energy of the dominant recombination pathway.[6,29] The data obtained (Fig. 5.6) are quite close to the band gaps reported for the employed perovskite materials[1], and calculated optical band gaps (inset of Fig. A-5.2) suggesting that recombination is determined by the bulk of the perovskite layer itself at open-circuit conditions. An activation energy smaller than the band-gap would indicate, in contrast, that surface-mediated recombination is relatively more important.[29]

The *HF* peak in the frequency plot (Fig. 5.2) can be regarded as a quantification of the kinetics of recombination if we take this signal as the main contribution to recombination. In Figure 5.7 the characteristic *HF* time constants are plotted as a function of the open-circuit potential. Note that the characteristic time constant was extracted from Eq. 3.23.

Table 5.1. Ideality factors for the studied solar cells as obtained from impedance and open-circuit potential measurement, using the two excitation wavelengths of λ_{blue} = 465 nm (blue) and λ_{red} = 635 nm (red).

Configuration	**Thickness (nm)**	**Ideality factor**	
		R_{HF} **vs.** V_{OC}	V_{OC} **vs.** $ln(I_0)$
MAI/P3HT	300 (0.8M)	1.92 (blue)	2.08
		1.85 (red)	2.08
	500 (1.2M)	1.89	2.33
		2.04	2.27
MAI/Spiro	300 (0.8M)	2.44	2.44
		2.27	2.33
	500 (1.2M)	1.92	2.44
		2.01	2.50
MIX/Spiro	650 (0.8M)	1.67	1.67
		2.13	1.75
	950 (1.2M)	1.61	1.79
		1.72	1.82

An exponential relationship was obtained, which is in accordance to previous literature.[12,21–23] Longer time constants (apparent lifetime) are obtained for spiro-based cells in accordance with its larger V_{OC} at 1-sun illumination. In addition, and in line with the results for the *HF* resistance, no significant differences were obtained between blue and red light excitations.

This reestablishes the fact that most of the recombination events determining the *HF* signal take place in the bulk of the perovskite and that no surface-mediated recombination is affecting the V_{OC}. It is worth to note that thickness dependence is now observed. This is due to the scaling of the bulk capacitance with thickness as explained below (Fig. A-5.9).

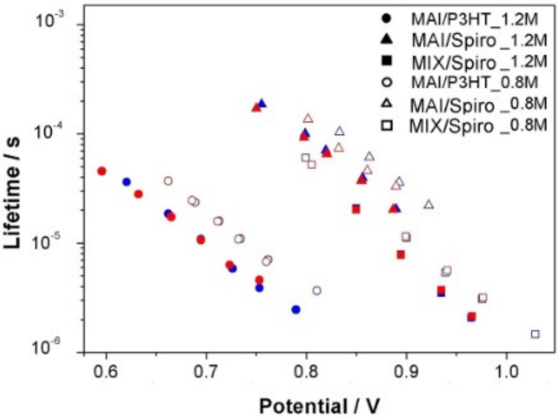

Figure 5.7. High-frequency time constant (apparent lifetime) extracted from the inverse of the high-frequency peak of the impedance experiment. Results are plotted versus open-circuit potential using the two excitation wavelengths of λ_{blue} = 465 nm and λ_{red} = 635 nm. Data for the configurations described in Table A-5.1 are included.

The results contained in Figures 5.2-5.4, 5.6, A-5.5 and A-5.8 can be rationalized in the following manner. Coincidence of the red and blue light *HF* signals (Figs. 5.3, 5.4 and 5.7), and the reproduction of the optical band gap from the potential versus temperature experiments (Figs. 5.6 and A-5.8) suggest that it is quasi-Fermi level splitting within the perovskite layer what determines the V_{OC}. However, according to some reports[9,12,27] the nature of the contacts can affect substantially the recombination rate.

From Eq. 2.17 (*Chapter* 2), the recombination rate in a perovskite-based device can be expressed in its most general form as

$$U_{rec} = -\frac{dn}{dt} = k_{rad}np + \left(k_{Tp}p_0n^{\gamma}, k_{Tn}n_0p^{\gamma}\right) + k_{S1}n_{ESL}p_s + k_{S2}n_sp_{HSL} \qquad (5.1)$$

The first term is the bulk bimolecular (radiative) recombination between free photogenerated electrons and holes. The terms in parenthesis correspond to trap-assisted recombination for either p-type or n-type doping. The last two terms represent the interfacial recombination of electrons in the ESL with holes in the perovskite and holes in the HTM with electrons in the perovskite, respectively. Note that, as it was explained in *Chapter* 2, γ = 1 for SRH recombination for a doped semiconductor.[30]

Zarazúa and coworkers[12] assumed that the perovskite/HTM is an ideal contact not contributing significantly to the recombination loss, and that the perovskite behaves as a p-type semiconductor with holes accumulated at the ESL surface. On the other hand, Pockett *et al.*[27] noticed that both the *LF* and *HF* resistances have the same illumination intensity dependence and they attributed this fact to the coupling of electron-hole recombination and ionic motion. Similarly, we have shown in *Chapte*r 4 that the *LF* feature related to the hysteresis phenomena was connected to specific interactions between the contact and the constituting ions of the perovskite. Based on all these previous findings, we propose the following equation to describe the recombination rate

$$U_{rec} \approx -\frac{dn}{dt} = k_{rad}np + k_T p_0 n^{\gamma} + k_{S,ionic} n_{ESL} p_s \tag{5.2}$$

This leaves three routes of recombination for photogenerated carriers in the device. The first two terms depend on the concentration of photogenerated carriers in the bulk of the perovskite. The third one depends on the concentration of electrons at the contact and the concentration of photogenerated holes at the surface. An additional surface-mediated term related to the perovskite/HTM interface can also be important in certain cases or if the perovskite behaves as a *n*-type semiconductor.[31]

We postulate that although recombination at the surface can be coupled to the bulk recombination via slow ionic motion and/or surface adsorption, the main process determining the recombination rate and the open-circuit potential is the trap-mediated bulk recombination term (see also Eq. 2.17 in *Chapter* 2)

$$U_{rec} = -\frac{dn}{dt} \approx k_T p_0 n^{\gamma} \tag{5.3}$$

Neglecting drift transport in the active layer[14], the continuity equation for electrons in the active layer of the device at steady-state can be written as

$$D_n \frac{d^2 n}{dx^2} - U_{rec} + I_0(\lambda)\alpha(\lambda) exp[-\alpha(\lambda)x] = 0 \tag{5.4}$$

where α is the wavelength-dependent absorption coefficient and I_0 is the incident photon flux. Eqs. 5.3 and 5.4 can be solved analytically for $\gamma = 1$ (linear recombination).[32] For $\gamma \neq 1$ the equation has to be solved numerically.[23,33]

On the other hand, at open-circuit conditions the generation rate of photogenerated carriers G should exactly compensate the recombination rate: $U_{rec} = G$. Using Eq. 5.3 the open-circuit potential should thus conform to the following equation

$$\frac{J_{00}}{qd} exp\left(-\gamma \frac{E_g - qV_{OC}}{2k_B T}\right) = G \tag{5.5}$$

from which one obtains (see also Eq. 2.9 in *Chapter* 2)

$$V_{OC} = \frac{E_g}{q} - \frac{mk_BT}{q} ln\left(\frac{J_{00}}{qdG}\right) \tag{5.6}$$

where m, the ideality factor, is given by $m = 2/\gamma = 1/\beta$. Note that a similar relationship but with $m = 1$ would have been obtained in the radiative limit, with no trap-assisted recombination, where only the first term in Eq. 5.2 is considered in the derivation.[3,20]

Eqs. 2.22 and 5.6 provide a theoretical foundation to explain recombination and the observed *HF* impedance response in the solar cell. Fig. 5.3 shows indeed that the *HF* recombination resistance as extracted from the open-circuit impedance experiment follows an exponential law with respect to open-circuit potential. From the slope, the β-parameter, and hence the ideality factor, can be extracted. Results are shown in Table 5.1. The ideality factor can also be obtained from the V_{OC}-lnI plot (Fig. 5.4) in accordance to Eq. 5.6. As shown in Table 5.1 the ideality factor values obtained from both the resistance and the voltage routes coincide very well for all configurations studied. Finally, Eq. 5.6 also predicts a linear dependence of the Voc with respect to temperature, which is actually observed in the temperature experiment (Fig. 5.6 and Fig. A-5.8). Extrapolation of the data to $T \rightarrow 0$ yields a value very close to the optical band gap of the material.

On the other hand, the exponential law of the recombination resistance can also be extended to the high-frequency time constant (Fig. 5.7), as the associated capacitance (Eq. 3.22) does not exhibit any voltage dependence (Fig. A-5.9). This is characteristic of a capacitance of a dielectric nature as discussed elsewhere.[10,23] As a matter of fact, this high-frequency capacitance does decrease with increased thickness as expected from a bulk, geometric, capacitance ($C = A\varepsilon/d$).

The similar recombination kinetics with the charge generation profile could also be explained by a carrier diffusion length which exceeds the active layer thickness and masks any spatial inhomogeneity of the recombination kinetics. To clarify this point we have solved numerically Eqs. 5.3 and 5.4 for both slow recombination (long diffusion length) and fast recombination (short diffusion length) and extracted the dark currents, which can be considered a measure of the recombination loss in the device. The numerical simulation is aimed at clarifying the effect of the carrier diffusion length and it is not intended to fully reproduce the current-voltage characteristics of the studied devices which will require a more sophisticated approach.[34] Results are shown in the appendix C in Figure A-5.10. It is to be noted that the combined effect of optical absorption length and diffusion length was already considered in the linear model of

Södergren and coworkers.[32] Remarkably, the dark current in the linear model (Eq. 17 in Ref.[32]) does not depend on the optical absorption coefficient α. We have checked this fact by extracting the dark currents from the numerical simulation. For the linear case the analytical result is reproduced and the dark current remains unchanged with the illumination wavelength. However, the situation changes if $\gamma \neq 1$. For slow recombination, corresponding roughly to a carrier diffusion length of ~ 1 μm[14] "red" and "blue" dark current are approximately the same. In contrast, introducing a faster recombination, (diffusion length shorter than the film thickness), leads to significant differences between the dark currents obtained under blue and red light excitation.

From the theoretical and numerical approach presented above and the analysis of the overall data we can make the following assumption for recombination in the cells analysed in this work. Unchanged *HF* time constant, recombination resistances and open-circuit potential with generation profile (colour and directional experiments) indicates that either (1) the main recombination pathway, defined as the one that determines the V_{OC}, takes place in the bulk of the perovskite layer or (2) that a long diffusion length is masking possible inhomogeneities, at least in the freshly fabricated devices. However, the reproduction of the optical band gaps for the Spiro-based cells strongly suggests that it is bulk recombination kinetics what determines the open-circuit potential. The ideality factors obtained, close to 2, indicates that recombination is trap-limited in accordance to Eq. 5.3 and $\gamma \sim 1$.[5,7] When pure MAI is replaced by the optimized MIX perovskite material, recombination events remain within the perovskite, but the mechanism changes as evidenced by the significant variation of the ideality factor.

In spite of the recombination taking place within the perovskite layer, the role of the selective contacts is critical. Mesoporous TiO_2 and spiro-OMeTAD behave very much as ideal (ohmic) contacts. This is in accordance with our temperature-dependent experiment, in which the band gaps of MAI and the MIX perovskite material when spiro-OMeTAD is used as HTM are extracted. In contrast, replacing the spiro-OMeTAD by P3HT leads to a lower E_g, which is an indication that in this case surface mediated recombination can be more important.[6,29] In addition, the *HF* recombination rate gets significantly enhanced as observed in Figures 5.3, 5.7 and A-5.3. Both observations suggest that the perovskite/P3HT interface introduces additional surface recombination routes that makes the approximation leading to Eqs. 5.2 and 5.6 not completely exact, with a possible extra term accounting for recombination at the perovskite/P3HT (k_{s2} term in Eq. 5.1). Additionally, poorer hole extraction capacity can also accelerate recombination both in the bulk of the perovskite material and at the interfaces, as discussed in Ref.[17] Hence, the *LF* resistance, which could be associated with the surface-mediated recombination, shows a clearer difference between red and blue light excitations in the MAI/P3HT cells (Fig. A-5.5).

The above interpretation is valid for fresh devices only. Degradation in the devices modifies significantly the *HF* recombination mechanism, which now becomes dependent on the generation profile. Additionally, the ideality factor was also changed (Fig. A-5.7). The internal quantum efficiencies (Fig. 5.5) suggest that the diffusion length becomes shorter upon degradation. As shown by the numerical simulation, a short diffusion length can lead to differences between red and blue light illumination, even for a bulk recombination term as the one appearing in Eq. 5.3. This numerical prediction is confirmed when the dark current of the degraded devices are plotted for both illumination wavelengths (Fig. A-5.11). The bulk recombination explains why, even for the degraded cell, Eq. 5.6 applies and the band gap is still roughly reproduced at $T \rightarrow 0$ (Fig. A-5.8). However, the possible occurrence of surface-mediated recombination routes cannot be ruled out as observed by Bi *et al.*[20] Our results, obtained for perovskite layers in which an excess of PbI_2 is used, are in line with the findings reported.

5.4 Conclusion

In this *Chapter*, we have investigated the nature of recombination in perovskite solar cells using a combination of impedance spectroscopy experiments and voltage-illumination measurements using different temperatures, excitation wavelengths and illumination directions. The results show that the recombination route that determines the open-circuit potential in fresh, well-performing devices takes place in the bulk of the perovskite layer. Inadequate charge extraction and surface-mediated low-frequency recombination can also contribute to acceleration of the recombination rate and decrease substantially the open-circuit potential. Recombination features in degraded devices do in contrast depend on excitation wavelength, which is attributed to shorter carrier diffusion lengths. A general model is proposed to explain the open-circuit voltage and recombination resistance in perovskite solar cells.

5.5 References

1 J. S. Manser, J. A. Christians and P. V. Kamat, Intriguing Optoelectronic Properties of Metal Halide Perovskites, *Chem. Rev.*, 2016, **116**, 12956–13008.

2 W. E. I. Sha, X. Ren, L. Chen and W. C. H. Choy, The efficiency limit of CH $_3$ NH $_3$ PbI $_3$ perovskite solar cells, *Appl. Phys. Lett.*, 2015, **106**, 221104.

3 W. Tress, N. Marinova, O. Inganäs, M. K. Nazeeruddin, S. M. Zakeeruddin and M. Graetzel, Predicting the Open-Circuit Voltage of CH $_3$ NH $_3$ PbI $_3$ Perovskite Solar Cells Using Electroluminescence and Photovoltaic Quantum Efficiency Spectra: the Role of Radiative and Non-Radiative Recombination, *Adv. Energy Mater.*, 2015, **5**, 1400812.

4 G.-J. A. H. Wetzelaer, M. Scheepers, A. M. Sempere, C. Momblona, J. Ávila and H. J. Bolink, Trap-Assisted Non-Radiative Recombination in Organic-Inorganic Perovskite Solar Cells, *Adv. Mater.*, 2015, **27**, 1837–1841.

5 S. D. Stranks, V. M. Burlakov, T. Leijtens, J. M. Ball, A. Goriely and H. J. Snaith, Recombination Kinetics in Organic-Inorganic Perovskites: Excitons, Free Charge, and Subgap States, *Phys. Rev. Appl.*, , DOI:10.1103/PhysRevApplied.2.034007.

6 W. L. Leong, Z.-E. Ooi, D. Sabba, C. Yi, S. M. Zakeeruddin, M. Graetzel, J. M. Gordon, E. A. Katz and N. Mathews, Identifying Fundamental Limitations in Halide Perovskite Solar Cells, *Adv. Mater.*, 2016, **28**, 2439–2445.

7 T. Leijtens, G. E. Eperon, A. J. Barker, G. Grancini, W. Zhang, J. M. Ball, A. R. S. Kandada, H. J. Snaith and A. Petrozza, Carrier trapping and recombination: the role of defect physics in enhancing the open circuit voltage of metal halide perovskite solar cells, *Energy Environ. Sci.*, 2016, **9**, 3472–3481.

8 L. Calió, S. Kazim, M. Grätzel and S. Ahmad, Hole-Transport Materials for Perovskite Solar Cells, *Angew. Chem. Int. Ed.*, 2016, **55**, 14522–14545.

9 D. Bi, L. Yang, G. Boschloo, A. Hagfeldt and E. M. J. Johansson, Effect of Different Hole Transport Materials on Recombination in CH $_3$ NH $_3$ PbI $_3$ Perovskite-Sensitized Mesoscopic Solar Cells, *J. Phys. Chem. Lett.*, 2013, **4**, 1532–1536.

10 A. Guerrero, G. Garcia-Belmonte, I. Mora-Sero, J. Bisquert, Y. S. Kang, T. J. Jacobsson, J.-P. Correa-Baena and A. Hagfeldt, Properties of Contact and Bulk Impedances in Hybrid Lead Halide Perovskite Solar Cells Including Inductive Loop Elements, *J. Phys. Chem. C*, 2016, **120**, 8023–8032.

11 K. Pydzińska, J. Karolczak, I. Kosta, R. Tena-Zaera, A. Todinova, J. Idígoras, J. A. Anta and M. Ziółek, Determination of Interfacial Charge-Transfer Rate Constants in Perovskite Solar Cells, *ChemSusChem*, 2016, **9**,

1647–1659.

12 I. Zarazua, G. Han, P. P. Boix, S. Mhaisalkar, F. Fabregat-Santiago, I. Mora-Seró, J. Bisquert and G. Garcia-Belmonte, Surface Recombination and Collection Efficiency in Perovskite Solar Cells from Impedance Analysis, *J. Phys. Chem. Lett.*, 2016, **7**, 5105–5113.

13 G. Xing, N. Mathews, S. Sun, S. S. Lim, Y. M. Lam, M. Gratzel, S. Mhaisalkar and T. C. Sum, Long-Range Balanced Electron- and Hole-Transport Lengths in Organic-Inorganic CH3NH3PbI3, *Science*, 2013, **342**, 344–347.

14 S. D. Stranks, G. E. Eperon, G. Grancini, C. Menelaou, M. J. P. Alcocer, T. Leijtens, L. M. Herz, A. Petrozza and H. J. Snaith, Electron-Hole Diffusion Lengths Exceeding 1 Micrometer in an Organometal Trihalide Perovskite Absorber, *Science*, 2013, **342**, 341–344.

15 C. Wehrenfennig, G. E. Eperon, M. B. Johnston, H. J. Snaith and L. M. Herz, High Charge Carrier Mobilities and Lifetimes in Organolead Trihalide Perovskites, *Adv. Mater.*, 2014, **26**, 1584–1589.

16 M. De Bastiani, V. D'Innocenzo, S. D. Stranks, H. J. Snaith and A. Petrozza, Role of the crystallization substrate on the photoluminescence properties of organo-lead mixed halides perovskites, *Apl Mater.*, 2014, **2**, 081509.

17 M. Salado, J. Idigoras, L. Calio, S. Kazim, M. K. Nazeeruddin, J. A. Anta and S. Ahmad, Interface Play between Perovskite and Hole Selective Layer on the Performance and Stability of Perovskite Solar Cells, *ACS Appl. Mater. Interfaces*, 2016, **8**, 34414–34421.

18 N. J. Jeon, J. H. Noh, W. S. Yang, Y. C. Kim, S. Ryu, J. Seo and S. I. Seok, Compositional engineering of perovskite materials for high-performance solar cells, *Nature*, 2015, **517**, 476–480.

19 S. N. Habisreutinger, T. Leijtens, G. E. Eperon, S. D. Stranks, R. J. Nicholas and H. J. Snaith, Carbon nanotube/polymer composites as a highly stable hole collection layer in perovskite solar cells, *Nano Lett.*, 2014, **14**, 5561–5568.

20 D. Bi, W. Tress, M. I. Dar, P. Gao, J. Luo, C. Renevier, K. Schenk, A. Abate, F. Giordano, J.-P. Correa Baena, J.-D. Decoppet, S. M. Zakeeruddin, M. K. Nazeeruddin, M. Grätzel and A. Hagfeldt, Efficient luminescent solar cells based on tailored mixed-cation perovskites, *Sci. Adv.*, 2016, **2**, e1501170.

21 E. Guillén, F. J. Ramos, J. A. Anta and S. Ahmad, Elucidating Transport-Recombination Mechanisms in Perovskite Solar Cells by Small-Perturbation Techniques, *J. Phys. Chem. C*, 2014, **118**, 22913–22922.

22 A. R. Pascoe, N. W. Duffy, A. D. Scully, F. Huang and Y.-B. Cheng, Insights into Planar CH $_3$ NH $_3$ PbI $_3$ Perovskite Solar Cells Using Impedance

Spectroscopy, *J. Phys. Chem. C*, 2015, **119**, 4444–4453.

23 A. Todinova, J. Idígoras, M. Salado, S. Kazim and J. A. Anta, Universal Features of Electron Dynamics in Solar Cells with TiO_2 Contact: From Dye Solar Cells to Perovskite Solar Cells, *J. Phys. Chem. Lett.*, 2015, **6**, 3923–3930.

24 L. Contreras, J. Idígoras, A. Todinova, M. Salado, S. Kazim, S. Ahmad and J. A. Anta, Specific cation interactions as the cause of slow dynamics and hysteresis in dye and perovskite solar cells: a small-perturbation study, *Phys. Chem. Chem. Phys.*, 2016, **18**, 31033–31042.

25 A. Todinova, L. Contreras-Bernal, M. Salado, S. Ahmad, N. Morillo, J. Idígoras and J. A. Anta, Towards a Universal Approach for the Analysis of Impedance Spectra of Perovskite Solar Cells: Equivalent Circuits and Empirical Analysis, *ChemElectroChem*, 2017, **4**, 2891–2901.

26 V. W. Bergmann, Y. Guo, H. Tanaka, I. M. Hermes, D. Li, A. Klasen, S. A. Bretschneider, E. Nakamura, R. Berger and S. A. L. Weber, Local Time-Dependent Charging in a Perovskite Solar Cell, *ACS Appl. Mater. Interfaces*, 2016, **8**, 19402–19409.

27 A. Pockett, G. E. Eperon, N. Sakai, H. J. Snaith, L. M. Peter and P. J. Cameron, Microseconds, milliseconds and seconds: deconvoluting the dynamic behaviour of planar perovskite solar cells, *Phys. Chem. Chem. Phys.*, 2017, **19**, 5959–5970.

28 M. T. Weller, O. J. Weber, P. F. Henry, A. M. Di Pumpo and T. C. Hansen, Complete structure and cation orientation in the perovskite photovoltaic methylammonium lead iodide between 100 and 352 K, *Chem. Commun.*, 2015, **51**, 4180–4183.

29 M. Turcu, O. Pakma and U. Rau, Interdependence of absorber composition and recombination mechanism in Cu (In, Ga)(Se, S) 2 heterojunction solar cells, *Appl. Phys. Lett.*, 2002, **80**, 2598–2600.

30 C.-T. Sah, R. N. Noyce and W. Shockley, Carrier generation and recombination in pn junctions and pn junction characteristics, *Proc. IRE*, 1957, **45**, 1228–1243.

31 L. A. Frolova, N. N. Dremova and P. A. Troshin, The chemical origin of the p-type and n-type doping effects in the hybrid methylammonium–lead iodide (MAPbI 3) perovskite solar cells, *Chem. Commun.*, 2015, **51**, 14917–14920.

32 S. Soedergren, A. Hagfeldt, J. Olsson and S.-E. Lindquist, Theoretical models for the action spectrum and the current-voltage characteristics of microporous semiconductor films in photoelectrochemical cells, *J. Phys. Chem.*, 1994, **98**, 5552–5556.

33 J. A. Anta, J. Idigoras, E. Guillen, J. Villanueva-Cab, H. J. Mandujano-

Ramirez, G. Oskam, L. Pelleja and E. Palomares, A continuity equation for the simulation of the current–voltage curve and the time-dependent properties of dye-sensitized solar cells, *Phys. Chem. Chem. Phys.*, 2012, **14**, 10285–10299.

34 Y. Zhou and A. Gray-Weale, A numerical model for charge transport and energy conversion of perovskite solar cells, *Phys. Chem. Chem. Phys.*, 2016, **18**, 4476–4486.

Chapter 6

The Role of Surface Recombination on the Performance of Perovskite Solar cells: Effect of Morphology and Crystalline Phase of TiO_2 Contact

In this Chapter, the impact of the ESL architecture (1D and 3D morphologies) and the nanocrystalline phase (anatase and amorphous) is analysed. For anatase structures, similar PCE are achieved using an ESL either with 1D nanocolumns or the classical 3D nanoparticle film. However, lower power conversion efficiencies and different optoelectronic properties are found for perovskite devices based on amorphous 1D films. Calculations using a drift-diffusion model which explicitly considers the selective contacts reproduces qualitatively the main features observed experimentally. Results in this Chapter demonstrate that for a solar cell in which the contact is working properly the open-circuit photovoltage is mainly determined by bulk recombination, whereas the introduction of a "bad contact" shifts the balance to surface recombination.

This chapter is based on Publication 4 of this Thesis: Idígoras *et al.* Adv. Mater. Interfaces, 2018, 0, 1801076.

6.1 Introduction

As it has been shown in *Chapter* 5, the appropriate choice of selective contacts is critical for obtaining well-performing devices. In particular, it has been demonstrated that the nature of HTM affects to the nature of recombination in perovskite solar cells by adding surface-mediated recombination in the case of “inadequate” hole selective contacts. In this *Chapter*, the focus is on the morphology and crystalline phase of the ESL and the impact on the performance of the solar cell.

In particular, the purpose of this *Chapter* is twofold. First, we have tested the performance of the plasma-enhanced chemical vapour deposition (PECVD) technique to prepare TiO_2 films to be used as ESL in perovskite solar devices. PECVD is a well-established technique in electronics and microelectronics, solar cells, mechanical engineering, and optical industries for the fabrication of passive and active components. It provides an environmentally friendly (low-power and precursor consumption and solvent less approach) for the manufacturing in large scale with a finely control in the composition (including doping), microstructure and structure of thin films, coatings and interfaces in multilayer systems.[1–7] Although this methodology has been traditionally applied in the deposition of compact layers, during the last years, Borras *et al.* have settled the conditions for the fabrication of tailored porous and nanostructured TiO_2 thin films at low temperature (ranging from RT for amorphous to 250 ºC for anatase crystalline layers).[7] Second, we have aimed to establish the effect of the nature of the ESL, in terms on morphology and crystallinity, on the photovoltaic performance. In particular, we investigate how bulk or contact-induced recombination routes do influence the IV curve and the hysteretic behaviour. As it was said in previous *Chapters,* the locus and nature recombination on PSCs as well as the origin of hysteresis in the IV curve have been object of intense debate in the recent literature.[8–17]

In this *Chapter* we investigate the impact of the different nanostructures employed as ESL on the optoelectronic properties and the hysteresis. We have measured IV curves and run photoluminescence and impedance spectroscopy experiments. Following the methodology described in *Chapte*r 5,[11] the latter is carried out under two different excitation wavelengths, characterized by different optical penetration lengths in the perovskite layer, so that surface effects can be detected. In addition, drift-diffusion modeling, with explicit consideration of the ion/electron dynamics and the presence of the selective contacts, is used to generate IV curves.[18]

6.2 Fabrication and characterization of devices

Fabrication of perovskite solar cells

Different methodologies were employed to prepare the different ETLs. For the standard configuration, a mesoporous layer of TiO_2 was deposited on top of a TiO_2 compact layer. On the other hand, the TiO_2 nanocolumns deposition (anatase phase and amorphous) was carried out in a microwave electron cyclotron resonance (MWECR) PECVD reactor working in downstream configuration. TiO_2 nanocolumns were performed in the labs of the ICMSE (Drs. Ana Borrás and Angel Barranco). For all the device configurations, a pure methylammonium ($MAPbI_3$) layer was deposited as active layer at environmental humidity conditions (relative humidity ≈ 50 %). According the methodology reported,[19] the perovskite precursor solution was prepared for a ratio DMSO:Pb^{2+} of 0.75 (Table 3.2 in *Chapter* 3). After perovskite deposition, spiro-OMeTAD solution was spin coated. Finally, 60 nm of gold was deposited by thermal evaporation. (See *Chapter* 3 for details)

Characterization of devices

IV curves were documented with a solar simulator (*ABET-Sun2000*) with an AM 1.5G filter. Photovoltaic parameters including J_{SC}, V_{OC}, FF, and PCE were extracted from the IV curves of the solar cells. The current-voltage characteristic was measured with scan rate of 100 mV/s after an initial poling of 20 s at 1.2 V. The illumination for the different IS measurements was provided by white, red (λ = 635 nm) and blue (λ = 465 nm) LEDs and over a wide range of DC light intensities. IS measurements were performed at the open circuit potential. A 20 mV perturbation in the 10^6–10^{-2} Hz range was utilized to obtain the spectra. To compensate for the different response under blue and red-light due to the different optical absorption, all parameters were monitored and plotted as a function of the open-circuit potential generated by each type of bias light. For the structural characterization, SEM images of the samples were obtained. X-ray diffractograms were recorded on a Rigaku diffractometer using CuKα source. The measurements were performed at grazing angle geometry. The samples were mounted without any further modification and the divergence slit were adjusted to the dimension of the films. The scan range of 10º–60º was selected with an acquisition time of 3º min^{-1}. A baseline correction was applied to the diffractograms to compensate for the noise arising from the substrate. For optical characterization, UV–vis absorption spectra and photoluminescence measurements were recorded.

6.3 Results and discussion

To isolate the effect of the nanostructure and nanocrystalline phase of the different TiO_2 films, a fixed thickness of 200 nm was employed for all the different ETLs studied. Figure 6.1A–C gathers cross-section SEM images of the three ETLs showing their corresponding characteristic microstructures, i.e., a homogeneous 3D distribution of nanoparticles (*Np-Anatase*) and vertical nanocolumns (Nc) for the PECVD thin films.

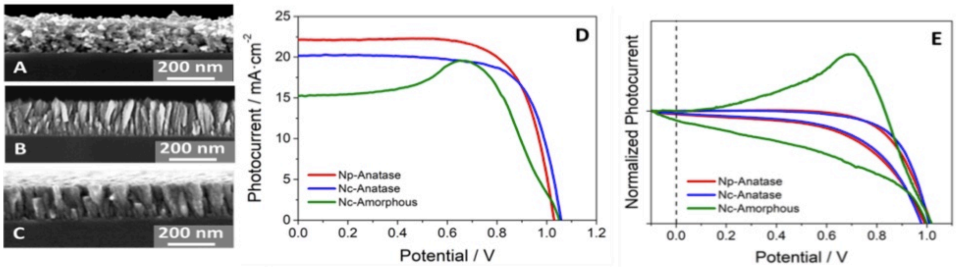

Figure 6.1. Cross-section SEM views of the (A) *Np-Anatase*, (B) *Nc-Anatase* and (C) *Nc-amorphous* films deposited on silicon wafer. (D) Current-voltage characteristic in reverse scan under 1 sun – AM 1.5 illumination and (E) cyclic voltammetry using a white-LED as light source (10 $mW\cdot cm^{-2}$) for the different device configurations. A scan rate of 100 mV/s with a poling of 20 s at 1.2V was employed in all three cases.

In the case of the *Nc-anatase,* the columns show a feather-like morphology with sharp edges and rough surface. *Nc-amorphous* presents a domed form with the column diameter slightly thinner at the interface with the substrate. Figure A-6.1 in appendix D contains X-ray diffraction data of these TiO_2 films.

On top of the TiO_2 layer, a film of $MAPbI_3$ was deposited. Spiro-OMeTAD was used as hole selective layer in all cases. Figure A-6.2 shows that the quality of the perovskite layer and their interface with the hole transport material deposited on top is not affected by the morphology of the TiO_2, and that there are no pinholes or voids that might compromise the stability of the device.[20] Figure A-6.3 also shows that the absorption properties of the perovskite films are basically unaffected by the morphology of the TiO_2 layer. Hence, we can be fairly confident on the fact that only the electrical effect of the TiO_2/perovskite interface is analysed for each configuration. Figure 1D shows the best current–voltage characteristic obtained for the three device configurations measured under standard conditions (100 mW cm^{-2}—AM 1.5 illumination). In particular, average efficiencies of 14.9%, 14.4% were obtained for *Np-Anatase*, *Nc-Anatase* devices, respectively (see also Fig. A-6.4). For *Nc-Amorphous* devices, the estimation of the efficiency is compromised by the appearance of a bump in the 0.6–0.8 voltage range (a lower efficiency is obtained in the forward scan, see Fig. 6.1E) and therefore only an indicative value can be reported. No significant differences were found between the nanoparticle film (J_{SC}: 19.8 mA·cm^{-2}, V_{OC}: 1020 mV, FF: 0.73) and the nanocolumnar film (J_{SC}: 19.4 mA mA·cm^{-2}, V_{OC}:: 1025 mV, FF: 0.73) as long as they have the same anatase TiO_2 crystalline phase (see Fig. A-6.1 for the comparison of the XRD diagrams). In contrast, significant changes were observed when the nanocolumnar layer employed as ETL in perovskite devices is amorphous and does not show any crystalline phase (Fig. A-6.1 and A-6.4). In spite of showing a similar V_{OC} (1020 mV) to the ones obtained for *Np-Anatase* and *Nc-Anatase* devices (Fig. 6.1D; Table A-6.1), lower J_{SC}: values (15.9 mA·cm^{-2}) were recorded and a prominent bump in the vicinity of the maximum power point is clearly visible. Note that the same scan rate of 100 mV/s is used for all devices. Similar behaviour has been found in both DSSCs (see Fig. 4.1 in *Chapter* 4) and PSCs with strong hysteresis,[9,10] In line with these results, as shown in Fig. 6.1E, when the current–voltage characteristics were measured by cyclic voltammetry, *Nc-Amorphous* devices show strong hysteresis between reverse and forward scans in contrast to the *Np-Anatase* and Nc-Anatase devices, where the hysteresis is less significant. In particular, hysteresis indexes of 0.11, 0.13, and 0.61 were calculated for *Np-Anatase*, *Nc-Anatase*, and *Np-Amorphous,* respectively. To investigate the influence of the different TiO_2 films employed as ETLs on the charge extraction/separation efficiency, steady-state photoluminescence spectra of the perovskite films deposited on top of each ETL were measured (Fig. 6.2).

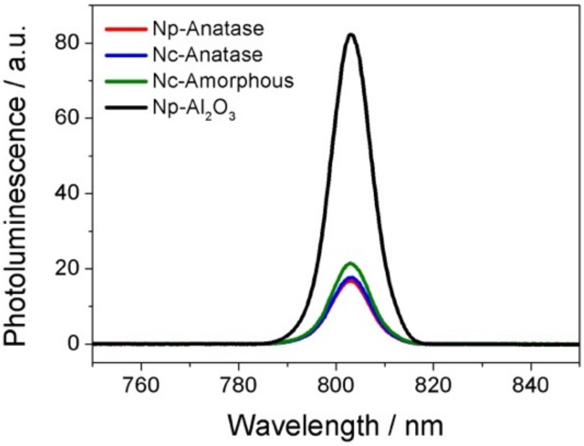

Figure 6.2. Steady state photoluminescence spectra of perovskite deposited on top of the different ETLs. Al_2O_3 film was employed as reference. The excitation wavelength was 532 nm.

In addition, a mesoporous Al_2O_3 nanoparticle film was also employed as reference due to its conduction band position and, consequently, its inability to accept electrons from the perovskite layer.[21] In line with a previous work,[22] using an excitation wavelength of 532 nm, PL peaks appear in the range of 785–815 nm with an emission maximum at 804 nm. The PL signal arises from radiative recombination processes within the perovskite material and therefore a faster electron injection from the perovskite film to the ETL results in a reduction of the PL signal. It is important to remember that the optical and structural properties of the perovskite film are not affected by the nature of the TiO_2 layer and therefore by means of the PL experiment we probe the quality of the interface in connection to the transfer of electrons toward the selective layer only. The higher PL intensity was obtained when Al_2O_3 film was employed as ETL as a consequence of no electron extraction. Faster charge extraction was observed for the rest of ETLs, in the following sequence: *Np-Anatase* > *Nc-Anatase* > *Nc-Amorphous*, with only a slight difference between the two anatase TiO_2 layers. The worse charge extraction efficiency of *Nc-Amorphous* layers (Fig. 6.2) could explain its lower J_{SC} (Fig. 6.1D; Table A-6.1) However, in relative terms to the reference Al_2O_3 film, the photoluminescence difference between the three TiO_2 layers is too small to have an impact on performance. As it was shown in *Chapter* 4, interfacial charge accumulation has also been related to the hysteretic behaviour (Fig. 6.1E).

To further analyse the impact of the different TiO_2 layers employed as ETLs on the electronic dynamics that governs the photovoltaic performance, impedance spectroscopy measurements at open circuit were performed. In Figure 6.3, the impedance response in the form of Nyquist, frequency-dependent imaginary impedance Z" and capacitance plots are reported.

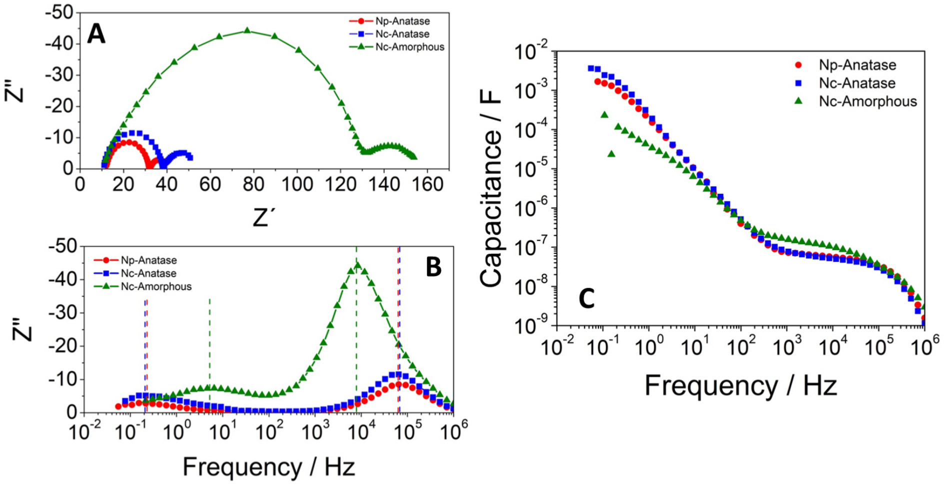

Figure 6.3. (A) Nyquist impedance spectra, (B) impedance frequency plot of the imaginary part (Z") and (C) frequency-dependent apparent capacitance obtained for the different device configurations under open-circuit conditions and under white light illumination. The data were obtained for a photovoltage of 0.98 V at constant illumination.

As shown Figure 6.3A, the impedance spectra obtained for the different devices were characterized by two signals that appear at high and low frequency. The meaning of these signals has already been described in *Chapter* 3. These two arcs (Fig. 6.3A) will only be well-distinguished when the peak maxima on the impedance frequency plots (Fig. 6.3B) lie separated enough in the frequency scale. In particular, for both *Np-Anatase* and *Nc-Anatase* the *HF* and *LF* peaks appear, under an applied potential closer to 1-sun V_{OC} (≈980 mV), at 10^5 and 0.1 Hz, respectively. In contrast, *Nc-Amorphous* devices show the *HF* and *LF* peaks at 10^4 and 10 Hz, respectively.

The frequency-dependent apparent capacitance for the different devices is shown in Figure 6.3C. As it was said in *Chapter* 3, different polarization processes were attributed to each plateau.[15,23–25] The *HF* component is determined by the dielectric polarization of the perovskite in the bulk, whereas the *LF* plateau has been associated with the ETL/perovskite interface charge accumulation. It has been claimed in *Chapter* 4 that the hysteresis found in the current–voltage characteristics is associated with higher values of *LF* apparent capacitance.[12,15] However, in this case *Nc-Amorphous* devices show the most pronounced hysteretic behaviour (Fig. 6.1E) in spite of showing lower *LF* capacitance values (≈10^{-4} F) than in *Np-Anatase* and *Nc-Anatase* (≈10^{-2} F). Furthermore, a new polarization process appears at mid frequencies for *Nc-Amorphous* devices. This new feature appears in the range of 10^3–10^4 Hz (Fig. 6.3C), in the same range where the *HF* peak for *Nc-Amorphous* devices was found (Fig. 6.3B). Thus, the presence of two time constants close in frequencies could explain the nonsymmetric shape of the *HF* semicircle (Fig. 6.3A) and the *HF* peak in the impedance frequency plots (Fig. 6.3B) of *Nc-Amorphous* devices. A similar feature has previously been found for degraded perovskite devices.[26] as well as for cells with a nonoptimized contact or when an insulating SiO_2 scaffold is placed on top of the TiO_2 selective layer.[27]

To better distinguish the time constants of the different processes found in the *HF* region of *Nc-Amorphous* devices, we have plotted the impedance phase shift versus frequency (Bode plot, Fig. 6.4A). In contrast to Figure 6.3B, two peaks appear in the *HF* range (*HF*1 ≈ 10^4 Hz and *HF*2 ≈10^5 Hz), under an applied potential closer to 1-sun V_{OC} for *Nc-Amorphous* devices. Interestingly enough one of them (*HF*1) coincides in frequencies with the *HF* peak of *Np-Anatase* and *Nc-Anatase devices*. Considering the *HF* region only, Figure 6.4B shows the associated time constants (τ) estimated from Eq. 3.23, where f is the frequency peak maximum directly extracted from the phase Bode plot in Figure. 6.4A. As hinted in previous *Chapters*, the *HF* component can be associated with charge recombination processes and, consequently, the HF time constant could be understood as a measure of the recombination rate of photogenerated charges.[28,29]

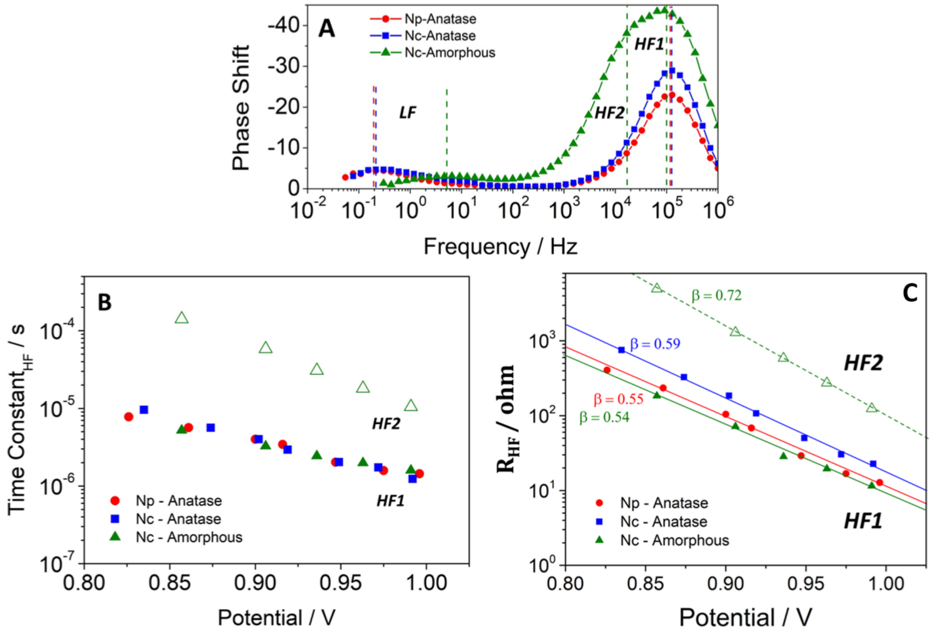

Figure 6.4. (A) Impedance frequency plot of phase shift, (B) *HF* time constants extracted as 1/2πf for the different device configurations under open-circuit conditions and under white light illumination. (C) *HF* resistance as extracted from fittings of the impedance spectra using *Voight* circuit (see inset Fig. 3.9A) Solid and open symbols correspond to the two time constants observed in the amorphous spectra in the *HF* region.

From the analysis of Figure 6.4, we can draw the following conclusions. First, *Np-Anatase* and *Nc-Anatase* devices show the same bulk recombination rate. Second, *Nc-Amorphous* devices exhibit two different kinetic processes in the high frequency region. As mentioned, the *HF*1 time constant, coincides remarkably well with the single *HF* time constant (10^{-6}–10^{-5} s) detected in the anatase films and attributed to charge recombination. In contrast, the *HF*2 time constant was found in the range of 10^{-5}–10^{-4} s with a larger slope with respect to photopotential. Figure 6.4C shows the *HF* resistances (R_{HF}) as a function of the V_{OC} extracted by fitting the impedance response to a simple *Voight* equivalent circuit (see inset Fig. 3.9A in *Chapter* 3). In particular, the *HF*1 recombination resistance is found to vary exponentially with the open-circuit potential as predicted by Eq. 2.22 (*Chapter* 2). As shown in Figure 6.4C, the *HF*1 resistance found for the three types of films yields β-parameter values around 0.56, very similar as the values obtained in *Chapter* 5 for fresh devices.[11,30] The *HF*2 time resistance is also found to fit to Eq. 2.22 although with a different β-parameter value of 0.72. This suggests a different mechanism, possibly recombination, for *Nc-Amorphous* devices.

To cast light on the origin of *HF* time constants found for *Nc-Amorphous* devices, impedance spectroscopy was performed using two different illumination wavelengths (like we did in *Chapter* 5). Considering the absorption spectra of perovskite devices (Fig. A-6.3) and the Beer–Lambert law, a different charge generation profile inside perovskite layer will be produced using (λ = 465 nm) blue and (λ = 635 nm) red illuminations due to the different spatial penetration of the optical excitation wavelengths.[31] Figure 6.5 shows the impedance phase shift versus frequency and time constant of the *HF* component that was extracted from Eq. 3.23 for *Nc-Amorphous* devices using blue and red illuminations. Figure 6.5A brings to light the importance of where the charge has been photogenerated as shown by the different impedance responses obtained under the different optical excitation wavelengths. As shown in Figure 6.5B, the blue and red *HF*1 time constants coincide quite well in the studied voltage range. Similar results were found for *Np-Anatase* devices when impedance spectroscopy was performed under blue and red illuminations (Fig. A-6.5). However, the time constant *HF*2 does not only show a visible difference between the two time constants, but also a different slope. In particular, slower kinetics are observed when blue illumination was used as excitation wavelength. This behaviour is consistent with the larger resistance observed in the Nyquist plot under blue illumination (Fig. A-6.6).

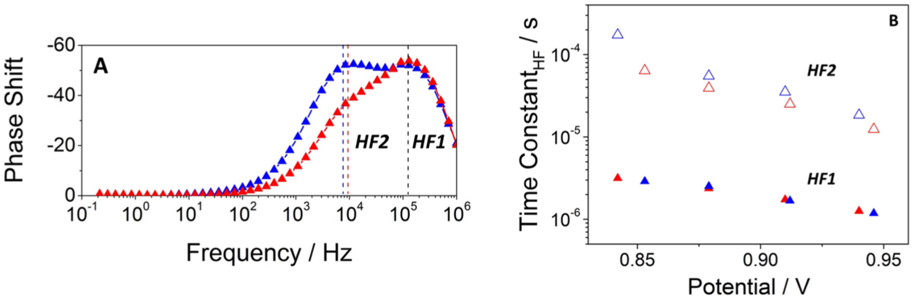

Figure 6.5. (A) Impedance frequency plot of phase shift and (B) *HF* time constants extracted as $1/2\pi f$ for *Nc-Amorphous* devices at open-circuit conditions and using red and blue light illumination.

It is relevant to elucidate what is the physical origin of the additional *HF*2 time constant observed in the *Nc-Amorphous* devices and the strong hysteresis with a marked bump that it is observed in the IV curve. As noted above, the *HF*2 signal shows a different value when the impedance experiment is done at a situation where more carriers are photogenerated close to the front contact. All this evidence points to an interfacial process as the cause of the signal. The fact that amorphous contacts generate much less current at short-circuit suggests also that surface recombination may be having an important role in this case. As regards recombination, two main recombination mechanisms of photogenerated charges have been extensively discussed in the literature.

On the one hand, a recombination process mediated via a trap-limited mechanism in the bulk of the perovskites.[10,11,17,30] And, on the other hand, a surface mediated recombination at the selective contacts.[24,32,33] However, it is possible that the both recombination mechanisms could act together if the selective layer are characterized by a low charge extraction efficiency, as it is the case of *Nc-amorphous* layers studied here. As it was previously shown (*Chapter* 5), the coincidence of the *HF*1 time constants obtained under blue and red illuminations, its time scale and the values of ideality factor (m ≈ 1.8) extracted from resistance versus potential plot (Fig. 6.4C), indicate that this signal corresponds to recombination in the bulk of the perovskite layer via a trap-limited mechanism.[8,11,30,34] In contrast, we attribute the different behaviour found for the *HF*2 time constants under blue and red illumination along with the ideality factor closer to 1 (m ≈ 1.4) to a surface-mediated recombination mechanism or, alternatively, to a slow transport process. In this respect, it is important to bear in mind that impedance time constants are not recombination "lifetimes," especially for perovskite solar cells.[20,22,35]

To confirm this interpretation, drift-diffusion modeling was performed by he group of Prof. Walker in the Department of Physics (University of Bath) to simulate the IV curve for different relative values of surface versus bulk recombination. In these calculations the electron–hole dynamics, including transport and recombination, are coupled to the motion of iodide vacancies within the perovskite layer (see details in appendix D). In Figure 6.6 results for the IV curves for two cases, high and low surface recombination at the TiO_2/perovskite interface, are shown.

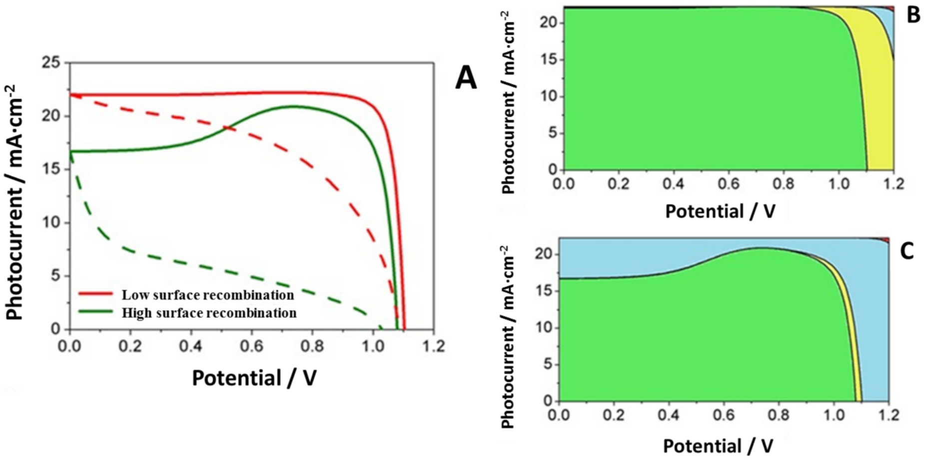

Figure 6.6. (A) Simulated IV curves for reverse (solid lines) and forward (dashed lines) when either high or low surface recombination rates at the TiO_2/perovskite interface are considered in the calculations. The rest of the parameters are kept fixed. (B, C) Relative contributions to the total current: extracted current (green), bulk recombination (yellow), surface recombination at the TiO_2 interface (blue) and surface recombination at the spiro-OMeTAD interface (red).

The numerical simulation shows that a high value of the surface recombination rate does not only reduces the short-circuit photocurrent without affecting the V_{OC}, but also induces more hysteresis in the voltage scan. This is perfectly in line with the experimental observations (Fig. 6.1D; Fig. A-6.4). Furthermore, the critical impact of the surface recombination term explains the appearance of the additional time constant in the impedance spectrum for the device with *Nc-amorphous* contact, as well its dependence on the excitation wavelength.

In summary, considering the same behaviour obtained for the fastest recombination rate extracted from impedance spectroscopy (Fig. 6.4B and 6.5B) and the same V_{OC} values (1020 mV) obtained from the current–voltage characteristics (Fig. 6.1D; Fig. A-6.4) for all the different device configurations, trap-limited recombination in the bulk of the perovskites seems to be the main candidate to explain the V_{OC} of perovskite devices, at least for anatase-base contacts. This is in line with recent reports with state-of-the-art solar cells and with the results obtained in *Chapter* 5.[11,17,30] However, an additional process appears for *Nc-amorphous* contacts, which also exhibit a bump in the current–voltage characteristics and strong hysteresis. We attribute this additional process and the IV curve shape to surface recombination at the TiO_2/perovskite interface. It is also important to state that at open-circuit, for *Nc-amorphous* contacts, bulk recombination still amounts to up to a third of the surface recombination, which explains the presence of *HF*1 signal in the impedance spectrum in these devices.

6.4 Conclusion

We have analysed the impact of the structural and crystalline properties of different TiO_2 films employed as ETL on the photovoltaic and optoelectronic behaviour of perovskite solar devices. In particular, we have investigated the effect of ETLs based on 3D nanoparticle and 1D nanocolumns films deposited by spin-coating method and plasma-enhanced chemical vapour deposition, respectively. Additionally, we have analysed the effect of the nanocrystalline phase of the ETL by comparing anatase and amorphous TiO_2 nanocolumnar films. Two main conclusions can be extracted from this Chapter. On the one hand, the similar power conversion efficiency (≈14.7%) and optoelectronic behaviour obtained for the both anatase TiO_2 films (three and 1D structure) employed as ETL bring to light the capacity to prepare well-performing 1D photoanode by plasma-enhanced chemical vapour deposition technique, which is a very simple, reliable, industrially scalable and low-temperature deposition method. Second, regardless of the structural and crystalline properties of the different TiO_2 films employed as ETL, all devices show the same open-circuit photopotential although quite different short-circuit photocurrent. This behaviour can be explained by two different charge recombination mechanisms present in devices based on amorphous nanocolumnar films as ETL. The results extracted from impedance analysis and drift-diffusion modeling reveal that the recombination mechanism that determines the V_{OC} is governed by a process mediated by traps in the bulk of the perovskite. However, the second charge recombination mechanism found for *Nc-Amorphous* device suggests that surface-mediated recombination at the ETL/perovskite interface determines the J_{SC} and results in hysteresis.

6.5 References

1 A. Barranco, A. Borras, A. R. Gonzalez-Elipe and A. Palmero, Perspectives on oblique angle deposition of thin films: from fundamentals to devices, *Prog. Mater. Sci.*, 2016, **76**, 59–153.

2 K. L. Choy, Chemical vapour deposition of coatings, *Prog. Mater. Sci.*, 2003, **48**, 57–170.

3 L. Martinu and D. Poitras, Plasma deposition of optical films and coatings: a review, *J. Vac. Sci. Technol. Vac. Surf. Films*, 2000, **18**, 2619–2645.

4 K. K. Ostrikov, U. Cvelbar and A. B. Murphy, Plasma nanoscience: setting directions, tackling grand challenges, *J. Phys. Appl. Phys.*, 2011, **44**, 174001.

5 P. R. i Cabarrocas, Plasma enhanced chemical vapor deposition of silicon thin films for large area electronics, *Curr. Opin. Solid State Mater. Sci.*, 2002, **6**, 439–444.

6 A. Borrás, J. R. Sánchez-Valencia, J. Garrido-Molinero, A. Barranco and A. R. González-Elipe, Porosity and microstructure of plasma deposited TiO2 thin films, *Microporous Mesoporous Mater.*, 2009, **118**, 314–324.

7 A. Borras, J. R. Sanchez-Valencia, R. Widmer, V. J. Rico, A. Justo and A. R. Gonzalez-Elipe, Growth of crystalline TiO2 by plasma enhanced chemical vapor deposition, *Cryst. Growth Des.*, 2009, **9**, 2868–2876.

8 W. L. Leong, Z.-E. Ooi, D. Sabba, C. Yi, S. M. Zakeeruddin, M. Graetzel, J. M. Gordon, E. A. Katz and N. Mathews, Identifying Fundamental Limitations in Halide Perovskite Solar Cells, *Adv. Mater.*, 2016, **28**, 2439–2445.

9 D. Bi, W. Tress, M. I. Dar, P. Gao, J. Luo, C. Renevier, K. Schenk, A. Abate, F. Giordano, J.-P. Correa Baena, J.-D. Decoppet, S. M. Zakeeruddin, M. K. Nazeeruddin, M. Grätzel and A. Hagfeldt, Efficient luminescent solar cells based on tailored mixed-cation perovskites, *Sci. Adv.*, 2016, **2**, e1501170.

10 J.-P. Correa-Baena, S.-H. Turren-Cruz, W. Tress, A. Hagfeldt, C. Aranda, L. Shooshtari, J. Bisquert and A. Guerrero, Changes from Bulk to Surface Recombination Mechanisms between Pristine and Cycled Perovskite Solar Cells, *ACS Energy Lett.*, 2017, **2**, 681–688.

11 L. Contreras-Bernal, M. Salado, A. Todinova, L. Calio, S. Ahmad, J. Idígoras and J. A. Anta, Origin and Whereabouts of Recombination in Perovskite Solar Cells, *J. Phys. Chem. C*, 2017, **121**, 9705–9713.

12 L. Contreras, J. Idígoras, A. Todinova, M. Salado, S. Kazim, S. Ahmad and J. A. Anta, Specific cation interactions as the cause of slow dynamics and hysteresis in dye and perovskite solar cells: a small-perturbation study, *Phys.*

Chem. Chem. Phys., 2016, **18**, 31033–31042.

13 S. Ravishankar, O. Almora, C. Echeverría-Arrondo, E. Ghahremanirad, C. Aranda, A. Guerrero, F. Fabregat-Santiago, A. Zaban, G. Garcia-Belmonte and J. Bisquert, Surface polarization model for the dynamic hysteresis of perovskite solar cells, *J. Phys. Chem. Lett.*, 2017, **8**, 915–921.

14 Y. Zou and R. J. Holmes, Temperature-Dependent Bias Poling and Hysteresis in Planar Organo-Metal Halide Perovskite Photovoltaic Cells, *Adv. Energy Mater.*, 2016, **6**, 1501994.

15 H.-S. Kim, I.-H. Jang, N. Ahn, M. Choi, A. Guerrero, J. Bisquert and N.-G. Park, Control of $I - V$ Hysteresis in $CH_3NH_3PbI_3$ Perovskite Solar Cell, *J. Phys. Chem. Lett.*, 2015, **6**, 4633–4639.

16 G. Richardson, S. E. O’Kane, R. G. Niemann, T. A. Peltola, J. M. Foster, P. J. Cameron and A. B. Walker, Can slow-moving ions explain hysteresis in the current–voltage curves of perovskite solar cells?, *Energy Environ. Sci.*, 2016, **9**, 1476–1485.

17 S. Ravishankar, S. Gharibzadeh, C. Roldán-Carmona, G. Grancini, Y. Lee, M. Ralaiarisoa, A. M. Asiri, N. Koch, J. Bisquert and M. K. Nazeeruddin, Influence of Charge Transport Layers on Open-Circuit Voltage and Hysteresis in Perovskite Solar Cells, *Joule*, 2018, **2**, 788–798.

18 N. E. Courtier, G. Richardson and J. M. Foster, A fast and robust numerical scheme for solving models of charge carrier transport and ion vacancy motion in perovskite solar cells, *Appl. Math. Model.*, 2018, **63**, 329–348.

19 C. Aranda, C. Cristobal, L. Shooshtari, C. Li, S. Huettner and A. Guerrero, Formation criteria of high efficiency perovskite solar cells under ambient conditions, *Sustain. Energy Fuels*, 2017, **1**, 540–547.

20 A. Abate, S. Paek, F. Giordano, J.-P. Correa-Baena, M. Saliba, P. Gao, T. Matsui, J. Ko, S. M. Zakeeruddin and K. H. Dahmen, Silolothiophene-linked triphenylamines as stable hole transporting materials for high efficiency perovskite solar cells, *Energy Environ. Sci.*, 2015, **8**, 2946–2953.

21 J. M. Ball, M. M. Lee, A. Hey and H. J. Snaith, Low-temperature processed meso-superstructured to thin-film perovskite solar cells, *Energy Environ. Sci.*, 2013, **6**, 1739.

22 M. Salado, J. Idigoras, L. Calio, S. Kazim, M. K. Nazeeruddin, J. A. Anta and S. Ahmad, Interface Play between Perovskite and Hole Selective Layer on the Performance and Stability of Perovskite Solar Cells, *ACS Appl. Mater. Interfaces*, 2016, **8**, 34414–34421.

23 I. Zarazua, J. Bisquert and G. Garcia-Belmonte, Light-Induced Space-Charge Accumulation Zone as Photovoltaic Mechanism in Perovskite Solar

Cells, *J. Phys. Chem. Lett.*, 2016, **7**, 525–528.

24 A. Guerrero, G. Garcia-Belmonte, I. Mora-Sero, J. Bisquert, Y. S. Kang, T. J. Jacobsson, J.-P. Correa-Baena and A. Hagfeldt, Properties of Contact and Bulk Impedances in Hybrid Lead Halide Perovskite Solar Cells Including Inductive Loop Elements, *J. Phys. Chem. C*, 2016, **120**, 8023–8032.

25 M. Bag, L. A. Renna, R. Y. Adhikari, S. Karak, F. Liu, P. M. Lahti, T. P. Russell, M. T. Tuominen and D. Venkataraman, Kinetics of Ion Transport in Perovskite Active Layers and Its Implications for Active Layer Stability, *J. Am. Chem. Soc.*, 2015, **137**, 13130–13137.

26 M. Salado, L. Contreras-Bernal, L. Caliò, A. Todinova, C. López-Santos, S. Ahmad, A. Borras, J. Idígoras and J. A. Anta, Impact of moisture on efficiency-determining electronic processes in perovskite solar cells, *J. Mater. Chem. A*, 2017, **5**, 10917–10927.

27 M. Anaya, W. Zhang, B. C. Hames, Y. Li, F. Fabregat-Santiago, M. E. Calvo, H. J. Snaith, H. Míguez and I. Mora-Seró, Electron injection and scaffold effects in perovskite solar cells, *J. Mater. Chem. C*, 2017, **5**, 634–644.

28 A. Todinova, J. Idígoras, M. Salado, S. Kazim and J. A. Anta, Universal Features of Electron Dynamics in Solar Cells with TiO_2 Contact: From Dye Solar Cells to Perovskite Solar Cells, *J. Phys. Chem. Lett.*, 2015, **6**, 3923–3930.

29 K. Pydzińska, J. Karolczak, I. Kosta, R. Tena-Zaera, A. Todinova, J. Idígoras, J. A. Anta and M. Ziółek, Determination of Interfacial Charge-Transfer Rate Constants in Perovskite Solar Cells, *ChemSusChem*, 2016, **9**, 1647–1659.

30 W. Tress, M. Yavari, K. Domanski, P. Yadav, B. Niesen, J. P. Correa Baena, A. Hagfeldt and M. Graetzel, Interpretation and evolution of open-circuit voltage, recombination, ideality factor and subgap defect states during reversible light-soaking and irreversible degradation of perovskite solar cells, *Energy Environ. Sci.*, 2018, **11**, 151–165.

31 Y. Yang, M. Yang, D. T. Moore, Y. Yan, E. M. Miller, K. Zhu and M. C. Beard, Top and bottom surfaces limit carrier lifetime in lead iodide perovskite films, *Nat. Energy*, 2017, **2**, 16207.

32 W. Nie, H. Tsai, R. Asadpour, J.-C. Blancon, A. J. Neukirch, G. Gupta, J. J. Crochet, M. Chhowalla, S. Tretiak and M. A. Alam, High-efficiency solution-processed perovskite solar cells with millimeter-scale grains, *Science*, 2015, **347**, 522–525.

33 D. Li, S. A. Bretschneider, V. W. Bergmann, I. M. Hermes, J. Mars, A. Klasen, H. Lu, W. Tremel, M. Mezger and H.-J. Butt, Humidity-induced grain boundaries in MAPbI3 perovskite films, *J. Phys. Chem. C*, 2016, **120**, 6363–6368.

34 W. Tress, Perovskite Solar Cells on the Way to Their Radiative Efficiency Limit - Insights Into a Success Story of High Open-Circuit Voltage and Low Recombination, *Adv. Energy Mater.*, 2017, **7**, 1602358.

35 E. Guillén, F. J. Ramos, J. A. Anta and S. Ahmad, Elucidating Transport-Recombination Mechanisms in Perovskite Solar Cells by Small-Perturbation Techniques, *J. Phys. Chem. C*, 2014, **118**, 22913–22922.

Chapter 7

Impact of Moisture on Efficiency-Determining Electronic Processes in Perovskite Solar cells

In this Chapter, moisture-induced degradation of perovskite solar cells is thoroughly investigated by structural (SEM, EDS, XRD and XPS) and device characterization (impedance and intensity modulated photocurrent spectroscopies) techniques. Both the influence of the perovskite composition and the nature of the hole selective material is analysed. For a fixed degradation degree, all configurations show similar features in the small-perturbation analysis. A new mid-frequency signal appears in the impedance response, which seems to be related to charge accumulation at the interfaces. In addition, faster recombination, with a more important surface contribution, and slower transport is clearly inferred from our results. Both features can be associated with the deterioration of the contacts and the formation of a higher number of grain boundaries.

This chapter is based on Publication 3 of this Thesis: Salado *et. al.* J. Mater. Chem. A, 2017, 5, 10917–10927.

7.1 Introduction

As it has been mentioned several times in this Thesis, hybrid organic-inorganic halide perovskite solar cells have arisen as an efficiency and low-cost PV technology owing to their excellent optoelectronic properties.[1–5] However, in spite of great improvement of efficiency in last few years, the lack of a long-term stability restricts its outdoor photovoltaic applications[6] and, consequently, its commercialization.

It is well-known that the stability of perovskite solar cells and therefore their photovoltaic performance are intimately associated to the degradation of the perovskite layer. As it was previously indicated (see *Chapter* 2), the main causes behind perovskite degradation are related to different environmental factors,[7–9] such as moisture, temperature, oxygen and UV light, which could give rise to different degradation pathways. Niu *et al.* suggested that the perovskite degradation starts with the deprotonation of the methylammonium cation by water to produce methylamine, hydrogen iodide and lead iodide.[10] Yang *et al.* proposed the formation of colorless hydrated $(CH_3NH_3)_4PbI_6{\cdot}2H_2O$ as a result of perovskite hydration and the formation of lead iodide as final product.[11] On the other hand, Haque *et al.* described the perovskite degradation by the coupled effect of molecular oxygen and light suggesting that reactive oxygen species and the organic cation of perovskite react among themselves.[12] In any case, many approaches have been developed in order to prevent the perovskite degradation and guarantee the device stability. Among them stand out the effective passivation of devices by the use of hydrophobic polymers layers, the employment of photopolymerized fluorinated coatings, hydrophobic hole-selective materials, hydrophobic carbon electrodes and a thin blocking layer between perovskite and electron-selective layers.[13–19]

However, the impact of these environmental factors on perovskite degradation kinetics depends on other intrinsic properties such as thermal and electrical stability, which is determined by the perovskite composition. Therefore, special attention has been paid to the perovskite composition in order to achieve a more stable crystal structure and guarantee a long-term stability by the entire or partial inclusion of different ions with different sizes into the three-dimensional network. For instance, the beneficial effect in terms of stability of a partial insertion of bromine into the perovskite structure was reported.[20,21] Similar results were found for the inclusion of chloride.[22] In the both cases, the smaller ionic radii of Br^- and Cl^- with respect to I^- leads to a more compact structure in which the organic cations are less exposed. More recently, Petrus and coworkers reported the impact of the excess of PbI_2 as precursor on perovskite stability against moisture exposure.[23] In relation to the organic cations, *tolerance factor t* (Eq. 1.1 in *Chapter* 1) values of 0.88 and 0.83 were found for perovskites containing MA and FA, respectively.[24] The higher thermal stability found for $FAPbI_3$ was associated with the more-stable cubic crystal phase with respect to the tetragonal one attributed to $MAPbI_3$, which could be related to the different interaction of these cations with the inorganic matrix.[25,26] Similar results were found by Snaith *et al.* when they compared $CsPbI_2Br$ and $MAPbI_2Br$ and demonstrated the stability of the former owing to the appropriate ionic radii of Cs^+.[27] Triple and quadruple organic cation perovskites (MA, FA,Cs and Rb) as well as the incorporation of a large organic cation as guanidinium into the $MAPbI_3$ crystal structure have also been investigated to improve the stability of devices.[28–30]

Up to the date, previous studies related to the perovskite stability have mainly investigated the different perovskite degradation mechanisms under environmental factors or different approaches to prevent the perovskite degradation. SEM and STEM (scanning transmission electron microscope) images, EDS mapping, UV-Vis absorbance, XRD diffraction patterns, Raman and IR spectroscopy techniques were commonly used to characterize the extent of perovskite degradation and its kinetics. However, in this thesis, small-perturbation optoelectronic techniques have been used to investigate the impact of moisture on the electronic processes that determine the photovoltaic performance. It is important to better assess how the perovskite improvements investigated in the literature really affect the functioning of the device in terms of stability and efficiency. In order to correlate the moisture effect to this, we have analysed the charge transport and recombination processes using impedance spectroscopy and intensity-modulated photocurrent spectroscopy. In this *Chapter,* we have investigated both the influence of the perovskite composition ($MAPbI_3$ = *MAI* and $Cs_{0.05}FA_{0.81}$ $MA_{0.14}PbI_{0.85}$ $Br_{0.15}$ = *MIX*) and the influence of the hole selective material (spiro-OMeTAD and P3HT) on the device stability. For simplicity we will use the following notation to refer to the different device configurations studied: *MAI/Spiro*, *MAI/P3HT*, *MIX/Spiro* and *MIX/P3HT*.

7.2 Fabrication and characterization of devices

Fabrication of perovskite solar cells

Perovskite devices with mesoporous regular architecture were fabricated following the methodology described in *Chapter* 3. First of all, FTO TEC15 were cleaned following the solvent sequence: Hellmanex solution; Deionized water; Ethanol; Isopropanol. Then, TiO_2 compact layer was deposited by spray pyrolysis. After that, a mesoporous layer of TiO_2 was deposited on top of a TiO_2 compact layer. Then pure methyl ammonium ($MAPbI_3$) and mixed cation perovskite ($Cs_{0.05}FA_{0.81}$ $MA_{0.14}PbI_{0.85}$ $Br_{0.15}$) were deposited as active layer inside a glove box (Fig. A-7.1). For that, perovskite precursor solution of 1.2 M for $MAPbI_3$ and 1.4 M for a mixed cation perovskite were used. The thickness obtained for the different perovskite compositions are shown in Table 3.4. After perovskite deposition, spiro-OMeTAD or P3HT solution was spin coated. Finally, 80 nm of gold was deposited by thermal evaporation. (See *Chapter* 3 for details)

Characterization of devices

The devices were characterized using current-voltage characteristics by two different light sources: (1) a solar simulator (ABET-Sun2000) (2) a white light emitting diode (LED, LUXEON). The illumination for the different IS measurements was provided by white, red ($\lambda = 635$ nm) and blue ($\lambda = 465$ nm) LEDs and over a wide range of DC light intensities. This allows for probing the devices at different positions of the Fermi level in the semiconductor and for different optical generation profiles.[31] IS measurements were performed at the open circuit potential. A 20 mV perturbation in the 10^6-10^{-2} Hz range was utilized to obtain the spectra. IMPS measurements were performed at short-circuit in the 10^6 to 10^{-2} Hz range. To avoid any additional degradation process related to the moisture, the measurements were carried out under N_2-atmosphere. For the structural characterization, perovskite films were prepared by spin coating onto Si wafers. SEM images of the samples were obtained. Electron Backscatter Diffraction (EBSD) images were obtained using NordlysMax3 detector (Oxford Instruments). Energy Dispersive Spectroscopy (EDS) was performed using a Silicon Drift Detector (Oxford Instruments). X-ray diffractograms were recorded on a Rigaku diffractometer using CuKα source. The measurements were performed at grazing angle geometry. The samples were mounted without any further modification and the divergence slit were adjusted to the dimension of the films. The scan range of 10°- 60° was selected with an acquisition time of 3 degree/min. A baseline correction was applied to the diffractograms to compensate for the noise arising from the substrate. XPS characterization was performed in a Phoibos 100 DLD X-ray spectrometer from SPECS. The spectra were collected in the pass energy constant mode at a value of 50 eV for the general spectra and 30 eV for the different peaks using a Mg Kα source. C1s signal at 284.5 eV was utilized for calibration of the binding energy in the spectra. Static water contact angle (WCA) measurements were provided by a Data Physics setup by depositing bidistilled water drops of 1μL. The given values correspond to a statistics over 10 values. The WCAs were evaluated for pinning droplets several seconds after the contact with the surfaces.

7.3 Results and discussion

PCEs in the range 12-16 % were obtained under standard conditions (1 sun - AM 1.5 illumination) for the different devices configurations (Fig. A-7.2 in appendix E). Current-Voltage characteristics of the different PSCs were measured in reverse scan at a scan rate of 100 mV/s. In particular, average efficiencies of 15.3 %, 13.2 %, 13 % and 12.5 % were obtained for MAI/Spiro, MAI/P3HT, MIX/Spiro and MIX/P3HT devices, respectively (Table A-7.1 in appendix E). In line with the literature and the results of *Chapter* 5,[32–34] these results highlight the impact of the perovskite composition and the material used as HTM on the photovoltaic performance. For both perovskite compositions, better efficiencies were obtained when Spiro was used as HTM with respect to P3HT as a result of the higher V_{OC}. Additionally, in spite of showing similar J_{SC} and V_{OC} for the both HTM, worse efficiencies were obtained for MIX devices due to its lower fill factor. These different devices will be used for the following discussion.

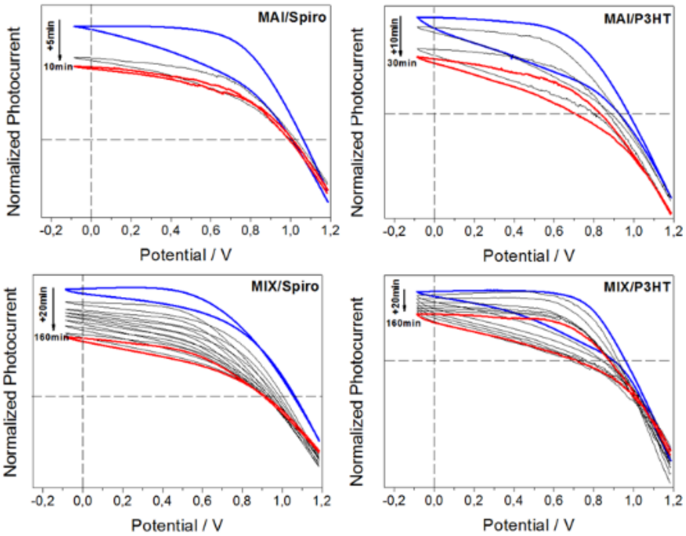

Figure 7.1. Normalized IV curves for the different PSCs (blue) before and (black, red) during the moisture exposure measured in the reverse scan and forward scan (cyclic voltammetry) under light intensity of 10 mW·cm^{-2} (white LED). The measurements were performed with a scan rate of 100 mV/s at room temperature.

In order to investigate the impact of the moisture exposure on the device stability, the photovoltaic performance of the different PSCs were measured inside a hermetic chamber-holder with a constant flow of air with a RH > 90%. Figure 7.1 shows current-voltage characteristics of PSCs measured by cyclic voltammetry before and during the moisture exposure. The measurements were started with a reverse scan after a dwelling time of 10 s at 1.2 V, and were then continued with a forward scan.

As shown Figure 7.1, moisture exposure induces negatively effects in the photovoltaic performance of the different PSCs. Both V_{OC} and J_{SC} tend to decrease with respect to the moisture exposure time. In particular, an efficiency drop of 51 % and 19 % after 10 min for MAI based devices and 60 % and 42 % after 160 min for MIX-based devices were recorded when Spiro and P3HT were used as HTM, respectively. From these results, the following trend was extracted. Firstly, focusing on the impact of the perovskite composition, the degradation process was faster when MAI was employed as active layer in contrast to degradation rate found for MIX perovskite. The same result was found when Spiro as well as P3HT were used as HTM. As it has been previously reported, the longer device stability obtained for MIX samples was not only due to the partial inclusion of bromine anions,[20,21] but also to the combination of MA, FA and Cs cations.[28,31–35] This combination gives rise to a more thermally and structurally stable perovskite. And secondly, in relation to the nature of the HTM, Spiro-based devices are significantly less stable than those with P3HT as HTM.

In order to cast light into the perovskite degradation kinetics obtained for the different PSCs, SEM was used to investigate the effect of moisture exposure on the device stability. Figure 7.2 shows SEM images obtained for bare perovskites and MAI/HTM films deposited on Si/cTiO$_2$/mTiO$_2$ before and after moisture exposure.

Before moisture exposure, both uncovered perovskites layers formed homogeneous and pinholes-free films, with larger grain size in the case of MIX perovskite (Fig. A-7.1). However, after moisture exposure remarkable morphological changes were observable in both cases as shown Figure 7.2. In the case of bare MAI layers, large perovskite crystals with well-defined faces appeared leading to extensive pin-holes after 1 hour under moisture exposure. For longer times (5 hours), larger structures with dendritic shape were formed. In contrast, as it was expected according to the literature,[20,21,28] no significant change was observed for MIX layers for at least 1 hour under moisture exposure. Nevertheless, after 5 hours of exposure, large perovskite crystals with reduced pin-holes around them were formed. The formation of these large perovskite structures seems to be related to the perovskite aggregation process (Fig. A-7.3). In contrast to a previous report,[36] EDS analysis showed the same Pb/I ratio for fresh and degraded samples.

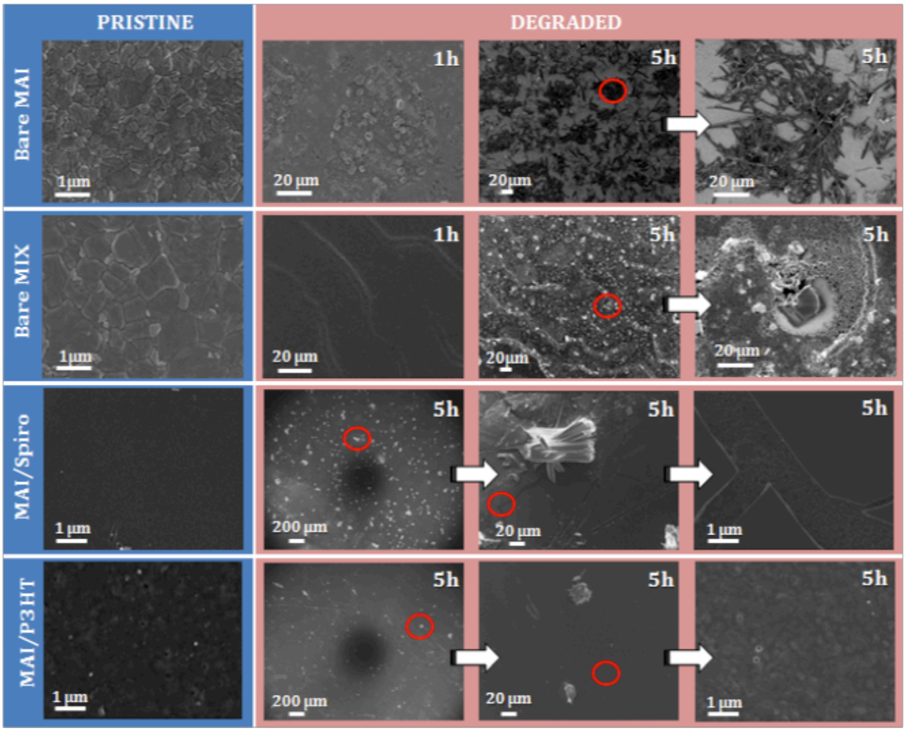

Figure 7.2: Plane-view scanning electron microscopy (SEM) images for the MAI, MIX, MAI/Spiro and MAI/P3HT layers after moisture exposure (RH= 90%) for 1 and 5h at room temperature**.**

To investigate the influence of the HTM on the device stability, MAI perovskite was used as active layer, as it is less stable. Longer moisture exposure times (5 hours) were used. Not significant changes appeared after only 1 hour as exposure time. As shown in Figure 7.2, as a result of the perovskite degradation, an increased number of emerging structures coming from the underlying perovskite layer appeared when Spiro was used as HTM. These new formed crystals are possible reason to the fracture of the Spiro layer. In contrast, after 5 hours under moisture exposure the P3HT layer appears unchanged. This behaviour can be ascribed to the hydrophobic character of P3HT layer,[18] which makes the penetration/percolation of water molecules towards the underlying perovskite layer more difficult. Similar behaviour was previously reported using UV-Vis and FTIR spectroscopy (Fourier-transform infrared spectroscopy).[11,37] The water contact angles (WCAs) for the different configurations were reported in Table A-7.2. WCAs >100° and <80° where found for perovskite/P3HT and perovskite/Spiro configurations, respectively. These results claim the hydrophobic and hydrophilic character of P3HT and Spiro layer, respectively. Therefore, it seems reasonable to assume that the short stability obtained for MAI/Spiro devices was connected to both the perovskite decomposition process, higher affinity to water and consequent degradation of the Spiro layer.

The presence of hydrophilic dopants in the Spiro is actually an additional source of instability.

Figure 7.3 shows XRD patterns of the two perovskites (MAI and MIX) with and without HTM (Spiro and P3HT) before and after moisture exposure. The characteristic diffraction peaks of tetragonal perovskite phase (14.1°, 28.5° and 31.9°)[23,38] were obtained for fresh samples, which remained at the same position when the samples were subjected to humidity (RH > 90%) exposure for 1 hour. As it was previously reported, any additional peak appears as a consequence of HTMs. Nevertheless, additional diffraction peaks previously related to the formation of hydrated perovskite complex and PbI_2 were found after moisture exposure at 10.5° and 12.7°, respectively.[23,38–40] Focusing on these two diffraction peaks, different behaviour can be observed depending on the perovskite composition and/or HTM. Firstly, for uncovered perovskite layers these two peaks were only observable for MAI perovskite after moisture exposure. And secondly, contrary to expectation, higher signal intensities for these two diffraction peaks were found for MAI/Spiro with respect to the uncovered MAI sample. Similar behaviour was found for MIX perovskite. In this case, the signal previously attributed to PbI_2 was only found for MIX/Spiro sample after moisture exposure, whereas it was not observed for bare MIX and MIX/P3HT samples.

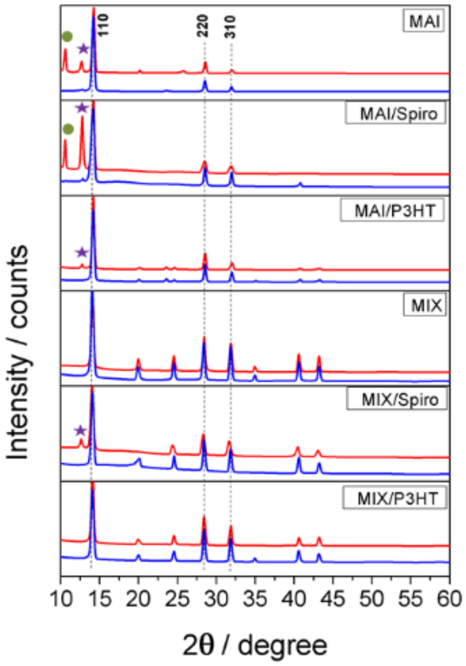

Figure 7.3. X-ray diffraction for the different (MAI and MIX) perovskite layers with and without the HTM (Spiro and P3HT) deposited on top (blue line) before and (red line) after moisture exposure for 1 hour. The positions of the XRD peaks for (purple star) PbI_2 and (green circle) hydrated complex are marked in the graphs.

Therefore, the rapid degradation kinetics found for MAI/Spiro samples (Fig. 7.1) could not only be related to the perovskite composition and/or the degradation provoked by the Spiro (Fig. 7.2), but also to a possible interfacial interaction of both layers.[41] We have further analysed the chemical composition of fresh and degraded devices by XPS. The comparison of the atomic percentages of different elements (Pb, I, O, C, N, S, F and Ti) in surface is shown in Table A-7.3. In line with Figure 7.2, part of the TiO_2 layer was revealed for uncovered MAI after moisture exposure as suggest the high Ti percentage. A decrease of the Pb/I ratio was found for both uncovered perovskite. However, the difference was higher for MAI perovskite. In particular, after moisture exposure the Pb/I ratio changed from 0.85 to 0.5 and 0.6 to 0.4 for uncovered MAI and MIX perovskite. Finally, after moisture exposure, a percentage below 1% of I only appears in Spiro-based devices, whereas it was not detected in P3HT-based devices. Considering these results, the following trend can be established to define device stability: MAI/Spiro < MAI/P3HT < MIX/Spiro < MIX/P3HT.

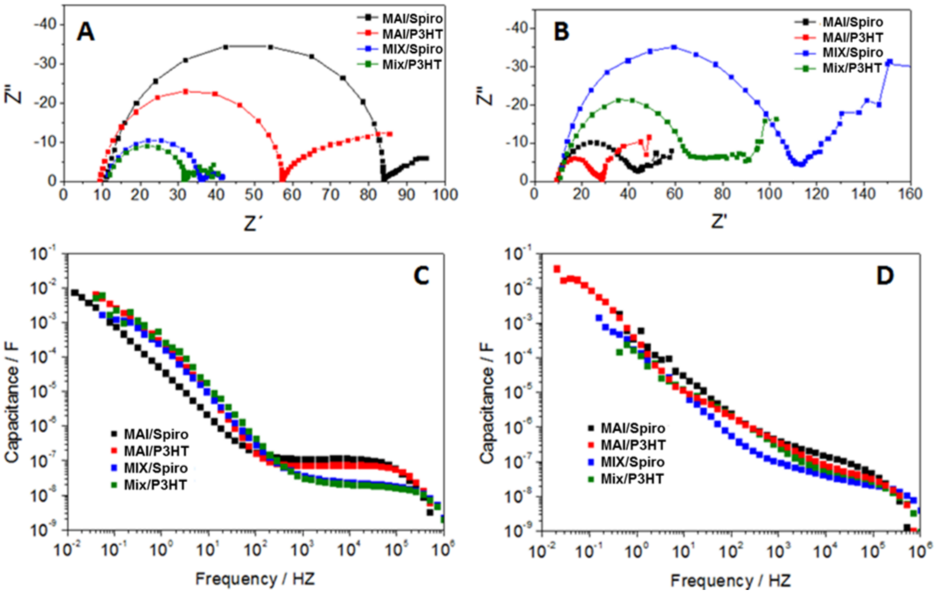

Figure 7.4. (A, B) Impedance spectra and (C, D) frequency-dependent apparent capacitance obtained at open-circuit condition and under white light illumination for (A, C) fresh and (B, D) degraded PSCs. The illumination intensity was fixed as such so the photopotential close to the 1-sun V_{OC} is generated (Table A-7.1).

Once the impact of the moisture exposure on the device stability has been assessed according to the perovskite composition and the material employed as HTM, we focus our attention on the electronic processes determining the photovoltaic performance. To study the effect of moisture exposure on the device performance, we analyse the impedance response in the form of Nyquist and frequency-dependent apparent capacitance plots (Fig. 7.4). At this point, it is important to remark that the different PSCs were subjected to different moisture exposure times bearing in mind the different degradation kinetics demonstrated above. Therefore, in order to safely isolate the effect of the degradation rate, a photocurrent drop of 50% was employed as criteria for the exposure time. After the moisture exposure, the PCSs were flushed with dry nitrogen for 1 hour before starting the characterization by impedance spectroscopy.

As shown in Figure 7.4A, the impedance spectra obtained for fresh PSCs were characterized by two signals. These two signals will only be well-detected when the peak maxima on impedance frequency plots are sufficiently well separated (Fig. A-7.4). As it was described in *Chapter* 3, the signal appearing at high frequencies, the closest one to the origin and the largest semicircle, has been attributed to electronic transport/recombination processes,[42–44] whereas the signal appearing at low frequencies has been related to ionic motion and charge accumulation at contacts.[45] These two signals exhibit significant changes in the impedance spectra after moisture exposure. In particular, a distortion of the *HF* semicircle was found for degraded PSCs (Fig. 7.4B). This behaviour seems to be more remarkable for degraded P3HT-based devices. This feature could explain the non-symmetric shape of the *HF* peak in the impedance frequency plots that was found for degraded PSCs (Fig. A-7.4). The non-symmetric shape suggests that the time constant of a process previously hidden under the *HF* semicircle after degradation becomes now resolved or, alternatively, the appearance of a new capacitive process. The general response of the frequency-dependent apparent capacitance for fresh and degraded devices is shown in Figure 7.4C and 7.4D, respectively. According to the literature,[46–49] each plateau is related to a certain specific polarization process (see *Chapter* 3). In accordance to the different thicknesses of the perovskite layers (d) (Fig. A-7.5) and the expression for the bulk capacitance $C = A\varepsilon/d$, higher *HF* capacitance values were found for MAI-based devices. Focusing on the effect of the moisture exposure, although the capacitance values observed for *HF* and *LF* plateaus are in the same range ($\approx 10^{-7}$ F/cm^{-2} and $\approx 10^{-2}$ F/cm^{-2}, respectively) for fresh and degraded devices, the fact is that a new polarization process in the range of $\approx 10^{-6}$ - 10^{-5} F/cm^{-2} was found at mid frequencies after moisture exposure. This effect seems to be more pronounced for P3HT-based devices.

A similar behaviour has been previously reported for PSCs with less efficient external contacts. In particular, impedance spectra and frequency-dependent capacitance plots were characterized by the presence of an additional *MF* component when TiO_2 and Nb_2O_5 were employed as electron selective layer in aged devices.[46] Guerrero and coworkers assigned this characteristic feature with the charge accumulation at the ESL/perovskite interface due to the low charge extraction efficiency of these selective contacts. Additionally, an interfacial recombination enhancement was suggested as a consequence of this charge accumulation process. Nevertheless, it should be considered that this charge separation/extraction process is not only determined by the ESL but also by the perovskite itself and the material used as HTM. As reported, the interfacial interactions between the selective contacts and the perovskite layer affect the energetic barriers that determine the charge separation/extraction processes.[47,52–55] Considering the devices are characterized by the same ESL, the *MF* component could be associated with an interfacial charge accumulation process. This accumulation is produced by the perovskite composition and material employed as HSL which can not only determine the charge extraction at the ESL/perovskite interface, but also at the perovskite/HTM interface. This interpretation could explain the difference found for Spiro and P3HT-based devices (Fig. 7.4 and Fig. A-7.4).

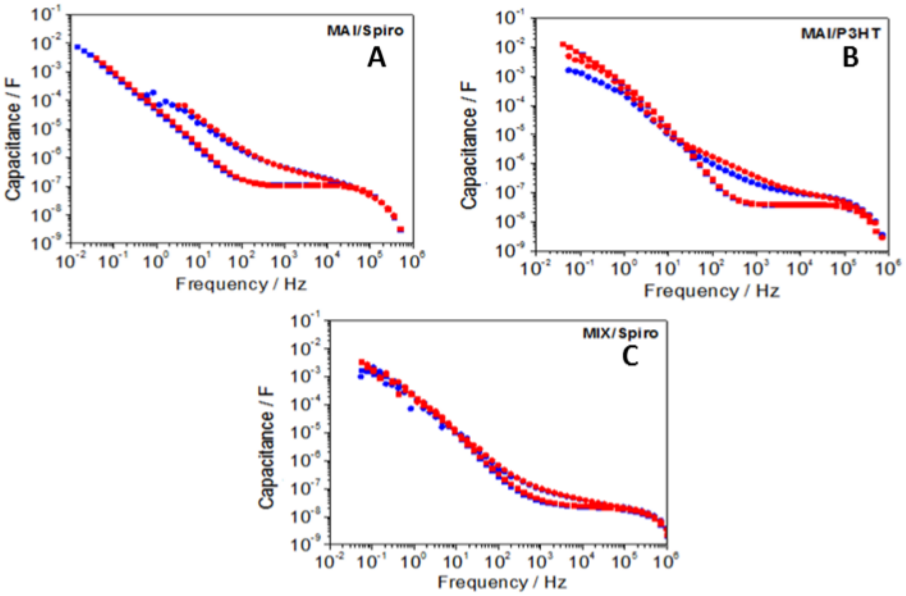

Figure 7.5. Frequency-dependent apparent capacitance obtained at open-circuit condition and under illumination for (squares) fresh and (circles) degraded MAI/Spiro, MAI/P3HT and MIX/Spiro devices using the two excitation wavelengths of (blue) λ_{blue} = 465 nm and (red) λ_{red} = 635 nm.

To cast light into the origin of this new feature appearing at mid frequencies after moisture exposure, impedance spectroscopy was measured using two different illumination wavelengths (blue and red illumination) to modify the charge generation profile inside the perovskite layer like we did in *Chapter* 5 and 6. From that, a higher concentration of photogenerated charge would be expected at the ESL/perovskite interface than at the perovskite/HTM one under blue illumination. In contrast, the profile of photogenerated charge is more uniform under red illumination.[31,56] Figure 7.5 shows the apparent capacitance-frequency response under blue and red illumination for MAI/Spiro, MAI/P3HT and MIX/Spiro devices before and after moisture exposure.

In line with Figures 7.4C and 7.4D, the apparent capacitance-frequency response obtained under blue and red illumination was characterized by the presence of a characteristic polarization process appearing at mid frequencies (10^4–10^2 Hz) which overlaps with the *HF* plateau (bulk capacitance) after moisture exposure. For fresh devices the apparent capacitance-frequency response was not affected by electron-hole generation profile produced as a result of the different optical excitation wavelengths employed during the impedance spectroscopy.

A similar behaviour was found for degraded MAI/Spiro and MIX/Spiro devices. In contrast, a significant difference was found at mid frequencies for degraded MAI/P3HT devices when the electron-hole generation profile was modified. In particular, higher *MF* capacitance values were found when the availability of the photogenerated charges was higher at the perovskite/HTM interface (red illumination) with respect to when charge was photogenerated preferentially in the vicinity of the ESL (blue illumination). This behaviour is also brought to light in the Nyquist plots by the presence of the *MF* semicircle for degraded MAI/P3HT devices under red illumination (Fig. A-7.6). Therefore, a more important interfacial charge accumulation process seems to take place after moisture exposure when P3HT was used as HTM and consequently, a poorer hole extraction is expected at the perovskite/P3HT interface with respect to perovskite/Spiro. This possible interpretation could not only explain the distorted *HF* semicircle and/or the apparent *MF* semicircle found in Nyquist plot of impedance response for degraded devices, respectively (Fig. 7.4B and Fig. A-7.6), but also the more remarkable *MF* capacitive process observed for P3HT-based devices (Fig. 7.4D). On the other hand, as mentioned above, the energetic barriers that determine the charge extraction/separation also depends on the perovskite material. As shown in Figure 7.5C, when the Spiro was used as HTM the capacitance-frequency response obtained under blue and red illumination shows the same behaviour before and after moisture exposure. Similar results were found for MAI/Spiro devices (Fig. 7.5A). Nevertheless, this *MF* capacitive signal seems to be less visible after moisture exposure which suggest a better electron and hole extraction in both interfaces even after moisture exposure. This robustness of the electronic properties of the Spiro contact explains the normally better photocurrents obtained in devices when such material was used.

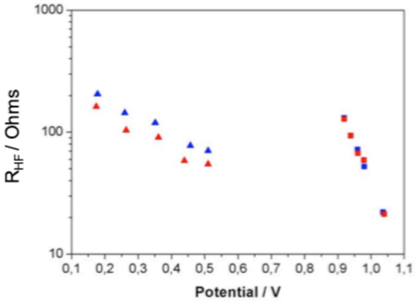

Figure 7.6. Recombination (*HF*) resistance versus open-circuit potential as extracted from fittings of the impedance spectra using the two excitation wavelengths of (blue) λ_{blue} = 465 nm and (red) λ_{red} = 635 nm for (squares) fresh and (triangles) degraded MAI/Spiro device.

In order to understand the differences found in the Nyquist plot of impedance spectra under different optical excitation wavelengths for degraded devices (Fig. A-7.6), the *HF* signal was investigated. Figure 7.6 shows the *HF* resistance (R_{HF}) extracted by fitting the impedance response under blue and red illumination for fresh and degraded MAI/Spiro devices to simple *Voight* equivalent circuit (see inset Fig. 3.9A in *Chapter* 3).[57] To be sure about the fitting, the time constant (τ) were estimated from Eq. 3.22; and Eq. 3.23 (*Chapter* 3). The same behaviour was obtained for both fresh and degraded devices (Fig. A-7.7).

Specifically, the R_{HF} shows the same behaviour for fresh devices regardless of the electron-hole generation profile. In contrast, a minor difference was found after moisture exposure when the optical excitation wavelength was changed. For degraded devices, lower values of R_{HF} were found when the red illumination was used as optical excitation. In other words, the photogenerated charge at the perovskite/HTM interface seems to recombine more strongly than the photogenerated charge at the ESL/perovskite interface for a degraded device. On the other hand, a remarkable change of the slope (β-parameter) of the R_{HF} for both optical excitations was observed with respect to fresh devices. Similar results were obtained for the different devices when a white LED was employed as illumination source before and after moisture exposure (Fig. A-7.8). This observation suggests that the charge that has been mainly photogenerated at the ESL/perovskite and perovskite/HTM interface are subjected to different recombination mechanisms after moisture exposure. As it was observed in previous *Chapters,*[31,58] the results obtained for fresh devices suggest that the main recombination process is mediated via a trap-limited mechanism in the bulk of the perovskite.[59–63] However, surface recombination could be more important as a consequence of perovskite degradation by moisture.[38,64,65] Therefore, the increase of this surface-mediated recombination seems to be intimately related to the larger interfacial charge accumulation described (Fig. 7.5). Similar results were expected for the rest of devices studied in this *Chapter* as revealed by Nyquist and impedance frequency plots obtained under both optical excitations showing the same behaviour (Fig. A-7.6 and Fig. A-7.9, respectively).

This interpretation seems to be in line with the conclusions previously reported by A. Leguy *et al.*[38] In particular, they related the efficiency drop after moisture exposure to the isolation of the perovskite grains which would reduce the charge transport leading to an increased recombination at the grain interfaces. In other words, the grain insulating effect could limit the charge transport and improve the charge recombination giving rise to a shorter charge diffusion lengths.[64,65] In order to consolidate this assumption, IMPS was measured to provide information about the different charge transport processes.

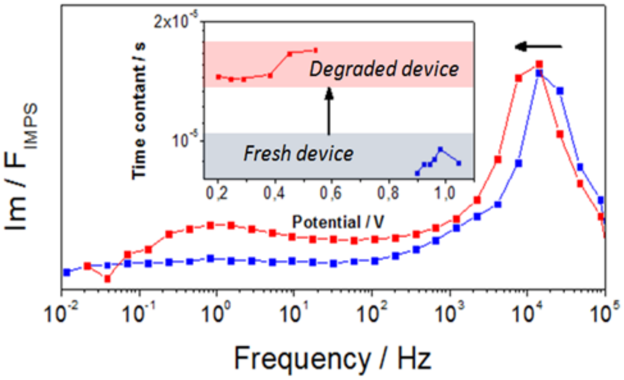

Figure 7.7. IMPS frequency plot of the imaginary part for MAI/Spiro device (blue) before and (red) after moisture exposure obtained under white illumination.

As shown in Figure 7.7, IMPS frequency plot shows two well differentiated peaks with respect to the frequency scale which have been previously related to different charge transport processes characterized by different time constants.[45,66,67] As it was indicated in *Chapter* 3, the *HF* peak (≈10^4 Hz) can be associated with the electron transport inside the perovskite layer, whereas the *LF* peak (≈1 Hz) was attributed to ionic motion. In addition, a peak at mid frequencies was also found and related to the electron transport process in the mesoporous TiO_2 matrix.[45,67] Nevertheless, this *MF* peak was not resolved in our case (Fig. 7.7). Considering the *HF* peak only, a lower charge diffusion coefficient (D_n) is expected for degraded devices, since the *HF* peak appears at lower frequencies (D_n was extracted from Eq. 4.3 in *Chapter* 4).[68] A smaller diffusion coefficient gives rise to shorter charge diffusion lengths, in line with the faster recombination observed in the degraded samples.

7.4 Conclusion

We have investigated the effect of the moisture-induced degradation of perovskite solar cells using a combination of structural characterization (SEM, EDS, XRD and XPS) and small-perturbation optoelectronic (impedance and intensity modulated photocurrent spectroscopies) techniques. We studied the influence of the perovskite composition and HTM employed on the device stability. In particular, our results reveal a lower degradation rate for perovskite solar cells based on ($Cs_{0.05}FA_{0.81}$ $MA_{0.14}PbI_{0.85}$ $Br_{0.15}$) as active layer and P3HT as HTM. On the other hand, the effect of the moisture-induced degradation on the electronic processes that determine the photovoltaic performance in perovskite solar cell was also investigated. Regardless of the device configuration, the charge recombination is governed by the bulk of the perovskite layer via a trap-limited mechanism. However, the moisture-induced degradation modifies the charge recombination mechanism. The additional mid-frequency component recorded in both Nyquist and frequency plots after moisture exposure suggests an interfacial charge accumulation. This charge accumulation process can accelerate the charge recombination rate due to a greater contribution of a surface-mediated recombination route. As a consequence of the moisture-induced degradation, a slower electron transport in perovskite layers was also observed, which can be traced back to the formation of more grain boundaries.

7.5 References

1 G. Xing, N. Mathews, S. Sun, S. S. Lim, Y. M. Lam, M. Gratzel, S. Mhaisalkar and T. C. Sum, Long-Range Balanced Electron- and Hole-Transport Lengths in Organic-Inorganic CH3NH3PbI3, *Science*, 2013, **342**, 344–347.

2 S. D. Stranks, G. E. Eperon, G. Grancini, C. Menelaou, M. J. P. Alcocer, T. Leijtens, L. M. Herz, A. Petrozza and H. J. Snaith, Electron-Hole Diffusion Lengths Exceeding 1 Micrometer in an Organometal Trihalide Perovskite Absorber, *Science*, 2013, **342**, 341–344.

3 W. Tress, N. Marinova, O. Inganäs, M. K. Nazeeruddin, S. M. Zakeeruddin and M. Graetzel, Predicting the Open-Circuit Voltage of CH $_3$ NH $_3$ PbI $_3$ Perovskite Solar Cells Using Electroluminescence and Photovoltaic Quantum Efficiency Spectra: the Role of Radiative and Non-Radiative Recombination, *Adv. Energy Mater.*, 2015, **5**, 1400812.

4 N. Pellet, P. Gao, G. Gregori, T.-Y. Yang, M. K. Nazeeruddin, J. Maier and M. Grätzel, Mixed-Organic-Cation Perovskite Photovoltaics for Enhanced Solar-Light Harvesting, *Angew. Chem. Int. Ed.*, 2014, **53**, 3151–3157.

5 Y. Ogomi, A. Morita, S. Tsukamoto, T. Saitho, N. Fujikawa, Q. Shen, T. Toyoda, K. Yoshino, S. S. Pandey, T. Ma and S. Hayase, CH $_3$ NH $_3$ Sn $_x$ Pb $_{(1-x)}$ I $_3$ Perovskite Solar Cells Covering up to 1060 nm, *J. Phys. Chem. Lett.*, 2014, **5**, 1004–1011.

6 Y. Reyna, M. Salado, S. Kazim, A. Pérez-Tomas, S. Ahmad and M. Lira-Cantu, Performance and stability of mixed FAPbI 3(0.85) MAPbBr 3(0.15) halide perovskite solar cells under outdoor conditions and the effect of low light irradiation, *Nano Energy*, 2016, **30**, 570–579.

7 B. Li, Y. Li, C. Zheng, D. Gao and W. Huang, Advancements in the stability of perovskite solar cells: degradation mechanisms and improvement approaches, *RSC Adv.*, 2016, **6**, 38079–38091.

8 Z. Wang, Z. Shi, T. Li, Y. Chen and W. Huang, Stability of Perovskite Solar Cells: A Prospective on the Substitution of the A Cation and X Anion, *Angew. Chem. Int. Ed.*, 2017, **56**, 1190–1212.

9 T. A. Berhe, W.-N. Su, C.-H. Chen, C.-J. Pan, J.-H. Cheng, H.-M. Chen, M.-C. Tsai, L.-Y. Chen, A. A. Dubale and B.-J. Hwang, Organometal halide perovskite solar cells: degradation and stability, *Energy Environ. Sci.*, 2016, **9**, 323–356.

10 G. Niu, W. Li, F. Meng, L. Wang, H. Dong and Y. Qiu, Study on the stability of CH $_3$ NH $_3$ PbI $_3$ films and the effect of post-modification by aluminum oxide in all-solid-state hybrid solar cells, *J Mater Chem A*, 2014, **2**, 705–710.

11 J. Yang, B. D. Siempelkamp, D. Liu and T. L. Kelly, Investigation of

$CH_3NH_3PbI_3$ Degradation Rates and Mechanisms in Controlled Humidity Environments Using *in Situ* Techniques, *ACS Nano*, 2015, **9**, 1955–1963.

12 D. Bryant, N. Aristidou, S. Pont, I. Sanchez-Molina, T. Chotchunangatchaval, S. Wheeler, J. R. Durrant and S. A. Haque, Light and oxygen induced degradation limits the operational stability of methylammonium lead triiodide perovskite solar cells, *Energy Environ. Sci.*, 2016, **9**, 1655–1660.

13 S. M. Kang, N. Ahn, J.-W. Lee, M. Choi and N.-G. Park, Water-repellent perovskite solar cell, *J Mater Chem A*, 2014, **2**, 20017–20021.

14 S. Guarnera, A. Abate, W. Zhang, J. M. Foster, G. Richardson, A. Petrozza and H. J. Snaith, Improving the Long-Term Stability of Perovskite Solar Cells with a Porous Al_2O_3 Buffer Layer, *J. Phys. Chem. Lett.*, 2015, **6**, 432–437.

15 L. Zheng, Y.-H. Chung, Y. Ma, L. Zhang, L. Xiao, Z. Chen, S. Wang, B. Qu and Q. Gong, A hydrophobic hole transporting oligothiophene for planar perovskite solar cells with improved stability, *Chem Commun*, 2014, **50**, 11196–11199.

16 I. Hwang, I. Jeong, J. Lee, M. J. Ko and K. Yong, Enhancing Stability of Perovskite Solar Cells to Moisture by the Facile Hydrophobic Passivation, *ACS Appl. Mater. Interfaces*, 2015, **7**, 17330–17336.

17 F. Bella, G. Griffini, J.-P. Correa-Baena, G. Saracco, M. Gratzel, A. Hagfeldt, S. Turri and C. Gerbaldi, Improving efficiency and stability of perovskite solar cells with photocurable fluoropolymers, *Science*, 2016, **354**, 203–206.

18 Y. S. Kwon, J. Lim, H.-J. Yun, Y.-H. Kim and T. Park, A diketopyrrolopyrrole-containing hole transporting conjugated polymer for use in efficient stable organic–inorganic hybrid solar cells based on a perovskite, *Energy Environ. Sci.*, 2014, **7**, 1454.

19 M. Salado, F. J. Ramos, V. M. Manzanares, P. Gao, M. K. Nazeeruddin, P. J. Dyson and S. Ahmad, Extending the Lifetime of Perovskite Solar Cells using a Perfluorinated Dopant, *ChemSusChem*, 2016, **9**, 2708–2714.

20 J. H. Noh, S. H. Im, J. H. Heo, T. N. Mandal and S. I. Seok, Chemical Management for Colorful, Efficient, and Stable Inorganic–Organic Hybrid Nanostructured Solar Cells, *Nano Lett.*, 2013, **13**, 1764–1769.

21 R. K. Misra, S. Aharon, B. Li, D. Mogilyansky, I. Visoly-Fisher, L. Etgar and E. A. Katz, Temperature- and Component-Dependent Degradation of Perovskite Photovoltaic Materials under Concentrated Sunlight, *J. Phys. Chem. Lett.*, 2015, **6**, 326–330.

22 A. Poglitsch and D. Weber, Dynamic disorder in

methylammoniumtrihalogenoplumbates (II) observed by millimeter-wave spectroscopy, *J. Chem. Phys.*, 1987, **87**, 6373–6378.

23 M. L. Petrus, Y. Hu, D. Moia, P. Calado, A. M. A. Leguy, P. R. F. Barnes and P. Docampo, The Influence of Water Vapor on the Stability and Processing of Hybrid Perovskite Solar Cells Made from Non-Stoichiometric Precursor Mixtures, *ChemSusChem*, 2016, **9**, 2699–2707.

24 Y. Zhao and K. Zhu, Organic–inorganic hybrid lead halide perovskites for optoelectronic and electronic applications, *Chem. Soc. Rev.*, 2016, **45**, 655–689.

25 A. Amat, E. Mosconi, E. Ronca, C. Quarti, P. Umari, M. K. Nazeeruddin, M. Grätzel and F. De Angelis, Cation-Induced Band-Gap Tuning in Organohalide Perovskites: Interplay of Spin–Orbit Coupling and Octahedra Tilting, *Nano Lett.*, 2014, **14**, 3608–3616.

26 F. Shojaei and W.-J. Yin, Stability Trend of Tilted Perovskites, *J. Phys. Chem. C*, 2018, **122**, 15214–15219.

27 R. J. Sutton, G. E. Eperon, L. Miranda, E. S. Parrott, B. A. Kamino, J. B. Patel, M. T. Hörantner, M. B. Johnston, A. A. Haghighirad, D. T. Moore and H. J. Snaith, Bandgap-Tunable Cesium Lead Halide Perovskites with High Thermal Stability for Efficient Solar Cells, *Adv. Energy Mater.*, **6**, 1502458.

28 M. Saliba, T. Matsui, J.-Y. Seo, K. Domanski, J.-P. Correa-Baena, M. K. Nazeeruddin, S. M. Zakeeruddin, W. Tress, A. Abate, A. Hagfeldt and M. Grätzel, Cesium-containing triple cation perovskite solar cells: improved stability, reproducibility and high efficiency, *Energy Environ. Sci.*, 2016, **9**, 1989–1997.

29 M. Saliba, T. Matsui, K. Domanski, J.-Y. Seo, A. Ummadisingu, S. M. Zakeeruddin, J.-P. Correa-Baena, W. R. Tress, A. Abate, A. Hagfeldt and M. Gratzel, Incorporation of rubidium cations into perovskite solar cells improves photovoltaic performance, *Science*, 2016, **354**, 206–209.

30 A. D. Jodlowski, C. Roldán-Carmona, G. Grancini, M. Salado, M. Ralaiarisoa, S. Ahmad, N. Koch, L. Camacho, G. de Miguel and M. K. Nazeeruddin, Large guanidinium cation mixed with methylammonium in lead iodide perovskites for 19% efficient solar cells, *Nat. Energy*, 2017, **2**, 972–979.

31 L. Contreras-Bernal, M. Salado, A. Todinova, L. Calio, A. Shahzada, J. Idígoras and J. A. Anta, Origin and Whereabouts of Recombination in Perovskite Solar Cells, *J. Phys. Chem. C*.

32 D. Bi, L. Yang, G. Boschloo, A. Hagfeldt and E. M. J. Johansson, Effect of Different Hole Transport Materials on Recombination in CH $_3$ NH $_3$ PbI $_3$ Perovskite-Sensitized Mesoscopic Solar Cells, *J. Phys. Chem. Lett.*, 2013, **4**, 1532–1536.

33 N. J. Jeon, J. H. Noh, W. S. Yang, Y. C. Kim, S. Ryu, J. Seo and S. I. Seok, Compositional engineering of perovskite materials for high-performance solar cells, *Nature*, 2015, **517**, 476–480.

34 M. Salado, J. Idigoras, L. Calio, S. Kazim, M. K. Nazeeruddin, J. A. Anta and S. Ahmad, Interface Play between Perovskite and Hole Selective Layer on the Performance and Stability of Perovskite Solar Cells, *ACS Appl. Mater. Interfaces*, 2016, **8**, 34414–34421.

35 M. Deepa, M. Salado, L. Calio, S. Kazim, S. M. Shivaprasad and S. Ahmad, Cesium power: low Cs levels impart stability to perovskite solar cells, *Phys. Chem. Chem. Phys.*, 2017, **19**, 4069–4077.

36 N. Aristidou, I. Sanchez-Molina, T. Chotchuangchutchaval, M. Brown, L. Martinez, T. Rath and S. A. Haque, The Role of Oxygen in the Degradation of Methylammonium Lead Trihalide Perovskite Photoactive Layers, *Angew. Chem. Int. Ed.*, 2015, **54**, 8208–8212.

37 J. Idígoras, A. Todinova, J. R. Sánchez-Valencia, A. Barranco, A. Borrás and J. A. Anta, The interaction between hybrid organic–inorganic halide perovskite and selective contacts in perovskite solar cells: an infrared spectroscopy study, *Phys. Chem. Chem. Phys.*, 2016, **18**, 13583–13590.

38 A. M. A. Leguy, Y. Hu, M. Campoy-Quiles, M. I. Alonso, O. J. Weber, P. Azarhoosh, M. van Schilfgaarde, M. T. Weller, T. Bein, J. Nelson, P. Docampo and P. R. F. Barnes, Reversible Hydration of $CH_3NH_3PbI_3$ in Films, Single Crystals, and Solar Cells, *Chem. Mater.*, 2015, **27**, 3397–3407.

39 X. Guo, C. McCleese, C. Kolodziej, A. C. S. Samia, Y. Zhao and C. Burda, Identification and characterization of the intermediate phase in hybrid organic–inorganic $MAPbI_3$ perovskite, *Dalton Trans.*, 2016, **45**, 3806–3813.

40 X. Guo, C. McCleese, W.-C. Lin and C. Burda, Curing of degraded MAPbI perovskite films, *RSC Adv.*, 2016, **6**, 60620–60625.

41 J. Carrillo, A. Guerrero, S. Rahimnejad, O. Almora, I. Zarazua, E. Mas-Marza, J. Bisquert and G. Garcia-Belmonte, Ionic Reactivity at Contacts and Aging of Methylammonium Lead Triiodide Perovskite Solar Cells, *Adv. Energy Mater.*, 2016, **6**, 1502246.

42 I. Zarazua, G. Han, P. P. Boix, S. Mhaisalkar, F. Fabregat-Santiago, I. Mora-Seró, J. Bisquert and G. Garcia-Belmonte, Surface Recombination and Collection Efficiency in Perovskite Solar Cells from Impedance Analysis, *J. Phys. Chem. Lett.*, 2016, **7**, 5105–5113.

43 E. Guillén, F. J. Ramos, J. A. Anta and S. Ahmad, Elucidating Transport-Recombination Mechanisms in Perovskite Solar Cells by Small-Perturbation Techniques, *J. Phys. Chem. C*, 2014, **118**, 22913–22922.

44 F. Fabregat-Santiago, G. Garcia-Belmonte, I. Mora-Seró and J.

Bisquert, Characterization of nanostructured hybrid and organic solar cells by impedance spectroscopy, *Phys. Chem. Chem. Phys.*, 2011, **13**, 9083.

45 L. Contreras, J. Idígoras, A. Todinova, M. Salado, S. Kazim, S. Ahmad and J. A. Anta, Specific cation interactions as the cause of slow dynamics and hysteresis in dye and perovskite solar cells: a small-perturbation study, *Phys. Chem. Chem. Phys.*, 2016, **18**, 31033–31042.

46 A. Guerrero, G. Garcia-Belmonte, I. Mora-Sero, J. Bisquert, Y. S. Kang, T. J. Jacobsson, J.-P. Correa-Baena and A. Hagfeldt, Properties of Contact and Bulk Impedances in Hybrid Lead Halide Perovskite Solar Cells Including Inductive Loop Elements, *J. Phys. Chem. C*, 2016, **120**, 8023–8032.

47 I. Zarazua, J. Bisquert and G. Garcia-Belmonte, Light-Induced Space-Charge Accumulation Zone as Photovoltaic Mechanism in Perovskite Solar Cells, *J. Phys. Chem. Lett.*, 2016, **7**, 525–528.

48 M. Bag, L. A. Renna, R. Y. Adhikari, S. Karak, F. Liu, P. M. Lahti, T. P. Russell, M. T. Tuominen and D. Venkataraman, Kinetics of Ion Transport in Perovskite Active Layers and Its Implications for Active Layer Stability, *J. Am. Chem. Soc.*, 2015, **137**, 13130–13137.

49 H.-S. Kim, I.-H. Jang, N. Ahn, M. Choi, A. Guerrero, J. Bisquert and N.-G. Park, Control of $I-V$ Hysteresis in $\mathrm{CH_3NH_3PbI_3}$ Perovskite Solar Cell, *J. Phys. Chem. Lett.*, 2015, **6**, 4633–4639.

50 H.-S. Kim, I.-H. Jang, N. Ahn, M. Choi, A. Guerrero, J. Bisquert and N.-G. Park, Control of I–V Hysteresis in CH3NH3PbI3 Perovskite Solar Cell, *J. Phys. Chem. Lett.*, 2015, **6**, 4633–4639.

51 M. Bag, L. A. Renna, R. Y. Adhikari, S. Karak, F. Liu, P. M. Lahti, T. P. Russell, M. T. Tuominen and D. Venkataraman, Kinetics of Ion Transport in Perovskite Active Layers and Its Implications for Active Layer Stability, *J. Am. Chem. Soc.*, 2015, **137**, 13130–13137.

52 S. N. Habisreutinger, T. Leijtens, G. E. Eperon, S. D. Stranks, R. J. Nicholas and H. J. Snaith, Enhanced Hole Extraction in Perovskite Solar Cells Through Carbon Nanotubes, *J. Phys. Chem. Lett.*, 2014, **5**, 4207–4212.

53 J. P. Correa Baena, L. Steier, W. Tress, M. Saliba, S. Neutzner, T. Matsui, F. Giordano, T. J. Jacobsson, A. R. Srimath Kandada, S. M. Zakeeruddin, A. Petrozza, A. Abate, M. K. Nazeeruddin, M. Grätzel and A. Hagfeldt, Highly efficient planar perovskite solar cells through band alignment engineering, *Energy Environ. Sci.*, 2015, **8**, 2928–2934.

54 K. Pydzińska, J. Karolczak, I. Kosta, R. Tena-Zaera, A. Todinova, J. Idígoras, J. A. Anta and M. Ziółek, Determination of Interfacial Charge-Transfer Rate Constants in Perovskite Solar Cells, *ChemSusChem*, 2016, **9**, 1647–1659.

55 Y. Zou and R. J. Holmes, Temperature-Dependent Bias Poling and Hysteresis in Planar Organo-Metal Halide Perovskite Photovoltaic Cells, *Adv. Energy Mater.*, 2016, **6**, 1501994.

56 D. Bi, W. Tress, M. I. Dar, P. Gao, J. Luo, C. Renevier, K. Schenk, A. Abate, F. Giordano, J.-P. Correa Baena, J.-D. Decoppet, S. M. Zakeeruddin, M. K. Nazeeruddin, M. Grätzel and A. Hagfeldt, Efficient luminescent solar cells based on tailored mixed-cation perovskites, *Sci. Adv.*, 2016, **2**, e1501170.

57 A. Todinova, L. Contreras-Bernal, M. Salado, S. Ahmad, N. Morillo, J. Idígoras and J. A. Anta, Towards a Universal Approach for the Analysis of Impedance Spectra of Perovskite Solar Cells: Equivalent Circuits and Empirical Analysis, *ChemElectroChem*, 2017, **4**, 2891–2901.

58 J. Idígoras, L. Contreras-Bernal, J. M. Cave, N. E. Courtier, Á. Barranco, A. Borras, J. R. Sánchez-Valencia, J. A. Anta and A. B. Walker, The Role of Surface Recombination on the Performance of Perovskite Solar Cells: Effect of Morphology and Crystalline Phase of TiO2 Contact, *Adv. Mater. Interfaces*, **0**, 1801076.

59 C. Wehrenfennig, M. Liu, H. J. Snaith, M. B. Johnston and L. M. Herz, Charge-carrier dynamics in vapour-deposited films of the organolead halide perovskite $CH_3NH_3PbI_{3-x}Cl_x$, *Energy Env. Sci*, 2014, **7**, 2269–2275.

60 J. S. Manser and P. V. Kamat, Band filling with free charge carriers in organometal halide perovskites, *Nat. Photonics*, 2014, **8**, 737–743.

61 Y. Yang, M. Yang, Z. Li, R. Crisp, K. Zhu and M. C. Beard, Comparison of Recombination Dynamics in $CH_3NH_3PbBr_3$ and $CH_3NH_3PbI_3$ Perovskite Films: Influence of Exciton Binding Energy, *J. Phys. Chem. Lett.*, 2015, **6**, 4688–4692.

62 W. Rehman, R. L. Milot, G. E. Eperon, C. Wehrenfennig, J. L. Boland, H. J. Snaith, M. B. Johnston and L. M. Herz, Charge-Carrier Dynamics and Mobilities in Formamidinium Lead Mixed-Halide Perovskites, *Adv. Mater.*, 2015, **27**, 7938–7944.

63 J.-P. Correa-Baena, S.-H. Turren-Cruz, W. Tress, A. Hagfeldt, C. Aranda, L. Shooshtari, J. Bisquert and A. Guerrero, Changes from Bulk to Surface Recombination Mechanisms between Pristine and Cycled Perovskite Solar Cells, *ACS Energy Lett.*, 2017, **2**, 681–688.

64 D. Li, S. A. Bretschneider, V. W. Bergmann, I. M. Hermes, J. Mars, A. Klasen, H. Lu, W. Tremel, M. Mezger and H.-J. Butt, Humidity-induced grain boundaries in MAPbI3 perovskite films, *J. Phys. Chem. C*, 2016, **120**, 6363–6368.

65 W. Nie, H. Tsai, R. Asadpour, J.-C. Blancon, A. J. Neukirch, G. Gupta, J. J. Crochet, M. Chhowalla, S. Tretiak and M. A. Alam, High-efficiency

solution-processed perovskite solar cells with millimeter-scale grains, *Science*, 2015, **347**, 522–525.

66 E. Guillén, F. J. Ramos, J. A. Anta and S. Ahmad, Elucidating Transport-Recombination Mechanisms in Perovskite Solar Cells by Small-Perturbation Techniques, *J. Phys. Chem. C*, 2014, **118**, 22913–22922.

67 J.-P. Correa-Baena, M. Anaya, G. Lozano, W. Tress, K. Domanski, M. Saliba, T. Matsui, T. J. Jacobsson, M. E. Calvo, A. Abate, M. Grätzel, H. Míguez and A. Hagfeldt, Unbroken Perovskite: Interplay of Morphology, Electro-optical Properties, and Ionic Movement, *Adv. Mater.*, 2016, **28**, 5031–5037.

68 F. Fabregat-Santiago, G. Garcia-Belmonte, I. Mora-Seró and J. Bisquert, Characterization of nanostructured hybrid and organic solar cells by impedance spectroscopy, *Phys. Chem. Chem. Phys.*, 2011, **13**, 9083.

Chapter 8

Impedance Analysis of Perovskite Solar Cells: a Case Study

An impedance spectroscopy analysis of two perovskite solar cells with quite distinct optical and electrical characteristics (*$MAPbI_3$ and $CsPbBr_3$-based devices*) has been carried out. *The main aim of the analysis is to establish how, regardless the inherent complexity of the impedance spectrum due to ionic effects, information like ideality factors, recombination losses and the collection efficiency can be qualitative and quantitatively assessed from impedance experiments at operating conditions.*

This chapter is based on Publication 7 of this Thesis: Contreras-Bernal *et. al.* Manuscript in preparation to be submitted to Advanced Energy Materials, 2019.

8.1 Introduction

As it has been shown in previous *Chapters*, photovoltaic halide perovskites behave as a sort of “soft” semiconductor where electronic and ionic condition are mixed.[1–3] This feature appears to be related to the occurrence of different kinetic processes that take place in quite separated time scales: electronic transport and recombination in the ns-μs range,[4–6] ionic redistribution and hysteresis in the ms-seconds range,[7–10] and reversible and irreversible degradation processes for seconds, minutes and even in a longer time scale.[11–13] In particular, it is generally accepted that recombination is especially slow and diffusion lengths especially long in PSCs, leading to open-circuit photovoltages very close to the theoretical limits.[4,14–16]

In this context, advanced optoelectronic techniques such as impedance spectroscopy[17,18] are particularly appealing to study solar cells, as they allow the characterization in a broad range of time scales. A typical impedance experiment consists in setting a small frequency-modulated (AC) signal (voltage perturbation) which is applied in addition to a stationary (DC) voltage. By registering the AC response in terms of current one can extract the complex frequency-dependent impedance and obtain information about internal processes of PSCs occurring at different time scales (μs – s) (see *Chapter* 3 for details). This makes it possible to distinguish processes of distinct kinetics, like those based on either pure electronic changes (supposed to be fast) or, indirectly, those based on ionic changes either in the bulk or at interfaces (supposed to be slow). Thus, impedance spectroscopy can be theoretically used as characterization method of PSCs and provide a basis to quantify transport rates, recombination losses, interfacial charge accumulation processes characteristic geometric capacitances, ionic diffusion coefficients, etc. occurring in these time domains.

The main drawback of IS, especially as regards its exploitation to characterize PSCs, is that an interpretation of the spectra is still not well-established in the field yet, as it is for other systems such as dye-sensitized solar cells.[17] Several factors contribute to this. First of all, the impedance experiment itself produces internal electrical fields that displace and reorganize the ions, altering the electrical features.[19] Secondly, there is a large variety of equivalent circuits “in the market” to fit the spectra. Due to the existence of the afore-mentioned disparity of kinetics, different types of circuit happen to yield the same fitted parameters.[20] In previous *chapters* we have used a *Voight* type equivalent circuit aimed at extracting basically resistances and capacitances, but the "true" equivalent circuit is far from being well established. As a consequence, the interpretation of the obtained fitted parameters is not univocally understood yet.

Thus, the following questions can be formulated in order to establish IS as a useful tool to assess the performance of a perovskite solar cell: in spite of the ionic effects and inherent complexity of the spectrum, can we still quantify recombination, and charge collection at working conditions?

Herein, to provide a deeper electrical and phenomenological characterization with new insights in the physical process that determine the photovoltaic response of PSCs under working conditions, we have chosen two configurations characterized by very different optical characteristics and band gaps and a quite distinct hysteretic behaviour in the current density-voltage curve. In particular, we analysed the electrical properties of $MAPbI_3$ and $CsPbBr_3$ devices under illumination, being these materials probably the most studied hybrid and inorganic perovskites, respectively. In order to understand the spectra, the impedance parameters (time constants, resistances and capacitances) are analysed, for both configurations, as a function of three experimental variables: (1) illumination intensity and open-circuit voltage, (2) DC voltage and (3) temperature. From experiment (1) it will be shown how the ideality factor can be extracted, and how it can be qualitatively compared to the recombination rates of PSC with different optical band gaps. From experiment (2) we can follow how the IV curve can be traced down from the impedance response. From experiment (3) we can differentiate between electronic and ionic process and extract activation energies.

8.2 Fabrication and characterization of devices

Fabrication of perovskite solar cells

Perovskite devices with mesoporous regular architecture were fabricated following the methodology described in *Chapter* 3. First of all, FTO TEC15 were cleaned following the solvent sequence: Hellmanex solution; Deionized water; Ethanol; Isopropanol. Then, TiO_2 compact layer was deposited by spray pyrolysis. After that, a mesoporous layer of TiO_2 was deposited on top of a TiO_2 compact layer. For $MAPbI_3$ based devices, a pure methylammonium lead iodide solution was deposited as active layer at environmental humidity conditions (relative humidity ≈ 42 %). According the methodology reported,[21] the perovskite precursor solutions was prepared for a ratio DMSO:Pb^{2+} of 1 (Table 3.2). For $CsPbBr_3$ based devices a two-step sequential deposition technique was employed. After perovskites deposition, spiro-OMeTAD solution was spin coated. Finally, 60 nm of gold was deposited by thermal evaporation. (See *Chapter* 3 for details).

Characterization of devices

Current-voltage characteristics of the devices were obtained using a solar simulator (*ABET-Sun2000*) with AM 1.5G filter. The current-voltage characteristics were determined by applying an external potential bias to the cell and measuring the photocurrent using an Autolab/PGSTAT302N potentiostat. The current-voltage characteristics were measured with a scan rate of 100 mV/s and a sweep delay of 20s. Incident Photon-to-current Conversion efficiency was measured using an Oriel Xenon lamp coupled to McPherson monochromator. Light intensity was determined as a function of the wavelength using a calibrated silicon photodiode (PH-100 Si, GENTECE). The illumination for the IS measurements was provided by white LED over a wide range of DC light intensities. Two types of IS experiments were performed: (1) at open circuit (OC) under varying illumination intensities (parameters are extracted, analysed and plotted as a function of the resulting open-circuit photopotential) and (2) at non open circuit (NOC) conditions varying DC potential (voltage) while light intensity is fixed.[22] In this latter case the parameters are corrected for voltage drop due to the resulting DC current and the corresponding series resistance.[17] In the following, we will use the labels OC and NOC to refer to these two kinds of experiments. In both OC and NOC conditions a 20 mV perturbation in the 10^6-10^{-2} Hz range was applied. A response analyser module (PGSTAT302N/FRA2, Autolab) was utilized to analyse the frequency response of the devices. IMPS measurements were carried out by coupling the PGSTAT302N/FRA2 module to the LED. IMPS measurements were performed at short-circuit with a light perturbation corresponding to 10% of the DC background illumination intensity. Due to limitations of the experimental set-up, the measurement was limited to the 10^5 - 10^{-1}Hz frequency range. For the structural characterization, SEM and EDS images of the samples were performed. For optical characterization, UV–vis absorption spectra and photoluminescence measurements were recorded. Temperature-dependent experiments were carried out by means of a MHCS622CD Heating and Cooling Vacuum/gas tight Stage configured with MTDC600 temperature controller (Microptik).

8.3 Results and discussion

Pinhole-free and crystalline perovskite layers with close to 400 nm thickness in both cases were formed and characterised for the $MAPbI_3$ and $CsPbBr_3$ configurations (Fig. 8.1 and Figs. A-8.1, A-8.2 and A-8.3 in appendix F). As it is well known, the use of different cation and anion affects the morphological (Fig. A-8.1A) and optical properties (Fig. A-8.1B and A-8.1C).[23,24] Optical band-gaps were extracted from UV-Vis spectra for $MAPbI_3$ (1.61 eV) and

$CsPbBr_3$ (2.33 eV), Figure A-8.1C. A relatively long subgap tail is observed in the absorption spectra of $CsPbBr_3$, extending for about 0.6-0.7 eV, in contrast to the tail of only 0.02 eV for $MAPbI_3$ (Fig. A-8.1B).

Figure 8.1A shows the IV curves obtained for the best performing $MAPbI_3$ and $CsPbBr_3$ devices measured at 1 sun. Statistics of the photovoltaic parameters extracted from all fabricated devices is shown in Figure A-8.3 in the appendix F. Average Power Conversion Efficiency of 14.9% (short circuit current, J_{SC}: 19.2 mA·cm^{-2}, open-circuit potential, V_{OC}: 1037 mV and FF: 0.74) and 4.1% (J_{SC}: 5.3 mA·cm^{-2}, V_{OC}: 1254 mV and FF: 0.61) in a reverse scan of 100 mV/s were obtained for $MAPbI_3$ and $CsPbBr_3$ solar cells respectively.

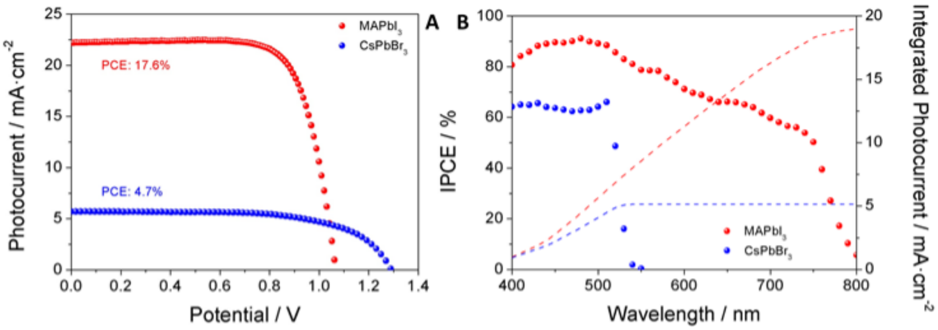

Figure 8.1. Photovoltaic characterization of $MAPbI_3$ and $CsPbBr_3$ films and solar cells: (A) Density current-voltage characteristic of $MAPbI_3$ and $CsPbBr_3$ based devices in reverse scan under 1 sun – AM 1.5G illumination. A scan rate of 100 mV/s after poling 20 s at 1.2V and 1.4V was employed for $MAPbI_3$ and $CsPbBr_3$ based devices, respectively. (B) IPCE as a function of monochromatic wavelength and the corresponding AM 1.5G illumination integrated photocurrent (Eq. 2.12 in *Chapter* 2).

The PCE of $CsPbBr_3$ is substantially lower than the one obtained for $MAPbI_3$. The lower J_{SC} is due to a wider band gap, and on the other hand, to a lower IPCE recorded for $CsPbBr_3$ cell, Figure 8.1B. The integrated photocurrents are in good agreement with the J_{SC} obtained from IV curve measurements, Figures 8.1B and A-8.3. After correction by the absorption coefficient, Internal Quantum Efficiencies at stationary conditions has also been measured at 465 and 630 nm and different light intensities. Values very close to 95% are obtained for $MAPbI_3$ based devices whereas a lower IQE (around 80-90%) is obtained for $CsPbBr_3$ devices.

Figures 8.2A and 8.2B show the variation of V_{OC} with respect to illumination intensity and temperature. The V_{OC} has a logarithmic dependence with respect to illumination intensity which follows the diode equation (see *Chapter* 5, Eq. 5.6). The slope determines the ideality factor of the solar cells, which lies between 1.7 and 2.2 for both configurations (Fig. 8.2A). The V_{OC} decreases linearly with respect to absolute temperature, except at lower temperatures (Fig.

8.2B). As it was shown in *Chapter* 5 (Eq. 5.6), the extrapolation to $T \rightarrow 0$ reproduces the optical band gap of each type of perovskite in good agreement with the optical characterization (Fig. A-8.1C).

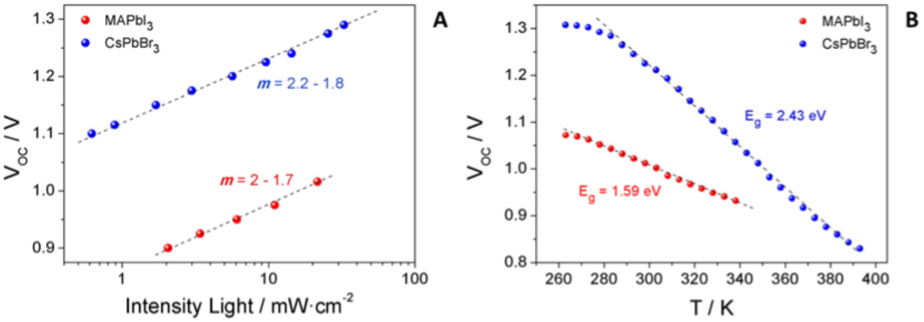

Figure 8.2. (A) V_{OC} vs. illumination intensity and (B) V_{OC} as a function of the temperature at a light intensity of 14 mW·cm^{-2} using a white-LED as light source. The ideality factors and the estimation of the band gap are shown in panel A and B, respectively.

Both kind of solar devices were characterized by impedance spectroscopy. Two types of IS experiments were performed: (1) at open circuit (OC) under varying illumination intensities (plotted as a function of the resulting V_{OC}) and (2) at non open circuit (NOC) conditions varying DC potential (voltage) while light intensity is fixed at 1 sun.[22] In this *Chapter* the parameters are corrected for voltage drop due to the resulting DC current and the corresponding series resistance.[17]

Figure 8.3 shows representative Nyquist (Z′-Z′′) plots of impedance spectra for both studied configurations under illumination at different applied potentials at OC and NOC conditions in the 10^6-10^{-2} Hz frequency range. The corresponding Bode plots are depicted in Figure A-8.4. At OC conditions, the Nyquist plots of MAPbI$_3$ based devices (Fig. 8.3A) are characterized by the presence of two arcs and the corresponding frequency plots show two peaks at high and low frequencies accordingly (Fig. A-8.4A). The impedance spectra of CsPbBr$_3$ based devices at OC conditions (Fig. 8.3B, A-8.4B) display a different behaviour depending on illumination. At very high OC photovoltages (1.3-1.2 V) there are two signals in the high frequency region (10^4-10^6 Hz) that merge into a single one as the V_{OC} is reduced. Under NOC conditions (Fig. 8.3C and 8.3D), the Nyquist plots for MAPbI$_3$ and CsPbBr$_3$ based devices were characterized by one complete and well-defined high-frequency arc and, depending on the applied DC potential, a second low frequency arc. The Bode plots display two peaks in the high and frequency regions accordingly, Figures A-8.4C and A-8.4D.

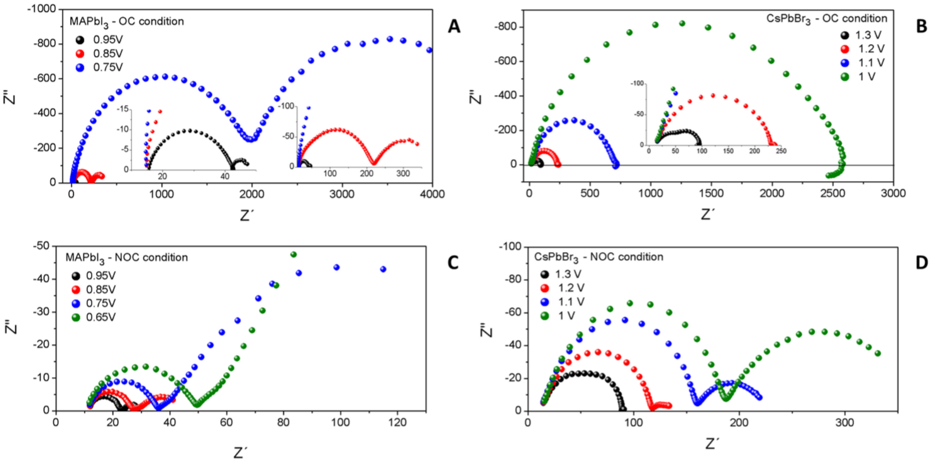

Figure 8.3. Nyquist plots of impedance spectra obtained under white LED illumination in the vicinity of the 1-sun open-circuit potential for (A, C) MAPbI$_3$ and (B, D) CsPbBr$_3$ based devices under illumination at (A, B) open-circuit (OC) and (C, D) and non-open-circuit (NOC) conditions. Insets: zoom at the high frequency region.

In spite of the presence of other minor features, the IS of perovskite solar cells is basically determined by the existence of two characteristic times, at high and low frequencies. Note that the characteristic times can be easily obtained from the reverse of the frequency at which a peak is observed in the Bode plot (see *Chapter* 3, Eq. 3.23). The corresponding arc in the Nyquist representation can be described by a parallel association of a resistor and a capacitor, where the time constant is the product of both of them (Eq. 3.22). In order to properly interpret these characteristic times and how a recombination rate or a collection efficiency can be inferred from them, we have performed additional experiments.

Temperature dependence of IS at short circuit conditions (i.e. 0 V DC bias in NOC) have been carried out, Figure A-8.5. It can be easily appreciated that the high frequency signal is independent of temperature. In contrast, the low frequency part varies with *T* and the low frequency signal gets shifted towards higher frequencies when the sample is heated. An activation energy of 36.9 kJ/mol was extracted from these data (Fig. A-8.5E) in agreement with *Chapter* 4 (Eq. 4.4). This finding suggests that it is in the low frequency region of the spectra where processes that are thermally activated (as could be ionic migrations and/or chemical reactions) are probed, whereas at high frequencies mainly pure electronic processes are determining the response. On the other hand, Figure A-8.6 summarizes the impact of illumination at NOC conditions. We observe that for MAPbI$_3$ based devices, the high frequency time constant shifts towards shorter time scales, whereas the low frequency one remains basically unaltered.

A proper interpretation or analysis of an impedance spectrum requires a suitable model based on rate (continuity) equations. From these equations, an equivalent circuit is derived, which is used to fit the experimental data. However, due to the complexity of the system with electronic and ionic conduction, there is no broad consensus on the equations ruling perovskite devices. These can include different boundary conditions, such as extracting ones for electrons and blocking ones for ions. On the other hand, the possibility of interfacial reactions cannot be ruled out.[25,26] The lack of a well-established model prevents taking full advantage of impedance characterization, which otherwise could allow to extract an important number of parameters. Nevertheless, in *Chapter* 5 we have shown a semi-empirical approach that allows to extract important parameters such as ideality factors and recombination losses. In this *Chapter*, we expand this approach to show that not only the parameters above but also the collection efficiency can be qualitative and quantitatively assessed at operating conditions.

The two features at high frequency (*HF*) and low frequency (*LF*) of the impedance spectra, Figure 8.3, have been fitted using a simplified equivalent circuit depicted in the inset of Figure 8.4B, and the obtained parameters are plotted in Figure 8.4. This equivalent circuit yields essentially the same results as those used in previous *Chapters* in which the two *RC* elements (or *R-CPE*) are placed in series.[20] R_S takes into account the series resistance induced by extracting contacts and wiring. C_{HF} is associated with the geometrical capacitance,[27] in line with the potential independent values obtained and in good agreement with *Chapter* 5 and previous works.[20,27–30] In contrast, the C_{LF} capacitance shows an exponential trend at high potentials:

$$C_{LF} = C_{00} exp\left(\frac{\alpha q V}{k_B T}\right) \tag{8.1}$$

where C_{00} is preexponential factor and α is a positive parameter. Interestingly, the data shows $\alpha = \beta$ (see Table 8.1) where β is obtained from the slope of the *LF* resistance, as also reported in the literature. [29,31,32] In addition, the C_{LF} becomes flat at the same V_d (device potential) at which the resistance reaches its saturation value. These facts point towards a coupled *LF* resistance and capacitance, with a corresponding characteristic time, $\tau_{LF} = R_{LF} \cdot C_{LF}$, roughly voltage independent (Fig. A-8.8). The complementary behaviour of the two circuit elements suggest that the same process that makes the *LF* capacitance to increase with illumination or DC applied voltage makes the *LF* resistance to decrease.

As previously discussed, there is no consensus on the interpretation of the elements producing the low frequency arc, but all the models point that ionic movement is related to the origin of this feature. This lack of consensus is mainly due to the difficulty of interpretation of the physical origin of each one of the parameters of the equivalent circuit. While, in DSSCs just one physical process can be assigned to each parameter in the case of PSCs, different processes present similar characteristic times and it is difficult to decouple their effect. Consequently, different processes affect the same feature. For example, *HF* arc has been previously ascribed (*Chapter* 5) to account for R_{rec} but it is also affected by selective contact or perovskite transport.[27,33,34] In the same, line, R_{rec} has been related with the *LF* arc[33] or with both,[3,6,32,35] as it is not straightforward to decouple the recombination contribution from other contributions, as transport or injection at the interfaces. Following Eq. 2.22 (see *Chapter* 2), we suggest that a resistance associated with R_{rec} in each case can be assigned to that presenting a slope $\beta = 1/m$, and consequently this resistance can be linearly linked to R_{rec}.

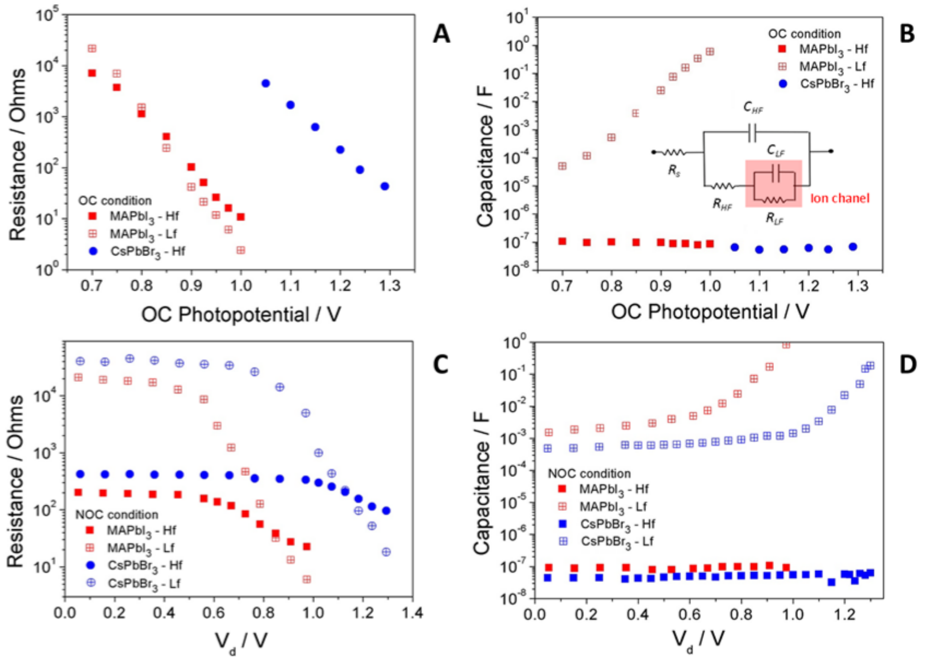

Figure 8.4. (A, B) Resistive and (C, D) capacitance elements as extracted from fittings of the impedance spectra obtained at (A, B) open-circuit (OC) and (C, D) non-open-circuits (NOC) conditions using the equivalent circuit model for (red) $MAPbI_3$ and (blue) $CsPbBr_3$ based devices.

Analysis of Figure 8.4 shows exponential behaviour for both resistances and for the *HF* capacitance in the high voltage region. The resistances in the OC experiment fit well to Eq. 2.22. The values of the corresponding slope parameters are collected in Table 8.1.

R_{HF} obtained for $MAPbI_3$ and $CsPbBr_3$-based devices show a similar β parameter value at OC conditions, of around 0.5. This follows the expected dependence for a dominating recombination resistance, R_{rec}, considering the ideality factor measured in Figure 8.2A. In contrast, values around 0.78 were found for the R_{LF} of $MAPbI_3$ devices at OC. It is worth mentioning the different voltage-dependence for the *LF* and *HF* resistances, which is not the case reported in previous works.[6,29]

Table 8.1. β and α parameter values extracted from the high frequency and low frequency resistances and capacitances fitted from impedance spectra for $MAPbI_3$ and $CsPbBr_3$ based devices at open-circuit (OC) and non-open-circuit (NOC) conditions (for NOC conditions only the exponential region is used in the fittings to Eqs. 2.22 and 8.1)

Device	**IS**	**β - R_{HF}**	**β - R_{LF}**	**α- C_{HF}**	**α- C_{LF}**
$MAPbI_3$	OC	0.56 - 0.5	0.81 - 0.75	flat	0.80 - 0.77
	NOC	0.15 - 0.13	0.51 - 0.46	flat	0.46 - 0.42
$CsPbBr_3$	OC	0.51 – 0.43	No signal	flat	No signal
	NOC	0.15 – 0.11	0.46 – 0.40	flat	0.46– 0.4

At NOC conditions the behaviour of the two resistances is quite different. Firstly, the exponential dependence is only observed at high DC potentials but becomes flat as the experiment approaches SC conditions, which suggests that the device is ruled by the shunt resistance at fixed light intensity and low applied bias. The transition between the two regimes occurs at voltages right below the maximum power point of the corresponding IV curves (Fig. 8.1A). Secondly, at high applied bias in NOC the slope in good agreement with the ideality factor is that at *LF*. Note that in Figure 8.4, NOC parameters are plotted as a function of the device potential, $V_d = V_{appl}-V_{series}$, where the applied voltage, V_{appl}, is corrected by the substraction of the voltage drop at the series resistance, V_{series}. It is important to stress out that the series resistance correction does not change significantly the slope of neither the two resistances (Fig. A-8.7).

Since at OC the R_{HF} slope is in good agreement with the ideality factor, indicating that this resistance is linearly proportional to R_{rec} as expected from Eqs. 5.6 (*Chapter* 5) and 2.22, the results are consistent with intrinsic or high injection conditions and a recombination reaction order of $\gamma \sim 1$, a signature of Shockley-Read-Hall recombination for both $MAPbI_3$ and $CsPbBr_3$.[28,36] As it has been mentioned above, Eq. 5.6 also predicts a linear dependence of V_{OC} versus absolute temperature. This behaviour is indeed reproduced in Figure 8.2B and the fact that the optical band gap is recovered by extrapolation to $T \rightarrow 0$, strongly suggests that, at least under OC conditions, the recombination process represented by the rate law (see Eq. 5.2 in *Chapter* 5) takes place in the bulk or it is determined by the perovskite layer only. This is consistent with the results obtained in *Chapter* 5 using ideality factor[36] and different optical penetrations of the light in impedance experiments with different excitation wavelengths.[28,37]

The exponential dependence of R_{HF} with voltage and its proportional connection to R_{rec} at OC allows for a direct comparison between $MAPbI_3$ and $CsPbBr_3$ recombination behaviours. To do that, it is necessary to take into account both the thermodynamic effect (different band gap) and the kinetic behaviour (recombination rate), plotting the impedance parameters at the same value of the photogenerated charge density. Eq. 2.18 (see *Chapter* 2) provides a means to do this. According to this expression, plotting versus $E_g/q - V_{oc}$ should guarantee that we are comparing cells of different band gaps at the same value of the photogenerated charge density. The correction is analogous to an analysis commonly done in dye-sensitized solar cells,[38,39] and would be valid if the $n = p$ condition is fulfilled, i.e., at intrinsic or at high injection conditions.

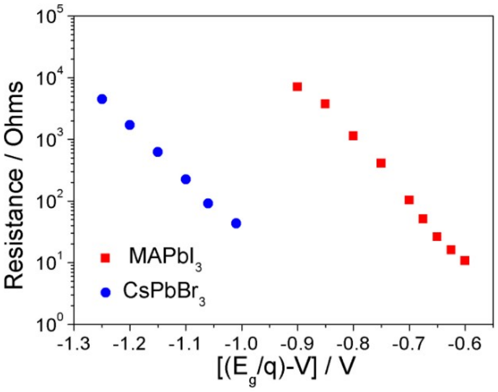

Figure 8.5. High frequency resistive element extracted from fittings of the impedance spectra obtained at open-circuit plots versus the photopotential corrected for the optical band gap of the perovskite.

Once the effect of the band gap is corrected for (Fig. 8.5), it becomes evident that the recombination rate in $CsPbBr_3$ based devices is substantially larger than in the $MAPbI_3$ ones. This could be expected from the potential loss with respect to the band gaps, which is ~ 1 V for $CsPbBr_3$ ($E_g/q - V_{OC} = 2.34 - 1.3$) versus ~ 0.45 V for $MAPbI_3$ ($E_g/q - V_{OC} = 1.55 - 1.1$). The difference roughly coincides with the voltage separation between the two resistances in Figure 8.5.

At NOC and high applied voltage, it is R_{LF} the one than presents a slope concurring with the ideality factor, and consequently, proportional to R_{rec}. Thus, the same correction of thermodynamic effect can be applied with similar results than those in Figure 8.5 (Fig. A-8.9).

The faster recombination in $CsPbBr_3$ devices, which is derived from the recombination resistance analysis, is most probably related to their rougher morphology and longer tail of subgap states observed in the absorption spectra (Fig. 8.1B). A relatively long *Urbach* tail will lead to a substantial V_{oc} loss with respect to the thermodynamic limit.[16] In addition, more crystal defects will cause as a more rapid recombination rate, that may cause additional voltage loss. Thus, recombination is of the same type as in $MAPbI_3$ cells, as indicated by a similar value of the ideality factor, but it is more rapid due to a higher concentration of defects (parameter p_0 in Eq 5.3). In a recent publication, a 300-400 mV voltage loss in bromine-based devices is attributed to surface recombination.[40] However, contrary to our results, the reported activation energy at $T \rightarrow 0$ is significantly lower than the optical band gap, and does not detect any Urbach tail in their IPCE measurements, showing that in their case the main voltage loss arises from band misalignment and recombination mediated by interfacial effects. Consequently, the T analysis allows discriminating between surface and bulk recombination, while impedance comparison permits comparing the recombination rate when the thermodynamic effect is corrected for as in Figure 8.5.

As mentioned in the introduction, the main objective of this *Chapter* is to establish an approach to quantify recombination losses and charge collection from the impedance spectrum. First of all, it is important to verify that the two resistances at NOC and steady-state conditions, can be used to reconstruct the IV,[17,22,35] taking into account all contributions related with recombination, transport, injection or series resistance:

$$J(V) = J_{SC} - A\int_0^{V_{app}} \frac{dV}{R_{tot}} \tag{8.2}$$

with $R_{tot} = R_s + R_{HF} + R_{LF}$ (A is the active area of the device). In Figure A-8.10 it is shown that the experimental curves for both $MAPbI_3$ and $CsPbBr_3$ based devices can be recovered, using Eq. 8.2, from the impedance data at NOC conditions.

Following previous work,[35] the charge collection efficiency, CCE, in a solar cell can be determined from the recombination resistance at OC and NOC conditions using the expression:

$$CCE \approx 1 - \frac{R_{rec(OC)}}{R_{rec(NOC)}} \tag{8.3}$$

where R_{rec} is the recombination resistance as defined by Eq. 2.22. Hence, at open-circuit $CCE = 0$ by definition and at short-circuit, for an optimal system with minimum recombination, R_{rec} $(V = 0) \rightarrow \infty$ and $CCE \rightarrow 1$.

The difficult bit is how to define and extract R_{rec} in the impedance spectrum. As outlined before, several possibilities have been claimed in the literature. Since no definitive theoretical model for impedance is well-established yet, we apply here an *empirical* approach. It has already been mentioned that the OC high frequency resistance is the only one whose voltage dependence predicts the correct ideality factor in line with Eqs. 5.6 and 2.22. However, at NOC conditions the R_{LF} is the one with a slope closer to the ideality factor. Thus, either high or low frequency resistance can be invoked as the true recombination resistance as well as the sum of the two. All three possibilities are tested in Figure A-8.11. Due to the fact that $R_{LF} >> R_{HF}$ (see Fig. 8.4C) at NOC conditions, only assuming $R_{rec} = R_{HF}$ yields values significantly different from 100%. As a matter of fact, only this possibility makes it possible to *discriminate* between $MAPbI_3$ and $CsPbBr_3$ cells. Results are presented in Figure 8.6.

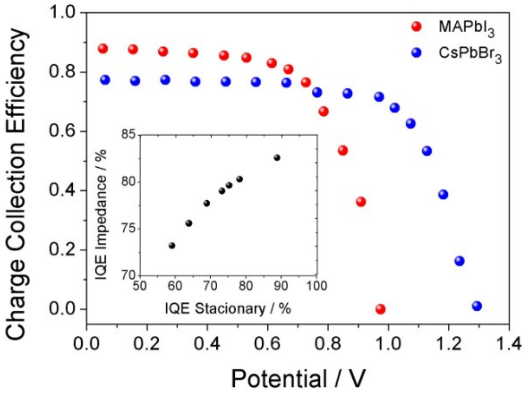

Figure 8.6. Charge collection efficiency as predicted by Eq. 8.3 using impedance data at OC and NOC conditions.

The collection efficiency of photogenerated electrons in the perovskite film can be considered an approximation to the IQE (assuming that there are no charge losses in the injection of chargers to the contacts). The variation of the collection efficiency in Figure 8.6 with DC potential resembles the shape of the IV curve. The curve yields the collection efficiency at SC conditions ($V = 0$). Values of ~ 0.9 and ~ 0.8 are obtained for $MAPbI_3$ and $CsPbBr_3$ based devices, respectively. These figures agree remarkably well with the IQE values measured for both configurations, which confirm the larger recombination loss for $CsPbBr_3$ cells.

Another indication that there is a substantial recombination loss in $CsPbBr_3$ devices, even at SC conditions, is evidenced by the maximum theoretical photocurrents, as obtained from integration of the measured absorptance (Fig. A-8.12. Values of 24.9 and 10.8 mA/cm^2 are obtained for $MAPbI_3$ and $CsPbBr_3$ based devices, respectively. When compared with the actual experimental values, 20 ± 2 and 5 ± 1 mA/cm^2, we infer that recombination losses (and possibly poorer injection too) are affecting critically the performance of the devices made with $CsPbBr_3$ perovskite.

The prediction of the collection efficiencies evidences that the impedance response changes from a regime where recombination is dominant: $V > V_{mp}$, and both resistances show an exponential behaviour (although with different slopes), and a regime where collection is dominant: $V < V_{mp}$ and both resistances become flat. As the recombination resistance increases exponentially as the voltage decreases, at low voltages the impedance response becomes determined by the other elements in the equivalent circuit like shunting and transport resistances, which are effectively voltage independent.

The previous results in terms of ideality factors and CCE point to the high frequency component as the impedance element that basically contains the information about recombination loss. However, the exponential behaviour of R_{Lf} at NOC conditions implies that this identification is not so straightforward. To provide additional assurance we have measured the IQE at short-circuit of a batch of $MAPbI_3$ based devices and plotted the results versus the predictions of Eq. 8.3 at $V = 0$ using $R_{rec} \approx R_{HF}$ in Eq. 8.3 for the determination of IQE. In this respect we have to bear in mind that CCE and IQE, although related, do not represent exactly the same thing and they can only be identified if there are not additional losses between photocarrier generation and carrier collection.

The results in the inset of Figure 8.6 reveal a clear correlation between both ways of determining the IQE and demonstrates that the impedance high frequency signal provides a way to assess the recombination loss in a perovskite solar cell. However, impedance values do not exactly coincide with IQE measurements, being the difference larger the less efficient a particular cell is. For instance, for the most efficient specimen of the batch the prediction of Eq. 8.3 is ~0.83, whereas the stationary measurement gives ~0.88. This means that R_{HF} cannot be naïvely identified with the recombination resistance and probably includes transport and ion-mediated dielectric relaxation mechanisms.[41]

In this respect, it is important to bear in mind that not all resistances needed to reconstruct to the IV curve are necessarily recombination resistances. This is the case of series, transport or dielectric contributions. They do not stem from a recombination mechanism and therefore must not be considered in the determination of the collection efficiency. An analogous situation occurs in dye-sensitized solar cells with viscous electrolytes[8,42] and solid-state hole conductors,[43] for which there are well-established impedance models. In the first case, an additional low frequency arc, arising from ionic transport in the electrolyte, should be considered in the reconstruction of the IV curve but it does not contribute to the electron recombination loss. In analogy with the solar cells studied here, both low and high frequency signals have a very distinct temperature dependence, consequence of their different nature (ionic, electronic).

8.4 Conclusion

In this *Chapter*, $MAPbI_3$ and $CsPbBr_3$ perovskite solar cells have been thoroughly studied by impedance spectroscopy at open-circuit and non-open-circuit conditions, at different illuminations and temperatures. Despite, the difficulty of decoupling of the different processes occurring in the photovoltaic device, a resistance linearly related with recombination resistance can be obtained by comparing the exponential slope with the ideality factor. We have shown that these resistances can be used to extract information, both qualitative and semi-quantitative, about the nature of recombination. Correction is needed if cells of different band gaps are compared. The use of this protocol allowed us to establish, as a case study, that $MAPbI_3$ and $CsPbBr_3$ perovskite solar cells analyzed in this work have the same recombination mechanism (trap-limited in the bulk) but it is much faster in $CsPbBr_3$ devices, possibly due to a larger concentration of subgap states.

On the other hand, high-frequency resistances measured at OC and NOC conditions are found to provide an estimation of the charge collection efficiency along the IV curve. However, both low and high frequency resistances probably include additional mechanisms such as transport and dielectric contributions. Further efforts are therefore required to develop a robust model to describe the impedance response of perovskite solar cells in order to get a fully quantitative description.

8.5 References

1 C. Eames, J. M. Frost, P. R. F. Barnes, B. C. O'Regan, A. Walsh and M. S. Islam, Ionic transport in hybrid lead iodide perovskite solar cells, *Nat. Commun.*, , DOI:10.1038/ncomms8497.

2 R. A. Kerner and B. P. Rand, Ionic–Electronic Ambipolar Transport in Metal Halide Perovskites: Can Electronic Conductivity Limit Ionic Diffusion?, *J. Phys. Chem. Lett.*, 2017, **9**, 132–137.

3 D. Moia, I. Gelmetti, P. Calado, W. Fisher, M. Stringer, O. Game, Y. Hu, P. Docampo, D. Lidzey and E. Palomares, Ionic-to-electronic transcarrier current amplification in hybrid perovskite solar cells, *ArXiv Prepr. ArXiv180506446*.

4 G. Xing, N. Mathews, S. Sun, S. S. Lim, Y. M. Lam, M. Gratzel, S. Mhaisalkar and T. C. Sum, Long-Range Balanced Electron- and Hole-Transport Lengths in Organic-Inorganic CH3NH3PbI3, *Science*, 2013, **342**, 344–347.

5 S. D. Stranks, V. M. Burlakov, T. Leijtens, J. M. Ball, A. Goriely and H. J. Snaith, Recombination Kinetics in Organic-Inorganic Perovskites: Excitons, Free Charge, and Subgap States, *Phys. Rev. Appl.*, , DOI:10.1103/PhysRevApplied.2.034007.

6 A. Pockett, G. E. Eperon, N. Sakai, H. J. Snaith, L. M. Peter and P. J. Cameron, Microseconds, milliseconds and seconds: deconvoluting the dynamic behaviour of planar perovskite solar cells, *Phys. Chem. Chem. Phys.*, 2017, **19**, 5959–5970.

7 C. Li, S. Tscheuschner, F. Paulus, P. E. Hopkinson, J. Kie\s sling, A. Köhler, Y. Vaynzof and S. Huettner, Iodine migration and its effect on hysteresis in perovskite solar cells, *Adv. Mater.*, 2016, **28**, 2446–2454.

8 L. Contreras, J. Idígoras, A. Todinova, M. Salado, S. Kazim, S. Ahmad and J. A. Anta, Specific cation interactions as the cause of slow dynamics and hysteresis in dye and perovskite solar cells: a small-perturbation study, *Phys. Chem. Chem. Phys.*, 2016, **18**, 31033–31042.

9 G. Richardson, S. E. O'Kane, R. G. Niemann, T. A. Peltola, J. M. Foster, P. J. Cameron and A. B. Walker, Can slow-moving ions explain hysteresis in the current–voltage curves of perovskite solar cells?, *Energy Environ. Sci.*, 2016, **9**, 1476–1485.

10 H. J. Snaith, A. Abate, J. M. Ball, G. E. Eperon, T. Leijtens, N. K. Noel, S. D. Stranks, J. T.-W. Wang, K. Wojciechowski and W. Zhang, Anomalous Hysteresis in Perovskite Solar Cells, *J. Phys. Chem. Lett.*, 2014, **5**, 1511–1515.

11 G. Niu, X. Guo and L. Wang, Review of recent progress in chemical stability of perovskite solar cells, *J. Mater. Chem. A*, 2015, **3**, 8970–8980.

12 K. Domanski, B. Roose, T. Matsui, M. Saliba, S.-H. Turren-Cruz, J.-P. Correa-Baena, C. R. Carmona, G. Richardson, J. M. Foster and F. De Angelis, Migration of cations induces reversible performance losses over day/night cycling in perovskite solar cells, *Energy Environ. Sci.*, 2017, **10**, 604–613.

13 M. Bag, L. A. Renna, R. Y. Adhikari, S. Karak, F. Liu, P. M. Lahti, T. P. Russell, M. T. Tuominen and D. Venkataraman, Kinetics of Ion Transport in Perovskite Active Layers and Its Implications for Active Layer Stability, *J. Am. Chem. Soc.*, 2015, **137**, 13130–13137.

14 S. D. Stranks, G. E. Eperon, G. Grancini, C. Menelaou, M. J. P. Alcocer, T. Leijtens, L. M. Herz, A. Petrozza and H. J. Snaith, Electron-Hole Diffusion Lengths Exceeding 1 Micrometer in an Organometal Trihalide Perovskite Absorber, *Science*, 2013, **342**, 341–344.

15 J. S. Manser, J. A. Christians and P. V. Kamat, Intriguing Optoelectronic Properties of Metal Halide Perovskites, *Chem. Rev.*, 2016, **116**, 12956–13008.

16 W. Tress, Perovskite Solar Cells on the Way to Their Radiative Efficiency Limit - Insights Into a Success Story of High Open-Circuit Voltage and Low Recombination, *Adv. Energy Mater.*, 2017, **7**, 1602358.

17 F. Fabregat-Santiago, G. Garcia-Belmonte, I. Mora-Seró and J. Bisquert, Characterization of nanostructured hybrid and organic solar cells by impedance spectroscopy, *Phys. Chem. Chem. Phys.*, 2011, **13**, 9083.

18 E. Barsoukov and J. R. Macdonald, *Impedance Spectroscopy: Theory, Experiment, and Applications*, John Wiley & Sons Inc, Hoboken, N.J, Edición: 2nd Edition., 2005.

19 D. Pitarch-Tena, T. T. Ngo, M. Vallés-Pelarda, T. Pauporté and I. Mora-Seró, Impedance Spectroscopy Measurements in Perovskite Solar Cells: Device Stability and Noise Reduction, *ACS Energy Lett.*, 2018, **3**, 1044–1048.

20 A. Todinova, L. Contreras‐Bernal, M. Salado, S. Ahmad, N. Morillo, J. Idígoras and J. A. Anta, Towards a Universal Approach for the Analysis of Impedance Spectra of Perovskite Solar Cells: Equivalent Circuits and Empirical Analysis, *ChemElectroChem*, 2017, **4**, 2891–2901.

21 C. Aranda, C. Cristobal, L. Shooshtari, C. Li, S. Huettner and A. Guerrero, Formation criteria of high efficiency perovskite solar cells under ambient conditions, *Sustain. Energy Fuels*, 2017, **1**, 540–547.

22 F. Fabregat-Santiago, M. Kulbak, A. Zohar, M. Vallés-Pelarda, G. Hodes, D. Cahen and I. Mora-Seró, Deleterious effect of negative capacitance on the performance of halide perovskite solar cells, *ACS Energy Lett.*, 2017, **2**, 2007–2013.

23 E. T. Hoke, D. J. Slotcavage, E. R. Dohner, A. R. Bowring, H. I.

Karunadasa and M. D. McGehee, Reversible photo-induced trap formation in mixed-halide hybrid perovskites for photovoltaics, *Chem. Sci.*, 2015, **6**, 613–617.

24 G. E. Eperon, S. D. Stranks, C. Menelaou, M. B. Johnston, L. M. Herz and H. J. Snaith, Formamidinium lead trihalide: a broadly tunable perovskite for efficient planar heterojunction solar cells, *Energy Environ. Sci.*, 2014, **7**, 982.

25 A. Guerrero, J. You, C. Aranda, Y. S. Kang, G. Garcia-Belmonte, H. Zhou, J. Bisquert and Y. Yang, Interfacial Degradation of Planar Lead Halide Perovskite Solar Cells, *ACS Nano*, , DOI:10.1021/acsnano.5b03687.

26 M. D. Bastiani, G. Dell'Erba, M. Gandini, V. D'Innocenzo, S. Neutzner, A. R. S. Kandada, G. Grancini, M. Binda, M. Prato, J. M. Ball, M. Caironi and A. Petrozza, Ion Migration and the Role of Preconditioning Cycles in the Stabilization of the J–V Characteristics of Inverted Hybrid Perovskite Solar Cells, *Adv. Energy Mater.*, 2016, **6**, 1501453.

27 A. Guerrero, G. Garcia-Belmonte, I. Mora-Sero, J. Bisquert, Y. S. Kang, T. J. Jacobsson, J.-P. Correa-Baena and A. Hagfeldt, Properties of Contact and Bulk Impedances in Hybrid Lead Halide Perovskite Solar Cells Including Inductive Loop Elements, *J. Phys. Chem. C*, 2016, **120**, 8023–8032.

28 L. Contreras-Bernal, M. Salado, A. Todinova, L. Calio, S. Ahmad, J. Idígoras and J. A. Anta, Origin and Whereabouts of Recombination in Perovskite Solar Cells, *J. Phys. Chem. C*, 2017, **121**, 9705–9713.

29 I. Zarazua, G. Han, P. P. Boix, S. Mhaisalkar, F. Fabregat-Santiago, I. Mora-Seró, J. Bisquert and G. Garcia-Belmonte, Surface Recombination and Collection Efficiency in Perovskite Solar Cells from Impedance Analysis, *J. Phys. Chem. Lett.*, 2016, **7**, 5105–5113.

30 A. Pockett, G. E. Eperon, T. Peltola, H. J. Snaith, A. Walker, L. M. Peter and P. J. Cameron, Characterization of Planar Lead Halide Perovskite Solar Cells by Impedance Spectroscopy, Open-Circuit Photovoltage Decay, and Intensity-Modulated Photovoltage/Photocurrent Spectroscopy, *J. Phys. Chem. C*, 2015, **119**, 3456–3465.

31 I. Zarazua, J. Bisquert and G. Garcia-Belmonte, Light-Induced Space-Charge Accumulation Zone as Photovoltaic Mechanism in Perovskite Solar Cells, *J. Phys. Chem. Lett.*, 2016, **7**, 525–528.

32 Z. Zolfaghari, E. Hassanabadi, D. Pitarch-Tena, S. J. Yoon, Z. Shariatinia, J. van de Lagemaat, J. M. Luther and I. Mora-Seró, Operation Mechanism of Perovskite Quantum Dot Solar Cells Probed by Impedance Spectroscopy, *ACS Energy Lett.*, 2018, **4**, 251–258.

33 E. J. Juarez-perez, M. Wuβler, F. Fabregat-santiago, K. Lakus-wollny, E. Mankel, T. Mayer, W. Jaegermann and I. Mora-sero, *Role of the Selective*

Contacts in the Performance of Lead Halide Perovskite Solar Cells, .

34 M. Anaya, W. Zhang, B. C. Hames, Y. Li, F. Fabregat-Santiago, M. E. Calvo, H. J. Snaith, H. Míguez and I. Mora-Seró, Electron injection and scaffold effects in perovskite solar cells, *J. Mater. Chem. C*, 2017, **5**, 634–644.

35 I. Zarazúa, S. Sidhik, T. Lopéz-Luke, D. Esparza, E. De la Rosa, J. Reyes-Gomez, I. Mora-Seró and G. Garcia-Belmonte, Operating Mechanisms of Mesoscopic Perovskite Solar Cells through Impedance Spectroscopy and J–V Modeling, *J. Phys. Chem. Lett.*, 2017, **8**, 6073–6079.

36 W. Tress, M. Yavari, K. Domanski, P. Yadav, B. Niesen, J. P. C. Baena, A. Hagfeldt and M. Graetzel, Interpretation and evolution of open-circuit voltage, recombination, ideality factor and subgap defect states during reversible light-soaking and irreversible degradation of perovskite solar cells, *Energy Environ. Sci.*, 2018, **11**, 155–165.

37 D. Bi, W. Tress, M. I. Dar, P. Gao, J. Luo, C. Renevier, K. Schenk, A. Abate, F. Giordano, J.-P. Correa Baena, J.-D. Decoppet, S. M. Zakeeruddin, M. K. Nazeeruddin, M. Grätzel and A. Hagfeldt, Efficient luminescent solar cells based on tailored mixed-cation perovskites, *Sci. Adv.*, 2016, **2**, e1501170.

38 S. R. Raga, E. M. Barea and F. Fabregat-Santiago, Analysis of the Origin of Open Circuit Voltage in Dye Solar Cells, *J. Phys. Chem. Lett.*, 2012, **3**, 1629–1634.

39 J. Idígoras, L. Pellejà, E. Palomares and J. A. Anta, The redox pair chemical environment influence on the recombination loss in dye-sensitized solar cells, *J. Phys. Chem. C*, 2014, **118**, 3878–3889.

40 A. Zohar, M. Kulbak, I. Levine, G. Hodes, A. Kahn and D. Cahen, What Limits the Open-Circuit Voltage of Bromide Perovskite-Based Solar Cells?, *ACS Energy Lett.*, 2018, **4**, 1–7.

41 J. Bisquert, L. Bertoluzzi, I. Mora-Sero and G. Garcia-Belmonte, Theory of impedance and capacitance spectroscopy of solar cells with dielectric relaxation, drift-diffusion transport, and recombination, *J. Phys. Chem. C*, 2014, **118**, 18983–18991.

Chapter 9

Homeopathic Perovskite Solar Cells: Effect of Humidity during Fabrication on the Performance and Device Stability

Rapid degradation in humid environments is the major drawback of $MAPbI_3$*. In this Chapter, we have investigated the aging and degradation kinetics of* $MAPbI_3$ *films and devices fabricated under controlled conditions as a function of relative humidity, and compared their performance with those that were prepared under dry conditions. The aging and degradation kinetics is monitored by optical absorption and impedance spectroscopy measurements under monochromatic illumination at two different wavelengths. Aged devices show a substantial difference between the recombination rate under red and blue light illumination, which was attributed in previous Chapters to the enhancement of local recombination routes. Interestingly, we observe that this feature is less pronounced in devices prepared under conditions of the highest relative humidity of 50%. In addition, chemical analysis by XPS reveals the presence of coordinating water in the* $CH_3NH_3PbI_3$ *crystalline structure which seems to have a beneficial effect against degradation in a humid environment.*

This chapter is based on Publication 5 of this Thesis: Contreras-Bernal *et. al.* J. Phys. Chem. C, 2018, 122, 5341–5348.

9.1 Introduction

In previous *Chapters*, it has been mentioned that the stability of perovskite solar cells is mainly depending on the degradation of perovskite layer under several environmental factors such as light, heat, oxygen and/or moisture.[1,2] In connection with moisture-induced degradation, it has been proposed that the process for film degradation can be triggered by just a few molecules of water. In the particular case of $MAPbI_3$, H_2O is a Lewis base and can coordinate to the Pb atom and have an important influence on the hydrogen bonding between the MA and the Pb−I cage. The hydrates that can form during sample preparation modify the electronic properties of the material, even when no defect can be visually detected.[3,4] The effect of moisture in $MAPbI_3$ is easily detected by absorbance measurements[5] and even with the naked eye when the brownish perovskite film turns to yellow due to the formation of PbI_2.

Recently Guerrero *et al.* have shown that this donor property of the water molecules with the ammonium groups can be taken advantage of, and devised a preparation procedure under ambient conditions with relative humidity of up to 60%.[6] By controlling the proportion of the DMSO additive with respect to the Pb_2^+ concentration as a function of the RH of the ambient atmosphere, it is possible to fabricate highly homogeneous films under ambient conditions. Using this methodology, PCEs approaching 19% for devices fabricated in humid environment are achieved, which are in the range of the highest reported efficiencies for this type of perovskite prepared in dry conditions.[7,8]

On the other hand, using precursor formulations in which the two competing donors DMSO and ambient H_2O are not adequately balanced leads to the formation of chemical defects (plumbates, hydrates) that can act as recombination centers (see *Chapter* 2 for more information).

In this *Chapter*, the degradation kinetics and the electrical response of $MAPbI_3$ solar cells fabricated at environmental conditions have been investigated. During preparation, the RH of the environment is perfectly controlled. The perovskite films and devices have been analysed by optical absorption measurements and impedance spectroscopy analysis, respectively. The latter is carried out with two excitation wavelengths following the methodology described in *Chapter* 5. In addition, chemical XPS analysis was performed on the fabricated films.

9.2 Fabrication and characterization of devices

Fabrication of perovskite solar cells

Perovskite devices with mesoporous regular architecture were fabricated following the methodology described in *Chapter* 3. First of all, FTO TEC15 were cleaned following the solvent sequence: Hellmanex solution; Deionized water; Ethanol; Isopropanol. Then, TiO_2 compact layer was deposited by spray pyrolysis. After that, a mesoporous layer of TiO_2 was deposited on top of a TiO_2 compact layer. A pure methylammonium ($MAPbI_3$) layer was deposited as active layer at environmental humidity conditions. According the methodology reported,[6] for the different ambient moisture conditions (with a RH of 50%, 40%, 30% and 0%, this latter in glovebox), the molar ratio of DMSO in perovskite precursor solution was changed with values 0.75; 1; 1; 1.5, respectively. After perovskite deposition, spiro-OMeTAD solution was spin coated. Following, 60 nm of gold was deposited by thermal evaporation. Only for humidity conditions of 0% RH the devices were prepared inside an argon glove box from precursor solution $MAPbI_3$ 1.2 M. (See *Chapter* 3 for details).

Characterization of devices

IV curves were measured under a solar simulator (ABET-Sun2000) with an AM 1.5G filter. The current-voltage curves were obtained using a scan rate of 100 mV/s and sweep delay of 20 s. Aging was studied by subjecting perovskites solar devices prepared under different moisture conditions (RH: 0%, 30% 40% and 50%) to ambient air in darkness during 15 days under environmental moisture conditions with a RH in the range of 30% - 60%. In addition, perovskite films deposited on the TiO_2 substrate were subjected to an accelerating degradation treatment by exposing the film to humid air with a RH >85% for a relatively long period of time. The illumination for the IS measurements was provided by a red (λ = 635 nm) and blue (λ = 465 nm) LEDs over a wide range of DC light intensities. As it was shown in *Chapter* 5, this allows for probing the devices with two distinct optical penetrations.[9] In these experiments a 20 mV perturbation in the 10^6-10^{-2} Hz range was applied. The measurements were performed at the open circuit potential, the Fermi level (related to the open-circuit voltage) being fixed by the DC (bias) illumination intensity. To compensate for the different response under blue and red light due to the different optical absorption all parameters are monitored and plotted as a function of the open-circuit potential generated by each type of bias light. UV-Visible absorption spectra were recorded in the range of 400-850 nm. XPS was used to analyse the chemical composition and the presence of water in the samples. SEM images of the samples were performed as well.

9.3 Results and discussion

The photovoltaic parameters of fresh and aged devices prepared under different ambient moisture conditions (RH: 0, 30, 40 and 50%) are compared in Table 9.1 and Figure A-9.1 in appendix G. Devices were aged by subjecting the devices to environmental conditions with a RH in the range of 30-60% in darkness during 15 days, similar to the ISOS-D1-shelftest protocol where the humidity is controlled.[10] Fresh devices show an almost constant average energy conversion efficiency of around 14% (see Table 9.1). After aging, this efficiency is reduced by 1% for the devices fabricated in dry conditions. In contrast, the devices made under the highest humidity (50%) get their efficiencies even increased, with recorded values well exceeding 15%. It is observed that the efficiency loss is mainly due to a deterioration of the fill factor of the devices. The efficiency boost is, though, linked to an enhancement of the short-circuit photocurrent. This effect can be related to the increase of the optical absorbance of the $MAPbI_3$ upon accelerated degradation as shown and discussed in the appendix G (section A-9.2). The open-circuit potential remains basically unaltered after aging although a slight decrease can be detected.

Table 9.1. Photovoltaic parameters under AM1.5 1 sun illumination of fresh (top) and aged (bottom) $MAPbI_3$ solar cells fabricated under different humid conditions. Error bars extracted from statistical analysis of the measurements of 3-5 devices are added to the data.

RH (%)	J_{sc} (A·cm^{-2})	V_{OC} (V)	FF (%)	EFF (%)
		FRESH		
0	19.70 ± 0.88	1.05 ± 0.01	69.0 ± 0.6	14.4 ± 0.7
30	21.20 ± 0.52	1.01 ± 0.02	65.3 ± 1.9	14.0 ± 0.6
40	20.63 ± 1.41	1.04 ± 0.01	66.2 ± 6.5	14.2 ± 0.8
50	20.53 ± 0.35	1.04 ± 0.01	66.6 ± 1.6	14.2 ± 0.3
		AGED		
0	20.62 ± 0.18	1.04 ± 0.08	61.0 ± 4.7	13.1 ± 1.3
30	22.13 ± 0.89	0.96 ± 0.02	62.0 ± 3.3	13.4 ± 0.5
40	23.36 ± 0.81	0.95 ± 0.03	63.0 ± 4.0	14.1 ± 1.0
50	24.53 ± 0.52	1.01 ± 0.06	62.2 ± 3.3	15.4 ± 0.5

In Figure 9.1 a comparison between the absorbance degradation kinetics of samples prepared inside the glove box (dry conditions) and under ambient moisture conditions (RH: 50%) is depicted when stressed with humid air.

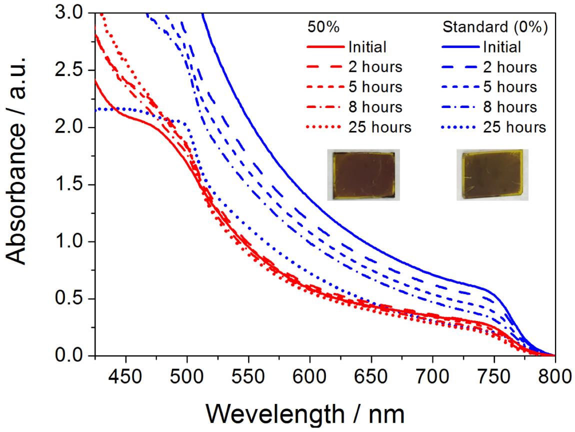

Figure 9.1. Optical absorption data of bare $MAPbI_3$ films deposited on TiO_2 substrates by solvent engineering under 50% RH (red lines) and at dry conditions (blue lines). Between 0 and 25 hours the films were exposed to a flow of humid air (> 85% RH). Photographs of the two films after the degradation treatment are also added to the picture. Note that the two recipes do not produce the same film thickness, hence the different initial absorption.

The absorption spectrum of a perovskite film prepared under a RH of 50% remains basically unaltered after being vented in very humid air (RH >85). In fact, even led to a slight increase of the absorbance at short wavelengths. This increase in absorbance has been correlated previously with a decrease of under-coordinated plumbate ions.[11] In contrast, the films prepared in the glove box show a dramatic decrease of the absorbance, especially after 25 hours. This result confirms the exceptional stability of the films formed under humid conditions towards moisture-induce degradation.

The stability of the perovskite films after moisture exposure can also be studied by SEM images of fresh and degraded films fabricated at three different humidity conditions: 30%, 40% and 50% (Fig. 9.2). Perovskite films deposited at RH of 40% was employed as reference. The used recipe produces homogeneous films with no pinholes and an approximately constant crystal size of around 200 nm. Degradation upon exposure to humid air (RH >85%) show up in the form of inhomogeneities and pinholes. An increase of the grain size is also observed.[12] The number of pinholes is reduced and the homogeneity of the sample is significantly improved against moisture exposure the larger is the humidity used in the preparation of the films. On the other hand, as mentioned, ambient water promotes increased crystalline domains from about 100 nm for the reference device to up to 500-600 nm. This observation can be explained by the action of ambient water, which acts as an additive that can promote Ostwald ripening effect and increase the domain size as recently reported with Guanidinium Thiocyanate.[13]

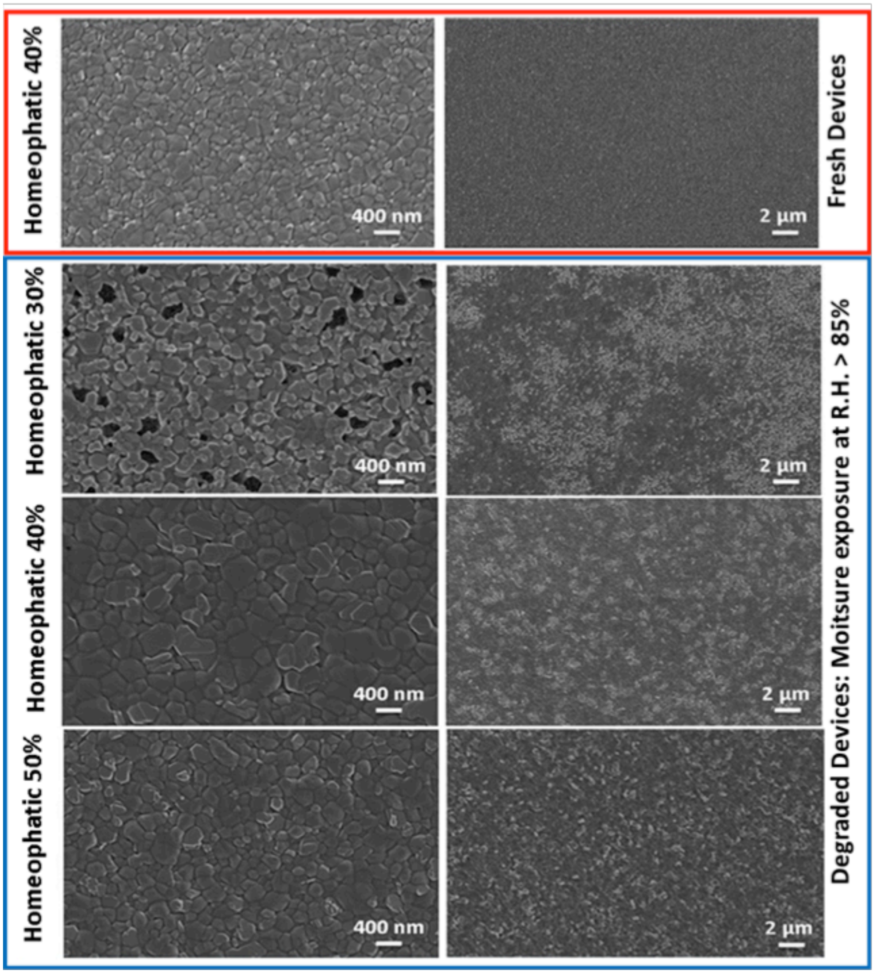

Figure 9.2. SEM images of fresh perovskite films fabricated at R.H.=40% (top) and after degradation (bottom). Results for degraded films with very humid air (> 85% R.H.) but prepared at different ambient humidity values are shown.

The robustness of the films fabricated under ambient conditions suggests that these films retain some water molecules in the crystalline structure, thus preventing further invasion by moisture. To test this hypothesis XPS measurements were performed for fresh samples deposited at different relative humidity values, that is, 0%, 30%, 40% and 50% (XPS measurements were performed by the group of Dr. Navas in the university of Cádiz). Figure A-9.3 in the appendix G shows the survey spectra for the samples. The peaks are assigned to the elements which compose the perovskite phase: C, N, Pb and I. In turn, no evidence of Ti is observed, which confirms that only the perovskite layer is analysed. However, a weak O 1s signal, produced by small amounts of water in the perovskite structure, can be detected. Figures A-9.4 and 9.3A show the O 1s signal obtained for fresh samples. The binding energy (BE) for O 1s signal for the four samples is about 531.5 eV. As reported previously, the presence of coordinating (hydrating) water appears in the range between 531.0 - 531.6 eV.[14] This signal at BE of 531.5 eV cannot be assigned to O^{2-} in the lattice of oxide species as this type of signal is typically observed at BE lower than 530 eV. For instance, in the case of lead oxides, they appear between 528.4 and 529.4 eV. Other typical assignation for O 1s signal is to adsorbed species, such as water, hydroxyl groups or carboxylates species, but these contributions normally show up at BE higher than 532 eV.[15–17] On the other hand, Figure 9.3B shows the Pb 4f signal for the sample exposed to 50% RH, which is considered as representative for all the samples analysed. The peaks for Pb $4f_{7/2}$ and $4f_{5/2}$ appear at 138.4 eV, and 143.3 eV, respectively. The 4.9 eV separation between this spin-orbit components is typical for Pb(II).[18] Figure 9.3B also includes a deconvolution of the Pb $4f_{7/2}$ signal. Two contributions can be extracted. The main contribution (peak 1) at a BE of 138.4 eV is assigned usually[18] to PbI_2. This is the contribution from the Pb-I bonds of the perovskite. The small contribution (peak 2) appears at about 137.4 eV. The signals around this value of BE for Pb $4f_{7/2}$ are usually ascribed to species in which Pb-O interactions are present.

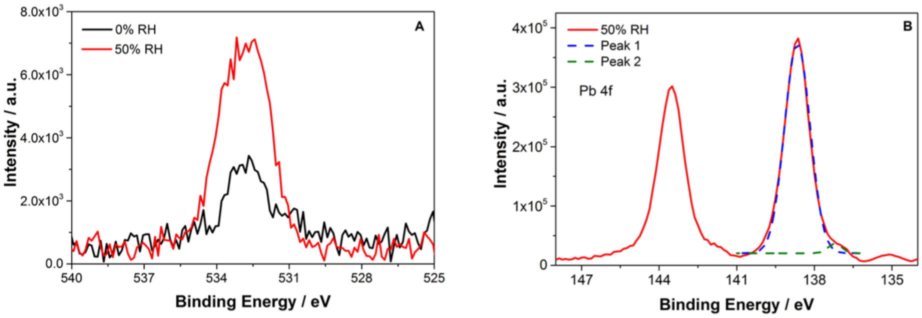

Figure 9.3. O 1s and Pb 4f signals obtained from XPS measurements of fresh perovskite thin films deposited on top of mesoporous TiO_2 layers fabricated at different ambient humidity values.

Therefore, for XPS measurements, the presence of coordinating water can be deduced from the energy position of the O 1s signal and it is confirmed with the analysis of the Pb 4f signal. Although a signal is observed in the sample deposited under dry conditions (RH: 0%) (probably due to residual water during sample manipulation), it is significantly smaller than the signal obtained in films deposited under ambient conditions with a RH of 50% . Nevertheless, due to the low intensity of the signal, the evolution of the water content with respect to the relative humidity (Fig. A-9.4) cannot be safely monitored from these measurements. In any case, the presence of coordinating water molecules around the Pb cations explains the molecular stability of the perovskite films towards inclusion of additional water during aging or degradation experiments.

Finally, to verify the change in the internal functioning of the perovskite solar cell upon aging, impedance spectroscopy measurements at open circuit were carried out. The IS response of PSCs is typically characterized by the appearance of two signals (peaks in the frequency plots or arcs in the Nyquist plot). The analysis of the evolution of these arcs can be inversely related with the recombination rate as it was previously described. Here, we focus on the *HF* region, in the 10^3- 10^6 range, which is bulk recombination (*Chapter* 5) and is affected by the transport in the selective contacts and interfaces.[19,20] The measurements were carried out with two excitation wavelengths, characterized by a different penetration of the light into the perovskite layer (see *Chapter* 5).[9]

The *HF* resistance (R_{HF}) has been extracted from the impedance spectra by fitting the data to a simple *Voight* circuit (see inset Fig. 3.9A in *Chapter* 3).[21] The corresponding high frequency resistance R_{HF} is plotted in Figure 9.4 as a function of the V_{OC} originated by the different illumination intensities applied, and the two excitation wavelengths employed in the experiment. The ideality factors extracted from β-parameter ($m=1/\ \beta$, see *Chapter* 5) are reported in Table 9.2.

Table 9.2. Ideality factors for fresh and aged (after environmental moisture exposure during 15 days, RH: 30-60%) cells as extracted from the high frequency resistances in Figure 9.4.

RH (%)	**Ideality factor**			
	Fresh cell		Degraded cell	
	Blue	Red	Blue	Red
0	2.38 ± 0.01	2.44 ± 0.02	2.94 ± 0.08	2.78 ± 0.08
30	1.75 ± 0.01	1.85 ± 0.09	2.44 ± 0.01	2.50 ± 0.06
40	1.69 ± 0.01	1.85 ± 0.01	1.92 ± 0.06	1.96 ± 0.06
50	2.08 ± 0.06	2.08 ± 0.14	1.75 ± 0.05	1.75 ± 0.01

The analysis of the ideality factors reveals that they are approximately the same for both blue and red light illumination. They have values close to 2, which can be attributed to bulk Shockley- Read-Hall recombination.[9,22–24] However, there is a clear net enhancement in the recombination rate after degradation, as evidenced by the lower values of R_{HF} in Figure 9.4. This result is in line with reduction of the V_{OC} at 1 sun illumination reported in Table 9.1, which indicates that the inclusion of ambient water into the perovskite structure introduces recombination centers and additional routes of non-radiative recombination.

Furthermore, the degraded devices exhibit a different value of the recombination resistance depending on whether red or blue light is used to generate the open-circuit potential. Lower values of R_{HF} are observed under red light illumination in all aged devices. Bearing in mind red light illumination produces photo-generated carriers further away from the TiO_2/perovskite interface in comparison with blue light due to the lower light absorption in the red, the results can be interpreted as (1) a magnification of the recombination loss close to the perovskite/hole transport material interface and/or (2) a global acceleration of the bulk recombination rate, leading to shorter diffusion lengths.[9]

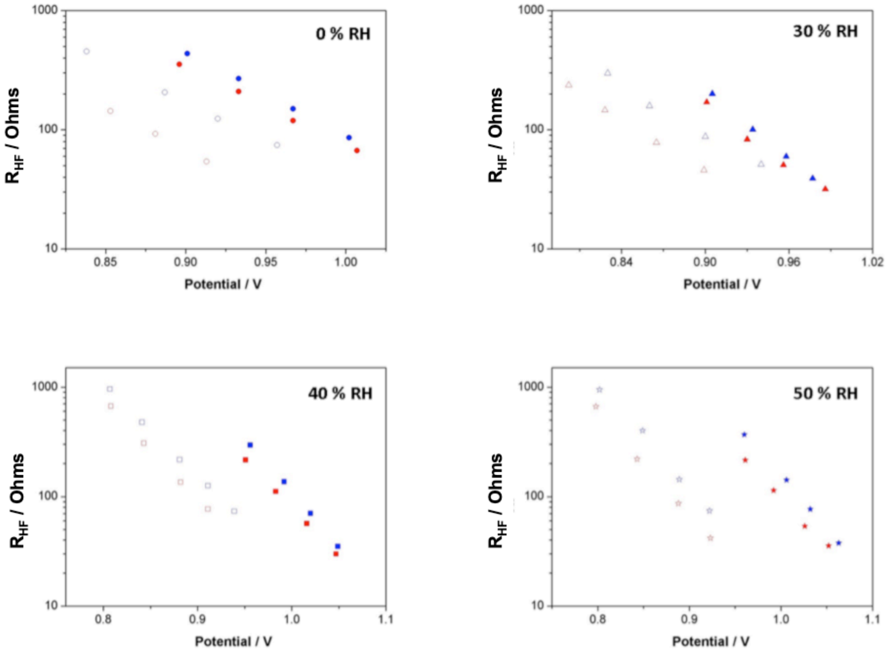

Figure 9.4. High frequency resistance versus open-circuit potential for fresh and aged (after environmental moisture exposure during 15 days, RH: 30-60%) devices prepared under different humidity conditions (a: 0%, b: 30%, c: 40%, d: 50%). Red and blue symbols stand for the data extracted under red and blue light illumination, respectively. Solid symbols correspond to fresh devices and open symbols to aged devices.

An important property also arises from the analysis of the results: those cells which are fabricated at conditions of higher humidity tend to withstand better the negative effect of aging. Thus, devices prepared at 0% and 30% humidity, show a clear splitting of the "red" and "blue" resistances upon degradation. In contrast, cells made at 40% and 50% humidity show less disparity between the two values of R_{HF}.

Similar conclusions can be extracted from the analysis of the frequency plots (Fig. 9.5). In the studied frequency range, a distinct peak at around 10^4-10^5 Hz is detected.

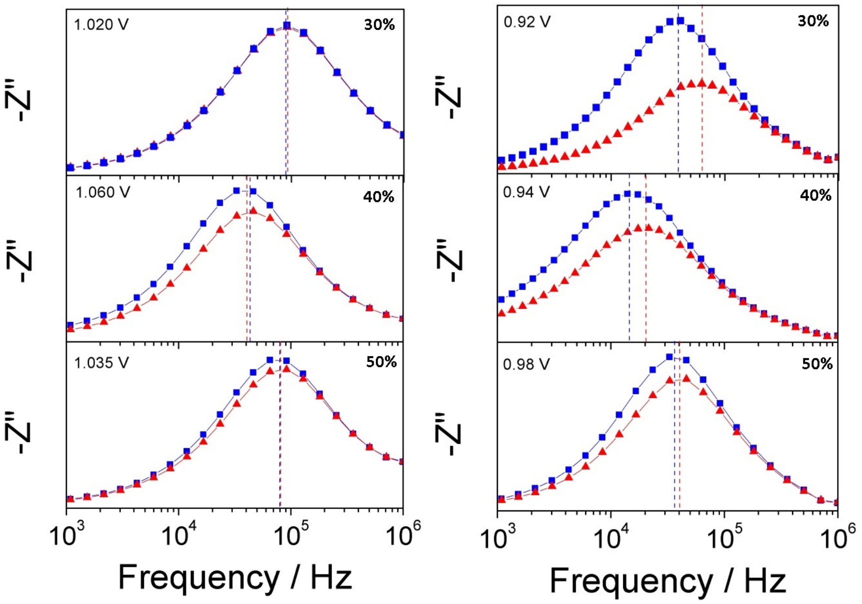

Figure 9.5. Imaginary part of the impedance in the 10^6-10^3 Hz frequency range for fresh (left) and aged (right) $MAPbI_3$ perovskite solar cells prepared at RH values of 30% (top), 40% (middle) and 50% (bottom). Aging was carried by environmental moisture exposure for 15 days with RH: 30-60%. Data obtained under red and blue light illumination are shown. The open-circuit photopotentials generated by the illumination are indicated in the graphs.

Although the inverse of the corresponding frequency signal cannot be considered a real carrier lifetime, its time scale and its behaviour for different architectures and Fermi level positions strongly suggest that it is related with the recombination rate of photogenerated carriers in the device (see *Chapter* 5 and Refs. [21,25,26]). The comparison of the behaviour of this signal for fresh and aged devices reveals that whereas for the former the “lifetime” is basically the same for red and blue light illuminations, the positions of the peaks for the latter are significantly different. Furthermore, the splitting of the red and blue signals tends to be more pronounced for the devices fabricated at lower humidity conditions.

The robustness of the prepared devices is also confirmed when the apparent capacitance extracted from impedance is analysed (Fig. A-9.5). In *Chapter* 7, solar devices used were fabricated at dry glove box conditions and showed the appearance of an additional capacitive process after aging, evidenced by a distortion of the high frequency arc and the disappearance of the mid-frequency plateau. Interestingly, these features are not observed for the devices fabricated at ambient humid conditions.

9.4 Conclusion

Preparation of $MAPbI_3$ perovskite films at controlled ambient humidity leads to solar cell devices which are more robust against moisture-induced aging and degradation than those prepared under dry conditions or low RH values. This is a consequence of the presence of small amounts of water, which are incorporated into the $MAPbI_3$ crystalline structure. Although this amount is small the impact on the degradation kinetics and on the optical/electronic properties is very high. The presence of crystallization water is confirmed by XPS analysis, that reveals the presence of small amounts of water, in the form of coordinating molecules around the Pb cations. Based on this observation we tentatively attribute the robustness of the perovskite films to the presence of these water molecules, which prevent the formation of additional hydrates that trigger the degradation mechanism.

On the other hand, degradation of samples prepared under dry conditions produces an acceleration of recombination. This is evidenced by a small deterioration of the V_{OC} and the increase of the recombination rate. Aging also leads to a different impedance response under different optical penetration depths of the bias light. These negative features are found to be larger for devices prepared at conditions of lower humidity. These results demonstrate that “homeopathic” additions of water during perovskite preparation are beneficial against moisture-induced aging.

9.5 References

1 Z. Wang, Z. Shi, T. Li, Y. Chen and W. Huang, Stability of Perovskite Solar Cells: A Prospective on the Substitution of the A Cation and X Anion, *Angew. Chem. Int. Ed.*, 2017, **56**, 1190–1212.

2 N. H. Tiep, Z. Ku and H. J. Fan, Recent Advances in Improving the Stability of Perovskite Solar Cells, *Adv. Energy Mater.*, 2016, **6**, 1501420.

3 A. M. A. Leguy, Y. Hu, M. Campoy-Quiles, M. I. Alonso, O. J. Weber, P. Azarhoosh, M. van Schilfgaarde, M. T. Weller, T. Bein, J. Nelson, P. Docampo and P. R. F. Barnes, Reversible Hydration of $CH_3NH_3PbI_3$ in Films, Single Crystals, and Solar Cells, *Chem. Mater.*, 2015, **27**, 3397–3407.

4 J. M. Frost, K. T. Butler, F. Brivio, C. H. Hendon, M. van Schilfgaarde and A. Walsh, Atomistic Origins of High-Performance in Hybrid Halide Perovskite Solar Cells, *Nano Lett.*, 2014, **14**, 2584–2590.

5 J. Yang, B. D. Siempelkamp, D. Liu and T. L. Kelly, Investigation of $CH_3NH_3PbI_3$ Degradation Rates and Mechanisms in Controlled Humidity Environments Using *in Situ* Techniques, *ACS Nano*, 2015, **9**, 1955–1963.

6 C. Aranda, C. Cristobal, L. Shooshtari, C. Li, S. Huettner and A. Guerrero, Formation criteria of high efficiency perovskite solar cells under ambient conditions, *Sustain. Energy Fuels*, 2017, **1**, 540–547.

7 J. Burschka, N. Pellet, S.-J. Moon, R. Humphry-Baker, P. Gao, M. K. Nazeeruddin and M. Grätzel, Sequential deposition as a route to high-performance perovskite-sensitized solar cells, *Nature*, 2013, **499**, 316–319.

8 D. Y. Son, J. W. Lee, Y. J. Choi, I. H. Jang, S. Lee, P. J. Yoo, H. Shin, N. Ahn, M. Choi, D. Kim and N. G. Park, Self-formed grain boundary healing layer for highly efficient CH3 NH3 PbI3 perovskite solar cells, *Nat. Energy*, 2016, **1**, 16081.

9 L. Contreras-Bernal, M. Salado, A. Todinova, L. Calio, S. Ahmad, J. Idígoras and J. A. Anta, Origin and Whereabouts of Recombination in Perovskite Solar Cells, *J. Phys. Chem. C*, 2017, **121**, 9705–9713.

10 M. O. Reese, S. A. Gevorgyan, M. Jørgensen, E. Bundgaard, S. R. Kurtz, D. S. Ginley, D. C. Olson, M. T. Lloyd, P. Morvillo and E. A. Katz, Consensus stability testing protocols for organic photovoltaic materials and devices, *Sol. Energy Mater. Sol. Cells*, 2011, **95**, 1253–1267.

11 S. Rahimnejad, A. Kovalenko, S. M. Forés, C. Aranda and A. Guerrero, Coordination Chemistry Dictates the Structural Defects in Lead Halide Perovskites, *ChemPhysChem*, 2016, **17**, 2795–2798.

12 B. Roose, A. Ummadisingu, J.-P. Correa-Baena, M. Saliba, A. Hagfeldt, M. Graetzel, U. Steiner and A. Abate, Spontaneous crystal

coalescence enables highly efficient perovskite solar cells, *Nano Energy*, 2017, **39**, 24–29.

13 N. D. Pham, V. T. Tiong, D. Yao, W. Martens, A. Guerrero, J. Bisquert and H. Wang, Guanidinium thiocyanate selective Ostwald ripening induced large grain for high performance perovskite solar cells, *Nano Energy*, 2017, **41**, 476–487.

14 M. C. Biesinger, B. P. Payne, A. P. Grosvenor, L. W. Lau, A. R. Gerson and R. S. C. Smart, Resolving surface chemical states in XPS analysis of first row transition metals, oxides and hydroxides: Cr, Mn, Fe, Co and Ni, *Appl. Surf. Sci.*, 2011, **257**, 2717–2730.

15 B. Schumacher, V. Plzak, J. Cai and R. J. Behm, Reproducibility of highly active Au/TiO 2 catalyst preparation and conditioning, *Catal. Lett.*, 2005, **101**, 215–224.

16 H. Liu, W. Yang, Y. Ma, Y. Cao, J. Yao, J. Zhang and T. Hu, Synthesis and characterization of titania prepared by using a photoassisted sol- gel method, *Langmuir*, 2003, **19**, 3001–3005.

17 Y. V. Zubavichus, Y. L. Slovokhotov, M. K. Nazeeruddin, S. M. Zakeeruddin, M. Grätzel and V. Shklover, Structural characterization of solar cell prototypes based on nanocrystalline TiO2 anatase sensitized with Ru complexes. X-ray diffraction, XPS, and XAFS spectroscopy study, *Chem. Mater.*, 2002, **14**, 3556–3563.

18 M. C. Biesinger, L. W. Lau, A. R. Gerson and R. S. C. Smart, Resolving surface chemical states in XPS analysis of first row transition metals, oxides and hydroxides: Sc, Ti, V, Cu and Zn, *Appl. Surf. Sci.*, 2010, **257**, 887–898.

19 A. Guerrero, G. Garcia-Belmonte, I. Mora-Sero, J. Bisquert, Y. S. Kang, T. J. Jacobsson, J.-P. Correa-Baena and A. Hagfeldt, Properties of Contact and Bulk Impedances in Hybrid Lead Halide Perovskite Solar Cells Including Inductive Loop Elements, *J. Phys. Chem. C*, 2016, **120**, 8023–8032.

20 E. J. Juarez-perez, M. Wuβler, F. Fabregat-santiago, K. Lakus-wollny, E. Mankel, T. Mayer, W. Jaegermann and I. Mora-sero, *Role of the Selective Contacts in the Performance of Lead Halide Perovskite Solar Cells*, .

21 A. Todinova, J. Idígoras, M. Salado, S. Kazim and J. A. Anta, Universal Features of Electron Dynamics in Solar Cells with TiO $_2$ Contact: From Dye Solar Cells to Perovskite Solar Cells, *J. Phys. Chem. Lett.*, 2015, **6**, 3923–3930.

22 D. Bi, W. Tress, M. I. Dar, P. Gao, J. Luo, C. Renevier, K. Schenk, A. Abate, F. Giordano, J.-P. Correa Baena, J.-D. Decoppet, S. M. Zakeeruddin, M. K. Nazeeruddin, M. Grätzel and A. Hagfeldt, Efficient luminescent solar cells based on tailored mixed-cation perovskites, *Sci. Adv.*, 2016, **2**, e1501170.

23 W. L. Leong, Z.-E. Ooi, D. Sabba, C. Yi, S. M. Zakeeruddin, M. Graetzel, J. M. Gordon, E. A. Katz and N. Mathews, Identifying Fundamental Limitations in Halide Perovskite Solar Cells, *Adv. Mater.*, 2016, **28**, 2439–2445.

24 W. Tress, M. Yavari, K. Domanski, P. Yadav, B. Niesen, J. P. Correa Baena, A. Hagfeldt and M. Graetzel, Interpretation and evolution of open-circuit voltage, recombination, ideality factor and subgap defect states during reversible light-soaking and irreversible degradation of perovskite solar cells, *Energy Environ. Sci.*, 2018, **11**, 151–165.

25 A. R. Pascoe, N. W. Duffy, A. D. Scully, F. Huang and Y.-B. Cheng, Insights into Planar $CH_3NH_3PbI_3$ Perovskite Solar Cells Using Impedance Spectroscopy, *J. Phys. Chem. C*, 2015, **119**, 4444–4453.

26 K. Pydzińska, J. Karolczak, I. Kosta, R. Tena-Zaera, A. Todinova, J. Idígoras, J. A. Anta and M. Ziółek, Determination of Interfacial Charge-Transfer Rate Constants in Perovskite Solar Cells, *ChemSusChem*, 2016, **9**, 1647–1659.

Chapter 10

Water Vapour Pressure as Determining Control Parameter to Fabricate High Efficiency Perovskite Solar Cells at Ambient Conditions

There is a need of experimental procedures that allow the fabrication of PSCs at ambient conditions in order to decrease substantially manufacturing costs. However, under ambient conditions, a delicate control of the moisture level in the atmosphere has to be enforced to achieve efficient and highly stable devices. In this Chapter, we show that it is the absolute content of water measured in the form of partial water vapour pressure (WVP) the only determining control parameter that needs to be considered during preparation. For that, $MAPbI_3$ *perovskite films were deposited under different WVP by changing the relative humidity and the lab temperature. In addition, we have extended the procedure to accomplish high-efficient* $FA_{0.83}MA_{0.17}PbI_3$ *devices at ambient conditions by adjusting DMSO proportion in precursor solution as a function of WVP only.*

This chapter is based on Publication 6 of this Thesis: Contreras-Bernal *et. al.* Manuscript submitted to Energy & Environmental Science and ArXiv.2019

10.1 Introduction

As many times it has been pointed out in this thesis, PSCs can be fabricated with competitive efficiency (PCE > 20 %)[1–6]. However, these high PCEs have been achieved using testing-devices with a small active area and fabricated under dry conditions inside a glove box. These two issues do not only increase the manufacturing cost and limit its industrial scale, but also restrict its commercialisation.[7–9]

Although perovskite films under certain moisture level have been achieved with a high quality,[10–13] the fact is that these devices have not reached yet the PCEs of their glove box counterparts.[14] Nevertheless, different strategies have been recently reported in the literature to optimize PSCs fabrication under ambient condition.[15–19] One of the most recent methodology is that proposed by Guerrero *et al.*[18] As we saw in previous *Chapter,* they demonstrated that it is possible to prepare highly efficient $MAPbI_3$ perovskite devices under different humidity conditions by controlling the DMSO: Pb^{2+} ratio in the precursor solution as a function of the relative humidity of the environment. We used this methodology in *Chapter* 9 to fabricate solar devices at ambient conditions, and showed that these devices are more robust against moisture-induced ageing and degradation than those prepared at low RH values or dry conditions.[20] On the other hand, the addition of both thiocyanate ions or orthosilicate in perovskite precursor solution[16,17,21] or the use of pre-heating treatments of the electron selective contact[15,19] have been suggested as other strategies to fabricate PSCs with high efficiency at ambient conditions.

In all reports up to the date related to the preparation of PSCs outside glove box, RH is considered as the main control parameter to fabricate solar devices. Nevertheless, RH is a relative parameter that depends of the saturation value of water vapour in air, which depends on the temperature. The maximum amount of water molecules in the vapour phase (saturation), which is able to hold a system is determined by the Clausius-Clapeyron equation

$$ln\, P_{ws} = -\frac{\Delta H_V}{RT} + C \tag{10.1}$$

where P_{ws} and ΔH_v are the saturation vapour pressure and the water vapourization enthalpy, respectively. R is de ideal gas constant and C is a constant. From Eq. 10.1, a larger vapour pressure is expected for higher temperatures with an exponential correlation. Therefore a small temperature change brings about a larger modification of water content in air, measured as their partial vapour pressure P_w.[22] RH is actually defined as[23]

$$RH\ (\%) = \frac{P_w}{P_{ws}} \cdot 100 \qquad (10.2)$$

Therefore, RH is not an indicative of absolute water content in air which is intimately related to the temperature of the system via Eq. 10.1. This could be the reason of the broad spread of PCE found in the literature for same type of perovskite prepared at the same values of RH, especially taking into account that a small temperature variation produces a huge change in P_w.[17,18] Therefore, RH is not by itself sufficient as control parameter to study and fabricate PSCs under atmospheric conditions. The ambient temperature needs to be considered as well.

In this context, it has been recently proposed to use the dew point as a control parameter in the fabrication procedure.[24] Playing with several temperatures at the same RH, these authors have found an optimum value of the dew point in which the PCE was the highest, showing that it is the absolute content of water the only parameter that matters. However, they only took into account the moisture levels during the annealing stage ignoring the fact that the water content in air affects the perovskite crystallization process in other stages of perovskite films fabrication as well.[12] In this study we choose to use the water vapour pressure (WVP) only as control parameter because it has a more direct and clear physical meaning associated to the RH, temperature and vapourization enthalpy via Eqs. 10.1 and 10.2.

Herein, the impact of WVP during the fabrication process of perovskite devices at ambient conditions in order to achieve high-efficiency solar devices is analysed. For that purpose, FTO/c-TiO_2/m-TiO_2/perovskite/spiro-OMeTAD based devices have been fabricated using $MAPbI_3$ perovskite precursor solution with different DMSO:Pb^{2+} ratio.[18] This perovskite precursor solution was deposited by spin-coating at different environmental conditions (outside glove box). In particular, $MAPbI_3$ based devices were fabricated at different temperatures and RH values. UV-Vis spectra, photoluminescence measurements and impedance spectroscopy analysis were employed as characterization techniques to explain the photovoltaic parameters obtained for the PSCs as function of WVP. Finally, by setting WVP as the main control humidity parameter, we have achieved $FA_{0.83}MA_{0.17}PbI_3$ based PSCs under highly humid conditions. To our best knowledge, this is the first work in the literature where the photovoltaic parameters are reported as a function of the absolute content of water molecules in air in the form of a partial water vapour pressure.

10.2 Fabrication and characterization of devices

Fabrication of perovskite solar cells

Perovskite devices with mesoporous regular architecture were fabricated following the methodology described in *Chapter* 3. First, FTO TEC15 were cleaned following the solvent sequence: Hellmanex solution; Deionized water; Ethanol; Isopropanol. Then, TiO_2 compact layer was deposited by spray pyrolysis. After that, a mesoporous layer of TiO_2 was deposited on top of a TiO_2 compact layer. A pure methylammonium ($MAPbI_3$) and double-cation perovskite ($FA_{0.83}MA_{0.17}PbI_3$) were deposited as active layer at environmental humidity conditions. According the methodology reported,[18] $MAPbI_3$ precursor solution was prepared with different DMSO:PbI_2 molar ratio (0; 0.5; 0.75; 1; 1.25; 1.5). While $FA_{0.83}MA_{0.17}PbI_3$ perovskite precursor solution was obtained by adjusting DMSO:PbI_2 molar ratio to 0.75. After perovskite deposition, spiro-OMeTAD solution was spin coated. Finally, 60 nm of gold was deposited by thermal evaporation. (See *Chapter* 3 for details)

Characterization of devices

IV curves were measured under a solar simulator (ABET-Sun2000) with an AM 1.5G filter. The current-voltage curves were obtained using a scan rate of 100 mV/s and sweep delay of 20 s. The illumination for the Impedance Spectroscopy measurements was provided by red (λ = 635 nm) and blue (λ = 465 nm) LEDs over a wide range of DC light intensities. As it was shown in *Chapter* 5, this allows for probing the devices with two distinct optical penetrations.[25] In these experiments a 20 mV perturbation in the 10^6 - 0.1 Hz range was applied. The measurements were performed at the open circuit potential, the Fermi level (related to the open-circuit voltage) being fixed by the DC (bias) illumination intensity. To compensate for the different response under blue and red light due to the different optical absorption all parameters are monitored and plotted as a function of the open-circuit potential generated by each type of bias light. UV-Visible absorption spectra in the range of 400-850 nm and Steady state photoluminescence spectra were recorded as well. X-ray diffractograms were recorded on a Bruker-A25 (D8 Advance) diffractometer using a Cu-Kα1 (1.5406 Å) source. The diffractometer was set in *Grazing incidence geometry* at 2°. SEM images of the samples were also taken.

10.3 Results and discussion

Figure 10.1 shows the best IV curves obtained for $MAPbI_3$ devices prepared at the same value of the RH (50 %) but different temperatures (298 K, 299 K and 301 K). In accordance to Eq. 10.1, higher temperature implies a larger value of the water content in the laboratory atmosphere. In particular, WVP values of 1.58, 1.72 and 1.85 kPa were derived from Eqs. 10.1 and 10.2 for those environmental conditions, respectively. PCEs of 16.7 ± 0.6 %, 11.4 ± 0.6 % and 11.3 ± 0.9 % were obtained at 1.58, 1.72 and 1.85 kPa, respectively. The statistical data of characterization photovoltaic parameters are shown in Figure A-10.1 (see appendix G) as a function of WVP.

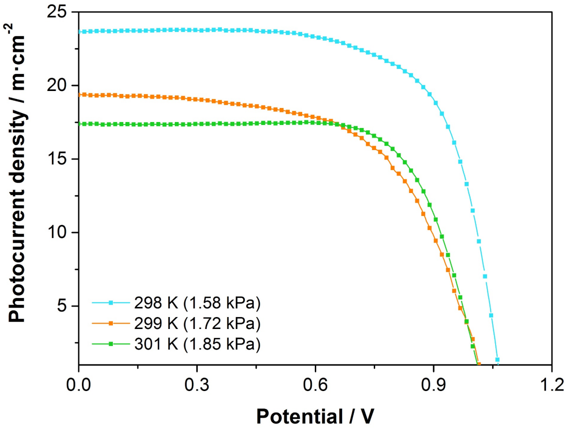

Figure 10.1. Current–voltage curves of $MAPbI_3$ perovskite devices prepared under different temperature conditions but same relative humidity (50 %) (resulting in different WVPs, as indicated). The curves have been measured in reverse scan under 1 sun—AM 1.5 illumination and using a mask of 0.16 cm^2. For all three cases, perovskite films were deposited from a solution precursor with a ratio DMSO:Pb^{2+} of 0.75.

It should be noted that similar PCE values were previously reported for $MAPbI_3$ devices deposited at 50% RH although no specific temperature data was given.[17,18] In this study we show, though, that small temperature changes have a strong impact on the performance, as a consequence of the big jump in the absolute content of water in air. Although the perovskite films looked homogenous regardless of the environmental conditions during the deposition process, a drop of J_{SC} and V_{OC} was clearly observed with the increase of temperature and, consequently, with higher WVPs (Figs. A-10.1B and A-10.1C). Therefore, these results plainly demonstrate the importance of WVP, as the main control parameter to take into account humidity, instead of RH as popularly used in PSC fabrication.

To analyse the effect of DMSO in perovskite precursor solution as a function of water content in air, precursor solutions with different DMSO:Pb^{2+} ratios were employed. WVPs of 1.66 kPa and 1.85 kPa (301 K and RH of 44 % and 49 %, respectively) were considered in these experiments. Figure A-10.2 shows the average photovoltaic parameters obtained using different DMSO:Pb^{2+} ratios in the precursor solutions. The optimum DMSO:Pb^{2+} ratio for the different WVP are in line with the mechanism previously discussed (see *Chapter* 2 and 9).[18,20] Under ambient conditions, the atmospheric H_2O molecules can be incorporated to the lead complex and compete with the DMSO in the coordination sphere of the lead ion. Thus, in humid atmospheres, it is necessary to adjust the content of DMSO in the perovskite precursor solution as a function of WVP to achieve the correct stoichiometry of the $PbI_2 \cdot H_2O \cdot DMSO$ complex. In general, lower amounts of DMSO are required to reach high efficiencies at higher WVP. In particular, an optimum DMSO:Pb^{2+} ratio of 1.0 and 0.75 were found for 1.66 kPa and 1.85 kPa, respectively, for which a maximum efficiency of 15.6 % and 12.5 % were obtained (Fig. A-10.2A). Nevertheless, in both cases, the values obtained using the different DMSO:Pb^{2+} ratios at these environmental conditions were mainly determined by the distinct J_{SC} values (Fig. A-10.2B). In contrast, no significant differences were found for V_{OC} values (Fig. A-10.2C). A further analysis is presented below.

On the other hand, regardless the DMSO:Pb^{2+} ratio, lower efficiencies were revealed for the highest WVP (Fig. A-10.2A). These results are line with the efficiency trends previously reported in which only the RH values were taken into account as main parameter (Fig. 10.1).[11,18] For atmospheric conditions of 1.85 kPa, lower efficiencies (around 12 % for ratio 0.75) were obtained as compared with those reported for the same perovskite deposition methodology (around 15 % for ratio 0.75).[18] This worse performing device could be due to fact that the PSCs were here fabricated at a higher temperature (301 K) than usually reported in literature.[11,19,24] Thus, although the RH were the same, the content of water in air (WVP) has been higher in our experiments than any other before. In this context, a drop of photovoltaic parameters was observed for 1.85 kPa with respect to 1.66 kPa, except to the FF that showed a similar value for intermediate ratios (Fig. A-10.2B, Fig. A-10.2C and Fig. A-10.2D). This further demonstrates that it is the absolute water content in air what really matters when the perovskite film is fabricated.

Average efficiencies for a large range of WVPs are shown in Figure 10.2. The range of WVP analysed corresponds to typical atmospheric conditions throughout one year in a region with Mediterranean climate. The highest efficiencies were found for WVP values lower than 1.66 kPa. Specifically, 16.8 ± 0.9 % efficiencies were obtained for devices prepared at 1.06 kPa (301 K and

28 % RH). In this regime (from 1.0 kPa to around 1.6 kPa), the performance of devices seems to be insensitive to the content of water in air as shown by the plateau obtained for the optimum DMSO:Pb^{2+} ratio of 1.0. The maximum efficiency found in this work (18.2 % for 1.06 kPa) is in line with the maximum reported PCE for $MAPbI_3$ devices.[18,26,27] However, WVPs beyond 1.7 kPa lead to a strong drop in efficiency. This is the case of 1.85 kPa (corresponding to 301 K and 49 % RH) in which the performance of the devices drops to 10.5 ± 1.6 % using even the optimum DMSO:Pb^{2+} ratio of 0.75. Previously, it has been reported that low performance of PSCs at high temperature could be due to a low solubility of perovskite materials in the precursor solution, which could affect the growth of perovskite crystals.[28,29] Nevertheless, it should be noted that the same high temperature was here reached to both the lowest and highest WVP analysed. Therefore, the dispersion in efficiencies appears to result from effects of atmospheric water content during the PSCs fabrication but not due to a change of perovskite solubility. This is an extra argument to further support the importance of using the absolute content of water as control during the perovskite deposition process.

On the other hand, we also observed that the stability under illumination and the reproducibility were worse for the bad performing devices. In consequence, a WVP value of around of 1.6 kPa appears to be an upper limit for safe fabrication of high efficiency devices at ambient conditions.

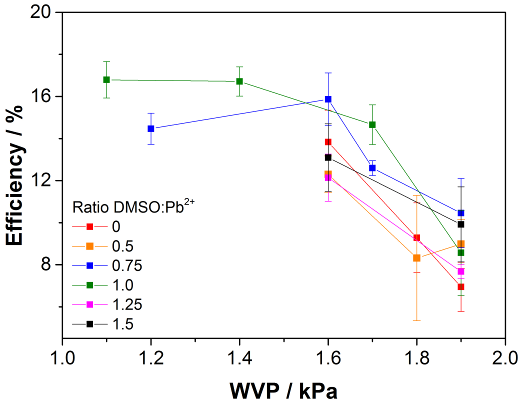

Figure 10.2. Efficiency obtained for $MAPbI_3$ devices as a function of the water vapour pressure (WVP) during perovskite deposition. Alternative values of the DMSO:Pb^{2+} ratio of the precursor are compared as indicated. The efficiency has been extracted from current-voltage curves measured under 1 sun—AM 1.5 illumination using a mask of 0.16 cm^2.

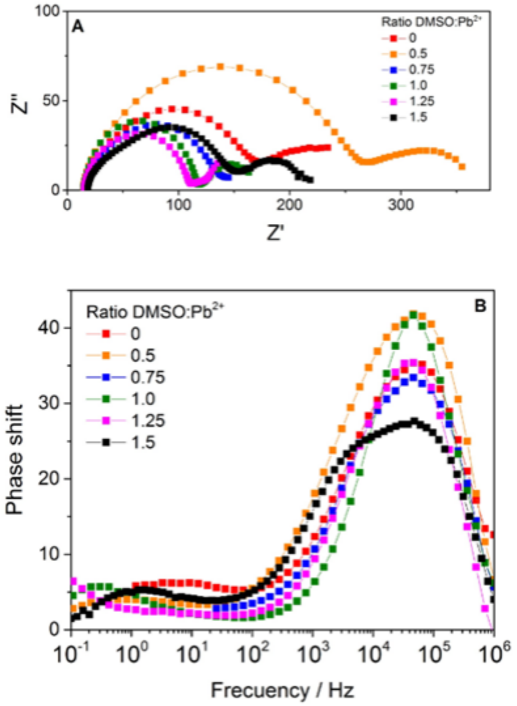

Figure 10.3. Impedance Nyquist (A) and Bode (B) plots for $MAPbI_3$ devices prepared with different DMSO:Pb^{2+} ratios at 1.66 kPa. Data obtained under red illumination (635 nm) are shown. The open-circuit photopotential generated by the illumination is 0.911 V.

As it has been shown above, the efficiency trends for a certain WVP are mainly governed by the photocurrent, whereas the V_{OC} happens to be basically insensitive to the DMSO content in the precursor solution (Fig. A-10.2). To analyse the impact of DMSO:Pb^{2+} ratios on performing devices, impedance spectroscopy measurements at open circuit potential in the range of frequency of 10^6-0.1 Hz were performed. Due to the lack of stability during impedance measurements shown by devices prepared under higher environmental WVP values, the impedance analysis was restricted to devices fabricated at 1.66 kPa. The measurements were carried out at two excitation wavelengths (465 nm and 635 nm) to establish the impact of different optical penetration lengths in the perovskite layer like we have already done in previous Chapters.[25,30,31] Figure 10.3A and 10.3B show the impedance response in the form of Nyquist and Bode plots, respectively, for various DMSO:Pb^{2+} ratios recorded at 635 nm. The impedance spectra were mainly characterized by two kinetics signals whose meanings were mentioned in *Chapter* 3. In this *Chapter*, we focus in high frequency signal at 10^5 Hz since this has been attributed to electronic transport and recombination processes in the perovskite layer.[25,32–35]

The *HF* resistance (R_{HF}) has been extracted from the impedance data by fitting to an *Voight* equivalent circuit [R_s−(R_{HF}·CPE_{HF})].[36] The R_{HF} obtained for the two excitation wavelengths are plotted as a function of open-circuit potential originated by different illumination intensity in Figure A-10.3. Results for the *HF* resistance are in line with previous impedance analysis (*Chapters* 5, 6 and 9):[25,30] The ideality factors were close to 2 and unchanged with respect to the generation profile, which is associated with Shockley−Read−Hall recombination in the bulk of the active layer.[25,37,38] Activation energy for recombination of the employed perovskite materials was also determined (1.60 eV) by extrapolating the V_{OC} for different temperature data to $T \rightarrow 0$[39] (Fig. A-10.4B). This activation energy was coincident with the band gap reported for $MAPbI_3$ perovskite[40] and with the optical band gap (Fig. A-10.4A) extracted from absorption data of the devices (1.63 eV), which confirms that the recombination is mainly determined by the bulk of the perovskite layer itself at open-circuit conditions. Besides, we found that the R_{HF} was basically independent from the DMSO:Pb^{2+} ratio, which explains the relative constancy of the V_{OC} values with respect to the precursor composition (Fig. A-10.2).

Nevertheless, when the R_{HF} extracted for two different WVPs (1.66 kPa and 1.85 kPa) is compared, lower values of R_{HF} for highest WVP but same ideality factor (close to 2) are obtained. This is shown in Figure A-10.3B. This indicates a clear net enhancement in the Shockley−Read−Hall recombination rate for 1.85 kPa, which explains the reduction of the open-circuit potential at 1 *sun* illumination reported in Figure 10.1, Figures A-10.1C and A-10.2C. This means that too much water in the crystalline structure of the perovskite (above the upper limit of 1.6 kPa mentioned above) triggers more recombination in the bulk of the perovskite, probably due to the formation of more recombination centers.

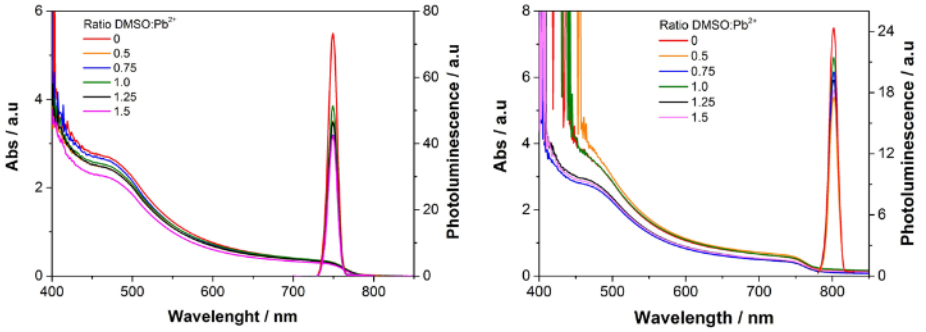

Figure 10.4. Optical absorption and normalized steady state photoluminescence spectra of $MAPbI_3$ films deposited on TiO_2 substrates from precursor solution with different DMSO:Pb^{2+} ratios. Data obtained for two WVP: 1.85 kPa (left) and 1.66 kPa (right). Excitation wavelength of 497 nm and 532 nm were used, respectively.

To investigate the influence of DMSO:Pb^{2+} ratio as a function of water content in air on both absorption and charge extraction/separation performance, steady-state photoluminescence and UV-Vis spectroscopy studies were conducted. These were done in perovskite films deposited on mesoporous TiO_2 at 1.66 kPa and 1.85 kPa, respectively and the results are presented in Figure 10.4. PL data have been normalized to the maximum absorbance found for each device by dividing the whole UV-Vis spectrum by the maximum intensity and multiplying the PL peak by the factor thus obtained. This way, a better comparison of different perovskite films is ensured.

From Figure 10.4, we infer that lower DMSO:Pb^{2+} ratios produce perovskite films with higher absorption spectra at short wavelengths regardless the WVP used. This effect is more acute at 1.66 KPa. Bearing in mind that the perovskite films thickness are similar for all devices studied (~ 400 nm), the changes in absorbance could arise from changes in lead ion coordination, which depends on the mixture solvent in the precursor solution.[41] This is in line with the improved crystallinity observed for DMSO:$Pb^{2+} \geq 1.0$ by the increase in the X-ray diffraction (XRD) peak intensity at 14.1°, as shown in Figure A-10.5. (This peak is associated with (110) plane of tetragonal $MAPbI_3$.) The XRD was carried out for perovskite films deposited at 1.01 kPa, for which a peak at 12.6° was also found for the different DMSO:Pb^{2+} ratios. This peak is attributed to the (001) lattice plane of hexagonal PbI_2. A qualitative analysis of these peaks revealed that the highest $PbI_2/MAPbI_3$ ratio is achieved for films prepared at DMSO:Pb^{2+} ratio ≤ 1.0 (Table A-10.1). Bearing in mind that the highest efficiency was obtained for ratio 1.0 for low WVP, this result points out that a certain PbI_2 content on perovskite films could be the reason of the better performing devices.[37,42]

It is also interesting to analyse the impact of the ratio on both light harvesting and electron injection. In Figure 10.4 it is observed that the lowest DMSO:Pb^{2+} ratio led to the highest photoluminescence peak intensities. Since the PL signal intensity arise from the radiative recombination processes inside perovskite material, an increased PL signal is indicative of slower electron injection from the perovskite film to the TiO_2 layer. Therefore, we conclude that injection and absorption are somehow compensated, which explains the relative insensitivity of the photocurrent with respect to the DMSO:Pb^{2+} ratio (Fig. A-10.2B). By contrast, there is a clear difference between the PL intensities revealed at different WVP. Faster charge extraction was obtained for the films prepared at 1.66 kPa than those prepared at 1.85 kPa. Furthermore, for 1.66 kPa, an increase of the absorbance at short wavelengths for lowest DMSO:Pb^{2+} ratios is also observed. These results are in line with the drop in photocurrent obtained at higher WVP (Fig. 10.1, Figs. A-10.1B and A-10.2B).

Scanning electron microscopy images show also a distinct perovskite morphology depending on the WVP and DMSO:Pb^{2+} ratio (Fig. A-10.6). The morphological change as function of DMSO content in precursor solution is in agreement with the data reported by Guerrero *et al.*[18] For 1.66 kPa, perovskite films deposited from precursor solutions with low content in DMSO (ratio 0.5) revealed a fiber-like morphology mixed with larger crystalline domains (Fig. A-10.6E), while for ratio 1.0 these fibers did not show up, and a totally covered surface is observed (Fig. A-10.6C). Although, large domains were also formed for highest content in DMSO (ratio 1.5), non-homogeneous films were detected (Fig. A-10.6A) due to presence of pin-holes. Therefore, an optimized stoichiometry of PbI_2:H_2O:DMSO leads to a more adequate morphology, in line with the best performing devices. The same trend was observed for films fabricated at 1.85 kPa. However, a higher pin-hole proportion was revealed for the highest DMSO:Pb^{2+} ratios (Fig. A-10.6B). Indeed, non-homogeneous films were already detected for ratio 1.0 (Fig. A-10.6D). On the other hand, smaller crystalline domains were observed when the films were prepared at higher WVPs. In particular, perovskite domains in the range of 200 nm and 100 nm were obtained for 1.66 kPa and 1.85 kPa, respectively. Considering that the grain boundaries increase the non-radiative recombination rate as well as adversely affect to charge extraction efficiency at the interface between perovskite and selective contact,[27,43] these results could explain the low V_{OC} (due to the larger concentration of recombination centers, as stated above) (Fig. 10.1, Fig. A-10.1 and Fig. A-10.2) and the poor injection efficiency (Fig. 10.4) obtained for devices prepared under higher WVP.

In order to show the wide applicability of a preparation method based on the control of the absolute water content in air, we have attempted the preparation of mixed perovskites at ambient conditions. Thus, we have extended the methodology reported[18] for fabrication of MA-devices under ambient conditions to formamidinium(FA)-devices by adjusting the DMSO proportion in precursor solution as a function of WVP. In particular, we fabricated $FA_{0.83}MA_{0.17}PbI_3$ at 1.56 kPa (302 K and 39 % RH). A planar configuration was chosen to simplify the manufacturing. Because DMSO coordinate worse for FA-perovskite than MA-perovskite,[44] we used a lower DMSO content in the solution precursor than that calibrated for $MAPbI_3$ (Fig. 10.2). By adjusting DMSO:Pb^{2+} ratio to 0.75, FA-devices with an efficiency of 14.7 % (J_{SC}: 19.14 mA·cm^{-2}; V_{OC}: 1.03 V; FF: 74.7%) were obtained (Fig. 10.5). This efficiency is much higher than reported in the literature for FA-type of perovskite deposited at the same RH (9 % PCE at 40% RH).[11]

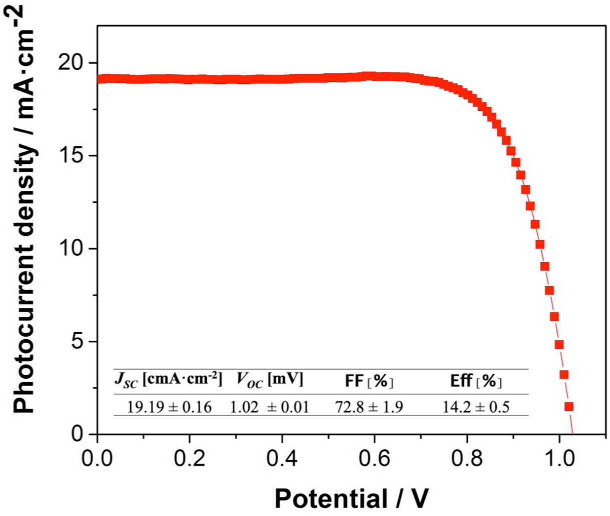

J_{SC} [cmA·cm^{-2}]	V_{OC} [mV]	FF [%]	Eff [%]
19.19 ± 0.16	1.02 ± 0.01	72.8 ± 1.9	14.2 ± 0.5

Figure 10.5. Current–voltage curve of the best $FA_{0.83}MA_{0.17}PbI_3$ devices prepared at 1.56 KPa (302 K and 39 % relative humidity) The curves have been measured in reverse scan under 1 sun—AM 1.5 illumination and using a mask of 0.16 cm^2. The table inset illustrates the photovoltaic parameters statistics for the 4 devices measured.

10.4 Conclusion

The PCE differences found for devices prepared at different room temperature for the same RH underlined the importance of using the water vapour pressure as the parameter that matters when controlling the humidity in the preparation of perovskite at ambient conditions. Taking into account WVP during perovskite deposition, a study of the effect of the absolute water content in air on the performance of devices was carried out. Simultaneously, the optimum DMSO content in precursor solution as a function of WVP was also analysed. Highest efficiencies were revealed for WVP values lower than 1.7 kPa and a DMSO:Pb^{2+} ratio of 1.0. The best performance of devices was related with increased photocurrent and higher open-circuit potential. These results were attributed to faster electron injection into the TiO_2 layer. Higher electron recombination resistances were found in devices prepared at lower WVP, which seems to be related to the larger grain size. We demonstrated the broad applicability of a procedure based on the control of the absolute water content in air by fabricating double-cation perovskites ($FA_{0.83}MA_{0.17}PbI_3$) under humid conditions by adjusting the DMSO proportion in precursor solution as a function of WVP. Efficiencies higher than those reported for similar devices at ambient conditions were obtained. The results here reported show the potentiality of a method of preparation of stable and highly efficient perovskites devices at ambient conditions for industrial application as long as the *absolute* content level of water vapour do not surpass certain levels.

10.5 References

1 W. S. Yang, B.-W. Park, E. H. Jung, N. J. Jeon, Y. C. Kim, D. U. Lee, S. S. Shin, J. Seo, E. K. Kim, J. H. Noh and S. I. Seok, Iodide management in formamidinium-lead-halide–based perovskite layers for efficient solar cells, *Science*, 2017, **356**, 1376–1379.

2 M. A. Green, Y. Hishikawa, E. D. Dunlop, D. H. Levi, J. Hohl-Ebinger and A. W. Y. Ho-Baillie, Solar cell efficiency tables (version 51), *Prog. Photovolt. Res. Appl.*, 2018, **26**, 3–12.

3 D. Yang, R. Yang, K. Wang, C. Wu, X. Zhu, J. Feng, X. Ren, G. Fang, S. Priya and S. Liu, High efficiency planar-type perovskite solar cells with negligible hysteresis using EDTA-complexed SnO2, *Nat. Commun.*, , DOI:10.1038/s41467-018-05760-x.

4 M. Saliba, T. Matsui, K. Domanski, J.-Y. Seo, A. Ummadisingu, S. M. Zakeeruddin, J.-P. Correa-Baena, W. R. Tress, A. Abate, A. Hagfeldt and M. Gratzel, Incorporation of rubidium cations into perovskite solar cells improves photovoltaic performance, *Science*, 2016, **354**, 206–209.

5 M. Saliba, T. Matsui, J.-Y. Seo, K. Domanski, J.-P. Correa-Baena, M. K. Nazeeruddin, S. M. Zakeeruddin, W. Tress, A. Abate, A. Hagfeldt and M. Grätzel, Cesium-containing triple cation perovskite solar cells: improved stability, reproducibility and high efficiency, *Energy Environ. Sci.*, 2016, **9**, 1989–1997.

6 K. T. Cho, S. Paek, G. Grancini, C. Roldán-Carmona, P. Gao, Y. Lee and M. K. Nazeeruddin, Highly efficient perovskite solar cells with a compositionally engineered perovskite/hole transporting material interface, *Energy Environ. Sci.*, 2017, **10**, 621–627.

7 A. Abate, J.-P. Correa-Baena, M. Saliba, M. S. Su'ait and F. Bella, Perovskite Solar Cells: From the Laboratory to the Assembly Line, *Chem. - Eur. J.*, 2018, **24**, 3083–3100.

8 S. Sun, T. Buonassisi and J.-P. Correa-Baena, State-of-the-Art Electron-Selective Contacts in Perovskite Solar Cells, *Adv. Mater. Interfaces*, 2018, 1800408.

9 M. Cai, Y. Wu, H. Chen, X. Yang, Y. Qiang and L. Han, Cost-Performance Analysis of Perovskite Solar Modules, *Adv. Sci.*, 2017, **4**, 1600269.

10 J. You, Y. (Michael) Yang, Z. Hong, T.-B. Song, L. Meng, Y. Liu, C. Jiang, H. Zhou, W.-H. Chang, G. Li and Y. Yang, Moisture assisted perovskite film growth for high performance solar cells, *Appl. Phys. Lett.*, 2014, **105**, 183902.

11 S. Wozny, M. Yang, A. M. Nardes, C. C. Mercado, S. Ferrere, M. O.

Reese, W. Zhou and K. Zhu, Controlled Humidity Study on the Formation of Higher Efficiency Formamidinium Lead Triiodide-Based Solar Cells, *Chem. Mater.*, 2015, **27**, 4814–4820.

12 Y. Xu, L. Zhu, J. Shi, X. Xu, J. Xiao, J. Dong, H. Wu, Y. Luo, D. Li and Q. Meng, The Effect of Humidity upon the Crystallization Process of Two-Step Spin-Coated Organic–Inorganic Perovskites, *ChemPhysChem*, 2016, **17**, 112–118.

13 G. E. Eperon, S. N. Habisreutinger, T. Leijtens, B. J. Bruijnaers, J. J. van Franeker, D. W. deQuilettes, S. Pathak, R. J. Sutton, G. Grancini, D. S. Ginger, R. A. J. Janssen, A. Petrozza and H. J. Snaith, The Importance of Moisture in Hybrid Lead Halide Perovskite Thin Film Fabrication, *ACS Nano*, 2015, **9**, 9380–9393.

14 Q. Jiang, L. Zhang, H. Wang, X. Yang, J. Meng, H. Liu, Z. Yin, J. Wu, X. Zhang and J. You, Enhanced Electron Extraction Using SnO2 for High-Efficiency Planar-Structure HC(NH2)2PbI3-Based Perovskite Solar Cells, *Nat. Energy*, 2016, **1**, 16177.

15 K. Huang, C. Wang, C. Zhang, S. Tong, H. Li, B. Liu, Y. Gao, Y. Dong, Y. Gao, Y. Peng and J. Yang, Efficient and stable planar heterojunction perovskite solar cells fabricated under ambient conditions with high humidity, *Org. Electron.*, 2018, **55**, 140–145.

16 A. Rapsomanikis, D. Karageorgopoulos, P. Lianos and E. Stathatos, High performance perovskite solar cells with functional highly porous TiO2 thin films constructed in ambient air, *Sol. Energy Mater. Sol. Cells*, 2016, **151**, 36–43.

17 B. A. de Carvalho, S. Kavadiya, S. Huang, D. M. Niedzwiedzki and P. Biswas, Highly Stable Perovskite Solar Cells Fabricated Under Humid Ambient Conditions, *IEEE J. Photovolt.*, 2017, **7**, 532–538.

18 C. Aranda, C. Cristobal, L. Shooshtari, C. Li, S. Huettner and A. Guerrero, Formation criteria of high efficiency perovskite solar cells under ambient conditions, *Sustain. Energy Fuels*, 2017, **1**, 540–547.

19 K. Sveinbjörnsson, K. Aitola, J. Zhang, M. B. Johansson, X. Zhang, J.-P. Correa-Baena, A. Hagfeldt, G. Boschloo and E. M. J. Johansson, Ambient air-processed mixed-ion perovskites for high-efficiency solar cells, *J. Mater. Chem. A*, 2016, **4**, 16536–16545.

20 L. Contreras-Bernal, C. Aranda, M. Valles-Pelarda, T. T. Ngo, S. Ramos-Terrón, J. J. Gallardo, J. Navas, A. Guerrero, I. Mora-Seró, J. Idígoras and J. A. Anta, Homeopathic Perovskite Solar Cells: Effect of Humidity during Fabrication on the Performance and Stability of the Device, *J. Phys. Chem. C*, 2018, **122**, 5341–5348.

21 Q. Tai, P. You, H. Sang, Z. Liu, C. Hu, H. L. W. Chan and F. Yan, Efficient and stable perovskite solar cells prepared in ambient air irrespective of the humidity, *Nat. Commun.*, 2016, **7**, 11105.

22 C. J. Adkins and C. J. Adkins, *An Introduction to Thermal Physics*, Cambridge University Press, 1987.

23 E. Slowinski and W. C. Wolsey, *Chemical Principles in the Laboratory*, Cengage Learning, 2008.

24 Y. Ko, C. Lee, Y. Kim, Y. Kim, Y. J. Yun and Y. Jun, Dew point temperature as an invariant replacement for relative humidity for advanced perovskite solar cell fabrication systems, *J. Mater. Chem. A*, 2018, **6**, 20695–20701.

25 L. Contreras-Bernal, M. Salado, A. Todinova, L. Calio, S. Ahmad, J. Idígoras and J. A. Anta, Origin and Whereabouts of Recombination in Perovskite Solar Cells, *J. Phys. Chem. C*, 2017, **121**, 9705–9713.

26 J. Burschka, N. Pellet, S.-J. Moon, R. Humphry-Baker, P. Gao, M. K. Nazeeruddin and M. Grätzel, Sequential deposition as a route to high-performance perovskite-sensitized solar cells, *Nature*, 2013, **499**, 316–319.

27 D. Y. Son, J. W. Lee, Y. J. Choi, I. H. Jang, S. Lee, P. J. Yoo, H. Shin, N. Ahn, M. Choi, D. Kim and N. G. Park, Self-formed grain boundary healing layer for highly efficient CH3 NH3 PbI3 perovskite solar cells, *Nat. Energy*, 2016, **1**, 16081.

28 M. Saliba, J.-P. Correa-Baena, C. M. Wolff, M. Stolterfoht, N. Phung, S. Albrecht, D. Neher and A. Abate, How to Make over 20% Efficient Perovskite Solar Cells in Regular (n–i–p) and Inverted (p–i–n) Architectures, *Chem. Mater.*, , DOI:10.1021/acs.chemmater.8b00136.

29 M. I. Saidaminov, A. L. Abdelhady, B. Murali, E. Alarousu, V. M. Burlakov, W. Peng, I. Dursun, L. Wang, Y. He, G. Maculan, A. Goriely, T. Wu, O. F. Mohammed and O. M. Bakr, High-quality bulk hybrid perovskite single crystals within minutes by inverse temperature crystallization, *Nat. Commun.*, , DOI:10.1038/ncomms8586.

30 M. Salado, L. Contreras-Bernal, L. Caliò, A. Todinova, C. López-Santos, S. Ahmad, A. Borras, J. Idígoras and J. A. Anta, Impact of moisture on efficiency-determining electronic processes in perovskite solar cells, *J. Mater. Chem. A*, 2017, **5**, 10917–10927.

31 J. Idígoras, L. Contreras‐Bernal, J. M. Cave, N. E. Courtier, Á. Barranco, A. Borras, J. R. Sánchez‐Valencia, J. A. Anta and A. B. Walker, The Role of Surface Recombination on the Performance of Perovskite Solar Cells: Effect of Morphology and Crystalline Phase of TiO2 Contact, *Adv. Mater. Interfaces*, **0**, 1801076.

32 E. Guillén, F. J. Ramos, J. A. Anta and S. Ahmad, Elucidating Transport-Recombination Mechanisms in Perovskite Solar Cells by Small-Perturbation Techniques, *J. Phys. Chem. C*, 2014, **118**, 22913–22922.

33 A. Todinova, J. Idígoras, M. Salado, S. Kazim and J. A. Anta, Universal Features of Electron Dynamics in Solar Cells with TiO_2 Contact: From Dye Solar Cells to Perovskite Solar Cells, *J. Phys. Chem. Lett.*, 2015, **6**, 3923–3930.

34 M. Bag, L. A. Renna, R. Y. Adhikari, S. Karak, F. Liu, P. M. Lahti, T. P. Russell, M. T. Tuominen and D. Venkataraman, Kinetics of Ion Transport in Perovskite Active Layers and Its Implications for Active Layer Stability, *J. Am. Chem. Soc.*, 2015, **137**, 13130–13137.

35 A. Guerrero, G. Garcia-Belmonte, I. Mora-Sero, J. Bisquert, Y. S. Kang, T. J. Jacobsson, J.-P. Correa-Baena and A. Hagfeldt, Properties of Contact and Bulk Impedances in Hybrid Lead Halide Perovskite Solar Cells Including Inductive Loop Elements, *J. Phys. Chem. C*, 2016, **120**, 8023–8032.

36 A. Todinova, L. Contreras-Bernal, M. Salado, S. Ahmad, N. Morillo, J. Idígoras and J. A. Anta, Towards a Universal Approach for the Analysis of Impedance Spectra of Perovskite Solar Cells: Equivalent Circuits and Empirical Analysis, *ChemElectroChem*, 2017, **4**, 2891–2901.

37 D. Bi, W. Tress, M. I. Dar, P. Gao, J. Luo, C. Renevier, K. Schenk, A. Abate, F. Giordano, J.-P. Correa Baena, J.-D. Decoppet, S. M. Zakeeruddin, M. K. Nazeeruddin, M. Grätzel and A. Hagfeldt, Efficient luminescent solar cells based on tailored mixed-cation perovskites, *Sci. Adv.*, 2016, **2**, e1501170.

38 W. Tress, M. Yavari, K. Domanski, P. Yadav, B. Niesen, J. P. Correa Baena, A. Hagfeldt and M. Graetzel, Interpretation and evolution of open-circuit voltage, recombination, ideality factor and subgap defect states during reversible light-soaking and irreversible degradation of perovskite solar cells, *Energy Environ. Sci.*, 2018, **11**, 151–165.

39 W. L. Leong, Z.-E. Ooi, D. Sabba, C. Yi, S. M. Zakeeruddin, M. Graetzel, J. M. Gordon, E. A. Katz and N. Mathews, Identifying Fundamental Limitations in Halide Perovskite Solar Cells, *Adv. Mater.*, 2016, **28**, 2439–2445.

40 J. S. Manser, J. A. Christians and P. V. Kamat, Intriguing Optoelectronic Properties of Metal Halide Perovskites, *Chem. Rev.*, 2016, **116**, 12956–13008.

41 S. Rahimnejad, A. Kovalenko, S. M. Forés, C. Aranda and A. Guerrero, Coordination Chemistry Dictates the Structural Defects in Lead Halide Perovskites, *ChemPhysChem*, 2016, **17**, 2795–2798.

42 M. L. Petrus, Y. Hu, D. Moia, P. Calado, A. M. A. Leguy, P. R. F. Barnes and P. Docampo, The Influence of Water Vapor on the Stability and Processing of Hybrid Perovskite Solar Cells Made from Non-Stoichiometric

Precursor Mixtures, *ChemSusChem*, 2016, **9**, 2699–2707.

43 R. Long, J. Liu and O. V. Prezhdo, Unravelling the Effects of Grain Boundary and Chemical Doping on Electron–Hole Recombination in $CH_3NH_3PbI_3$ Perovskite by Time-Domain Atomistic Simulation, *J. Am. Chem. Soc.*, 2016, **138**, 3884–3890.

44 T. Liu, Y. Zong, Y. Zhou, M. Yang, Z. Li, O. S. Game, K. Zhu, R. Zhu, Q. Gong and N. P. Padture, High-Performance Formamidinium-Based Perovskite Solar Cells via Microstructure-Mediated δ-to-α Phase Transformation, *Chem. Mater.*, 2017, **29**, 3246–3250.

General Conclusions

In this thesis, organic-inorganic metal halide perovskite solar cells have been object of a fundamental study aimed at understanding the different electronic and ionic mechanisms that determine the performance and photovoltaic response of these devices.

In *Chapter* 4, we studied the hysteretic behaviour in perovskite solar cells analysing the low-frequency component of IS and IMPS spectra. Our results point to the coupled effect of ionic migration charge accumulation at TiO_2/perovskite interface, and surface recombination under the electrode polarization as the origin of the hysteresis. In particular, we suggest that the chemical interaction between TiO_2 and cations in the perovskite is a key factor of this phenomenon. These interactions can modify the energy barriers that determine the charge separation process likely due to the modification of the space charge layer and the enhancement of surface recombination routes.

In *Chapters* 5 and 8, interpretation models of the information extracted from the small perturbation techniques have been brought. In these *Chapters*, we show that the high frequency component of the impedance spectrum provides information (qualitative and semi-quantitative) about the nature and magnitude of recombination in perovskitesolar cells. In particular, the high frequency resistance can be related to the recombination rate and be used to obtain the ideality factor and to estimate the charge collection efficiency. Besides that, we have set a protocol that allows us to compare perovskites devices with different band gaps.

We use these models, in *Chapters* 5 and 6, to show that the main recombination route in fresh devices takes place in the bulk of perovskite layer, which is what determines the open-circuit potential of the device. In the case of inadequate selective contacts (hole or electrons selective contacts) or degraded devices, an additional recombination mechanism, surface-mediated recombination, decreases the open-open circuit potential and short-circuit photocurrent. We associate this new process to worse charge extraction at the selective contacts. In particular, in case of inadequate electron selective contacts, this lower charge extraction efficiency does not only promote the surface-mediated recombination (TiO_2/perovskite interface), but also a higher interfacial charge accumulation. Both factors lead to more hysteresis.

Regarding this latter point, in *Chapter* 7, the devices degraded by the exposure at humidity ambient show a faster recombination than the fresh devices due to the coupled effect to the bulk recombination and the surface-mediated recombination. The greater contribution of the latter in degraded devices is revealed by interfacial charge accumulation processes and slower electron transport inside the perovskite layer.

In *Chapter* 9, we analysed the stability under humidity atmosphere of perovskite devices prepared at ambient conditions. Our results reveal that fabrication of perovskite solar cells under high humidity conditions leads to devices that are more robust against moisture-induced ageing and degradation than those prepared at low relative humidity values or in dry environments. We propose that this higher humidity stability is due to the incorporation of small amounts of water in the perovskite crystalline structure during preparation at ambient conditions. In connection with this, in *Chapter* 10, we propose to use the water vapour pressure as the main humidity control parameter to fabricate high efficiency perovskite devices at ambient conditions. Using this parameter instead of the more popular of "Relative Humidity", perovskite precursor solutions are prepared with the suitable stoichiometry to obtain high quality perovskite films that show faster electron injection into the TiO_2 layer, lower recombination resistance, overall improved efficiencies and enhanced stability.

In summary, we believe that the results of this thesis will help the community to better understand the limiting mechanisms in the performance of perovskite solar cells, both in terms of recombination losses and degradation. This knowledge is crucial to achieve stable devices suitable for industrial implementation and commercialization.

Appendix

SECTION A

Chapter 3. Materials and Methods

Table A-3.1. List of chemical, company and product code

Chemical	Company	CAS number
Hellmanex III	Sigma_Aldrich	0000000000
Isopropanol	Panreac	67-63-0
Ethanol absolute	VWR chemicals	64-17-5
TiO_2 paste 30NR-D	Greatcell Solar	0000000000
TiO_2 paste 18NR-T	Greatcell Solar	0000000000
Acetonitrile	Panreac	75-05-8
Lithium iodine	Sigma_Aldrich	10377-51-2
4-terc-butylpyridine	Sigma_Aldrich	3978-81-2
Titanium tetraisopropoxide	Sigma_Aldrich	546-68-9
Titanium diisopropoxide bis(acetylacetonate)	Sigma_Aldrich	17927-72-9
Lead(II) bromide	Sigma_Aldrich	10031-22-8
Lead(II) iodide	Sigma_Aldrich	10101-63-0
Methylammonium bromide	Greatcell Solar	6876-37-5
Methylammonium iodide	Greatcell Solar	14965-49-2
Formamidinium iodide	Greatcell Solar	879643-71-7
Cesium bromide	Sigma_Aldrich	7787-69-1
Cesium iodide	Sigma_Aldrich	7789-17-5
Dimethyl sulfoxide pure	Panreac	67-68-5
N,N-Dimethylformamide	Panreac	68-12-2
Clorobenzene	Sigma_Aldrich	108-90-7
Diethyl ether	Sigma_Aldrich	60-29-7
Spiro-OMeTAD	Sigma_Aldrich	207739-72-8
LITFSI	sigma_Aldrich	90076-65-6
P3HT	Sigma_Aldrich	156074-98-5

Fabrication of perovskite solar cell

To prepare reproducible and high efficiency perovskite solar cells, some important details need to be taken into account:

Substrate Cleaning

i. If the isopropanol is not used at the end of the solvent sequence, stains can be observed in the FTO surface.

ii. Although the cleaning is a simple step, it is an important one because it can introduce variability in the photovoltaic results. Therefore, every substrate needs to look spotless before moving on to the next step.

Electron selective contact

i. As dust can cause inhomogeneity, before the deposition of any bottom layer, the substrate should blow with soft compressed air to remove it.
ii. The titanium solution sprays in less than 5 min can lead to a drop open-circuit potential.
iii. The titanium diisopropoxide bis(acetylacetonate) solution must be kept in inert atmosphere, or if it not possible, in low relative humidity. This reactive might degrade when it is bad stored. A change of colour indicates degradation.
iv. The FTO/*c*-TiO_2 substrates can be stored in low humidity for a week.
v. If the *c*-TiO_2 or *m*-TiO_2 layer has been deposited for over 24h, the samples need to be warmed at 100 ºC for a brief time (1- 2 min) in order to remove as humidity as possible from them.
vi. The 100 µL of TiO_2 mesoporous solution need to diffuse on *c*-TiO_2 film before the spinning. Otherwise, the substrate should be discarded.
vii. The TiO_2 dispersion needs to be stored under continuous stirring.
viii. The *c*-TiO_2 and *m*-TiO_2 films need to look homogeneous and semitransparent. Those that do not look good should be discarded.
ix. The pure oxygen as carrier gas is advised instead of dry air. The titanium must be Ti^{4+} when is deposited, so, if the pure oxygen is used, possible Ti^{3+} traces will be oxidated to Ti^{4+}.

Perovskite film deposition

i. The chemical reagents such as lead salts and halogen organic salts must be stored in inert atmosphere, or if this is not possible, in RH lower than 10 %.
ii. For lead salts, a glass vial should be used; otherwise, the lead salt will take a long time to be completely dissolved.
iii. The lead salts solutions can be stored for two days. However, before adding the MAI, the lead solution has to be warmed and cooled again.
iv. Due to the delicacy of this step, the use of micropipettes and precision balance perfectly calibrated is required.
v. It is strictly to clean and wipe carefully the working place before beginning with this step. Any type of contamination needs to be avoided.

vi. In order to protect the perovskite films from environmental humidity, hole-transporting material should be placed on the perovskite films as soon as possible.
vii. For the perovskite deposition, a new micropipette tip is required for every substrate.
viii. Using a Pasteur pipette, which has been broken by the tip, the diethyl ether antisolvent is added. On the other hand, a 100-1000 μL micropipette is used to add the chlorobenzene antisolvent.
ix. To avoid the accumulation of solvents inside the glove box, this should be purged during the spinning and annealing of the substrate by using a constant flow of a noble gas (Ar or N_2).

Hole selective contact

i. The FK209 and LiTFSI solutions can be stored for months in inert atmosphere or if this is not possible, in RH lower than 10 %. However, the spiro-OMeTAD and P3HT solutions need to be prepared just before use.
ii. For spiro-OMeTAD, the few seconds of the spin-coated beginning, a colour change needs to be observed on the perovskite surface. If it is not observed, the substrate is discarded.
iii. The spiro-OMeTAD and P3HT films need to look homogeneous otherwise a drop of V_{OC} could be observed.

Metallic back contact

i. Before the gold deposition, the substrate is left in the dark and under low RH (20 %) overnight so that the lithium salt takes part in the HTM solutions.
ii. The substrate is blow with a soft compressed air to remove any particle of dust before covering it with the mask.

Section B

Chapter 4. Specific Cation Interactions as the Cause of Slow Dynamics and Hysteresis in Dye and Perovskite Solar Cells

Fabrication of dye-sensitize solar cells

Substrate cleaning

Fluorine-doped tin oxide-coated (FTO) glasses are used as working and counter-electrode. The choice of FTO glass substrates is a compromise between optical transmittance and sheet resistance: higher conductivity is normally related to lower transmittance. For this reason, TEC15 is employed for the deposition of the semiconductor film as working electrode, whereas TEC8 (Pilkington, resistance 8Ω/square, 80-81.5% visible transmittance) as counter-electrode in DSSCs.

The glasses are subjected to a rigorous cleaning protocol: 15 min of sonication in baths of Hellmanex solution, deionized water, isopropanol and ethanol, successively. Then the substrates are annealing to remove the organic matter. (500 ºC for 30 min).

Dye sensitization

As it was indicated in *Chapter* 4, the dye based on ruthenium-complexes N719 is employed in this thesis for sensitization of semiconductor photoanodes. For that, the TiO_2 films are immersed overnight under dark at room temperature. To avoid the aggregation of dye molecules chenodeoxycholic acid is used as coadsorbent. The bulky size of this molecule keeps dye molecules attached onto the surface of semiconductor well separated. After sensitization, the films were washed in the same solvent as employed in the dye solution and dried under air.

Electrolyte Solution

Electrolytes of varying viscosity have been prepared by using different ratio of acetonitrile (Acn) and room temperature ionic-liquid (RTIL) as solvents. The ionic liquid used is 1-Buthyl-1-Methylpyrrolidinium bis(trifluoromethane sulfonyl)imide (Pyr) and the redox pair chosen is the iodide/iodine. The composition and concentration from every electrolyte is showed in the Table A-4.1.

Table A-4.1. Composition and acronyms of the electrolytes for the DSSCs studied in this thesis. I_2: Iodine ,BMII:1-butyl-3-methylimidalozliumiodide, LiI: Lithium iodide, TBP: 4-tertbutylpiridine, GuSCN: Guanidine thiocyanate, Acn: Acetonitrile, Pyr: 1-Buthyl-1-Methylpyrrolidinium bis(trifluoromethanesulfonyl)imide. RTIL means room temperature ionic-liquid.

Electrolyte	Solvent [V/V %]	Solutes
Acn	100 (Acn)	0.03 M I_2 + 1 M BMII + 0.05 M LiI + 0.5 M TBP+ 0.1 M GuSCN
Pyr 50	50:50 (Acn/RTIL)	
Pyr75	25:75 (Acn/RTIL)	
Pyr100	100 (RTIL)	

Table A-4.2. Photovoltaic parameters measured under 1 sun - AM 1.5 illumination for the different devices. Error bars are estimated from the results of three devices of the same configuration.

Devcice	J_{SC} [mA·cm^{-2}]	V_{OC} [mV]	Fill Factor [%]	Efficiency [%]
Acn	13.4 ± 0.2	770± 8	68± 2	7.0 ± 0.2
Pyr50	12.3 ± 0.2	721 ±9	59± 1	5.2 ± 0.1
Pyr75	2.8 ± 0.4	680±12	72 ± 2	1.5± 0.1
Pyr100	1.5± 0.2	675± 5	66± 3	0.6 ± 0.2
MAI	20 ± 0.7	980 ± 20	70 ± 4	13.5 ± 1
MAI/FAI	19.9 ± 0.4	885 ± 30	66 ± 1	11.5 ± 0.5

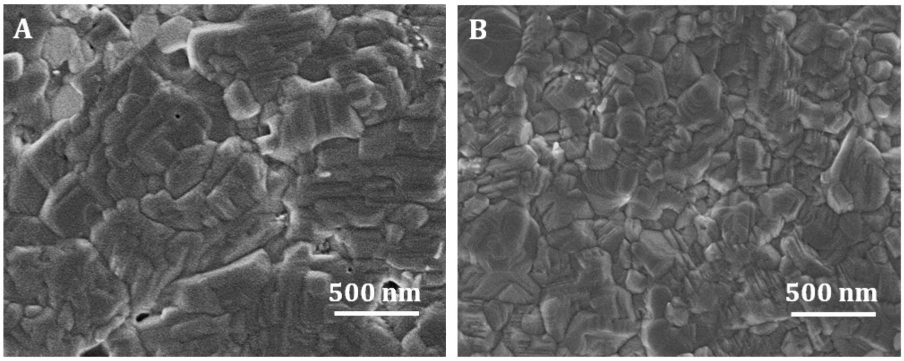

Figure A-4.1: Plane-view scanning electron microscopy (SEM) images for the (A) $MAPbI_3$ and (B) $MA_{0.6}FA_{0.4}PbI_3$ perovskite layers.

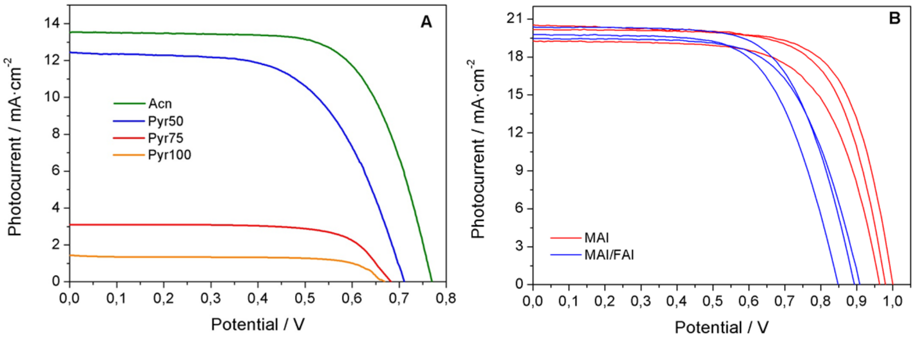

Figure A-4.2. Current-voltage curves of the different (A) DSSCs and (B) PSCs under 1 sun – AM 1.5 illumination in forward scan and reverse scan, respectively. Scan rate of 35mV/s and 100mV/s with a waiting time of 30s at 1V and 1.2V were employed for DSSCs and PSC, respectively..

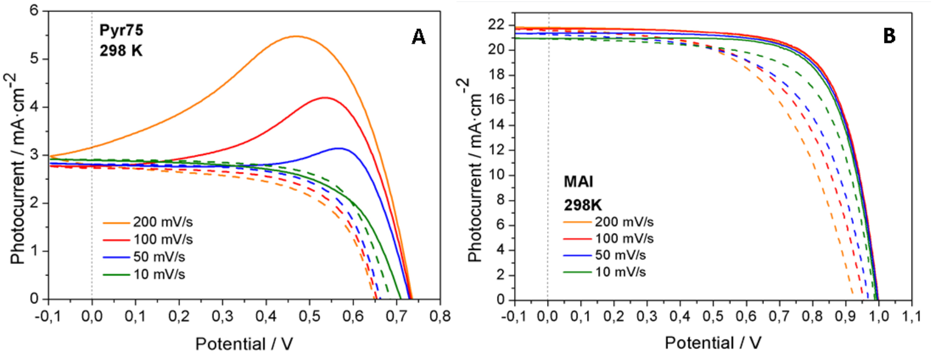

Figure A-4.3. Current-voltage curves of Pyr75 and MAI devices measured in the reverse scan (line) and forward scan (dash line) under light intensity of 10 mW·cm^{-2} using a green LED.

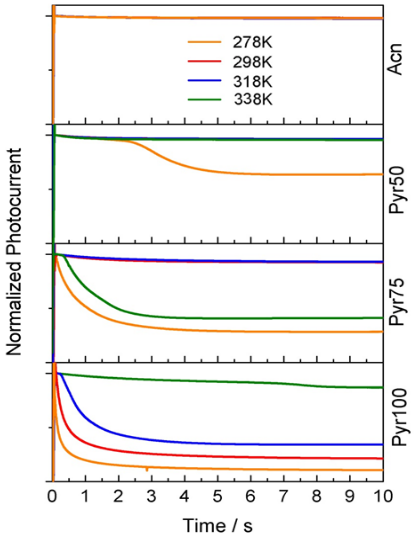

Figure A-4.4. Time-dependence photocurrent density for different DSSCs at different temperatures measured under light intensity of 10 mW·cm^{-2} using a green LED.

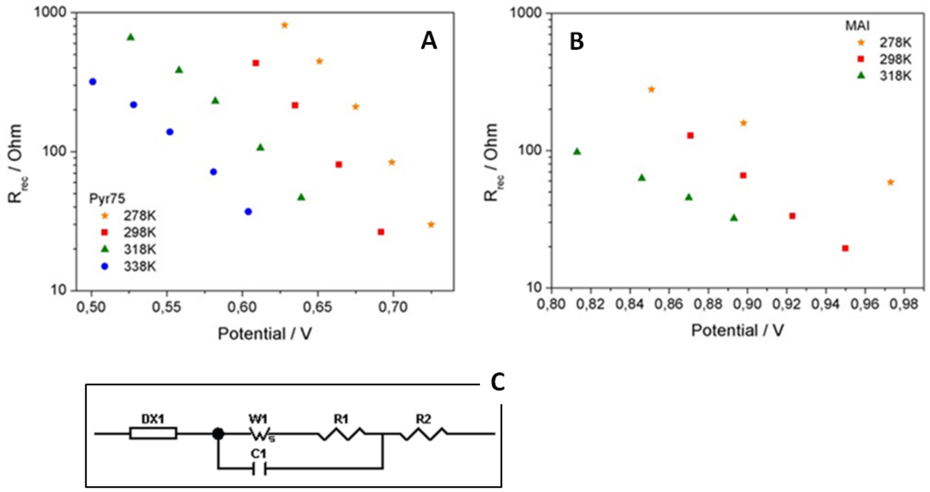

Figure A-4.5. Electron recombination resistance data as extracted from impedance spectroscopy measurements for (A) Pyr75 and (B) MAI samples. Equivalent circuits used for the fitting of the impedance spectra for (C) DSSCs (transmission line model, where DX1 is the distributed element for the diffusion-recombination transmission line [see Ref.[1]] R1 is charge transfer resistance, C1 is double layer capacitance, W1 is Warburg diffusion impedance and R2 is series resistance).

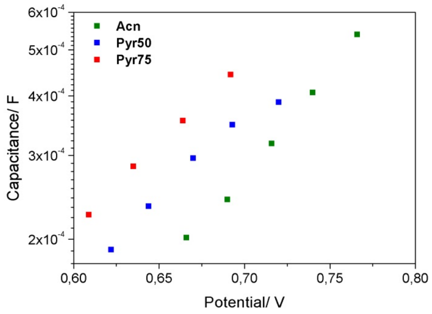

Figure A-4.6. Chemical capacitance data as extracted from impedance spectroscopy measurements for DSSCs using the transmission line model.

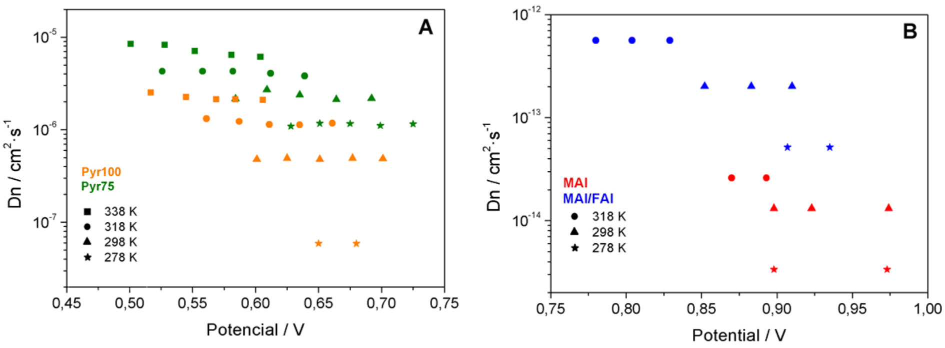

Figure A-4.7. Ionic diffusion coefficients data as extracted from impedance spectroscopy measurements for (A) DSSCs and (B) PSCs.

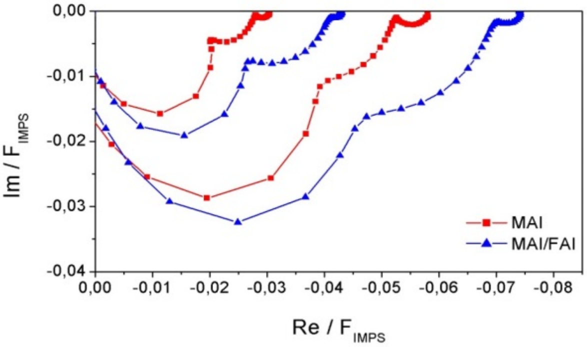

Figure A-4.8. IMPS response of MAI and MAI/FAI perovskites at two different illumination intensities.

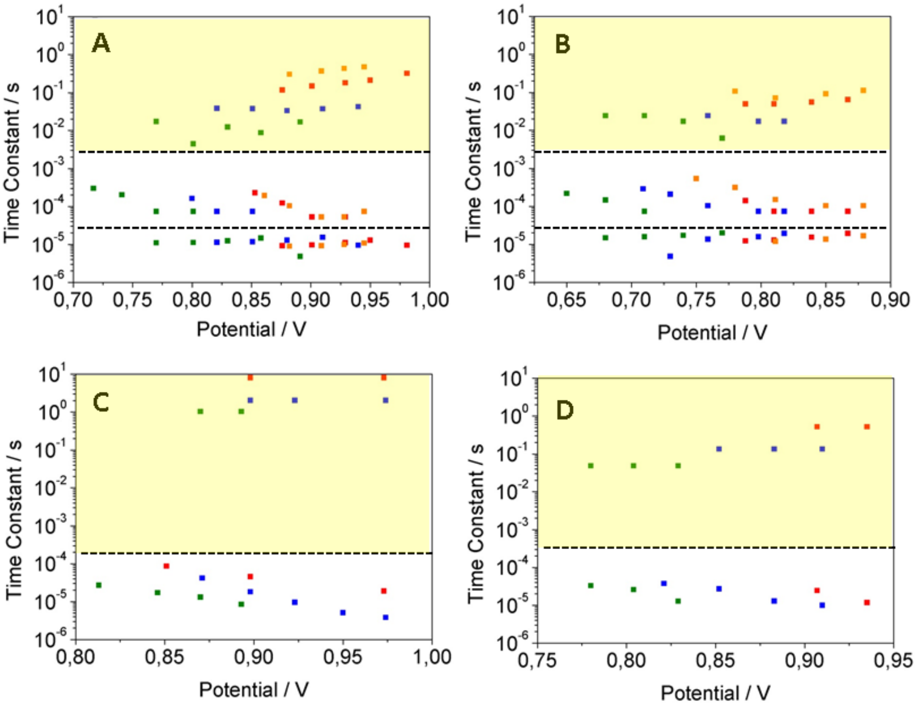

Figure A-4.9. Characteristic time constants extracted from (A, B) IMPS and IS (C, D) frequency plots for (A,C) MAI and (B, D) MAI/FAI samples at different temperatures: (green) 318K, (blue) 298K, (red) 278K and (orange) 258K.

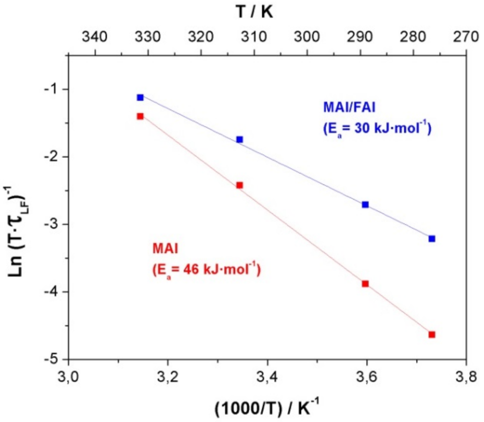

Figure A-4.10. Arrhenius-like plot $\ln(T/\tau_{LF})^{-1}$ versus 1000/T for MAI and MAI/FAI devices. τ_{LF} was extracted from the IMPS low-frequency component.

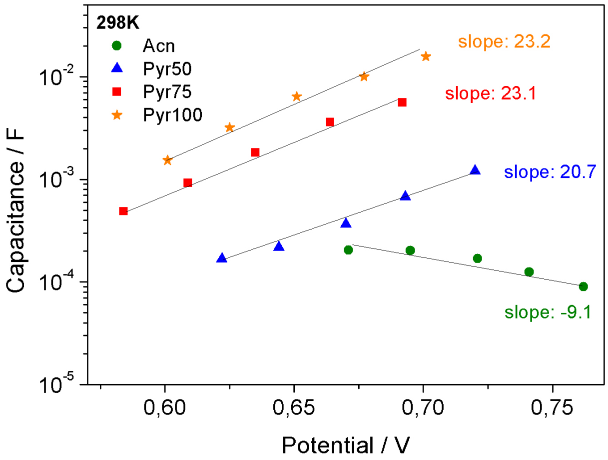

Figure A-4.11. Low-frequency capacitance (Fig. 4.3C) with respect to open-circuit potential extracted for the different DSSC compositions studied. The labels indicate the slope in V^{-1} obtained from both data sets.

Section C

Chapter 5. Origin and Whereabouts of Recombination in Perovskite Solar cells

Table A-5.1. Device configurations, photovoltaic parameters including statistics and best efficiencies of the solar cells studied in *Chapter* 5.

Configuration	Thickness (nm)	J_{SC} [mA·cm^{-2}]	V_{OC} [mV]	Fill Factor [%]	Efficiency [%]
MAI/P3HT	300 (0.8M)	14.8 ± 0.9	645 ± 7	65 ± 1	6.6
	500 (1.2M)	13.5 ± 0.5	735 ± 30	69 ± 1	7.3
MAI/Spiro	300 (0.8M)	16.2 ± 0.2	903 ± 21	68 ± 8	11.6
	500 (1.2M)	17.6 ± 0.9	953 ± 16	69 ± 3	11.8
MIX/Spiro	650 (0.8M)	20.0 ± 0.2	967 ± 16	67 ± 1	13.5
	950 (1.2M)	20.1 ± 0.4	932 ± 19	64 ± 2	13.1

Best values:

Configuration	Thickness (nm)	J_{SC} [mA·cm^{-2}]	V_{OC} [mV]	Fill Factor [%]	Efficiency [%]
MAI/P3HT	300 (0.8M)	14.23	0.687	65.5	6.40
	500 (1.2M)	17.46	0.878	67.9	10.41
MAI/Spiro	300 (0.8M)	16.03	0.898	74.0	10.66
	500 (1.2M)	19.15	0.969	72.5	13.46
MIX/Spiro	650 (0.8M)	20.48	0.998	69.4	14.23
	950 (1.2M)	20.19	0.957	70.7	13.69

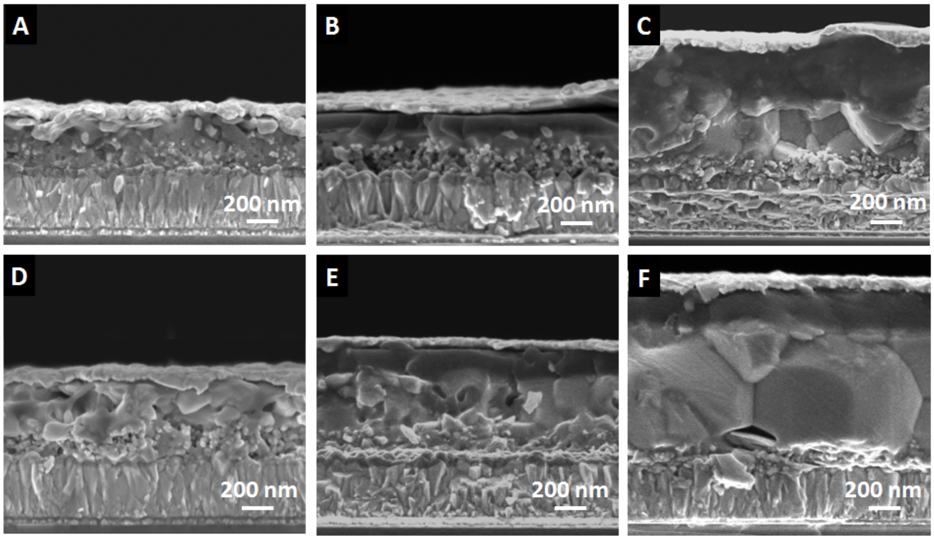

Figure A-5.1. SEM cross-sectional images of the studied devices for different device configurations. (A,D) MAI/P3HT, (B,E) MAI/Spiro and (C,F) MIX/Spiro and different concentration of perovskite precursors: (A,B,C) 0.8M and (D,E,F) 1.2M.

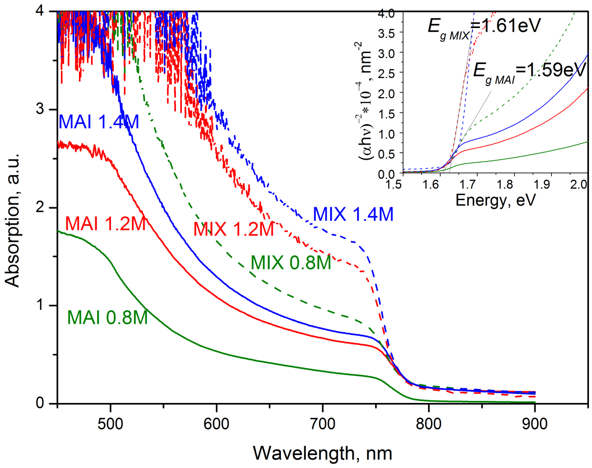

Figure A-5.2. UV/Vis absorption spectra of the perovskite layers studied in this work. The inset illustrates the estimation of the optical band gap from the measured spectra.

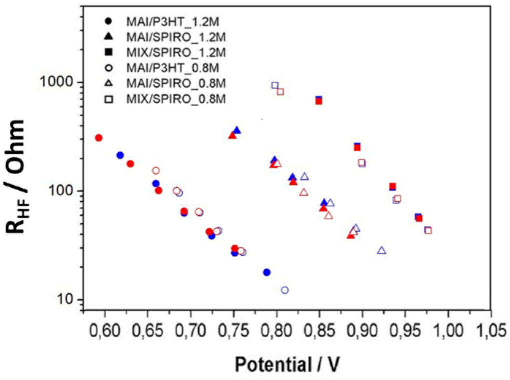

Figure A-5.3. High-frequency resistances as extracted from fittings of the impedance spectra using the two excitation wavelengths of λ_{blue} = 465 nm and λ_{red} = 635 nm.

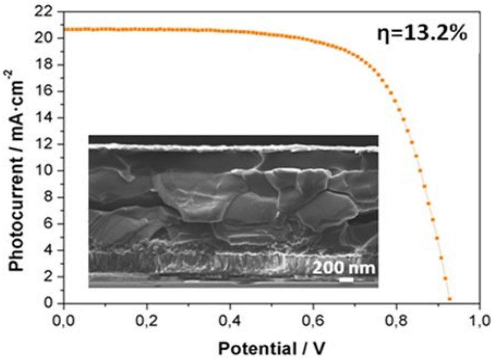

Figure A-5.4. Current-voltage curve for backward scans (scan rate = 100 mV/s) for a concentration of perovskite precursor of 1.4M. Inset shows the SEM cross-sectional image.

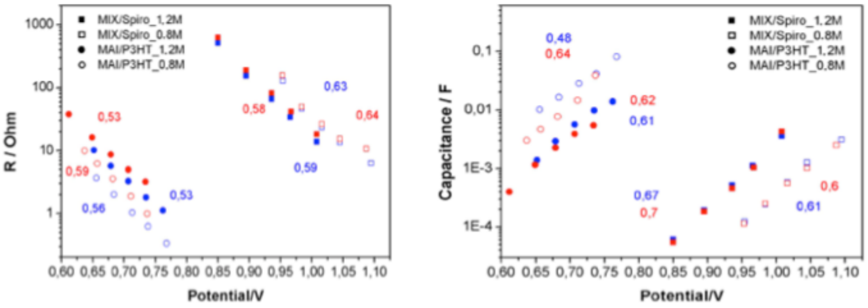

Figure A-5.5. Low-frequency resistances and associated capacitances as extracted from fittings of the impedance spectra for the configurations indicated using the two excitation wavelengths of λ_{blue} = 465 nm and λ_{red} = 635 nm. Slopes in units of q/k_BT are indicated in the graphs.

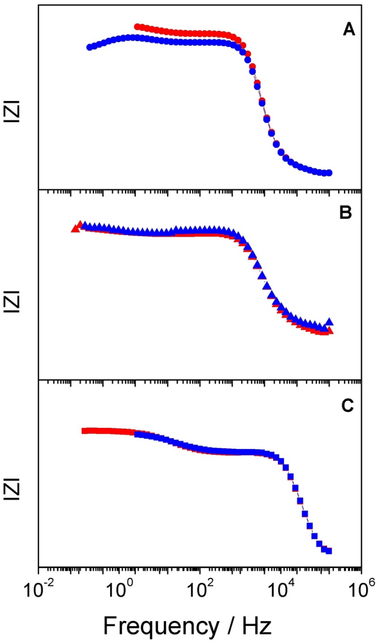

Figure A-5.6. Resistance Bode plot at open-circuit under the excitation wavelengths of λ_{blue} = 465 nm and λ_{red} = 635 nm for the configurations described in Table A-5.1 and for a precursor concentration of 1.2 M: (A) MAI/P3HT, (B) MAI/Spiro and (C) MIX/Spiro.

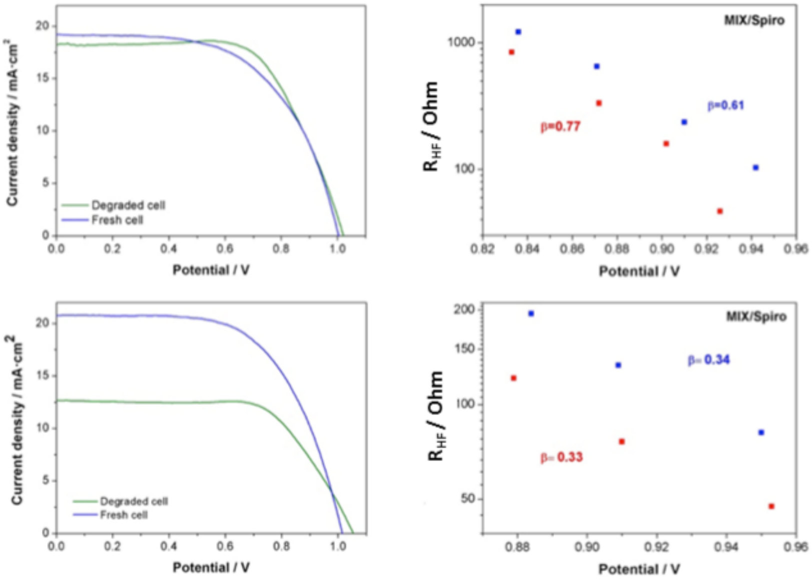

Figure A-5.7. Current-voltage curves for fresh and degraded MIX/Spiro cells (left) and high-frequency recombination resistance as extracted from fittings of the impedance spectra using the two excitation wavelengths of λ_{blue} = 465 nm and λ_{red} = 635 nm for degraded cells (right). Data at the top corresponds to cells being kept in the dark at ambient humidity during 6 days. In the case shown at the bottom, the cell was kept under ambient illumination during 6 days.

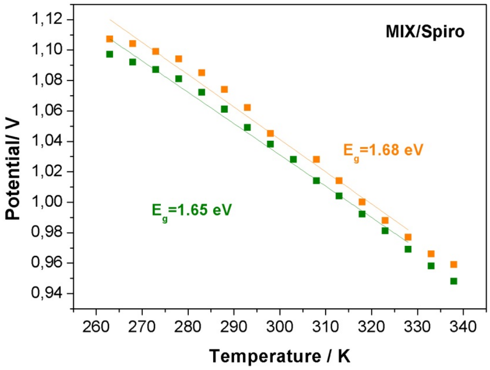

Figure A-5.8. Open-circuit potential as a function of temperature for the aged devices studied in Figure A-5.6 for white light and a light intensity of 14.15 W/m^2. Orange: dark degradation, Green: degradation under illumination

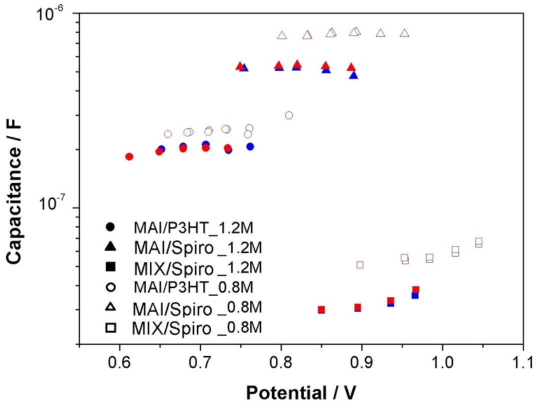

Figure A-5.9. High frequency capacitance as extracted from fittings of the impedance spectra using the two excitation wavelengths of λ_{blue} = 465 nm and λ_{red} = 635 nm, for the indicated cell configurations.

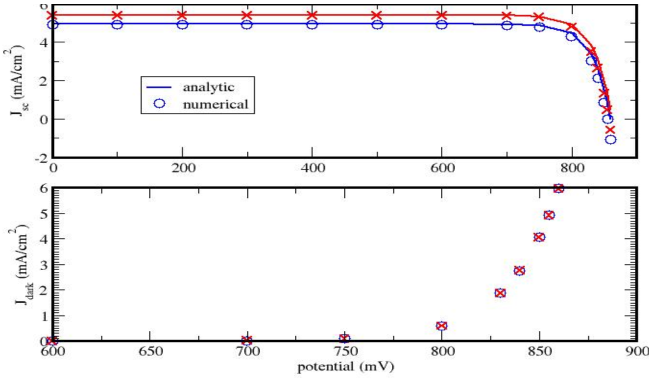

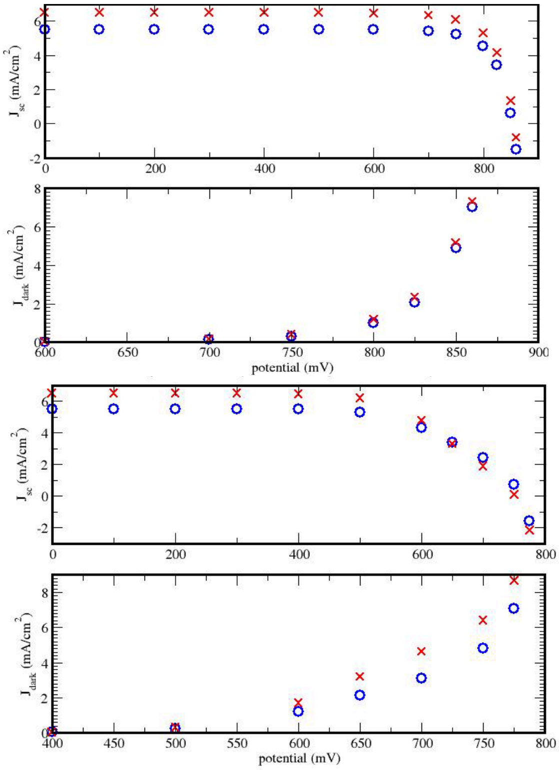

Figure A-5.10. Total and dark currents versus applied potential for both blue and red illumination as obtained from the numerical solution of Eqs. 5.3 and 5.4. Top panels: linear recombination case ($\gamma = 1$). Results of the analytical model of Södergren et al.[5] is added for comparison. Middle and bottom panels: non-linear recombination ($\gamma = 0.5$) with slow (middle) and rapid (bottom) recombination.

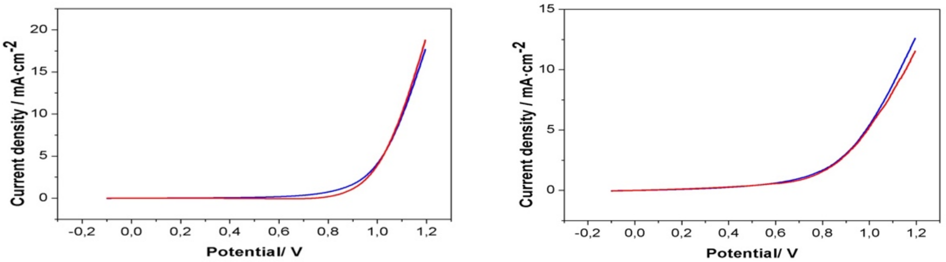

Figure A-5.11. Dark currents with both blue and red illumination for the degraded devices of Figure A-5.7. Left: degradation in the dark. Right: degradation under illumination.

Numerical solution of Eqs. 5.3 and 5.4

Eqs. 5.3 and 5.4 in the main text

$$U_{rec} \approx -\frac{dn}{dt} = k_T p_0 n^{\gamma} \tag{5.3}$$

$$D_n \frac{d^2n}{dx^2} - U_{rec} + I_0(\lambda)\alpha(\lambda)exp[-\alpha(\lambda)x] = 0 \tag{5.4}$$

can be solved numerically[2,3] to obtain the current-voltage curve and the dark current. The Forward Time Centered Space (FTCS) method was used with the following boundary conditions:[4]

$$n(x = 0, t) = n_0(V) \tag{A−5.1}$$

$$n(x, t = 0) = n_0(V) \tag{A−5.2}$$

$$\left(\frac{dn(x,t)}{dx}\right)_{x=d} = 0 \tag{A−5.3}$$

where d is the thickness of the active layer, V is the applied voltage and

$$n_0(V) = n_0^0 \exp\left(V/_{k_B T}\right) \tag{A−5.4}$$

Once the equation is solved the photocurrent density for a given value of the potential V is obtained from the stationary density profile at $x = 0$ (it is assumed that collection of electrons and holes in external contacts is the same):

$$J(V) = \left(\frac{dn(x,t)}{dx}\right)_{x=0, t\longrightarrow\infty} \tag{A−5.5}$$

Solving Eqs. 5.3 and 5.4 for different values of V, and using Eq. A-5.4 and Eq. A-5.5), the full IV curve can be obtained.

The following parameters were used in the simulations (intended to approximately reproduce the conditions of the MIX/Spiro devices). Absorption coefficient: α (λ = 465 nm) = 5 10^6 m^{-1} (blue), α (λ = 635 nm) = 2 10^6 m^{-1} (red), electron diffusion coefficient:[4] D_n = 2 10^{-6} m^2s^{-1}, photon flux: I_0 (λ = 465 nm) = 3.5 10^{20} m^2s^{-1} (blue), I_0 (λ = 635 nm) = 4.8 10^{20} m^2s^{-1} (red). Two recombination rates where considered: k_{rec} = 2 10^6 $m^{3(\gamma-1)}$ s^{-1}, corresponding to a diffusion length of L_n = 1 µm[4] and k_{rec} = 2 10^8 $m^{3(\gamma-1)}$ s^{-1} , which yields L_n = 0.1 µm for linear recombination (γ = 1). The numerical simulation was carried out using 300 points in x-space and 1.2 10^6 points in t-space, which were found to be enough to ensure convergence and that the steady-state is reached.

Results of the numerical simulation can be found in Figure A-5.5 for both linear (γ = 1), and non linear recombination (γ = 0.5). In the first case, simulated data where compared with the analytical results of Södergren et al.[4] In the second case, both slow and rapid recombination (long and short diffusion lenght) were compared. As explained in the main text, significant differences in the dark currents obtained between the red and the blue light illumination are only found in the non-linear case for a short-diffusion length.

Section D

Chapter 6. The Role of Surface Recombination on the Performance of Perovskite Solar Cells: Effect of Morphology and Crystalline Phase of TiO₂ Contact

Drift-Diffusion Device Modeling

The IV curves were numerically simulated using a fully-coupled drift-diffusion model of charge carrier and halide ion dynamics in a perovskite solar cell. The simulated device consisted of a TiO_2 electron selective layer, $MAPbI_3$ absorber layer and spiro-OMeTAD hole selective layer. Electrons were constrained to the perovskite and TiO_2, while holes were constrained to the perovskite and spiro-OMeTAD layer. Ion vacancies were constrained to the perovskite. In one spatial dimension x, the behaviour of each species of particle over time t is described by the drift-diffusion equation

$$\frac{\partial c}{\partial t} = D\frac{\partial}{\partial x}\left(\frac{qc}{k_B T}\frac{\partial \phi}{\partial x} - \frac{\partial c}{\partial x}\right) + G - R \qquad \text{(A-6.1)}$$

where c is the particle density, D the diffusion coefficient, q the elementary charge, k_B the Boltzmann constant, T the temperature, ϕ the electric potential, G any generation (sources) and R any recombination (sinks). The electric potential is found from the Poisson equation

$$\frac{\partial^2 \phi}{\partial x^2} = -\frac{\rho}{\varepsilon} \qquad \text{(A-6.2)}$$

where ρ is the net charge density and ε the permittivity of the material.
Electrons and holes are generated within the perovskite with a Beer-Lambert profile given by

$$G = F_{ph}\alpha e^{-\alpha x} \qquad \text{(A-6.3)}$$

where F_{ph} is the flux of photons incident on the device with energy above the band gap and α the absorptivity of the perovskite. Recombination within the bulk of the perovskite is calculated using a combination of bimolecular (direct relaxation across the band gap) and SRH schemes, given by

$$R_{bulk} = \beta\left(np - n_i^2\right) + \frac{\left(np - n_i^2\right)}{\tau_n p + \tau_p n} \qquad \text{(A-6.4)}$$

where n and p are the electron and hole densities, τ_n and τ_p the SRH pseudolifetimes for electrons and holes. The intrinsic carrier density n_i is defined from Eq. 2.8 (*Chapter* 2) as

$$np = N_C N_V exp\left(-\frac{E_g - (qV)}{2k_B T}\right) \qquad \text{(A-6.5)}$$

The surface recombination is also allowed, where a carrier in a transport layer recombines with an opposite carrier within the perovskite across the interface. This is modeled using a purely SRH mechanism, given by

$$R_S = \frac{np - n_i^2}{\frac{p}{v_n} + \frac{n}{v_p}} \qquad \text{(A-6.6)}$$

where v_n and v_p are the recombination velocities at the relevant interface. All parameters used in the model are given in Table A-6.1. The only parameter changed between the two IV scans is the hole recombination velocity at the TiO_2/$MAPbI_3$ interface, which it is increased from 10 m/s for *Np-Anatase* TiO_2 to 1000 m/s for the *Nc-Amorphous* TiO_2.

A finite difference scheme is used to discretise in space, and integrate over time using the MATLAB *ode15s* (The MathWorks Inc., Natick, MA, USA) solver adapted for quadruple-precision arithmetic using the Advanpix Multiprecision Computing Toolbox. (Advanpix LLC, Yokohama, Japan). A full description of the method is detailed in Courtier *et al.*[18] IV curves at 100 mV/s were simulated by varying the boundary conditions on the Poisson equation at this rate.

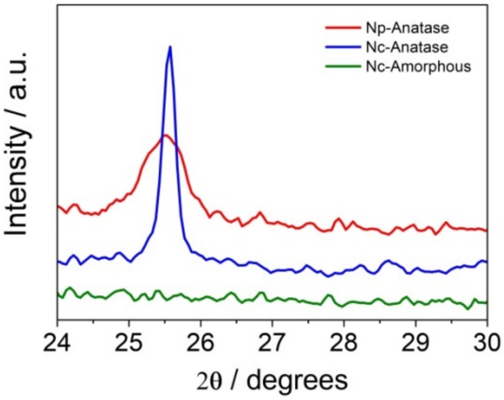

Figure A-6.1. X-ray diffraction for the different TiO_2 films employed as ETL in perovskite devices.

Table A-6.1. Parameters used in the drift-diffusion model to simulate the IV curve

Parameter	**Value**
Temperature	295 K
Incident photon flux	1.4×10^{17} cm^{-2}s^{-1}
MAPbI$_3$ absorber layer	
Width	400 nm
Permittivity	$24.1\varepsilon_0$
Electron diffusivity	1.7 cm^{2}s^{-1}
Hole diffusivity	1.7 cm^{2}s^{-1}
Conduction band energy	-3.7 eV
Valence band energy	-5.4 eV
Conduction band density of states	8.1×10^{18} cm^{-3}
Valence band density of states	5.8×10^{18} cm^{-3}
Absorptivity	1.3×10^{5} cm^{-1}
Ion vacancy density	1.6×10^{19} cm^{-3}
Ion vacancy diffusivity	1.2×10^{-13} cm^{2}s^{-1}
TiO$_2$(ESL)	
Width	50 nm
Permittivity	$3\varepsilon_0$
Electron diffusivity	0.15 cm^{2}s^{-1}
Doping density	1.7×10^{18} cm^{-3}
Conduction band energy	-3.95 eV
Spiro-OMeTAD (HTM)	
Width	200 nm
Permittivity	$40\varepsilon_0$
Hole diffusivity	0.15 cm^{2}s^{-1}
Doping density	8×10^{17} cm^{-3}
HOMO energy	-5.0 eV
Bulk recombination	
Bimolecular rec. coefficient	10^{-6} cm^{3}s^{-1}
SRH electron pseudolifetime	50 ps
SRH hole pseudolifetime	50 ns
Surface recombination velocities	
Electrons at TiO$_2$/MAPbI$_3$ interface	10^{5} ms^{-1}
Holes at TiO$_2$/MAPbI$_3$ interface	10 ms^{-1}, 1000 ms^{-1}
Electrons at MAPbI$_3$/spiro interface	0.01 ms^{-1}
Holes at MAPbI$_3$/spiro interface	10^{4} ms^{-1}

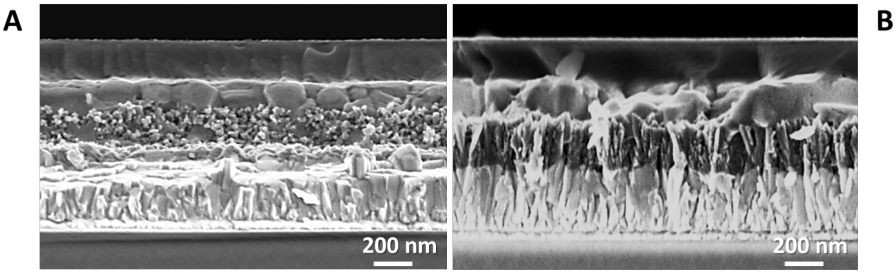

Figure A-6.2. Cross-section SEM images of perovskite films deposited on mesoporous (A) and nanocolumnar (B) TiO_2 substrates

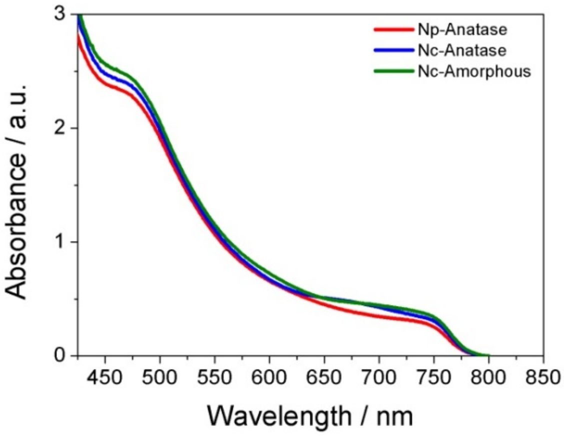

Figure A-6.3. UV-Vis absorption spectra of perovskite deposited on top of the different TiO_2 films employed as ETL in perovskite devices.

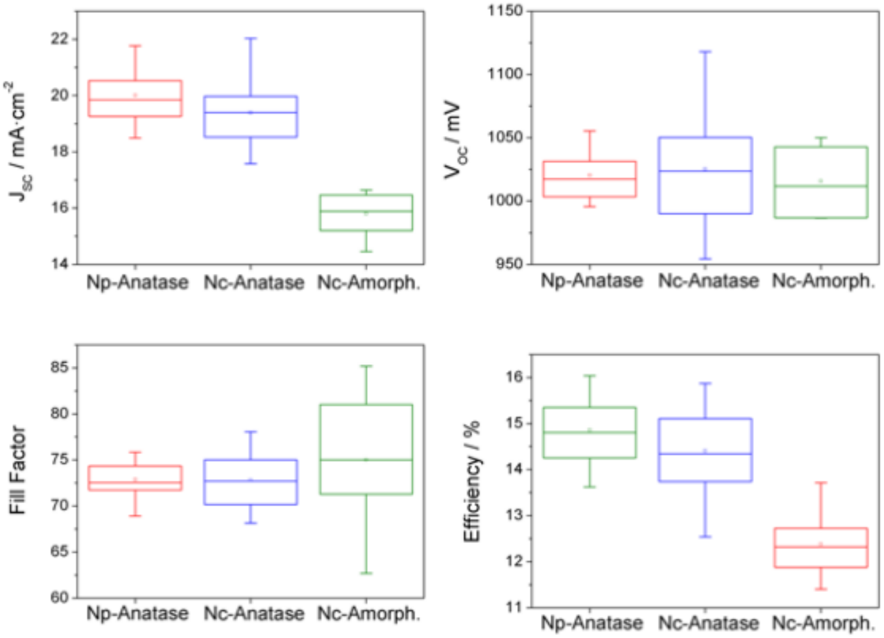

Figure A-6.4. Photovoltaic parameters statistics of the devices studied in this work. Data were obtained in reverse scan under AM1.5 - 1 sun illumination for perovskite solar devices based on the different nanostructure employed as electron transport layer. Note that at least 20 devices of each configuration were measured.

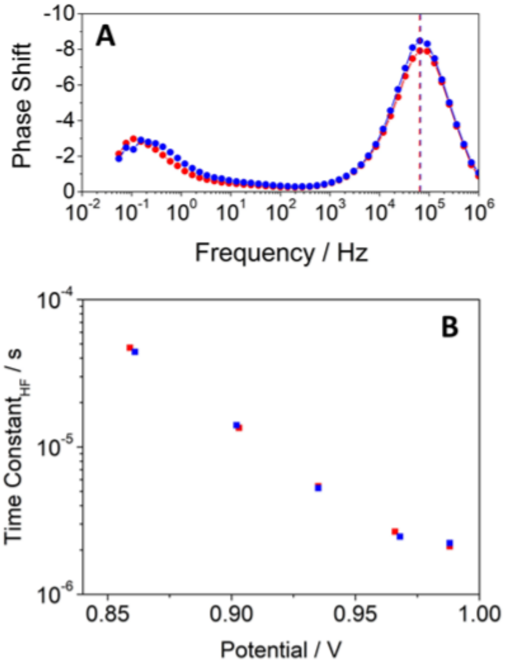

Figure A-6.5. (A) Impedance frequency plot of phase shift (Φ) and (B) *HF* time constants extracted as 1/2πf for *Np-Anatase* devices under open-circuit conditions and under red and blue light illumination

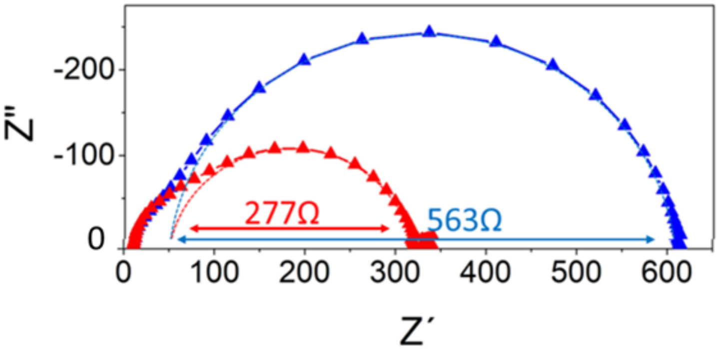

Figure A-6.6. Impedance spectra and under open circuit conditions and under blue and red illumination as excitation wavelengths for Ncolumns-Amorphous devices. An external potential of 0.988V was applied.

Section E

Chapter 7. Impact of Moisture on Efficiency-Determining Electronic Processes in Perovskite Solar Cells

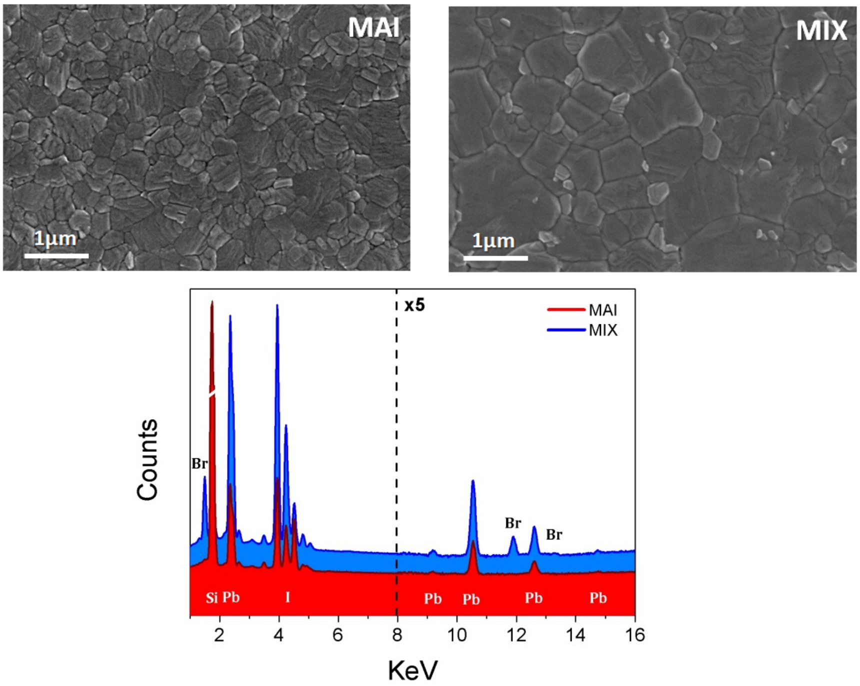

Figure A-7.1. (Up) Plane-view scanning electron microscopy (SEM) images for the (MAI) $MAPbI_3$ and (MIX) $Cs_{0.05}FA_{0.81}$ $MA_{0.14}PbI_{0.85}$ $Br_{0.15}$ perovskite layers. (Down) EDX spectra of the different perovskite layers deposited on Si/*c*TiO_2/*m*TiO_2.

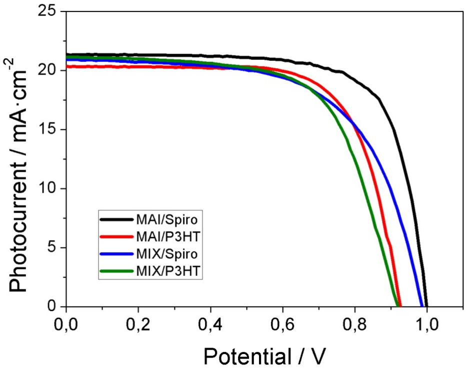

Figure A-7.2. Current-voltage characteristics of the different devices under 1 sun - AM1.5 illumination in reverse scan. A scan rate of 100mV/s with a poling of 30s at 1.2V was employed.

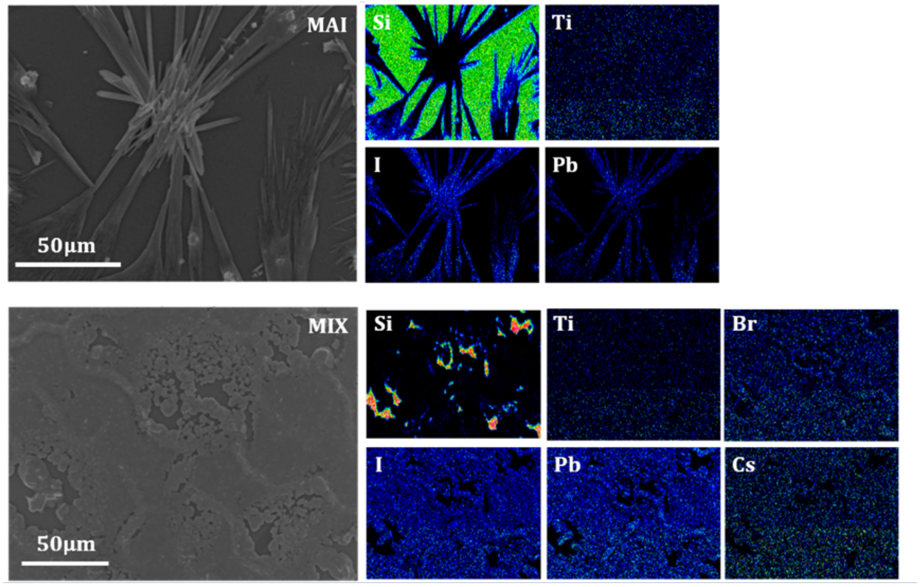

Figure A-7.3. EDX mapping of the different (MAI and MIX) perovskite layers deposited on Si/*c*TiO_2/*m*TiO_2 after moisture exposure (RH > 90%) for 5 hours at room temperature.

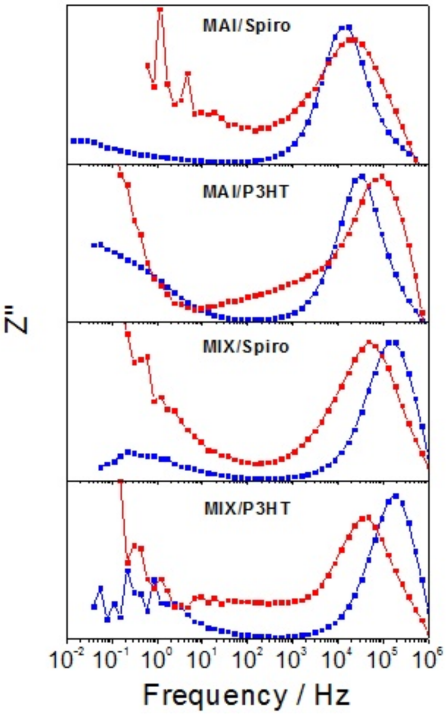

Figure A-7.4. Impedance frequency plots of the imaginary part for (blue) fresh and (red) degraded PSCs obtained at open-circuit conditions and under white illumination.

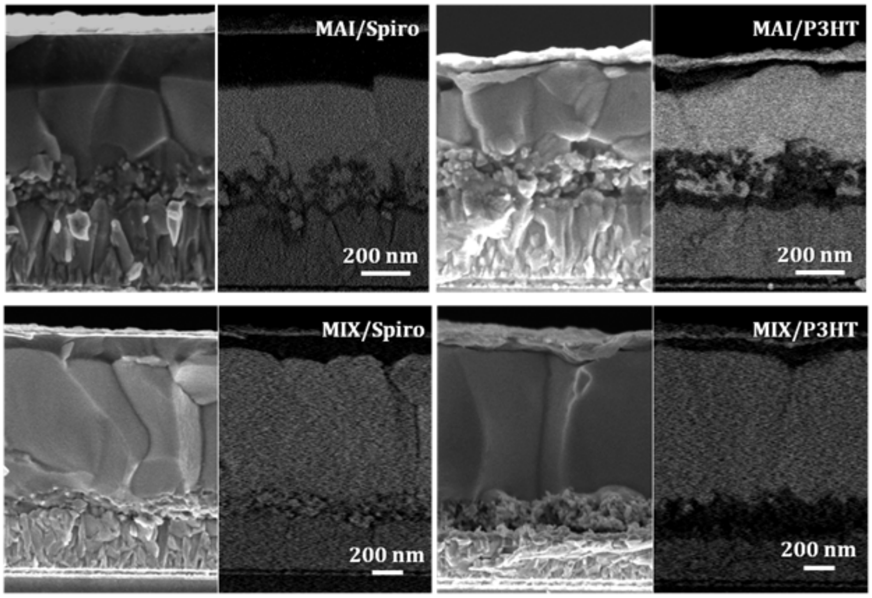

Figure A-7.5. (Right) cross-section scanning electron microscopy and (left) back scattering electron images for the different configurations. A thickness of 450 nm and 950 nm were found for MAI and MIX devices, respectively.

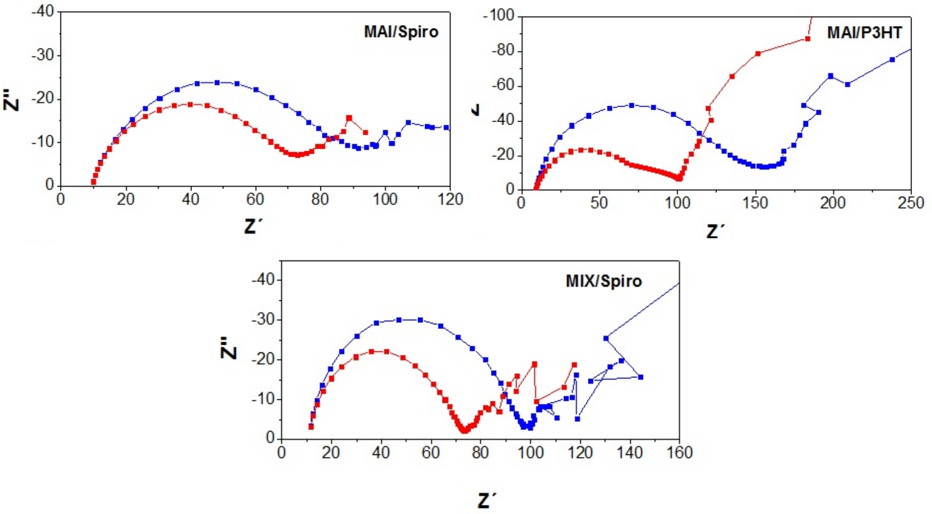

Figure A-7.6. Nyquist impedance spectra for degraded MAI/Spiro, MAI/P3HT and MIX/Spiro devices at open-circuit condition and under blue and red illumination.

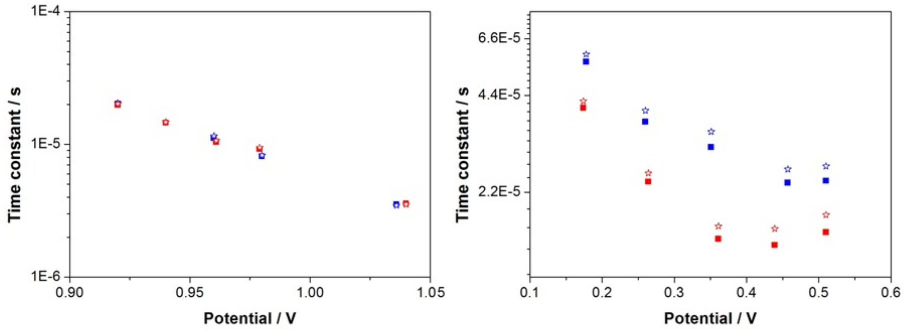

Figure A-7.7 .HF time constant extracted as (squares) $R_{rec} \cdot C_b$ and (stars) $1/2\pi f$ from impedance response for (right) fresh and (left) degraded MAI/Spiro devices at open-circuit conditions and under blue and red illumination.

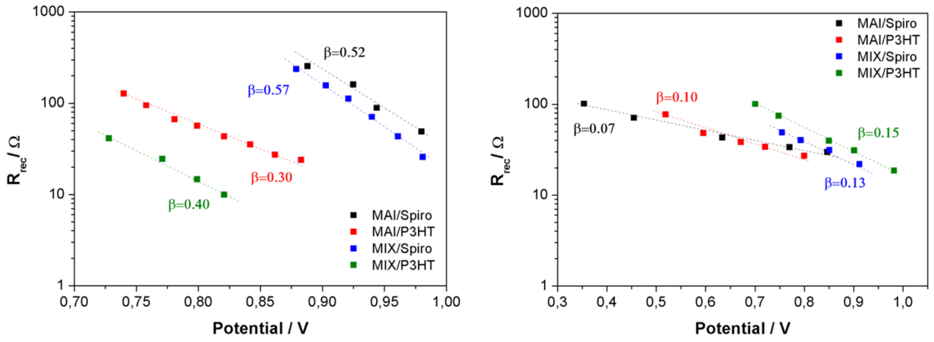

Figure A-7.8. Electron recombination resistance versus open-circuit potential and under white-light excitation extracted from fittings of the impedance spectra for the (left) fresh and (right) degraded PSCs.

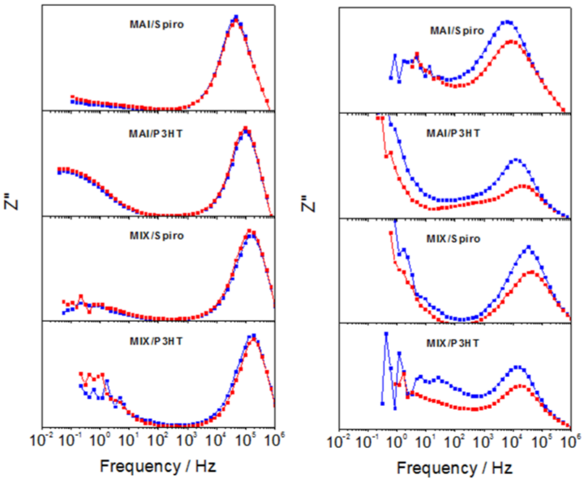

Figure A-7.9. Impedance frequency plots of the imaginary part for (left) fresh and (right) degraded PSCs obtained at open-circuit condition and under illumination using the two excitation wavelengths of λ_{blue} = 465 nm (blue) and λ_{red} = 635 nm (red).

Table A-7.1. Photovoltaic parameters measured under 1 sun - AM 1.5 illumination for the different devices in reverse scan. Error bars are estimated from the results of three best devices of the same configuration.

Device	J_{SC} [mA·cm^{-2}]	V_{OC} [mV]	Fill Factor [%]	Efficiency [%]
MAI/Spiro	20.9 ± 0.2	996 ± 5	73 ± 2	15.3 ± 0.9
MAI/P3HT	20.4 ± 0.3	940 ± 10	70 ± 5	13.2 ± 0.8
MIX/Spiro	21.2 ± 0.1	986± 4	64 ± 3	13 ± 1
MIX/P3HT	21.1 ± 0.2	912 ± 17	65 ± 1	12.5 ± 0.2

Table A-7.2. Static water contact angle of the different devices.

Device	Water Contact Angle
MAI	72.5 ± 2
MAI/Spiro	77 ± 2
MAI/P3HT	106 ± 3
MIX	87 ± 2
MIX/Spiro	78 ± 2
MIX/P3HT	105 ± 3

Table A-7.3. Atomic percentage of the elements present in the samples estimated after XPS characterization.

Device / At %	Pb	I	O	C	N	S	F	Ti
MAI	15.9	18.6	11.2	47.0	7.3	-	-	-
MAI (90% RH)	7.7	14.8	32.8	27.4	3.4	-	-	13.9
MAI/Spiro	-	-	14.1	73.2	4.5	2.4	5.8	-
MAI/Spiro (90% RH)	0.2	0.7	15.1	68.2	5.6	2.2	8.1	-
MAI/P3HT	-	-	-	88.8	-	11.2	-	-
MAI/P3HT (90% RH)	-	0.4	2.1	87.7	-	9.8	-	-
MIX	13.4	22.8	10.8	44.9	8.1	-	-	-
MIX (90% RH)	14.4	37.9	8.6	28.9	10.2	-	-	-
MIX/Spiro	-	-	12.7	77.2	4.4	2.0	3.6	-
MIX/Spiro (90% RH)	-	0.6	19.1	68.1	4.6	1.7	5.9	-
MIX/P3HT	-	-	-	89.6	-	10.4	-	-
MIX/P3HT (90% RH)	-	-	-	90.7	-	9.3	-	-

Section F

Chapter 8. Impedance analysis of perovskite solar cells: a case study

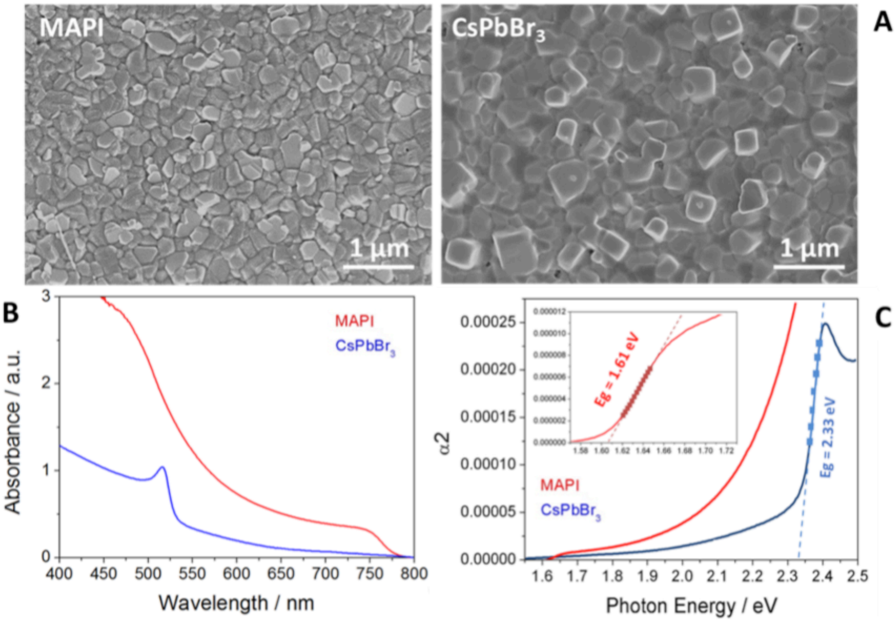

Figure A-8.1. Morphological, and optical characterization of $MAPbI_3$ and $CsPbBr_3$ films and solar cells: (A) Plane-view scanning electron microscope images (SEM), (B) UV-Vis spectra (C) Tauc plot

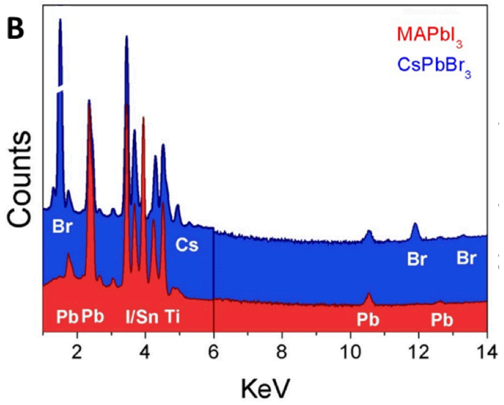

Figure A-8.2. EDX map of $MAPbI_3$ and $CsPbBr_3$ films.

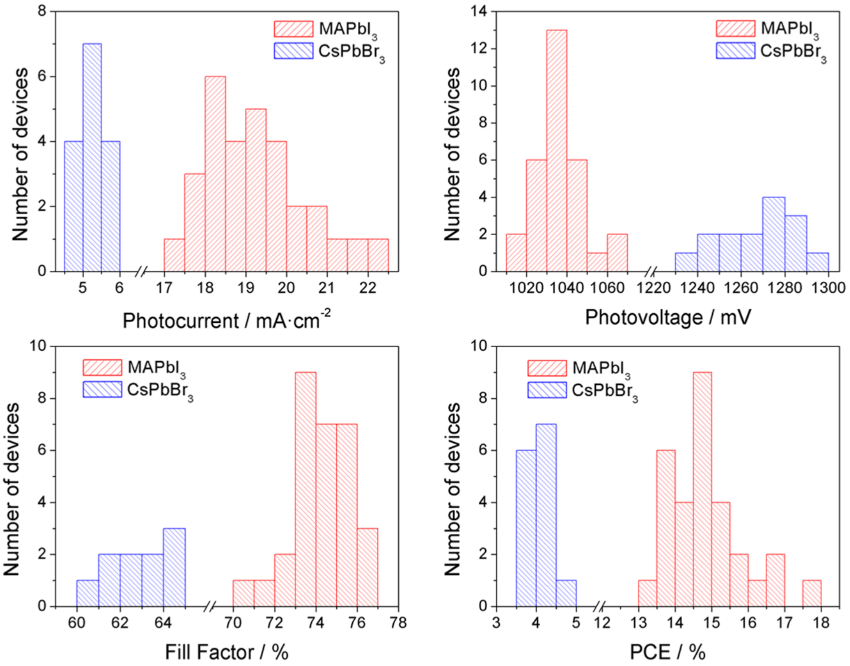

Figure A-8.3. Statistical data of photovoltaic parameters for $MAPbI_3$ and $CsPbBr_3$ solar cell devices.

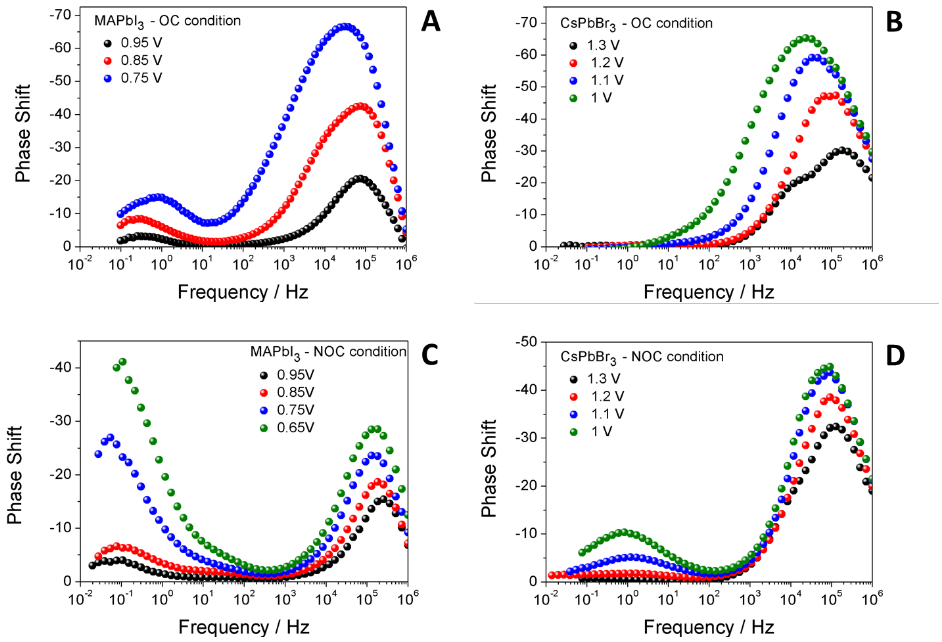

Figure A-8.4. Impedance Bode plots of MAPI and $CsPbBr_3$ solar cells at OC and NOC conditions.

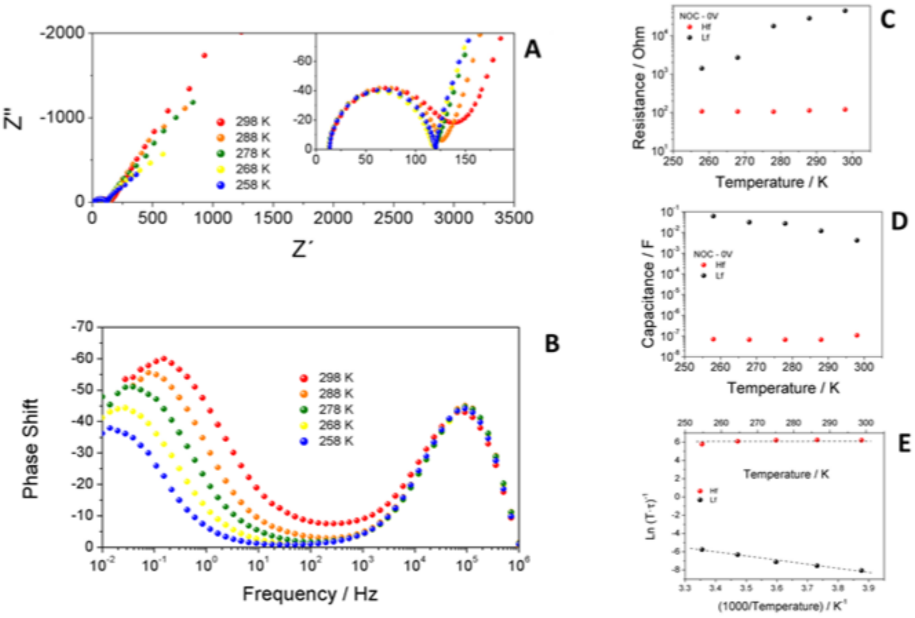

Figure A-8.5. (A) Impedance spectra and (B) frequency plot for MAPbI$_3$ based devices at SC conditions and different temperatures. (C) Arrhenius plot of the low and high frequency time constants. An activation energy of 36.9 kJ/mol can be extracted from the low frequency data. (D) and (E) resistances and capacitances at SC circuit as a function of temperature.

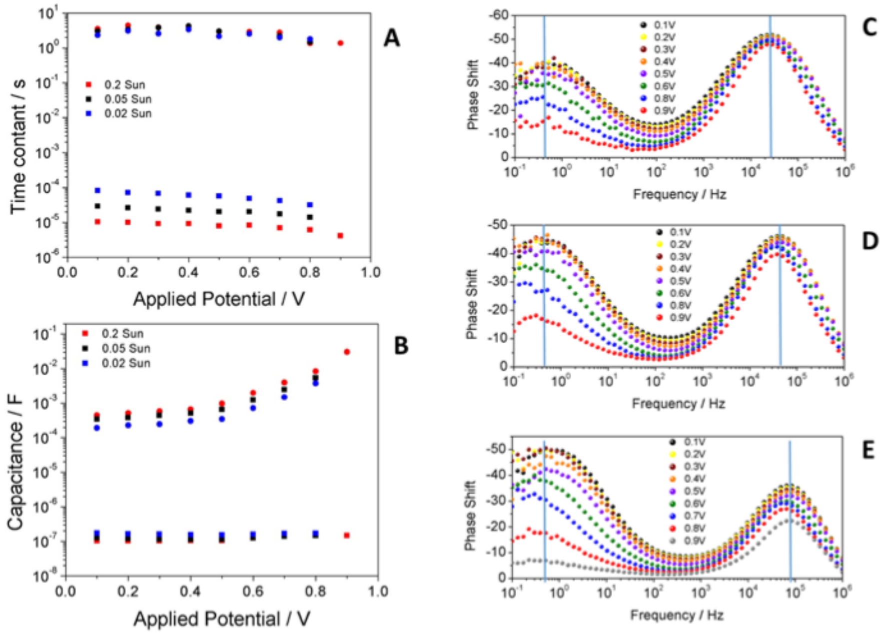

Figure A-8.6. Effect of illumination on the impedance response of MAPbI$_3$ based devices at NOC conditions. In Panels (A) and (B) the voltage dependence of both the high and low frequency time constants and capacitances is shown. Frequency Bode plots at 0.02, 0.05 and 0.2 suns are shown in panels (C), (D) and (E) respectively.

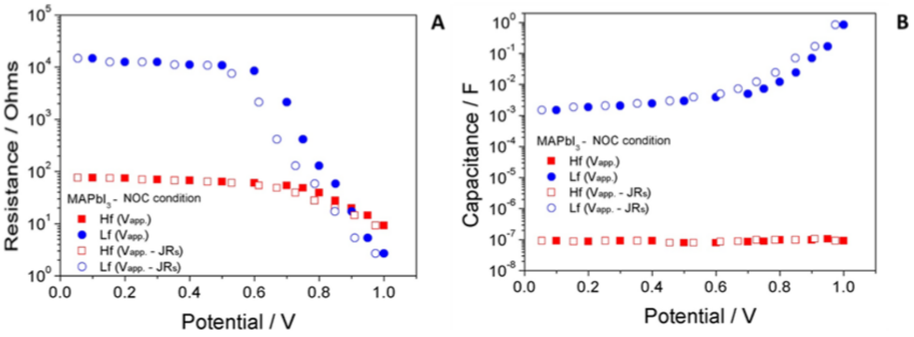

Figure A-8.7. Correction for voltage drop due to series resistance in the impedance measurements at NOC conditions for MAPbI$_3$ devices.

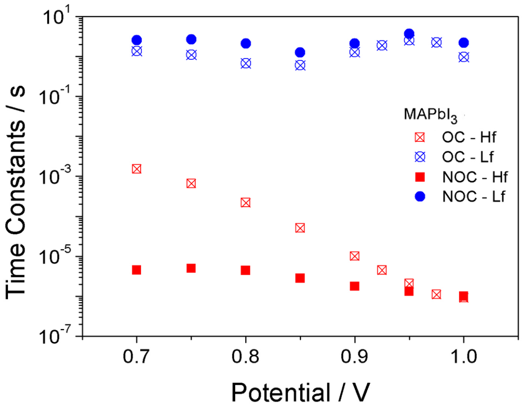

Figure A-8.8. High and low frequency time constants as extracted from fittings for MAPbI$_3$ based devices at OC and NOC conditions.

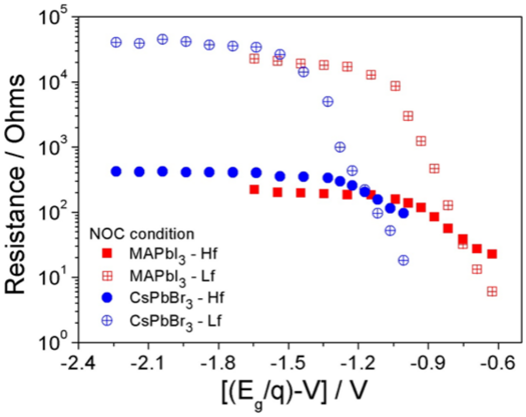

Figure A-8.9. High frequency resistive element extracted from fittings of the impedance spectra obtained at non open circuit plots versus the photopotential corrected for the optical band gap of the perovskites.

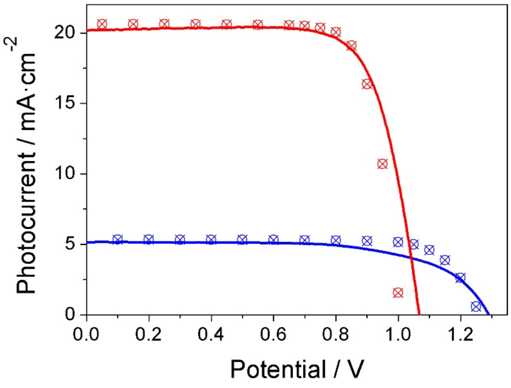

Figure A-8.10. Experimental JV curves (symbols) and reconstruction from the impedance data at NOC conditions using Eq. 8.2 in the main text (lines).

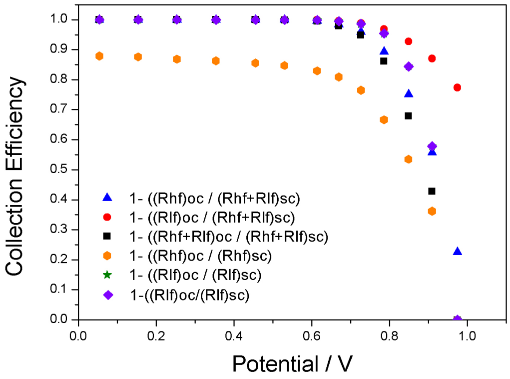

Figure A-8.11. Charge collection efficiency of $MAPbI_3$ solar cells as predicted by Eq. 8.3 using impedance data at OC and NOC conditions for several choices of R_{rec}.

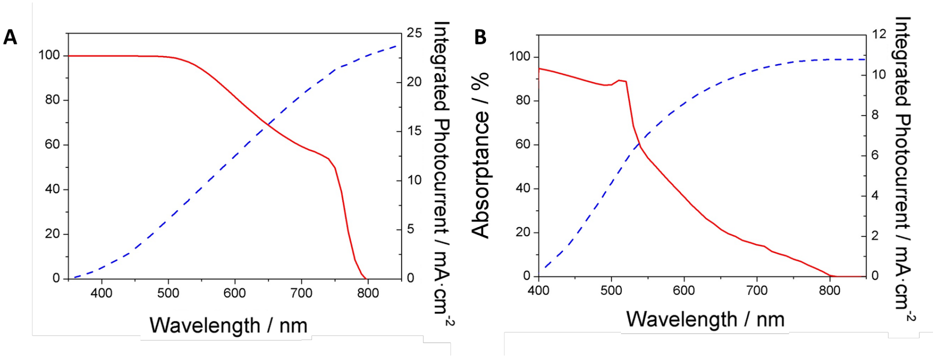

Figure A-8.12. Absorptance and integrated photocurrent for $MAPbI_3$ (A) and $CsPbBr_3$ (B). Total integrated photocurrent amounts to 24.9 and 10.8 mA/cm^2, respectively.

Section G

Chapter 9. Homeopathic perovskite solar cells: Effect of humidity during fabrication on the performance and device stability

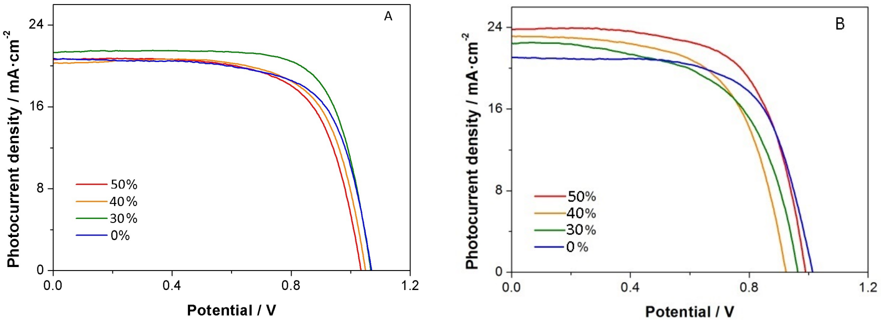

Figure A-9.1. Representative current-voltage curves (average of 3-5 devices –see Table 9.1 in main text) under AM1.5 1 sun illumination of (A) fresh and (B) aged $MAPbI_3$ solar cells fabricated under different humidity conditions (see main text for details).

Section A-9.2: absorbance of perovskite films after exposure to very humid air

In parallel to the photoelectrical characterization, optical absorption measurements of the $CH_3NH_3PbI_3$ bare films deposited on the TiO_2 substrates were also conducted. Figure A-9.2 shows the absorption spectra of the perovskite deposited under varying moisture conditions before and after exposure to a constant current of highly humid air (RH > 85%) at short and longer times (1 and 5 hours). Interestingly enough, the absorbance for the films prepared under high humidity conditions (40% and 50%) is observed to increase in time upon exposure to very humid air. These results appear to be in line with the increase of photocurrent detected in the aged devices. Integration of the corresponding *absorptance* ($1 - 10^{-A}$, with A the absorbance) convoluted with the AM1.5 solar spectrum between 350 nm and 800 nm provides an estimation of what would be the impact in terms of short-circuit photocurrent of the alleged better light harvesting of the aged films. Results for the 1-hour aged films yields an increment of 0.1, 0.8 and 0.9 mA/cm^2 for 30, 40 and 50% RH films, respectively. This is significantly less than the increase observed in J_{sc} upon aging. However, it must be noted that the optical absorption experiment was done on bare films subjected to very humid air, not on a full device, as it is the case of the measurement of J_{sc}, which is done on devices aged under ambient conditions. Furthermore, other effects affecting the photocurrent in the full device cannot be ruled out, as, for instance, improved charge collection at short circuit.

We can also observe that for the driest conditions (30%) the absorbance spectra recorded after 5 hours does not only show an intensity decrease, but also a change of shape. As previously reported[5,6] this shape is characteristic of degraded devices where the presence of PbI_2 is more remarkable and gives rise to a shoulder around 500 nm. This is less visible for degraded devices deposited under the moistest conditions (50%).

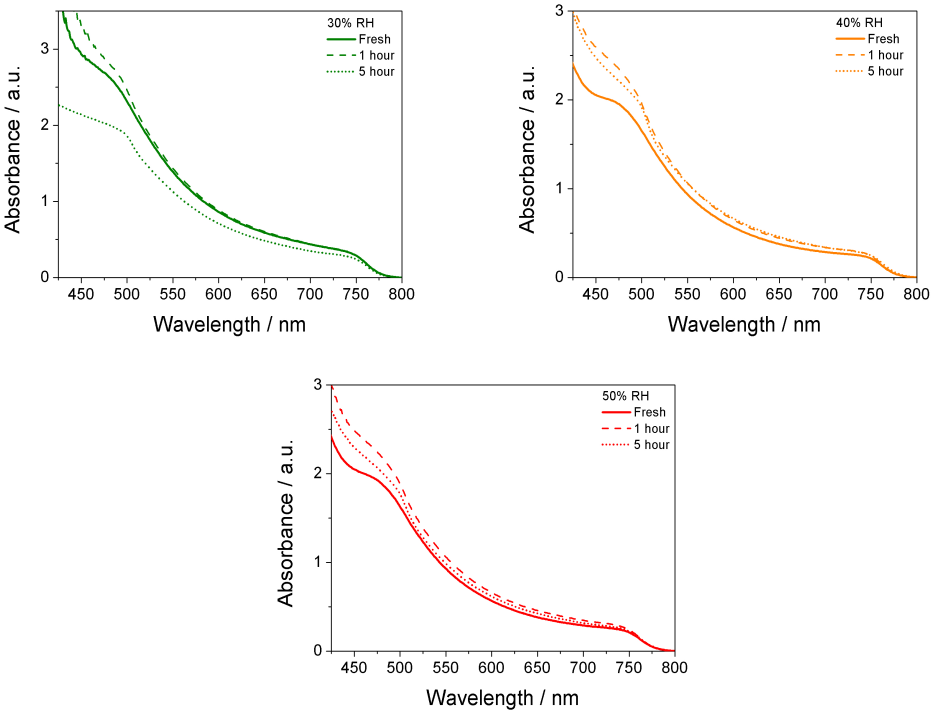

Figure A-9.2. Optical absorption data of bare $MAPbI_3$ films deposited on TiO_2 substrates under different environmental moisture conditions (30%, 40% and 50%). Absorbance data is shown for the pristine material (solid line) and after exposure times of 1h (dash line) and 5h (dot line) under a relative humidity >85%.

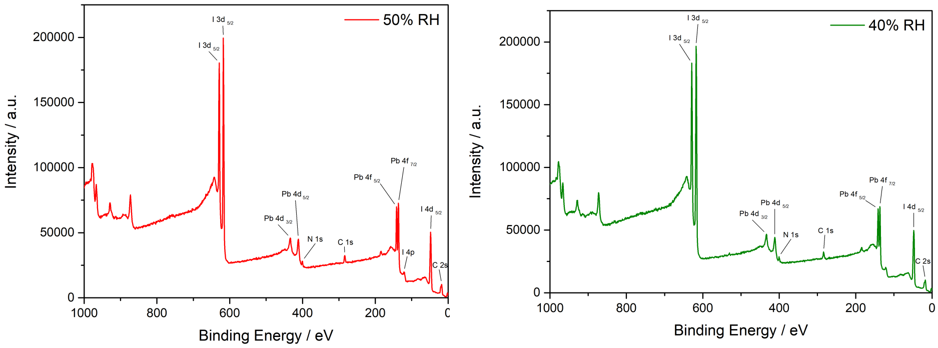

Figure A-9.3 XPS spectra of perovskite thin films deposited on mesoporous TiO_2

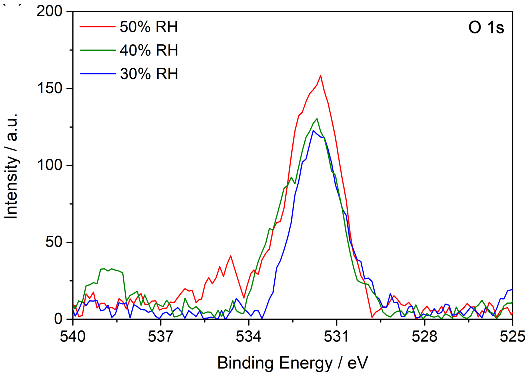

Figure A-9.4 O 1s signal obtained from XPS measurements of perovskite thin films fabricated at relative humidityvalues as indicated and deposited on mesoporous TiO_2

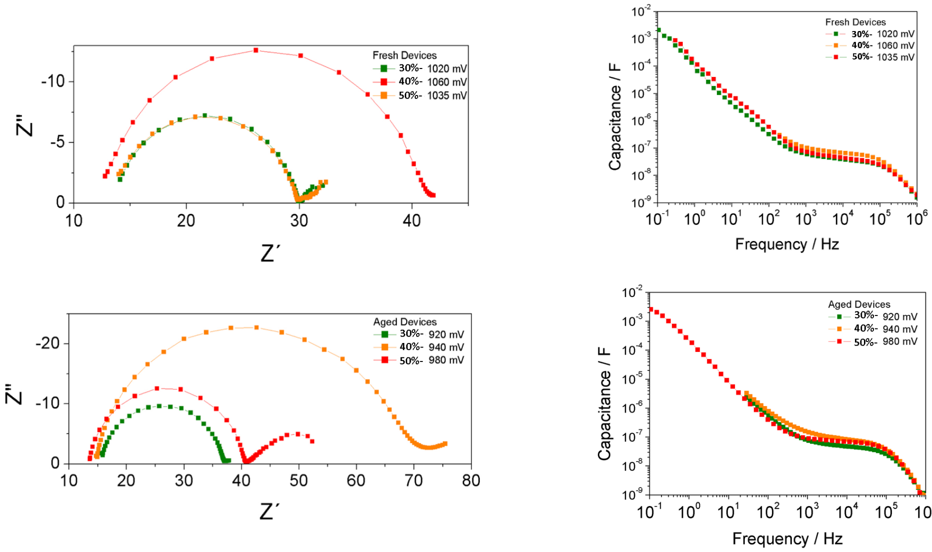

Figure A-9.5. Nyquist plots (left) and apparent capacitance (right) for fresh and aged devices as extracted from open-circuit impedance experiments with red light illumination.

Section H

Chapter 10. Water vapour pressure as determining control parameter to fabricate high efficiency perovskite solar cells at ambient conditions

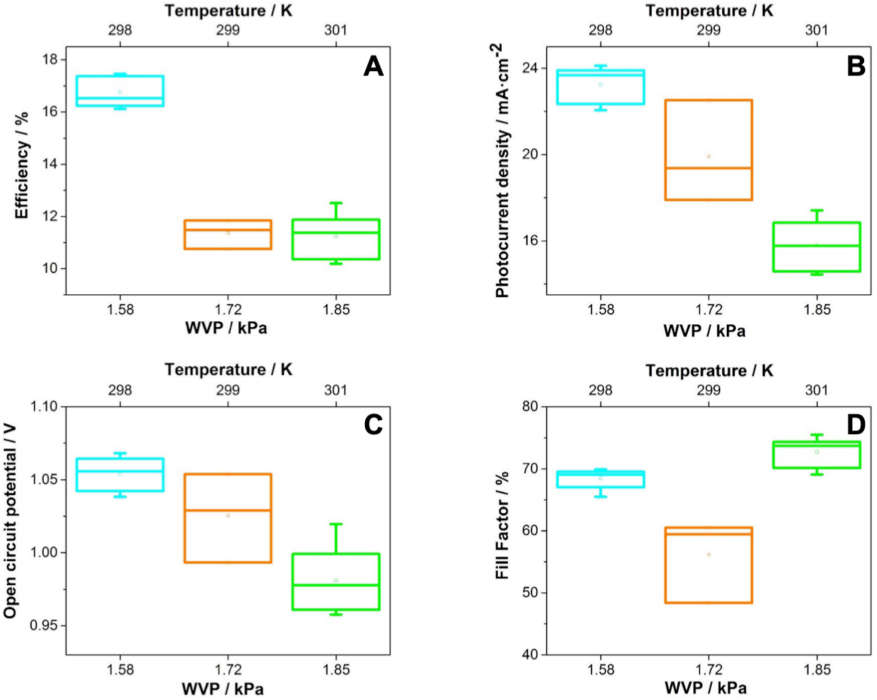

Figure A-10.1. Photovoltaic parameters statistics using analysis of variance (ANOVA) of $MAPbI_3$ devices prepared under different temperature conditions and a relative humidity of 50 %. Data were obtained in reverse scan under AM1.5 - 1 sun illumination for perovskite films deposited from a solution precursor with a ratio DMSO:Pb^{2+} of 0.75. Note that at least 6 devices of each configuration were measured.

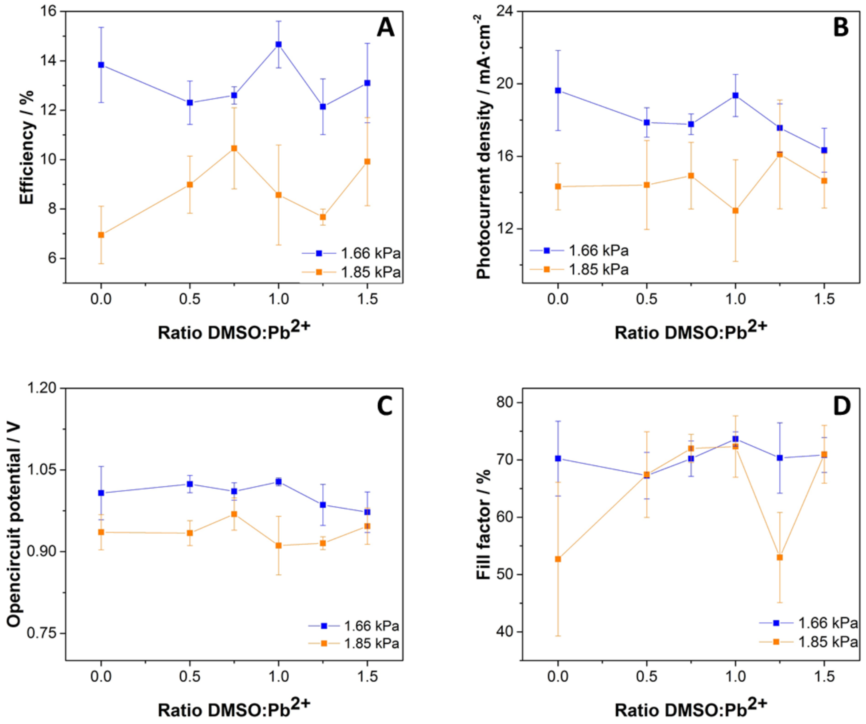

Figure A-10.2. Photovoltaic parameters of $MAPbI_3$ devices prepared from precursor solution with different DMSO:Pb^{2+} ratio for two water vapour pressure (WVP). Data were obtained in reverse scan under AM1.5 - 1 sun illumination for perovskite solar devices fabricated at 301 K and 44 % and 49 % R.H (1.66 kPa and 1.85 kPa, respectively).

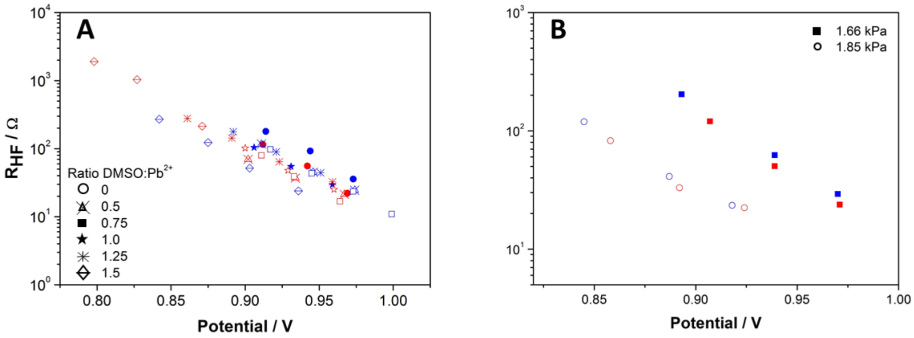

Figure A-10.3. Electron recombination resistance data as extracted from impedance spectroscopy measurements for $MAPbI_3$ devices prepared (A) from precursor solution with different DMSO:Pb^{2+} ratio and deposited under 1.66 kPa and (B) for two different water vapour pressure (WVP) for ratio 0.75.

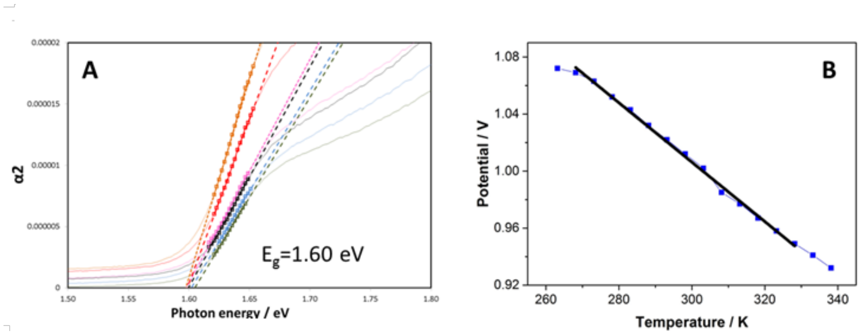

Figure A-10.4. (A) Illustration the estimation of the optical band gap from the measured spectra for $MAPbI_3$ devices prepared from precursor solution with different DMSO:Pb^{2+} ratio (B) Open-circuit potential as a function of temperature for $MAPbI_3$ devices from DMSO:Pb^{2+} ratio 1.0 for white light and a light intensity of 14.15 W/m^2. Data obtained for devices prepared under 1.66 kPa.

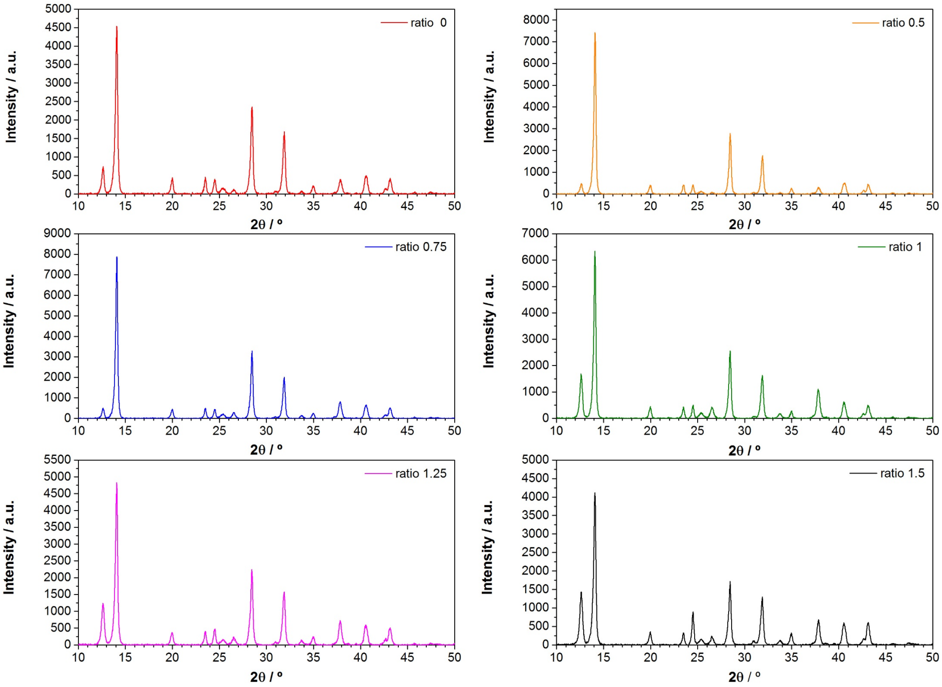

Figure A-10.5. XRD pattern of composite $MAPbI_3$/mesoporous-TiO_2 films prepared under 1.01 kPa (299 K and 30 % relative humidity).

Table A-10.1. PbI_2/ $MAPbI_3$ ratio for films deposited under 1.01 KPa (299 K and 30 % relative humidity).

Ratio DMSO:Pb^{2+}	PbI_2		$MAPbI_3$		I_1/I_2
	2θ	I_1	2θ	I_2	
0	12.65	740.9	14.08	4539.6	0.163
0.5	12.65	472.4	14.1	7424.5	0.064
0.75	12.63	498.7	14.1	7881.7	0.064
1	12.61	1690.6	14.08	6343.2	0.266
1.25	12.61	1241.8	14.08	4829.2	0.257
1.5	12.63	1438.4	14.1	4114.9	0.35

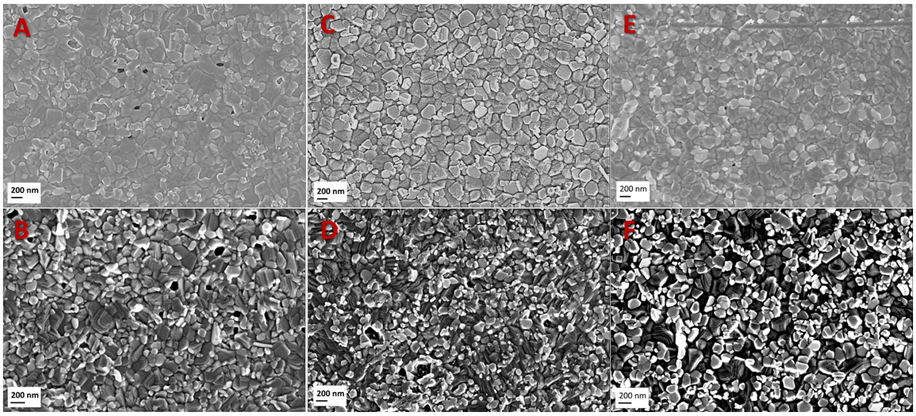

Figure A-10.6. Top-view scanning electron microscopy (SEM) images for $MAPbI_3$ films from precursor solution with DMSO:Pb^{2+} ratio 1.5 (A and B), 1.0 (C and D) and 0.5 (E and F) and deposited at1.66 kPa (A, C and E) and 1.85 kPa (B, D and F).

References

1 J. Bisquert, Theory of the Impedance of Electron Diffusion and Recombination in a Thin Layer, *J. Phys. Chem. B*, 2002, **106**, 325–333.

2 J. A. Anta, J. Idigoras, E. Guillen, J. Villanueva-Cab, H. J. Mandujano-Ramirez, G. Oskam, L. Pelleja and E. Palomares, A continuity equation for the simulation of the current–voltage curve and the time-dependent properties of dye-sensitized solar cells, *Phys. Chem. Chem. Phys.*, 2012, **14**, 10285–10299.

3 A. Todinova, J. Idígoras, M. Salado, S. Kazim and J. A. Anta, Universal Features of Electron Dynamics in Solar Cells with TiO $_2$ Contact: From Dye Solar Cells to Perovskite Solar Cells, *J. Phys. Chem. Lett.*, 2015, **6**, 3923–3930.

4 S. Soedergren, A. Hagfeldt, J. Olsson and S.-E. Lindquist, Theoretical

models for the action spectrum and the current-voltage characteristics of microporous semiconductor films in photoelectrochemical cells, *J. Phys. Chem.*, 1994, **98**, 5552–5556.

5 N. E. Courtier, G. Richardson and J. M. Foster, A fast and robust numerical scheme for solving models of charge carrier transport and ion vacancy motion in perovskite solar cells, *Appl. Math. Model.*, 2018, **63**, 329–348.

6 A. M. A. Leguy, Y. Hu, M. Campoy-Quiles, M. I. Alonso, O. J. Weber, P. Azarhoosh, M. van Schilfgaarde, M. T. Weller, T. Bein, J. Nelson, P. Docampo and P. R. F. Barnes, Reversible Hydration of CH3NH3PbI3 in Films, Single Crystals, and Solar Cells, *Chem. Mater.*, 2015, **27**, 3397–3407.

7 J. Yang, B. D. Siempelkamp, D. Liu and T. L. Kelly, Investigation of CH3NH3PbI3 Degradation Rates and Mechanisms in Controlled Humidity Environments Using in Situ Techniques, *ACS Nano*, 2015, **9**, 1955–1963.

List of abbreviations

AM 1.5G	*Air Mass 1.5 Global*
CB	*Conduction Band*
CPE	*Constant Phase Element*
DSSC	*Dye-Sensitized Solar Cell*
EDS	*Electron Dispersive Spectroscopy*
EQE	*External Quantum Efficiency*
ESL	*Electron Selective Layer*
ESM	*Electron Selective Material*
ETM	*Electron Transport Material*
FF	*Fill Factor*
HI	*Hysteresis Index*
HSL	*Hole Selective Layer*
HSM	*Hole Selective Material*
HTM	*Hole Transport Material*
IMPS	*Intensity-Modulated Photocurrent Spectroscopy*
IPCE	*Incident-Photon-to-Current-Efficiency*
IQE	*Internal Quantum Efficiency*
IS	*Impedance Spectroscopy*
NOC	*Non Open Circuit*
OC	*Open Circuit*
OPV	*Organic Photovoltaic*
PCE	*Power Conversion Efficiency*
PL	*Photoluminescence*
PV	*Photovoltaic*
QD	*Quantum Dot*
RH	*Relative Humidity*
RTIL	*Room Temperature Ionic-Liquid*
SC	*Short Circuit*
SEM	*Scanning electron microscopy*
SRH	*Shockley-Read-Hall (recombination)*
STEM	*Scanning Transmission Electron Microscope*
VB	*Valence Band*
WCA	*Water Contact Angle*
WVP	*Water Vapour Pressure*
XPS	*X-Ray Photoelectron Spectroscopy*
XRD	*X-Ray Diffraction*

Resumen

Debido al incremento de la demanda energética y al impacto medio ambiental derivado del uso de combustibles fósiles, las energías renovables se han posicionado en los últimos años como una alternativa limpia a las fuentes de energía tradicionales. Entre ellas, la energía solar fotovoltaica ha experimentado una revolución sin precedentes en los últimos años debido a la aparición de conceptos emergentes tales como los dispositivos solares basados en perovskitas organometálicas como material fotoactivo. Estos materiales fotovoltaicos se han convertido en competidores directos de las tecnologías convencionales gracias a sus extraordinarias propiedades optoelectrónicas y a la abundancia natural de sus precursores. No obstante, estos dispositivos de perovskitas presentan una serie de limitaciones que dificultan su producción a escala industrial. Estas son su baja estabilidad térmica y eléctrica en condiciones de operación y un tiempo de vida demasiado corto en condiciones ambientales.

Entender el funcionamiento fisicoquímico y electrónico de los procesos que determinan el rendimiento y la estabilidad de las celdas solares de perovskita es la clave para optimizar y comercializar estos dispositivos. Con esta motivación, esta tesis tiene como objetivo principal contribuir con un estudio profundo y fundamental de los diferentes mecanismos electrónicos e iónicos que determinan su respuesta fotovoltaica. En concreto, se han utilizado técnicas optoelectrónicas de pequeña perturbación (espectroscopía de impedancia y espectroscopía de fotocorriente modulada en intensidad) para tratar de entender los mecanismos de recombinación de carga que determinan el rendimiento fotovoltaico en dispositivos con diferentes arquitecturas y bajo diferentes condiciones de humedad. Estas técnicas se han usado también para explicar el fenómeno de la histéresis, el cuál se ha vinculado a los problemas de inestabilidad de los dispositivos de perovskitas. Paralelamente, hemos desarrollado modelos para interpretar la información que se puede extraer de las técnicas de pequeña perturbación. Finalmente, en esta tesis proponemos un nuevo parámetro de control para fabricar celdas solares de perovskitas de alta eficiencia en condiciones ambiente. Este nuevo parámetro, a la postre la presión parcial de vapor de agua, facilitaría la implementación industrial de esta tecnología ya que eliminaría la necesidad de usar cámaras de atmósfera controlada y trabajar, por ende, con dispositivos de mayor tamaño.

Agradecimientos

Es evidente que este trabajo no podría haberse realizado sin mis directores de tesis, Juan A. Anta y Jesús Idígoras. Gracias a los dos por vuestra dedicación, paciencia y apoyo, así como por haberme hecho sentir tan arropada durante estos tres años. Gracias Juan por la confianza prestada y por sacar tiempo, aún cuando no lo hay, para explicarme todo aquello que he necesitado. Gracias por tener en cuenta mis opiniones y por preocuparte de que la carrera investigadora que desarrollo sea prometedora. Jesús, gracias por tu gran acogida, por enseñarme todo lo que sabes y por invertir tanto tiempo en mi. Gracias por tu generosidad, por saber escuchar y tu compañía. Nunca supe que es tener un hermano mayor, pero intuyo que no debe alejarse mucho a como me tratas.

Gracias al resto de compañeros del grupo (pasados y presentes) por hacer las cosas fáciles. A Anna Todinova por enseñarme a tratar los datos de impedancia de las perovskitas y por animarme a hablar inglés. Gracias a Antonio Riquelme por su disposición a la ayuda y sus explicaciones del IMPS, y gracias a Susana Ramos por dejarme compartir con ella la frustración de las perovskitas.

Gracias también al resto de compañeros del área por crear un ambiente tan bueno de trabajo. Quisiera agradecer especialmente a Neftalí Morillo que me haya prestado siempre su ayuda tanto cuando se la he pedido como cuando ha visto que la necesitaba. Ha sido toda una suerte coincidir en esta etapa contigo.

Agradecer a Iván Mora el haberme acogido tan amablemente en su grupo durante mi breve estancia en el Instituto de Materiales Avanzados (INAM) en Castellón. Allí coincidí con Clara Aranda y Thi Tuyen a quienes les agradezco que me mostraran esos pequeños truquillos indispensables para hacer celdas eficientes de perovskitas.

Gracias a Thomas Berger por darme la oportunidad de trabajar durante tres meses bajo su tutela en la Universidad de Salzburgo. Gracias por darme un lugar en tu grupo, por pasar tiempo explicándome fotocatálisis y por propiciar que trabajara mano a mano con Juan Miguel Jiménez. Gracias Juanmi por tu compañía y ayuda así como por hacer de mi estancia en Salzburgo una experiencia inolvidable.

Gracias a Philippe Leclère por permitirme pasar unas semanas en su grupo en la Universidad de Mons y a su doctorando, Jaume Llacer, por sus explicaciones del microscopio de fuerza atómica.

Quisiera agradecer también a varios grupos de investigación las colaboraciones que han contribuido al desarrollo de esta tesis: al grupo de A. R. González-Elipe del Instituto de Ciencia de Materiales, al grupo de Alison B. Walker de la Universidad de Bath y a Javier Navas y Juan Jesús Gallardo de la Universidad de Cádiz.

Por último, quisiera dar las gracias a mi familia y amigos por su apoyo, ánimo y comprensión. A mis padres por traerme hasta aquí, y a Dani por su infinita paciencia y por creer más en mi de lo que yo muchas veces lo hago.